

Cover Page



Universiteit Leiden



The following handle holds various files of this Leiden University dissertation:  
<http://hdl.handle.net/1887/61006>

**Author:** Miotello, A.

**Title:** The puzzle of protoplanetary disk masses

**Issue Date:** 2018-03-07

# The puzzle of protoplanetary disk masses

## **Proefschrift**

ter verkrijging van  
de graad van doctor aan de Universiteit Leiden  
op gezag van de Rector Magnificus prof. mr. C. J. J. M. Stolker,  
volgens besluit van het College voor Promoties  
te verdedigen op woensdag 7 maart 2018  
klokke 11:15 uur

door

Anna Miotello

geboren te Gallarate, Italië  
in 1988

Promotiecommissie

Promotor Prof. dr. E. F. van Dishoeck

Co-promotor Dr. L. Testi ESO/INAF

Overige leden Prof. dr. E. A. Bergin University of Michigan

Prof. dr. I. Kamp Rijksuniversiteit Groningen

Prof. dr. I. Pascucci University of Arizona

Prof. dr. H. J. A. Röttgering

Prof. dr. A. G. G. M. Tielens

ISBN: 978-94-028-0940-4

Cover design by Laura Somaglino.

To my gang  
Carlo, Caterina, Ambrogio and Monica



---

# CONTENTS

<b>Chapter 1: Introduction</b>	<b>1</b>
1.1 Star formation and protoplanetary disks . . . . .	2
1.2 The Atacama Large Millimeter/submillimeter Array . . . . .	7
1.3 Disk dust mass determination . . . . .	9
1.4 Disk gas mass determination . . . . .	11
1.4.1 H <sub>2</sub> , the main gaseous component . . . . .	12
1.4.2 Gas masses from HD observations . . . . .	12
1.4.3 CO as gas mass tracer . . . . .	14
1.5 Physical-chemical modeling . . . . .	17
1.5.1 DALI . . . . .	17
1.6 This thesis and future outlook . . . . .	19
<b>Chapter 2: Protoplanetary disk masses from CO isotopologues line emission</b>	<b>23</b>
2.1 Introduction . . . . .	25
2.2 Model . . . . .	27
2.2.1 Isotope-selective processes . . . . .	28
2.2.2 Chemical network . . . . .	30
2.2.3 Parameters of the disk model . . . . .	31
2.2.4 Grid of models . . . . .	32
2.3 Results . . . . .	33
2.3.1 Abundances . . . . .	33
2.3.2 Line fluxes . . . . .	40
2.3.3 Line optical depth . . . . .	43
2.4 Discussion . . . . .	44
2.4.1 Beam convolutions . . . . .	44
2.4.2 Mass estimates . . . . .	47
2.4.3 TW Hya . . . . .	48
2.5 Summary and conclusions . . . . .	52

---

<b>Chapter 3: Determining protoplanetary disk gas masses from CO isotopologues line observations</b>	<b>55</b>
3.1 Introduction . . . . .	57
3.2 Model . . . . .	58
3.2.1 Physical structure . . . . .	59
3.2.2 Chemical network . . . . .	60
3.2.3 Grid of models . . . . .	61
3.3 Results . . . . .	65
3.3.1 Abundances . . . . .	65
3.3.2 Line intensities . . . . .	66
3.4 Discussion . . . . .	75
3.4.1 Comparison with parametric models . . . . .	75
3.4.2 Analysis of CO isotopologues observations . . . . .	79
3.4.3 Complementary tracers: [OI], [CI], and [CII] . . . . .	79
3.4.4 Effects of lower carbon abundance . . . . .	80
3.5 Summary and Conclusion . . . . .	81
Appendices	
3.A Additional tables and figures . . . . .	84
3.B Effects of carbon depletion on CO isotopologue line intensities . . . . .	93
<b>Chapter 4: Lupus disks with faint CO isotopologues: low gas/dust or high carbon depletion?</b>	<b>99</b>
4.1 Introduction . . . . .	101
4.2 ALMA observations . . . . .	103
4.3 Model . . . . .	103
4.4 Results . . . . .	104
4.4.1 Dust masses revisited . . . . .	104
4.4.2 Gas masses . . . . .	108
4.5 Discussion . . . . .	112
4.5.1 Gas-to-dust ratio . . . . .	112
4.5.2 Carbon depletion vs low gas masses . . . . .	113
4.5.3 Correlation between disk gas mass and stellar mass . . . . .	116
4.6 Summary and conclusion . . . . .	119
<b>Chapter 5: Probing protoplanetary disk gas surface density distribution with <sup>13</sup>CO emission</b>	<b>123</b>
5.1 Introduction . . . . .	125
5.2 Modeling . . . . .	127
5.2.1 DALI . . . . .	127
5.2.2 Grid of models . . . . .	127

---

5.3	Results	131
5.3.1	Simple power-law	131
5.3.2	Self-similar disk models	135
5.3.3	Inner disk surface density profile from C <sup>17</sup> O line intensity radial profiles	136
5.3.4	The “slope-pivot-region”	137
5.4	Discussion	139
5.5	Summary and conclusion	140

## Appendices

5.A	Additional figures	143
-----	--------------------	-----

## **Chapter 6: HD far infrared emission as a measure of protoplanetary disk mass**147

6.1	Introduction	149
6.2	Model	151
6.2.1	Density structure	152
6.2.2	Dust settling	152
6.2.3	Chemical network	153
6.2.4	Grid of models	154
6.3	Results	156
6.3.1	HD flux vs. disk gas mass	156
6.3.2	HD emitting layers	157
6.3.3	Influence of the vertical structure	159
6.3.4	Influence of the large grains	160
6.3.5	Influence of the gas-to-dust ratio	161
6.3.6	Line-to-Continuum ratios	164
6.3.7	Sensitivities of future FIR missions	166
6.4	Discussion	167
6.4.1	Determining the disk gas mass	167
6.4.2	HD 1-0 and HD 2-1 line fluxes	169
6.4.3	Comparing models to observations	170
6.4.4	Case study: TW Hya	171
6.5	Conclusions	174

## Appendices

6.A	Abundance and temperature maps of TW Hya	176
6.B	Abundance and emission maps of grid models	179
6.C	Effects of including hydrostatic equilibrium	181
6.C.1	The hydrostatic solver	181
6.C.2	Comparing with parametrized vertical structure	182
6.D	Deuterium chemistry	183

---

6.E Line fluxes of the TW Hya model . . . . .	184
---	-----

# 1

## INTRODUCTION

*The cosmos is within us.  
We are made of star-stuff.  
We are a way for the universe to know itself.*  
Carl Sagan

Since the beginning of human history, men have raised their eyes to the night sky and wondered about the meaning of such a majestic show (Fig. 12.1). Ancient civilizations from different parts of the world, from Egypt to China, from Oceania to southern America, have given life to myths and legends about the constellations and nebulosities that they could spot in the sky. Even throughout our European history many poets, painters and artists have taken inspiration from celestial events. The astonishment in front of the sky has always been accompanied by the need to understand the link between mankind and the universe. Now that science and technology have advanced and we are able to explain the physical and chemical structure of astronomical objects, this question has not been abandoned. Science has revealed to us that the connection of the cosmos with our existence is much deeper than any pre-scientific vision had dared to imagine. For example our knowledge on our hosting galaxy tells us that all phenomena happening in the Milky Way, from the presence of a black hole to that of supernova explosions up to the actual location of our Solar System, have cooperated to allow life to evolve up to the current status. Also, the growing zoo of discovered exoplanets allows us to compare their characteristics with those of our planetary system. Despite the large statistics, it seems that the configuration of our own Solar System is very “special” as shown by Morbidelli & Raymond (2016). Based on exoplanet observational surveys, the Sun-Jupiter system is as common as one in a thousand. On the other hand theoretical modeling favors Jupiter as the fundamental player in the Solar System’s evolution (Walsh et al. 2011; Izidoro et al. 2015).



**Figure 1.1:** The galactic center and dusty Milky Way as seen on March 26, 2017 on a new moon night from Cerro Paranal (photo taken by the author with Reflex camera, exposure 30s).

## 1.1 Star formation and protoplanetary disks

The question about our origins centers around star and planet formation. How do stars and planets orbiting around them form? What are the initial conditions needed to generate a planetary system similar to our own? Which roles do the physical architecture and chemical composition of these forming systems play?

On large scales, star formation begins with the formation of filamentary structures inside giant molecular clouds ( $\sim 10 - 100$  pc). Observations have shown that filaments are elongated structures with widths of  $\sim 0.1$  pc (André et al. 2010; Kennicutt & Evans 2012). Within these long filaments, typically several pc-long dozens of smaller fibers are created (Hacar et al. 2013) and eventually fragment into dense cores (Hacar & Tafalla 2011). These are defined as *prestellar cores* ( $n \sim 10^4 - 10^5 \text{ cm}^{-3}$ ), as they will likely collapse to form one or more stars. As the collapse proceeds, due to conservation of angular momentum a rotating disk-like structure is formed, through which matter accretes onto the forming protostar (Fig. 1.2). This is called either a *cir-*

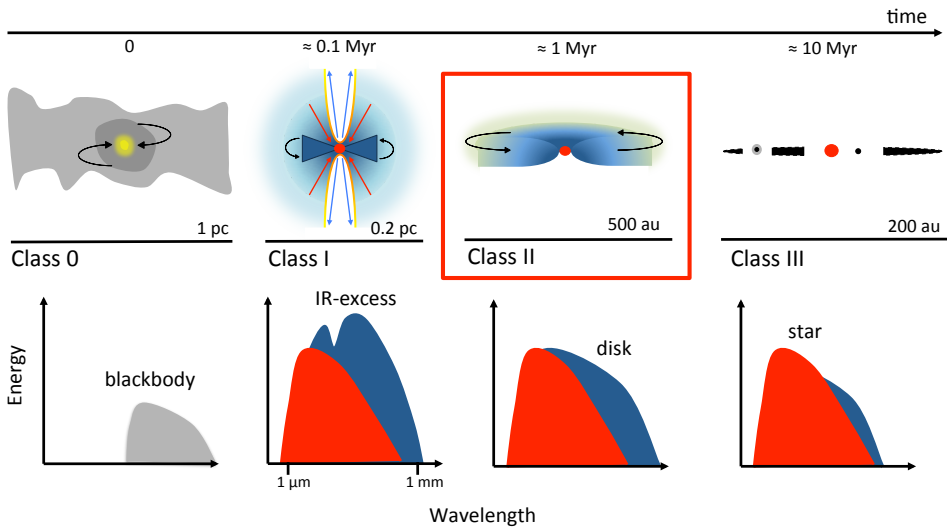


**Figure 1.2:** Sketch of the star and planet formation process in isolation. In the upper panel different evolutionary classes are sketched, while in the lower panel the respective observational features are shown through schematic SEDs. This thesis focuses on the stage of a pre-main sequence star with a disk, called the Class II stage.

*cumstellar disk*, or *accretion disk*, or *protoplanetary disk* depending on the community. The idea that the solar system was born from nebulous material was firstly introduced by Emanuel Swedenborg in 1734 and further developed by Immanuel Kant in 1755 as the *nebular hypothesis*. Afterwards, in 1796, Pierre-Simon Laplace proposed an independent but similar model, where the forming Sun was surrounded by a hot atmosphere. Such material would cool and flatten with time, creating rotating rings from which planets would form. This theory had some problems in explaining the angular momentum distribution between the Sun and planets. Therefore, Laplace's idea was abandoned at the beginning of the 20th century. The study of stellar accretion disks started then as a purely theoretical field in the 1970s from the work by Shakura & Sunyaev (1973). This was motivated by observations of accretion onto black holes in binary system, but the simple physical model proposed by Shakura & Sunyaev (1973) turned out to be applicable also for circumstellar disks. The first indirect observational evidence of circumstellar disks came then in the late 1980s at optical and mm wavelengths (Hartmann & Kenyon 1985, 1987; Sargent & Beckwith 1987). The advent of the *Infrared Astronomical Satellite* (IRAS) allowed a wider study



---

of disk properties through their Spectral Energy Distributions (SEDs) published by Strom et al. (1989). This statistical work was followed-up with a survey at mm wavelengths by Beckwith et al. (1990) which provided the first disk mass estimates from continuum emission from cold dust. The first direct image of a protoplanetary disk was taken some years later by O'dell & Wen (1994) with the *Hubble Space Telescope* (HST), which allowed to study disk morphology in much detail thanks to its high angular resolution. Interestingly, the first direct image of a gas-poor disk,  $\beta$  Pic, around a young star was taken by Smith & Terrile (1984), earlier than for gas-rich classical disks.

Our physical understanding of the different stages of star and planet formation is linked to an observational classification done based on studies of the SED shapes of different Young Stellar Objects (YSOs) in the mid- to near-infrared (MIR to NIR). Historically, it was expected that the release of accretion luminosity would be very bright in the infrared (see Wynn-Williams 1982, as a review). Therefore, much work went into surveying protostars at such wavelengths, but the amount of extinction and radiation reprocessing provided by the infalling material was underestimated. As shown by the sketch in Fig. 1.2, three different SED slopes were detected and used to classify Class I, Class II and Class III objects (Lada 1987).

- **Class I** YSOs are typically visible in the near IR, but not in the optical, with a rising spectrum in the mid-Infrared (mid-IR), called IR-excess. This is interpreted as a contribution of the forming star and disk to the thermal emission due to the presence of warm dust. An extended structure, called envelope, is still present and emits at longer wavelengths but its mass is much smaller than the protostar mass.
- **Class II** YSOs are optically visible with a decreasing SED in the IR. At short wavelengths the emission is dominated by the star, while the disk component emits at larger wavelengths. At this stage the envelope is completely dissipated and the disk is gas rich.
- **Class III** YSOs are also optically visible but they do not show any IR-excess. The disk is gas poor and larger bodies, such as planets and asteroids, must be already formed at this stage.
- Subsequently a stage even less evolved than the Class I phase, i.e. **Class 0** YSOs, was defined observationally by André (1995) as embedded YSOs which have  $L_{\text{submm}}/L_{\text{bol}} > 5 \times 10^{-3}$ ;  $L_{\text{submm}}$  is the sub-millimeter luminosity measured at wavelengths larger than  $350 \mu\text{m}$  and  $L_{\text{bol}}$  is the total bolometric luminosity. Class 0 sources are not detected in the NIR, but most of their emission ( $\gtrsim 99\%$  of the luminosity) is in the far-infrared. Class 0 protostars are bright in the  $50\text{-}200 \mu\text{m}$  range, which however unfortunately cannot be observed from

---

the ground. Moreover these embedded sources have strong emission in the sub-mm dominated by cool dust in the envelope ( $T_{\text{dust}} \sim 30\text{-}50$  K). At this stage the envelope mass is much larger than the forming protostar mass.

The focus of this thesis is on protoplanetary disks in their gas rich Class II phase through the modeling of their bulk gas component. Disks are generally divided in two categories, depending on the type of protostar they are orbiting around: T Tauri or Herbig. Herbig Ae/Be protostars are the higher mass counterparts of T Tauri protostars, with spectral types A and B and masses  $M_{\star} \gtrsim 2M_{\odot}$ . T Tauri stars are more common (spectral types K and M) and often show a characteristic ultraviolet (UV) excess in addition to the stellar photosphere, which is more prominent than in Herbig stars. The Herbig stars are widely studied as they are very bright, and so are also their disks. The process of high-mass star formation is far less understood than the low-mass star formation and will not be considered in this PhD thesis. The same holds for Brown Dwarfs (BDs), whose formation process is not studied here.

## Planet formation

How protoplanetary disks evolve from their gas rich phase to the formation of planetary systems is still an open question. Many planet formation theories have been developed so far, but none is able to correctly reproduce the needed timescales, or the properties observed in exoplanetary systems, as well as in our own solar system. The favorite scenario starts however with the coagulation of small (sub  $\mu\text{m}$ -sized) dust particles into larger pebbles, all the way out to planetary rocky cores (Hayashi 1981; Pollack et al. 1996). Dust growth can start already in the embedded phase (e.g. Miotello et al. 2014a) and as the ISM-like grains grow to larger sizes they start to decouple from the gas. They suffer a strong drag force and settle toward the midplane, where they can grow to even larger sizes due to the enhanced dust density. As they grow up to mm-cm sizes they start to drift inward and their velocity is maximized when they reach the meter size (at 1 au). As a consequence fragmentation due to collision becomes an important effect which stops the growth to larger bodies. Moreover the drift toward the central star becomes very fast, with timescales much shorter than those needed to grow larger bodies (Dullemond & Dominik 2005). This problem is known as the *meter size barrier* and was first formulated by Weidenschilling (1977).

A possible solution is found if a pressure maximum is present in the disk, which would trap the dust particles in a localized region of the disk (Whipple 1972). Such dust traps have been observed and modeled in protoplanetary disks and are thought to be created by gap-opening planets, vortices, or dead zones (Varnière & Tagger 2006; Armitage 2011; Zhu et al. 2011; Pinilla et al. 2012; Regály et al. 2012). Once the meter size barrier is overcome, as this must happen somehow, grain growth continues to reach planetesimal sizes, all the way to rocky planets. Once the planet

---

core reaches 10 Earth masses, gas can be accreted to form giant gaseous planets, as predicted by the *core accretion model*. This must occur before the gaseous disk is dispersed. Alternatively gas giants could be formed via *gravitational instability*, a very fast process which could occur already in the embedded phases of protoplanetary disks when they are massive and cold enough (Helled et al. 2014). Both theories alone however fail to reproduce the statistics on exoplanets orbits. The core-accretion model is able to explain  $\sim 90\%$  of the observed exoplanets, while the rest could be formed by gravitational instabilities (Matsuo et al. 2007).

### Disk dispersal

Disks are traditionally thought to undergo viscous evolution, which redistributes angular momentum within the disk and leads to accretion of matter onto the central star. Mass accretion would then be responsible for the dissipation of the disk material. In particular the mass accretion rate  $\dot{M}_{\text{acc}}$  onto the central protostar is theoretically expected to scale with the disk mass, and there is observational support for this as shown by Manara et al. (2016b). The exact mechanism responsible for viscous evolution is not yet known, but the favorite candidate is magneto-rotational instability (see Turner et al. 2014, as a review). One key problem is that viscous evolution alone is not efficient enough to account for the fast disk dispersal timescales that are observed in young stellar clusters ( $\sim 5$  Myr, Fedele et al. 2010, and reference therein). A process has to take over disk dispersal at  $2 - 6$  Myr as viscous evolution alone would imply disk dispersal timescales exceeding  $10^7 - 10^8$  yrs.

Some other effects may modify or overtake viscous evolution in disks. For instance magnetically driven winds may be extremely efficient in removing material from the disk but quantitative constraints are not yet available (Armitage et al. 2013; Bai et al. 2016). On the other hand, photoevaporation from the central object, or from external sources, may play an important role in dispersing the disk and extensive studies have been carried out on this subject (Johnstone et al. 1998; Clarke et al. 2001; Adams et al. 2004; Owen et al. 2010; Anderson et al. 2013; Facchini et al. 2016). Finally, the environment can further affect disk evolution by physical encounters. A disk can be truncated by the gravitational encounter with another member of its star-forming region.

### Main questions

One of the fundamental properties of disks is the total *mass*, as it determines their physics, evolution and the characteristics of the planetary outcomes. Nevertheless disk masses are not yet observationally determined with high confidence. Disks are composed of gas and dust grains, as are molecular clouds and cores. The dust does not have the ISM size distribution however, but the grains can easily reach mm-size

---

and such grains, which dominate the dust mass in disks, are not necessarily well mixed with the gas. Accordingly the mass determination of the gaseous and dusty components should in principle be carried out independently. Most of the disk mass is expected to be in the form of molecular gas, essentially molecular hydrogen ( $\text{H}_2$ ). However,  $\text{H}_2$ , under the disk thermo-physical conditions, is not easily excited and observable. Hence, traditionally, the presence of gas in disks has been constrained through carbon monoxide (CO) emission lines, easily excited in disks. However the emission is generally very optically thick, so using CO to measure accurately the gas mass is very difficult and model dependent. The main questions that are tackled in this PhD thesis are the following.

- Which is the best gas mass tracer in protoplanetary disks? Could the less abundant isotopologues of CO serve this purpose? Would hydrogen deuteride (HD) be a good alternative and what are its limitations?
- How can current and future ALMA observations be used to determine the masses of a statistically significant sample of disks?
- What is the actual gas-to-dust mass ratio in disks and how is its determination affected by elemental carbon and oxygen depletion?

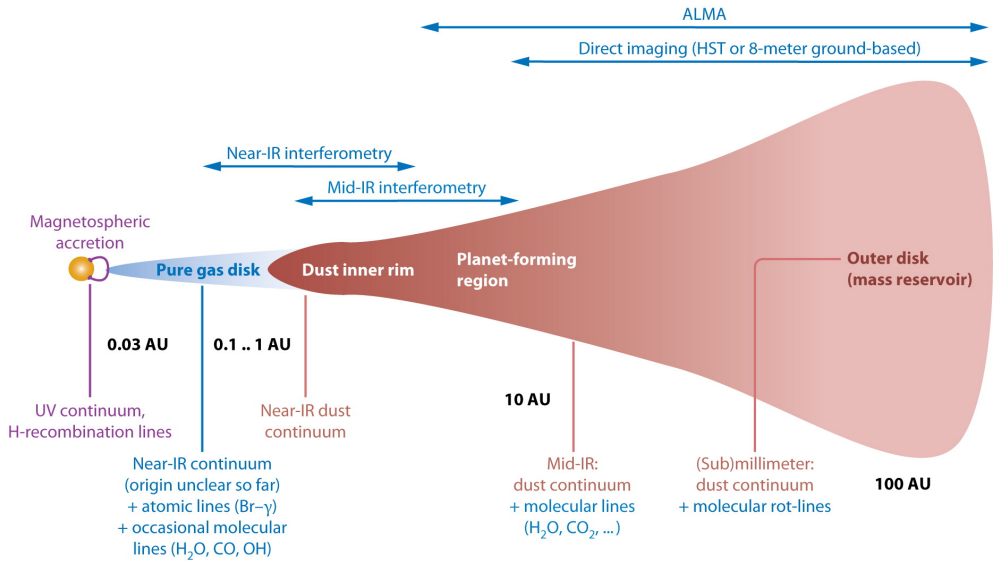
## 1.2 The Atacama Large Millimeter/submillimeter Array

Great improvements in the study of protoplanetary disks and their mass determination have been brought by the advent of ALMA, the Atacama Large Millimeter/submillimeter Array. This is a single facility composed of 66 high precision antennas located on the Chajnantor plateau, 5000 meters altitude in northern Chile.

ALMA<sup>1</sup> is sensitive to wavelengths where the bulk of the dust and molecular gas in disks emit (see Fig. 1.3). Moreover its extraordinary sensitivity and angular resolution allow to detect and resolve disk emission at high signal-to-noise (S/N) levels. It is very illustrative to compare ALMA current capabilities with some pre-ALMA interferometers, such as the Submillimeter Array (SMA), that has served the disk community for many years before. ALMA can achieve a continuum rms noise level below  $0.1 \mu\text{Jy}$  in less than one hour, while SMA would take approximately 81 nights to reach the same sensitivity.

---

<sup>1</sup>ALMA is an international partnership of the European Southern Observatory (ESO), the U.S. National Science Foundation (NSF) and the National Institutes of Natural Sciences (NINS) of Japan, together with NRC (Canada), NSC and ASIAA (Taiwan), and KASI (Republic of Korea), in cooperation with the Republic of Chile.



**AR** Dullemond CP, Monnier JD. 2010. *Annu. Rev. Astron. Astrophys.* 48:205–39

**Figure 1.3:** 2D sketch of a disk where its different regions are connected to the wavelength range in which it is observable. The top arrows show which techniques can spatially resolve which scales (from Dullemond & Monnier 2010). ALMA is very well suited to study the outer disk, where most of the mass is enclosed.

The ALMA disk community is following mainly two complementary observational strategies. On one hand complete surveys of disks are carried out to statistically study simultaneously the dust, through mm-continuum emission, and gas, through CO isotopologues (see Ansdell et al. 2016; Pascucci et al. 2016; Barenfeld et al. 2016; Ansdell et al. 2017, Fig. 1.4). Such surveys show that the bulk of the disk population is much fainter and possibly smaller than what we assumed as the average disk before the ALMA era. On the other hand the well studied large and bright disks, such as e.g. TW Hya (Fig. 1.5), HD163296, HL Tau, are now observed at extremely high angular resolution revealing exciting substructures that may be common in most if not all protoplanetary disks (ALMA Partnership et al. 2015; Andrews et al. 2016; Isella et al. 2016). Moreover, large cavities in gas and dust are observed in a subset of so-called *transitional disks* (see e.g. van der Marel et al. 2015, 2016). The results coming from both paths are transforming the field by complementing each other.

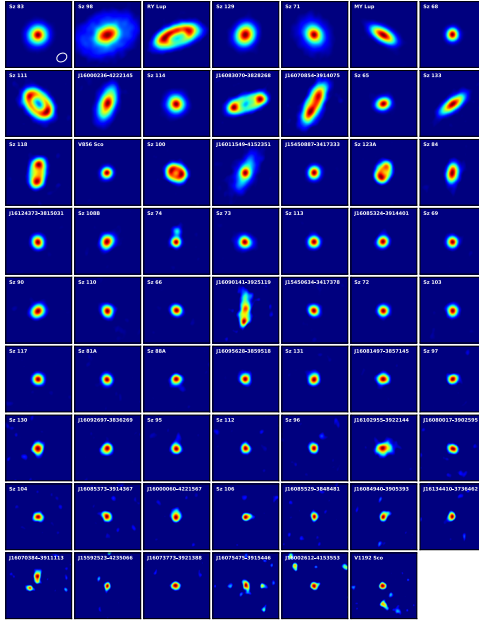


**Figure 1.4:** Dust continuum emission observed with ALMA in Band 7 for a large sample of disks in the Lupus star-forming region ( $d=150$  pc) at a resolution of  $\sim 0.3''$  ( $\sim 20 - 30$  au radius Ansdell et al. 2016). Each panel is  $2'' \times 2''$ . This "zoo" presents very different disk morphologies and a surprisingly high fraction of sources which appear very compact at this resolution and S/N.

The *Lupus disk survey* with ALMA (PI: J. P. Williams, Ansdell et al. 2016, Fig. 1.4) has provided most of the new observational constraints that have been employed in this thesis. More details will be presented in Chapter 4.

### 1.3 Disk dust mass determination

Dust is traditionally assumed to account only for 1% of the total disk mass. This comes from the assumption that disks present the same gas-to-dust ratio as that found in molecular clouds. In clouds the combination of various types of analyses has suggested that a factor of 100 is correct. Nevertheless, the mm-sized grains thermally emit broadband continuum radiation at mm wavelengths. Therefore dust emission from protoplanetary disks can be very bright and readily detectable by

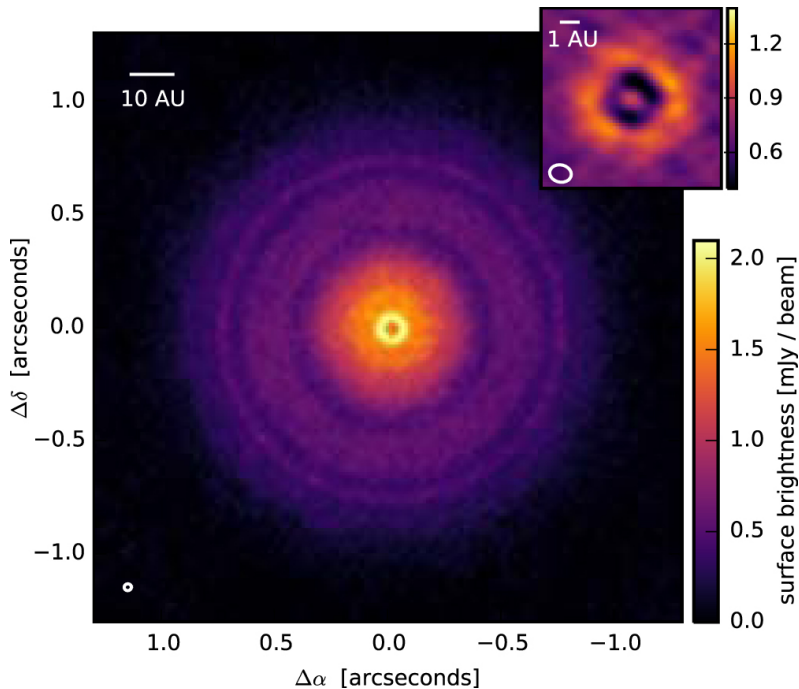


**Figure 1.5:** ALMA image of the  $870 \mu\text{m}$  continuum emission from the closest disk, TW Hya. The circular beam FWHM is 30 milliarcseconds, corresponding to a resolution of 1.6 au. The top right panel shows a zoomed region which is  $0.2''$  wide (10.8 au), highlighting the 1 au gap seen in the inner disk. (Credit: S. Andrews - Harvard-Smithsonian CfA, Andrews et al. 2016)

(sub-)mm interferometers. A number of studies of dust in disks have been carried out, several already with pre-ALMA interferometers, and are summarized in recent reviews (Williams & Cieza 2011; Dutrey et al. 2014; Testi et al. 2014; Andrews 2015).

At mm-wavelengths the dust thermal emission is generally in the optically thin regime for surface densities of  $\lesssim 3 \text{ g cm}^{-2}$  and the Rayleigh-Jeans approximation holds (Beckwith et al. 1990). Therefore it is straightforward to derive the following relation:

$$M_{\text{dust}} = \frac{F_{\nu} d^2}{\kappa_{\nu} B_{\nu}(T_{\text{dust}})} \quad (1.1)$$

(Hildebrand 1983). The mass retained in mm-sized grains  $M_{\text{dust}}$  is directly proportional to the flux at mm wavelengths  $F_{\nu}$ , where  $\nu \sim 300 \text{ GHz}$ . The other three variables involved are the distance of the source  $d$ , the dust opacity  $\kappa_{\nu}$  and the Planck function for a characteristic dust temperature  $B_{\nu}(T_{\text{dust}})$ .

---

The large observational uncertainty on  $d$  is being overcome by the advent of the GAIA mission, which is providing a new distance catalog with micro-arcsecond precision on the parallaxes. The SED can provide constraints on the dust temperature  $T_{\text{dust}}(r, z)$ , which is generally non constant throughout the disk. It is known that the disk temperature structure has vertical and radial gradients in the disk, making the surface layers much warmer than the midplane, which is however the region probed by mm-sized grains emission. These temperatures are generally low and constant and  $T_{\text{dust}}$  is often assumed to be  $\sim 20$  K, as this is the average dust temperature found in the outer disk in the Taurus star forming region (Andrews & Williams 2005). The dust opacity  $\kappa$  quantifies the dust absorption cross-section per unit mass. The opacity can be approximated by a power law of the frequency,

$$\kappa_{\nu} = \kappa_0 \left( \frac{\nu}{\nu_0} \right)^{\beta} \quad (1.2)$$

(Draine 2006). The normalization  $\kappa_0$  and the power law index  $\beta$  depend on the composition, shape and the size distribution of the dust grains (Pollack et al. 1994; Ossenkopf & Henning 1994). The latter can be constrained by multi-wavelength (sub-)millimeter continuum observations, as  $\beta = \alpha - 2$  in the optically thin and Rayleigh-Jeans regime, where  $\alpha$  is the measured spectral index (e.g. Ricci et al. 2010; Tazzari et al. 2016, and reference therein).

The total dust surface area is in the smallest sub- $\mu\text{m}$  sized grains but the total dust mass is mostly within the larger mm-sized particles (Testi et al. 2014). Therefore, mm continuum emission is a good probe of the bulk of the dust component in disks. Anyway, such observations can only provide a lower limit of the total mass of solids, as larger bodies are completely invisible at these and other wavelengths.

Traditionally dust masses are then converted in total disk masses by multiplying for a constant gas-to-dust ratio of 100, as that found in the ISM (Goldsmith et al. 1997). Recent higher resolution disk observations carried out with ALMA have shown that this assumption is not necessarily correct, as dust and gas emission present two different distributions.

## 1.4 Disk gas mass determination

Dust mass measurements are important to determine the evolution of dust particles to larger solids, all the way to planet formation. However, as the gas is the disk's dominant constituent, this controls the disk dynamics and evolution, including that of the dust. It would be ideal thus to measure disk gas masses directly from a gaseous tracer and independently from dust mass measurements.



---

### 1.4.1 H<sub>2</sub>, the main gaseous component

Molecular hydrogen (H<sub>2</sub>) is the main gaseous species present in disks but it does not strongly emit due to its molecular physics (Field et al. 1966). H<sub>2</sub> is light and the energy spacings between its rotational levels in the ground vibrational state are large. Furthermore, being a symmetric molecule it has no dipole moment but only weaker quadrupole transitions.

The fundamental ground state transition of molecular hydrogen is the  $J = 2 - 0$  or S(0) line, which has an energy spacing of 510 K at 28.2  $\mu\text{m}$ . This large energy spacing combined with the weaker quadrupole Einstein A coefficient makes it hard for H<sub>2</sub> to emit appreciably in cold environments such as protoplanetary disks with typical gas temperatures  $T_{\text{gas}} = 20$  K. One would need much higher temperatures,  $T_{\text{gas}} > 100$  K, which can be found only in the inner disk regions. Within a few tens of astronomical units (au) from the central star the large dust column densities imply high dust optical depths at 28.2  $\mu\text{m}$ , however. Thus, the emission of the warm gas where the ground state line of H<sub>2</sub> can be excited can be shielded by the optically-thick dust layer (Thi et al. 2001; Pascucci et al. 2006; Carmona et al. 2008; Bitner et al. 2008; Bary et al. 2008). Even if detected, H<sub>2</sub> is not a good tracer of the bulk of the disk mass which is retained in the outer disk regions (Pascucci et al. 2013).

Given that direct detection of molecular hydrogen is extremely difficult, one needs to find indirect tracers of the gas mass in protoplanetary disks.

### 1.4.2 Gas masses from HD observations

The closest molecule to H<sub>2</sub> is its less abundant isotopologue hydrogen deuteride (HD). HD chemistry is similar to that of H<sub>2</sub> as it does not freeze-out onto grains. Other molecules, e.g. CO and less volatile species, cannot survive in the gas phase at low temperatures but stick onto the icy grains through the so-called process of freeze-out (see Sect. 1.4.3). Also HD, like H<sub>2</sub>, can self-shield itself from the photodissociating UV photons, but at reduced efficiency (Wolcott-Green & Haiman 2011). The abundance of HD with respect to H<sub>2</sub> is  $\sim 3 \times 10^{-5}$ , obtained assuming the local [D]/[H] value but accounting for the fact that 2 hydrogen atoms compose molecular hydrogen.

In contrast to H<sub>2</sub>, HD has a small dipole moment which allows dipole transitions ( $\Delta J = 1$ ). The energy difference between the first and second rotational levels of HD is of  $\sim 20$  K and this means that at a temperature of  $T_{\text{gas}} \sim 20$  K the expected emission of HD is much larger than that of molecular hydrogen (see Fig. 1.6). The fundamental rotational transition of HD is at 112  $\mu\text{m}$  (Müller et al. 2005) and it was first detected in the ISM by the *Infrared Space Observatory* (ISO, Wright et al. 1999). It was also covered with increased sensitivity by the PACS instrument on the *Herschel Space Observatory*. This transition has been targeted for a sample of close and bright

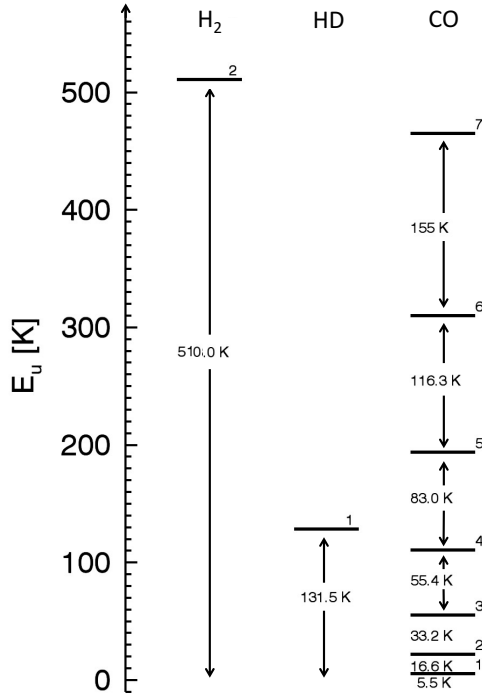


**Figure 1.6:** Rotational energy levels for  $H_2$  (left), HD (middle) and CO (right). The energy needed to excite the different transitions are reported in Kelvin and are much higher for  $H_2$ , than for HD and CO. In particular, thanks to its low- $J$  lines, CO is a good coolant even in cold environments such as disks.

protoplanetary disks, for a total of only 3 detections: TW Hya (Bergin et al. 2013), DM Tau, and GM Aur (McClure et al. 2016). The clear detection of HD in TW Hya was an important result as a very high disk mass, larger than  $5 \times 10^{-2} M_{\odot}$ , was determined for a relatively old disk ( $\sim 10$  Myr).

There are however some caveats in the conversion of HD into total disk mass. The main issue is that the emitting layer of the HD  $112 \mu\text{m}$  line is elevated above the midplane, where the gas temperature is larger than 30 K. This implies that a good knowledge of the disk vertical structure is needed in order not to under- or over-estimate the disk mass. Proper physical-chemical modeling combined with tracers of the disk vertical extent are needed to reduce the uncertainty related to HD-based mass determinations (see Chapter 6).

### 1.4.3 CO as gas mass tracer

In disks, carbon monoxide (CO) is the second most abundant molecule after  $H_2$  and it is the main gas-phase carrier of interstellar carbon. Furthermore, CO is chemically stable, it has a well studied chemistry and readily implemented in physical-chemical models, and is readily detectable. For these reasons carbon monoxide and its less abundant isotopologues are often used as tracers of gas properties, structure and kinematics in disks and in various other astronomical environments. In particular optically thin lines of less abundant isotopologues, which trace the gas column down to the midplane (van Zadelhoff et al. 2001), can be used as gas mass tracers. This however requires knowledge about the CO- $H_2$  abundance ratio. Surprisingly, the overall range of CO abundances in different environments such as molecular clouds, excluding the pre-stellar case where the effects of freeze-out are prevalent, is quite narrow between  $CO/H_2 \sim 0.5 - 4 \times 10^{-4}$  (see review by Bergin & Williams 2017, and references therein). If isotopologue lines are used, the elemental isotopic ratio is then an additional unknown parameter.

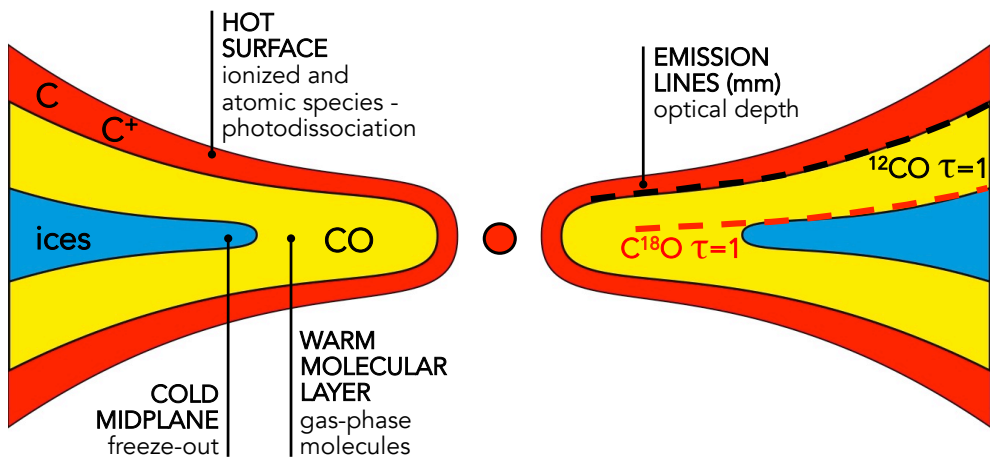


Figure 1.7: Simplified description of the disk thermo-chemical structure.

#### CO isotope-selective photodissociation and freeze-out

The main processes controlling the survival of carbon monoxide in the gas-phase in protoplanetary disks are CO *photodissociation* by UV photons and CO *freeze-out* onto dust grains (see Fig. 3.1).

CO photodissociation occurs through discrete (line-) absorption of UV photons into predissociative excited states, while absorption of continuum photons is negligible (Hudson 1971; Letzelter et al. 1987; Eidelsberg et al. 1992; Cacciani & Ubachs 2004). The energy needed to dissociate CO is 11.09 eV, thus CO photodissociation is initiated by photons at wavelengths between 911.75 Å and 1117.8 Å. The UV absorption lines are electronic transitions into vibrational levels of excited states and can become optically thick. This makes CO able to shield itself from photodissociating photons. More precisely the UV absorption lines of the main isotopologue  $^{12}\text{CO}$  become optically thick at a CO column density  $\sim 10^{15} \text{cm}^{-2}$  (van Dishoeck & Black 1988). In disks, this column density is reached at the surface of the warm molecular layer (Fig. 3.1). At a given height in the disk the photodissociation rate drops and CO is able to survive, both because of self-shielding and absorption of FUV continuum attenuation by small dust grains or PAHs.

Photodissociation occurs in a similar manner also for rarer isotopologues (e.g.,  $^{13}\text{CO}$ ,  $\text{C}^{18}\text{O}$ , and  $\text{C}^{17}\text{O}$ ), which can self-shield from UV photons and also mutually shield each other (Visser et al. 2009). Being less abundant than  $^{12}\text{CO}$ , self-shielding happens at higher column densities for rarer isotopologues and accordingly closer to the disk mid-plane. There are regions in the disk where  $^{12}\text{CO}$  is already self-shielded and can survive at high abundance, but the rare isotopologues are still photodissociated. There one would find isotopologue ratios (e.g.  $\text{C}^{18}\text{O}/^{12}\text{CO}$ ) that are much lower than the corresponding elemental isotope ratio  $^{18}\text{O}/^{16}\text{O}$ . In chemical models of disks, the abundance of the rare isotopologues is usually obtained by simply scaling the  $^{12}\text{CO}$  abundance with the local ISM elemental isotope ratio (Wilson & Rood 1994). However, in order to correctly interpret CO isotopologues observations, isotope-selective photodissociation needs to be included in the modeling.

Photodissociation rates are also affected by other effects in a depth-dependent manner. In particular, mutual-shielding adds to self-shielding when the UV absorption lines are blended with other species. More precisely, less abundant CO isotopologues can be mutually shielded by  $^{12}\text{CO}$ , as well as by H and  $\text{H}_2$ , if their UV absorption lines overlap. Moreover, at greater depths, the UV continuum radiation is attenuated by small dust grains and PAHs. The photodissociation rate for a particular isotopologue  $^x\text{C}^y\text{O}$  can be expressed by the following equation

$$k_{\text{PD}} = \Theta [N(\text{H}), N(\text{H}_2), N(^{12}\text{CO}), N(^x\text{C}^y\text{O})] k_{\text{PD}}^0, \quad (1.3)$$

where  $\Theta$  is a shielding function depending on the H,  $\text{H}_2$ ,  $^{12}\text{CO}$ , and  $^x\text{C}^y\text{O}$  column densities, and  $k_{\text{PD}}^0$  is the unshielded photodissociation rate, calculated using the local continuum radiation field. Detailed shielding functions for the various CO isotopologues have been computed by Visser et al. (2009) and adopted in this work.

At the low dust temperatures reached in the disk midplane and far from the central star, CO can freeze-out onto grains. This would decrease the amount of CO in

---

the gas-phase, reducing the line emission. CO freeze-out is a process of particular interest because CO ice is a starting point for prebiotic chemistry (Herbst & van Dishoeck 2009). Unlike photodissociation, freeze-out does not selectively affect different isotopologues, but it needs to be taken into account when modeling disk CO observations. The freeze-out temperature of carbon monoxide is  $\sim 20$  K for a pure CO ice with a binding energy of 855 K measured in the laboratory (Bisschop et al. 2006). It can vary between 17 K and 30 K varying the assumed density and binding energy in mixed ices (see Harsono et al. 2015, and reference therein).

### **[C]/[H] ratio and volatile carbon depletion**

Both CO photodissociation and freeze-out are molecular processes that have been very well characterized in the laboratory and are readily implemented in physical-chemical codes. However, there are additional processes that play a role in reducing the CO abundance with respect to molecular hydrogen. In particular, chemistry can act to reduce the volatile carbon budget available to create CO.

TW Hya, the closest and probably best studied disk, has been observed in the fundamental rotational transition of hydrogen deuteride (HD) with the *Herschel Space Observatory* (Bergin et al. 2013). Comparing with SMA  $C^{18}O$  data, Favre et al. (2013) found that the CO-based disk mass was two orders of magnitudes lower than the HD-based disk mass. This result has been confirmed by physical-chemical modeling of the source where freeze-out and isotope-selective photodissociation were treated explicitly (Kama et al. 2016b; Schwarz et al. 2016; Trapman et al. 2017, Chapter 6). This result has been interpreted as a large depletion of volatile carbon happening in the disk and leading to much fainter CO isotopologues lines. Similar results have then been more recently found in other two sources that were detected in HD (McClure et al. 2016).

Volatile carbon depletion may therefore be a more common process than what was initially thought. Which mechanism(s) is (are) responsible for carbon depletion in protoplanetary disks is still under debate. A possible explanation comes from gas-phase reactions initiated by X-ray and cosmic ray ionization of He. The resulting  $He^+$  atoms can react with gaseous CO and gradually extract the carbon, which can then be processed into more complex and less volatile molecules that can freeze onto cold dust grains at higher temperatures than CO (Aikawa et al. 1997; Bruderer et al. 2012; Favre et al. 2013; Bergin et al. 2014; Kama et al. 2016b; Yu et al. 2016). In addition, oxygen will also be removed from the gas due to freeze out of  $H_2O$ ,  $CO_2$  and CO, even more than carbon (Öberg et al. 2011; Walsh et al. 2015). Accordingly, a way to test the level of carbon depletion in disks is to compare observations of CO isotopologues with species like  $C_2H$  and  $c-C_3H_2$ , whose gas-phase abundances are particularly sensitive to the gaseous carbon abundance and  $[C]/[O]$  ratio. Indeed,  $C_2H$  is observed to have very strong emission in the TW Hya disk (Kastner et al.

---

2015; Bergin et al. 2016) and is particularly strong when both elements are depleted but gaseous  $[C]/[O]>1$  (Kama et al. 2016b). Alternatively, ice chemistry may be the fundamental process turning CO in more complex organics, such CH<sub>3</sub>OH, or in CO<sub>2</sub> and CH<sub>4</sub> ice (see e.g. Fig. 3c in Eistrup et al. 2016). Finally, volatile elements, such oxygen and carbon, may be locked up in large icy bodies in the midplane (Bergin et al. 2010; Hogerheijde et al. 2011; Du et al. 2017; Schoonenberg & Ormel 2017). These large pebbles cannot diffuse upward and participate in the gas-phase chemistry (see Du et al. 2015; Kama et al. 2016b). Such a process is likely the cause of the underabundance of gas-phase water in the surface layers of disks. Another way to trace the level of the volatile carbon available in the disk surface is through observations of the [CI] fine structure lines, as shown e.g. by Kama et al. (2016b).

## 1.5 Physical-chemical modeling

CO chemistry is fairly simple when compared with other molecules of astronomical interest. However, CO emission lines are sensitive to the gas and dust temperatures, which can vary significantly throughout the disk structure. A good thermo chemical-physical modeling of disks is therefore needed in order to interpret carbon monoxide observation in disks, and of its less abundant isotopologues. For this PhD thesis, the physical chemical code DALI (DustAndLines Bruderer et al. 2012; Bruderer 2013; Bruderer et al. 2014, see 1.5.1) has been used. Similar modeling codes are ProDiMo (Protoplanetary Disk Modeling Voitke et al. 2009), developed for the interpretation of IR lines observed with *Herschel*, ANDES (Akimkin et al. 2013), and the models by Gorti & Hollenbach (2004); Jonkheid et al. (2004).

### 1.5.1 DALI

DALI is a powerful physical-chemical code developed by Dr. Simon Bruderer and designed to model CO and simple molecules in disks, with a focus on the gas-phase. As low- $J$  CO lines arise from disk regions where the gas and dust temperatures are slightly decoupled, a proper modeling of the disk gas and dust thermal structure is needed and this is DALI's specialty. The modeling structure is presented in the flowchart in Fig. 1.8. Given a density structure and a stellar spectrum as inputs, the code solves the continuum radiative transfer using a 3D Monte Carlo method to calculate the dust temperature  $T_{\text{dust}}$  and local continuum radiation field from UV to mm wavelengths. A chemical network simulation then yields the chemical composition of the gas. The chemical abundances enter a non-LTE excitation calculation of the main atoms and molecules. The gas temperature  $T_{\text{gas}}$  is then obtained from the balance between heating and cooling processes. Since both the chemistry and the molecular excitation depend on  $T_{\text{gas}}$ , the problem is solved iteratively. At each point

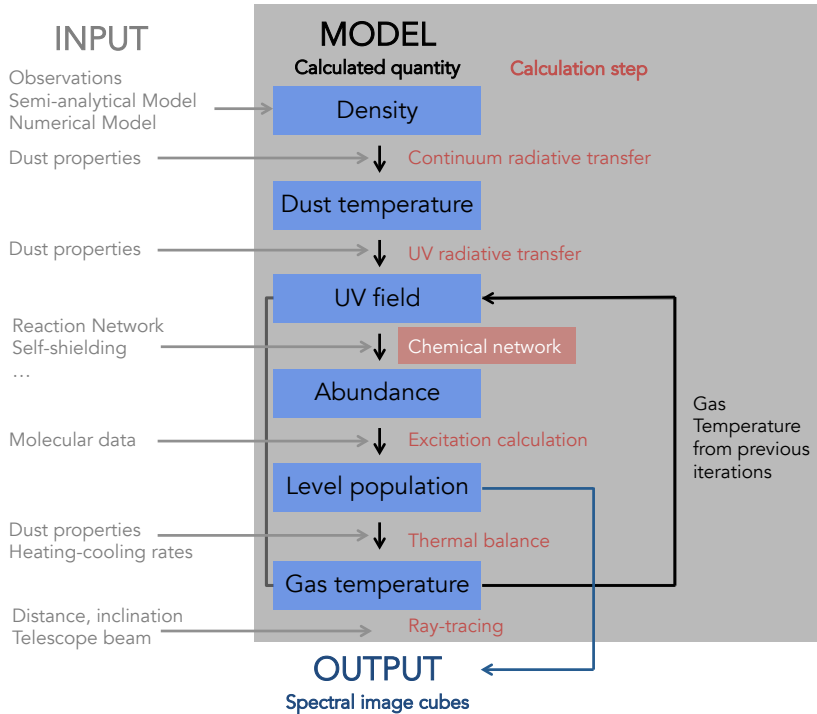


**Figure 1.8:** DALI modeling flowchart (Adopted from Bruderer et al. 2012). The chemical network calculation step is highlighted in red as this is the part of the code that has been augmented for this PhD thesis. More details are presented in Chapter 2 and 3.

in the disk  $T_{\text{gas}}$  is assumed to be equal to  $T_{\text{dust}}$ , the heating-cooling balance is run to get a new  $T_{\text{gas}}$  and the loop runs until the input and output values converge. When a self-consistent solution is found, spectral image cubes are created with a raytracer.

For this PhD thesis, DALI has been extended with a complete treatment of isotope-selective processes. This includes a chemical network with different isotopologues taken as independent species (e.g.,  $^{12}\text{CO}$ ,  $^{13}\text{CO}$ ,  $\text{C}^{18}\text{O}$ , and  $\text{C}^{17}\text{O}$ ) and reactions that enhance or decrease the abundance of one isotopologue over the other. In particular photodissociation, the main process regulating the CO abundance in the gas phase, has been implemented self consistently for CO isotopologues. Also, a simple HD chemistry has been added. More details on the implementation of the new features are presented in Chapters 2, 3, and 6.

---

## 1.6 This thesis and future outlook

Determining disk gas masses has been the leading question of this PhD thesis since its origin. CO isotopologues have been promising gas mass tracer candidates for many years and with the advent of ALMA their detection in disks has become routine. The still open question is if chemical isotope-selective effects play a major role in setting the mutual abundance ratios of CO isotopologues and in the determination of disk masses. Therefore this thesis starts from the modeling perspective. Subsequently a larger sample of CO isotopologue observations in disks has been provided by the Lupus Disk Survey with ALMA (Ansdell et al. 2016). The grid of models presented in Chapter 3 has therefore been compared with observations and some more observation-motivated projects have been carried out.

- In Chapter 2 isotope-selective photodissociation, the main process controlling the relative abundances of CO isotopologues in the CO-emissive layer, was properly treated for the first time in a physical-chemical disk model. The chemistry, thermal balance, line, and continuum radiative transfer were all considered together with a chemical network that treats  $^{13}\text{CO}$ ,  $\text{C}^{18}\text{O}$  and  $\text{C}^{17}\text{O}$  isotopologues as independent species. The main result is that isotope selective processes lead to regions in the disk where the isotopologues abundance ratios are considerably different from the elemental ratios. Accordingly, considering CO isotopologue ratios as constants may lead to underestimating disk masses by up to an order of magnitude or more.
- In Chapter 3 the small grid of models used in Chapter 2 to investigate the effects of CO isotope-selective photodissociation has been expanded. More than 800 disk models have been run for a range of disk and stellar parameters. Total fluxes have been ray-traced for different CO isotopologues and for various low  $J$ - transitions for different inclinations. This chapter shows that a combination of  $^{13}\text{CO}$  and  $\text{C}^{18}\text{O}$  total intensities allows inference of the total disk mass, although with larger uncertainties, compared with the earlier work by Williams & Best (2014). These uncertainties can be reduced by employing spatially resolved observations, i.e. the disk's radial extent, inclination and flaring. Finally, total line intensities for different CO isotopologue and for various low- $J$  transitions are provided as functions of disk mass and fitted to simple formulae. The effects of a lower gas-phase carbon abundance and different gas-to-dust ratios are investigated as well.
- In Chapter 4 the grid of physical-chemical models presented in Chapter 3 has been employed to analyze continuum and CO isotopologues ( $^{13}\text{CO } J = 3 - 2$  and  $\text{C}^{18}\text{O } J = 3 - 2$ ) observations of Lupus disks. Disk gas masses have been calculated for a total of 34 sources, expanding the sample of 10 disks studied



---

by Ansdell et al. (2016). This chapter shows that overall CO-based gas masses are very low for disks orbiting a solar mass-like star, often smaller than  $1M_J$ , if volatile carbon is not depleted. Accordingly, global gas-to-dust ratios are much lower than the expected ISM-value of 100, being predominantly between 1 and 10. Low CO-based gas masses and gas-to-dust ratios may indicate rapid loss of gas, or alternatively chemical evolution, e.g. via sequestering of carbon from CO to more complex molecules, or carbon locked up in larger bodies. The first hypothesis would imply that giant planet formation must be quick or rare, while for the latter the implication on planet formation timescales is less obvious.

- In Chapter 5 another important disk property has been investigated with DALI models, i.e. the gas surface density distribution  $\Sigma_{\text{gas}}$ . Reliable observational measurements of  $\Sigma_{\text{gas}}$  are key to understand disk evolution and the relative importance of different processes, as well as how planet formation occurs. This chapter investigates whether  $^{13}\text{CO}$  line radial profiles, such as those recently acquired by ALMA, can be employed as a probe of the gas surface density profile. By comparing with DALI simulations we find that  $^{13}\text{CO}$  radial profiles follow the density profile in the middle-outer disk. The emission drops in the very inner disk due to optical depth, and in the very outer disk due to a combination of freeze-out and inefficient self-shielding. Ranges of radii and line emission fluxes are provided to observers, where fitting line emission radial profiles gives reliable value for the surface density power-law index  $\gamma$ .
- In Chapter 6 simple deuterium chemistry has been added to the chemical network in DALI to simulate HD lines in disks. The aim is to examine the robustness of HD as a tracer of the disk gas mass, specifically the effect of gas mass on the HD far infrared emission and its sensitivity to the disk vertical structure. The uncertainty on HD-mass determination due to disk structure is found to be moderate and HD observations should be considered as an important science goal for future far-infrared missions.

The main conclusions of this thesis are the following:

1. CO isotope-selective photodissociation needs to be properly considered when modeling rare CO isotopologues emission. Otherwise,  $\text{C}^{18}\text{O}$  lines emission could be overestimated and the derived gas masses could be underestimated by up to an order of magnitude or more.
2. Disk gas masses can be inferred by a combination of  $^{13}\text{CO}$  and  $\text{C}^{18}\text{O}$  total intensities, although with non-negligible uncertainties, up to two orders of magnitude for very massive disks.

- 
3. CO-based disk gas masses derived in Lupus are extremely low, often smaller than  $1 M_J$  and the global gas-to-dust ratios are predominantly between 1 and 10. This may be interpreted as either rapid loss of gas, or fast chemical evolution.
  4. The shape of the disk surface density distribution can be constrained by spatially resolved  $^{13}\text{CO}$  observations, if optical depth, freeze-out and self shielding are properly considered in the modeling.
  5. HD far-infrared emission can be used to determine disk gas masses with moderate uncertainty which depends mainly on the disk vertical structure. Such observations should be considered as an important science goal for future far-infrared missions.

The question on disk gas masses remains open. CO isotopologues are still promising mass tracers candidates, as their detection is routine for ALMA, but they need to be calibrated. This thesis shows that the process of isotope-selective photodissociation is important for a good interpretation of CO isotopologues as gas mass tracers. However photodissociation, at least for the case of TW Hya and possibly for other disks, is not the main process responsible for the observed faint CO isotopologues lines. In turn, volatile carbon depletion is a process that needs to be further investigated and understood. Where does the carbon go? The detection of slightly more complex molecules, such as the hydrocarbons  $\text{C}_2\text{H}$  and  $\text{c-C}_3\text{H}_2$  could be a way to calibrate CO-based gas masses (see e.g., Bergin et al. 2016). Another option is to enlarge the sample of [CI] line detections, which allow inference of the volatile carbon abundance in the upper regions of the disk (see Kama et al. 2016b). Finally, if the HD fundamental lines can be covered at high enough spectral resolution with SPICA, their detection will provide an unique independent tracer of the disk mass.



# 2 | PROTOPLANETARY DISK MASSES FROM CO ISOTOPOLOGUES LINE EMISSION

---

A. Miotello, S. Bruderer, and E. F. van Dishoeck, *Protoplanetary disk masses from CO isotopologues line emission*, 2014, A&A, 572, A96

---

**Abstract** – One of the methods for deriving disk masses relies on direct observations of the gas, whose bulk mass is in the outer cold regions ( $T \lesssim 30\text{K}$ ). This zone can be well traced by rotational lines of less abundant CO isotopologues such as  $^{13}\text{CO}$ ,  $\text{C}^{18}\text{O}$ , and  $\text{C}^{17}\text{O}$ , which probe the gas down to the midplane. The total CO gas mass is then obtained with the isotopologue ratios taken to be constant at the elemental isotope values found in the local interstellar medium. This approach is imprecise, however, because isotope-selective processes are ignored. The aim of this work is an isotopologue-selective treatment of CO isotopologues, to obtain a more accurate determination of disk masses. The isotope-selective photodissociation, the main process controlling the abundances of CO isotopologues in the CO-emissive layer, is properly treated for the first time in a full-disk model. The chemistry, thermal balance, line, and continuum radiative transfer are all considered together with a chemical network that treats  $^{13}\text{CO}$ ,  $\text{C}^{18}\text{O}$  and  $\text{C}^{17}\text{O}$ , isotopes of all included atoms and molecules as independent species. Isotope selective processes lead to regions in the disk where the isotopologues abundance ratios of  $\text{C}^{18}\text{O}/^{12}\text{CO}$ , for example, are considerably different from the elemental  $^{18}\text{O}/^{16}\text{O}$  ratio. The results of this work show that considering CO isotopologue ratios as constants can lead to underestimating disk masses by up to an order of magnitude or more if grains have grown to larger sizes. This may explain observed discrepancies in mass determinations from different tracers. The dependence of the various isotopologues emission on stellar and disk parameters is investigated to set the framework for the analysis of ALMA data. Including CO isotope selective processes is crucial for determining the gas mass of the disk accurately (through ALMA observations) and thus for providing the amount of gas that may eventually form planets or change the dynamics of forming planetary systems.

---

## 2.1 Introduction

Despite considerable progress in the field of planet formation in recent years, many aspects are still far from understood (see Armitage 2011, for a review). It is clear that the initial conditions play an important role in the outcome of the planet formation process. Circumstellar disks, consisting of dust and gas, which orbit young stars are widely known to be the birth places of planets. One of the key properties for understanding how disks evolve to planetary systems is their overall mass, combined with their surface density distribution.

So far, virtually all disk mass determinations are based on observations of the millimeter (mm) continuum emission from dust grains (e.g., Beckwith et al. 1990; Dutrey et al. 1996; Mannings & Sargent 1997; Andrews & Williams 2005) (see Williams & Cieza 2011, for a review). To derive the total gas + dust disk mass from these data involves several steps and assumptions. First, a dust opacity value  $\kappa_\nu$  at the observed frequency  $\nu$  together with a dust temperature needs to be chosen to infer the total dust mass. The submillimeter dust opacity has been calibrated for dense cores against infrared extinction maps (Shirley et al. 2011) and found to agree well with theoretical opacities for coagulated grains with thin ice mantles (Ossenkopf & Henning 1994), but the dust grains in protoplanetary disks have probably grown to larger sizes with corresponding lower opacities at sub-mm wavelengths (e.g., Testi et al. 2003; Rodmann et al. 2006; Lommen et al. 2009; Ricci et al. 2010). These opacities may even vary with radial distance from the star, which adds another uncertainty (Guilloteau et al. 2011; Pérez et al. 2012; Birnstiel et al. 2012) (see Testi et al. 2014, for review). Second, a dust-to-gas mass ratio has to be assumed, which is usually taken to be the same as the interstellar ratio of 100. This conversion implicitly assumes that the gas and mm-sized dust grains have the same distribution. There is now growing observational evidence that mm-sized dust and gas can have very different spatial distributions in disks (e.g., Panić & Hogerheijde 2009; Andrews et al. 2012; van der Marel et al. 2013; Bruderer et al. 2014; Walsh et al. 2014), which invalidates the use of mm continuum data to trace the gas.

The alternative method for deriving disk masses relies on observations of the gas. The dominant constituent,  $\text{H}_2$ , is very difficult to observe directly because of its intrinsically weak lines at near- and mid-infrared wavelengths superposed on a strong continuum (e.g., Thi et al. 2001; Pascucci et al. 2006; Carmona et al. 2008; Bitner et al. 2008; Bary et al. 2008). Even if detected,  $\text{H}_2$  does not trace the bulk of the disk mass in most cases (e.g., Pascucci et al. 2013). HD is a good alternative probe, but its far-infrared lines have so far been detected for only one disk (Bergin et al. 2013), and there is no current facility sensitive enough for deep searches in other disks after *Herschel*.

This leaves CO as the best, and probably only, alternative to determine the gas

---

content of disks. In contrast with H<sub>2</sub> and HD, its pure rotational transitions at millimeter wavelengths are readily detected with a high signal-to-noise ratio in virtually all protoplanetary disks (e.g., Dutrey et al. 1996; Thi et al. 2001; Dent et al. 2005; Panić et al. 2008; Williams & Best 2014). It is the second-most abundant molecule after H<sub>2</sub>, with a chemistry that is in principle well understood. However, <sup>12</sup>CO is a poor tracer of the bulk of the gas mass because its lines become optically thick at the disk surface. Less abundant CO isotopologues such as <sup>13</sup>CO and C<sup>18</sup>O have more optically thin lines and as a consequence saturate deeper in the disk, with C<sup>18</sup>O probing down to the midplane (van Zadelhoff et al. 2001; Dartois et al. 2003). Therefore, the combination of several isotopologues can be used to investigate both the radial and vertical gas structure of the disk. With the advent of the Atacama Large Millimeter/submillimeter Array (ALMA<sup>1</sup>), high angular resolution observations of CO isotopologues in disks will become routine even for low-mass disks (e.g., Kóspál et al. 2013), allowing studies of the distribution of the cold (<100 K) gas in disks in much more detail than possible before. The ALMA data complement near-infrared vibration-rotation lines of CO, which mostly probe the warm gas in the inner few AU of the disk (e.g., Najita et al. 2003; Pontoppidan et al. 2008; Brittain et al. 2009; van der Plas et al. 2009; Brown et al. 2013).

The two main unknowns in the determination of the disk gas mass are the CO-H<sub>2</sub> abundance ratio and the isotopologue ratios. In the simplest situation, the bulk of the volatile carbon (i.e., the carbon that is not locked up refractory dust) is contained in gas-phase CO, leading to a CO/H<sub>2</sub> fractional abundance of  $\sim 2 \times 10^{-4}$ , consistent with a direct observation of this abundance in a warm dense cloud (Lacy et al. 1994). The isotopologue ratios are then usually taken to be constant at the <sup>13</sup>C, <sup>18</sup>O, and <sup>17</sup>O isotope values found in the local interstellar medium (ISM) (Wilson & Rood 1994). In reality, two processes act to decrease the CO abundance below its highest value: photodissociation and freeze-out. Photodissociation is effective in the surface layers of the disk, whereas freeze-out occurs in the cold ( $T_d < 20$  K) outer parts of the disk at the midplane. Indeed, a combination of both processes has been invoked to explain the low observed abundances of CO in disks compared with H<sub>2</sub> masses derived from dust observations (Dutrey et al. 1997; van Zadelhoff et al. 2001; Andrews et al. 2011). An additional effect is that the volatile carbon abundance and [C]/[O] ratio in the disk can be different from that in warm clouds (Öberg et al. 2011; Bruderer et al. 2012) and affect the CO abundance. Indeed, a recent study by Favre et al. (2013) of the one disk, TW Hya, for which the mass has been determined independently using HD far-infrared lines, finds a low C<sup>18</sup>O abundance and consequently a low overall carbon abundance, which the authors interpreted as due to conversion of gas-phase CO to other hydrocarbons. These other carbon-bearing species have a stronger binding energy to the grains than CO itself, and freeze-out rapidly preventing conversion

---

<sup>1</sup>[www.almaobservatory.org](http://www.almaobservatory.org)

---

back to CO (Bergin et al. 2014).

Of these processes, only photodissociation by ultraviolet (UV) photons can significantly affect the abundance ratios of  $^{12}\text{CO}$  and its isotopologues. CO is one of only a few molecules whose photodissociation is controlled by line processes that are initiated by discrete absorptions of photons into predissociative excited states and is thus subject to self-shielding (Bally & Langer 1982; van Dishoeck & Black 1988; Viala et al. 1988). For a CO column density of about  $10^{15} \text{ cm}^{-2}$ , the UV absorption lines saturate and the photodissociation rate decreases sharply, allowing the molecule to survive in the interior of the disk (Bruderer 2013). Because the abundances of isotopologues other than  $^{12}\text{CO}$  are lower, they are not self-shielded until deeper into the disk. This makes photodissociation an isotope-selective process, in particular for the rarer  $\text{C}^{18}\text{O}$  and  $\text{C}^{17}\text{O}$  isotopologues. Thus, there should be regions in the disk in which these two isotopologues are not yet shielded, but  $^{12}\text{CO}$  and  $^{13}\text{CO}$  are, resulting in an overabundance of  $^{12}\text{CO}$  and  $^{13}\text{CO}$  relative to  $\text{C}^{18}\text{O}$  and  $\text{C}^{17}\text{O}$ . A detailed study of CO isotope selective photodissociation incorporating the latest molecular physics information has been carried out by Visser et al. (2009) and applied to the case of a circumstellar disk. A single vertical cut in the disk was presented to illustrate the importance of isotope selective photodissociation, especially when grains have grown to larger sizes so that shielding by dust is diminished. If these effects are maximal in regions close to the CO freeze-out zone where most of the CO emission originates, the gas-phase emission lines can be significantly affected. Other studies have considered  $^{13}\text{CO}$  in disks, but not the rarer isotopologues (Willacy & Woods 2009).

The aim of our work is to properly treat the isotope-selective photodissociation in a full-disk model, in which the chemistry, gas thermal balance, and line and continuum radiative transfer are all considered together. The focus is on the emission of the various isotopologues and their dependence on stellar and disk parameters, to set the framework for the analysis of ALMA data and retrieval of surface density profiles and gas masses. In this first paper, we present only a limited set of representative disk models to illustrate the procedure and its uncertainties for a disk around a T Tauri and a Herbig Ae star. In Sect. 2, we present the model details, especially the implementation of isotope selective processes. In Sect. 3, the model results for our small grid are presented and the main effects of varying parameters identified. Finally, in Sect. 4, the model results and their implications for analyzing observations are discussed. In particular, the case of TW Hya is briefly discussed.

## 2.2 Model

For our modeling, we used the code DALI (dust and lines) code (Bruderer et al. 2012; Bruderer 2013), which is based on a radiative transfer, chemistry, and thermal-



---

balance model. Given a density structure as input, the code solves the continuum radiative transfer using a 3D Monte Carlo method to calculate the dust temperature  $T_{\text{dust}}$  and local continuum radiation field from UV to mm wavelengths. A chemical network simulation then yields the chemical composition of the gas. The chemical abundances enter a non-LTE excitation calculation of the main atoms and molecules. The gas temperature  $T_{\text{gas}}$  is then obtained from the balance between heating and cooling processes. Since both the chemistry and the molecular excitation depend on  $T_{\text{gas}}$ , the problem is solved iteratively. When a self-consistent solution is found, spectral image cubes are created with a raytracer. The DALI code has been tested with benchmark test problems (Bruderer et al. 2012; Bruderer 2013) and against observations (Bruderer et al. 2012; Fedele et al. 2013; Bruderer et al. 2014).

In this work, we have extended DALI with a complete treatment of isotope-selective processes. This includes a chemical network with different isotopologues taken as independent species (e.g.,  $^{12}\text{CO}$ ,  $^{13}\text{CO}$ ,  $\text{C}^{18}\text{O}$ , and  $\text{C}^{17}\text{O}$ ) and reactions that enhance or decrease the abundance of one isotopologue over the other.

### 2.2.1 Isotope-selective processes

The isotope selective processes included in the model are CO photodissociation and gas-phase reactions through which isotopes are exchanged between species (fractionation reactions).

#### Isotope-selective photodissociation

The main isotope-selective process in the gas phase is CO photodissociation (Visser et al. 2009, and references therein). CO is photodissociated through discrete (line-) absorption of UV photons into predissociative bound states. Absorption of continuum photons is negligible. Since the dissociation energy of CO is 11.09 eV, CO photodissociation can only occur at wavelengths between 911.75 Å and 1117.8 Å. The UV absorption lines are electronic transitions in vibrational levels of excited states and can become optically thick. Thus, CO can shield itself from photodissociating photons. In particular, the UV absorption lines of the main isotopologue  $^{12}\text{CO}$  become optically thick at a CO column density  $\sim 10^{15}\text{cm}^{-2}$  (van Dishoeck & Black 1988). In disks, this column density corresponds to the surface of the warm molecular layer. At a certain height in the disk, the photodissociation rate has dropped sufficiently for CO to survive, both because of self-shielding and absorption of FUV continuum attenuation by small dust grains or PAHs.

The rarer isotopologues (e.g.,  $^{13}\text{CO}$ ,  $\text{C}^{18}\text{O}$ , and  $\text{C}^{17}\text{O}$ ) can also self-shield from the dissociating photons, but at higher column densities and accordingly closer to the mid-plane. This results in regions where  $^{12}\text{CO}$  is already self-shielded and thus at high abundance, but the rare isotopologues are still photodissociated because of their

less efficient self-shielding. In these regions the isotopologue ratio (e.g.  $C^{18}O/^{12}CO$ ) can be much lower than the corresponding elemental isotope ratio  $[^{18}O]/[^{16}O]$ . In chemical models of disks, the abundance of the rare isotopologues is usually obtained by simply scaling the  $^{12}CO$  abundance with the local ISM elemental isotope ratio (Wilson & Rood 1994). However, to correctly deduce the total gas disk mass from rare CO isotopologues observations, isotope-selective photodissociation needs to be taken into account.

The depth-dependence of the photodissociation rates is affected by different effects. In addition to self-shielding, blending of UV absorption lines with other species can lead to mutual shielding. For example, rare CO isotopologues can be mutually shielded by  $^{12}CO$  if their UV absorption lines overlap. Mutual shielding by H and  $H_2$  is also important. At greater depths, the UV continuum radiation is attenuated by small dust grains and PAHs. The photodissociation rate for a particular isotopologue  $^xC^yO$  can be written as

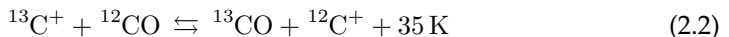
$$k_{PD} = \Theta [N(H), N(H_2), N(^{12}CO), N(^xC^yO)] k_{PD}^0, \quad (2.1)$$

where  $\Theta$  is a shielding function depending on the H,  $H_2$ ,  $^{12}CO$ , and  $^xC^yO$  column densities, and  $k_{PD}^0$  is the unshielded photodissociation rate, calculated using the local continuum radiation field.

In this work, the mutual and self-shielding factors  $\Theta$  were interpolated from the values given by Visser et al. (2009). We used their tables with intrinsic line widths  $b_{CO} = 0.3 \text{ km s}^{-1}$ ,  $b_{H_2} = 3 \text{ km s}^{-1}$ , and  $b_H = 5 \text{ km s}^{-1}$ , and excitation temperatures  $T_{ex,CO} = 20 \text{ K}$  and  $T_{ex,H_2} = 89.4 \text{ K}$ , values appropriate for the lower- $J$  lines. The column densities of H,  $H_2$ ,  $^{12}CO$  and  $^xC^yO$  were calculated as the minimum of the inward/upward column density from the local position. This approach has been verified in Bruderer (2013) against the method used in Bruderer et al. (2012), where the column densities are calculated together with the FUV radiation field by the Monte Carlo dust radiative transfer calculation (see Appendix A in Bruderer 2013). This method is computationally far less demanding, because it does not require a global iteration of the model.

### Fractionation reactions

In addition to isotope selective photodissociation, gas-phase reactions can also change the relative abundance of isotopologues. The most important reaction of this type is the ion-molecule reaction

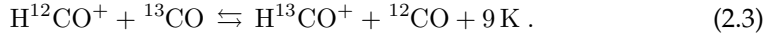


(see Watson et al. 1976; Woods & Willacy 2009, and references therein). The vibrational ground-state energy difference of  $^{12}CO$  and  $^{13}CO$  corresponds to a temperature of 35 K. Thus, at low temperature, the forward direction is preferred, which

---

leads to an increased abundance of  $^{13}\text{CO}$  relative to  $^{12}\text{CO}$  (Langer et al. 1984). At high temperature, forward and backward reactions are balanced and the  $^{12}\text{CO}/^{13}\text{CO}$  ratio is not altered by the reaction. Following Langer et al. (1984), the reaction rate coefficient for the backward reaction is  $k = \alpha(T/300\text{ K})^\beta \exp(-\gamma/T)$ , where  $\alpha = 4.42 \times 10^{-10} \text{ cm}^3 \text{ s}^{-1}$ ,  $\beta = -0.29$  and  $\gamma = 35 \text{ K}$ . For the forward reaction, the exponential factor is dropped ( $\gamma = 0$ ).

Another isotope-exchange reaction considered in our work is



Rate coefficients for this reaction have been measured by Smith & Adams (1980). As a result of the small vibrational ground state energy difference, which corresponds to temperatures lower than the CO freeze-out temperature, it has only a minor impact on disks, however.

## 2.2.2 Chemical network

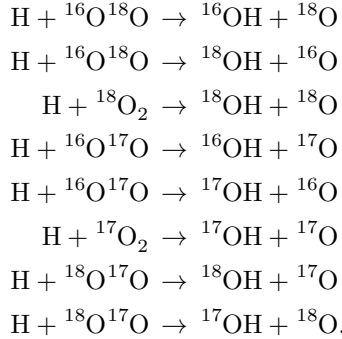
For our models, the list of chemical species by Bruderer et al. (2012) was extended to include different isotopologues as independent species. By adding the elements,  $^{13}\text{C}$ ,  $^{17}\text{O}$ , and  $^{18}\text{O}$ , in addition to H, He,  $^{12}\text{C}$ , N,  $^{16}\text{O}$ , Mg, Si, S, and Fe, the number of species was increased from 109 to 276. We accounted for all possible permutations. For example,  $\text{CO}_2$  was expanded into 12 independent species ( $^{12}\text{C}^{16}\text{O}_2$ ,  $^{12}\text{C}^{16}\text{O}^{17}\text{O}$ ,  $^{12}\text{C}^{17}\text{O}_2$ , etc.).

Our chemical reaction network is based on the UMIST 06 network (Woodall et al. 2007). It is an expansion of that used by Bruderer et al. (2012) and Bruderer (2013) to include reactions between isotopologues. The reaction types included are  $\text{H}_2$  formation on dust, freeze-out, thermal and non-thermal desorption, hydrogenation of simple species on ices, gas-phase reactions, photodissociation, X-ray and cosmic-ray induced reactions, PAH/small grain charge exchange/hydrogenation, and reactions with  $\text{H}_2^*$  (vibrationally excited  $\text{H}_2$ ). The details of the implementation of these reactions are described in Appendix A.3.1 of Bruderer et al. (2012). Specifically, a binding energy of 855 K was used for pure CO ice (Bisschop et al. 2006). The elemental abundances are also the same as in Bruderer et al. (2012). The isotope ratios are taken to be  $^{12}\text{C}/^{13}\text{C}=77$ ,  $^{16}\text{O}/^{18}\text{O}=560$  and  $^{16}\text{O}/^{17}\text{O}=1792$  (Wilson & Rood 1994).

Reactions involving the rarer isotopologues are duplicates of those involving the dominant isotopologue. For example, the reaction  $\text{H} + \text{O}_2 \rightarrow \text{OH} + \text{O}$  is expanded

---

to the reactions



This procedure increases the number of reactions included in the network from 1463 to 9755. Since most of the rate coefficients for these reactions involving isotopologues are unknown, we follow the procedure by Röllig & Ossenkopf (2013) and assume that the isotopologue reactions with the same reactants, but different products, have the original reaction rate divided by the number of out-going channels. This implies assigning an equal probability to all branches.

The fractionation reactions (Eqs. 2.2 and 2.3) were also added to the network. In addition to  ${}^{13}\text{C}$ , we also added the analogous reactions for  ${}^{18}\text{O}$  and  ${}^{17}\text{O}$ . When available, the reaction rate coefficients were taken from Röllig & Ossenkopf (2013), which are based on Langer et al. (1984). Coefficients for reactions with  ${}^{17}\text{O}$  are not provided, and extrapolations were made. For reaction (2.2), we used the same  $\alpha$  and  $\beta$  for  $\text{C}^{17}\text{O}$  as for  ${}^{13}\text{CO}$  and  $\text{C}^{18}\text{O}$  (Sect. 2.2.1). The value of  $\gamma$  was obtained from scaling with the reduced mass of  $\text{C}^{17}\text{O}$  following the procedure described in Langer et al. (1984). For reaction (2.3), the  $\alpha$  and  $\beta$  coefficients were taken to be the same as that with  ${}^{18}\text{O}$ . For  $\gamma$ , we assumed the value to be the mean of the values for  ${}^{16}\text{O}$  and  ${}^{18}\text{O}$ , since the mass of  ${}^{17}\text{O}$  is the median of the  ${}^{16}\text{O}$  and  ${}^{18}\text{O}$  masses. For the conditions in protoplanetary disks, reaction (2.3) is less important for chemical fractionation than reaction (2.2); hence, this simple assumption is appropriate.

### 2.2.3 Parameters of the disk model

For our modeling, we assumed a simple parameterized density structure, similar to that reported by Andrews et al. (2011). Assuming a viscously evolving disk, where the viscosity  $\nu = R^\gamma$  is a power law of the radius (Lynden-Bell & Pringle 1974; Hartmann et al. 1998), the surface density is given by

$$\Sigma_{\text{gas}} = \Sigma_c \left( \frac{R}{R_c} \right)^{-\gamma} \exp \left[ - \left( \frac{R}{R_c} \right)^{2-\gamma} \right], \quad (2.5)$$

with a characteristic radius  $R_c$  and a characteristic surface density  $\Sigma_c$ . The characteristic radius was fixed to  $R_c = 200$  AU and the characteristic surface density  $\Sigma_c$  adjusted to yield a total disk mass  $M_{\text{gas}}$  with the outer radius fixed to  $R_{\text{out}} = 400$  AU. The gas-to-dust ratio was assumed to be 100.

The vertical density structure follows a Gaussian with scale height angle  $h = h_c(R/R_c)^\psi$ . For the dust settling, two populations of grains were considered, small (0.005 - 1  $\mu\text{m}$ ) and large (1 - 1000  $\mu\text{m}$ ) (D'Alessio et al. 2006). The scale height is  $h$  for the the small and  $\chi h$  for the large grains, where  $\chi < 1$ . The distribution of the surface density of the two species is given by the factor  $f_{\text{large}}$  as  $\Sigma_{\text{dust}} = f_{\text{large}} \Sigma_{\text{large}} + (1 - f_{\text{large}}) \Sigma_{\text{small}}$ .

Other parameters of the model are the stellar FUV (6 -13.6 eV) and X-ray spectrum and the cosmic-ray ionization rate. To study the effects of different amounts of FUV photons compared with the bolometric luminosity, the stellar spectrum was assumed to be a black body at a given temperature  $T_{\text{eff}}$ . The strength of the FUV field in units of the interstellar radiation field  $G_0$  is given in Fig. 2.1 for a representative model. Here,  $G_0 = 1$  refers to the interstellar radiation field defined as in Draine (1978)  $\sim 2.7 \cdot 10^{-3} \text{erg s}^{-1} \text{cm}^{-2}$  with photon-energies  $E_\gamma$  between 6 eV and 13.6 eV. The X-ray spectrum was taken to be a thermal spectrum of  $7 \times 10^7$  K within 1 - 100 keV and the X-ray luminosity in this band  $L_X = 10^{30} \text{erg s}^{-1}$ . As discussed in Bruderer (2013), the X-ray luminosity is of minor importance for the intensity of CO pure rotational lines that are the focus in this work. The cosmic-ray ionization rate was set to  $5 \times 10^{-17} \text{s}^{-1}$ . We accounted for the interstellar UV radiation field and the cosmic microwave background as external sources of radiation.

The calculation was carried out on 75 cells in the radial direction and 60 in the vertical directions. In the radial direction the spatial grid is on a logarithmic scale up to 30 AU (35 cells) and on a linear scale from 30 AU to 400 AU (40 cells). The spectral grid of the continuum radiative transfer extends from 912  $\text{\AA}$  to 3 mm in 58 wavelength-bins. The wavelength dependence of the cross section was taken into account using data summarized in van Dishoeck et al. (2006).

The chemistry was solved in a time dependent manner, up to a chemical age of 1 Myr. The main difference to the steady-state solution is that carbon is not converted into methane ( $\text{CH}_4$ ) close to the mid-plane, since the time-scale of these reactions is longer than  $> 10$  Myr and thus is unlikely to proceed in disks. We ran models both with isotopologues and isotope-selective processes switched on (network *ISO*) or off (network *NOISO*).

## 2.2.4 Grid of models

The goal of our work is to understand the effect of isotope-selective processes in disks and to quantify their importance when rare isotopologue observations are used to measure the total gas mass. We ran a small grid of models to explore some of the

---

key parameters.

1. *Stellar spectrum.* The first parameter to explore is the fraction of FUV photons (912-2067 Å) over the entire stellar spectrum. A spectrum with  $T_{\text{eff}} = 4000$  K and  $T_{\text{eff}} = 10000$  K was considered, to simulate a T Tauri or Herbig Ae star. Accordingly, we ran models with a bolometric luminosity of  $L_{\text{bol}} = 1$  or  $10 L_{\odot}$ . Excess UV radiation due to accretion was taken into account for T Tauri stars. It was assumed that the gravitational potential energy of accreted mass is released with 100% efficiency as blackbody emission with  $T=10000$  K. The mass accretion rate was taken to be  $10^{-8} M_{\odot} \text{ yr}^{-1}$  and the luminosity was assumed to be emitted uniformly over the stellar surface. These assumptions result in  $L_{\text{FUV}}/L_{\text{bol}} = 1.5 \cdot 10^{-2}$  for the T Tauri case versus  $L_{\text{FUV}}/L_{\text{bol}} = 7.8 \cdot 10^{-2}$  for the Herbig case. The ratio of CO photodissociating photons (912-1100 Å) between the T Tauri and the Herbig cases is  $F_{\text{CO,pd}}(\text{T Tau})/F_{\text{CO,pd}}(\text{Her}) = 2.5 \cdot 10^{-2}$ . In all models, the interstellar UV field was included as well.
2. *Dust properties.* Since small grains are much more efficient in absorbing UV radiation, the ratio of large to small grains was varied. We considered  $f_{\text{large}} = 0.99$  in order to simulate a mixture of the two populations and  $f_{\text{large}} = 10^{-2}$  for the situation where only small grains are present in the disk (no or little grain growth).
3. *Disk mass.* Three different values for the total disk mass  $M_{\text{d}}$  were considered to cover a realistic range of disks ( $M_{\text{gas}} = 10^{-2}, 10^{-3}, 10^{-4} M_{\odot}$ ).

## 2.3 Results

### 2.3.1 Abundances

In Figure 2.2 we present the abundances of CO and its isotopologues computed using the ISO network and implementing the isotopologue shielding factors in a representative model (T Tauri star,  $M_{\text{disk}} = 10^{-2} M_{\odot}$ ,  $f_{\text{large}} = 10^{-2}$ ). In panel (a) a 2D distribution of  $^{12}\text{CO}$  in a disk quadrant is shown; the central star is located at the origin of the axis. As the disk surface is directly illuminated by the FUV stellar and interstellar radiation, CO is easily photodissociated and its abundance drops, such that  $n(\text{CO})/n_{\text{gas}}$  reaches values around  $10^{-8}$ . This so-called photodissociation layer results in a low-abundance region shown in green in panel (a) of Figure 2.2. The depth of this layer is not radially constant because it depends on the disk surface density structure and on the FUV flux. At large radii both  $\text{H}_2$  and CO column densities are lower and the FUV stellar flux is less strong: CO is not shielded until lower heights compared with regions at smaller radii. As soon as the UV absorption lines

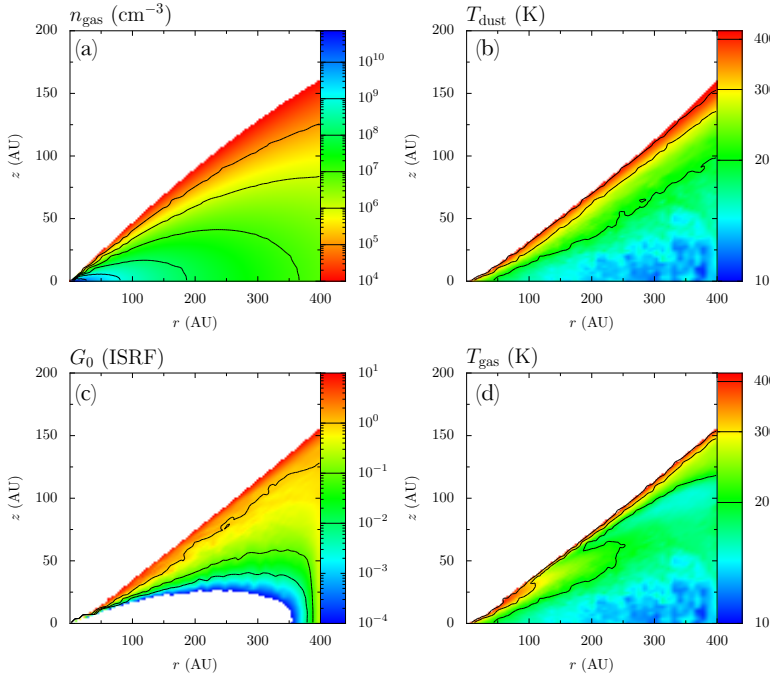


**Figure 2.1:** 2D representations of the results obtained including isotope-selective effects for a representative model ( $M_{\text{d}} = 10^{-2} M_{\odot}$ , T Tauri star,  $f_{\text{large}} = 10^{-2}$ ). The gas number density (panel a), the dust temperature (panel b), the FUV flux in units of  $G_0$  (panel c), and the gas temperature (panel d) are shown.

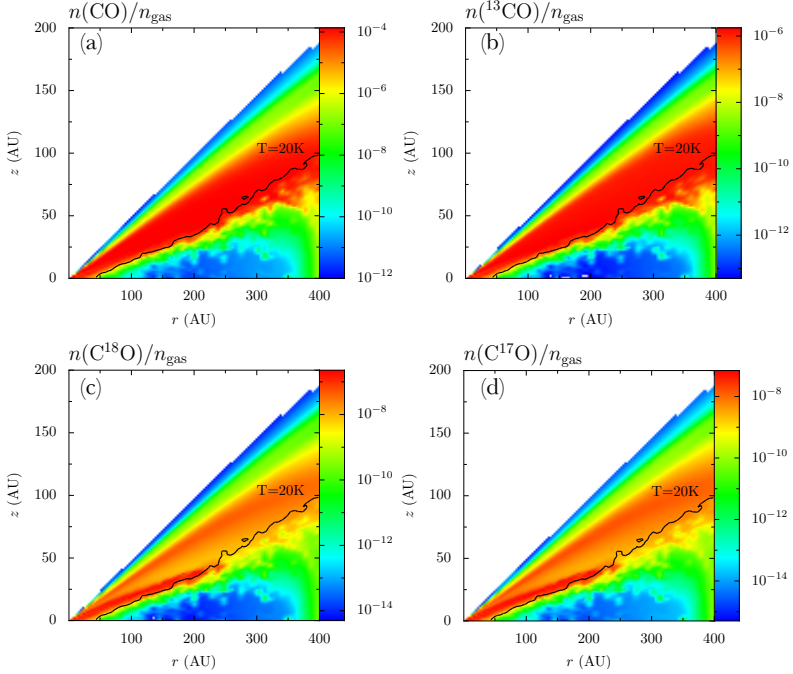


**Figure 2.2:** 2D representations of the results obtained including isotope-selective effects for a representative model ( $M_d = 10^{-2} M_\odot$ , T Tauri star,  $f_{\text{large}} = 10^{-2}$ ). The CO isotopologues abundances normalized to the total gas density are presented. The black solid line indicates the layer where the dust temperature is equal to 20 K. For lower  $T_{\text{dust}}$  values, CO freeze-out may become important.



**Table 2.1:** Parameters of the disk models.

Parameter	Range
<i>Chemistry</i>	
Chemical network	ISO / NOISO
Chemical age	1 Myr
<i>Physical structure</i>	
$\gamma$	1
$\psi$	0.1
$h_c$	0.1 rad
$R_c$	200 AU
$R_{\text{out}}$	400 AU
$M_{\text{gas}}$	$10^{-4}, 10^{-3}, 10^{-2} M_{\odot}$
Gas-to-dust ratio	100
$f_{\text{large}}$	$10^{-2}, 0.99$
$\chi$	1
<i>Stellar spectrum</i>	
T Tauri*	$T_{\text{eff}}=4000 \text{ K}, L_{\text{bol}}=1 L_{\odot}$
Herbig	$T_{\text{eff}}=10000 \text{ K}, L_{\text{bol}}=10 L_{\odot}$
$L_X$	$10^{30} \text{ erg s}^{-1}$
<i>Dust properties</i>	
Dust	0.005-1 $\mu\text{m}$ (small) 1-1000 $\mu\text{m}$ (large)

\* FUV excess added, see text.

saturate because of (self-) shielding, the photodissociation rate decreases steeply, allowing CO to survive in the interior of the disk. This warm, high-abundance layer of survived CO is shown in red in panel (a) of Figure 2.2. It extends from the surface up to the midplane at very small radii,  $R < 40 \text{ AU}$ , because the column densities there are high enough that CO can survive the strong stellar photodissociating flux, and the dust grains are warm enough to prevent freeze-out. At radii larger than 40 AU, the abundance of CO falls again at decreasing height toward the midplane. There the dust temperature is very low ( $T_{\text{dust}} \lesssim 20 \text{ K}$ ) because the UV stellar flux is well shielded by the higher regions. At such temperatures CO molecules freeze out onto dust grains, therefore the abundance of gaseous CO decreases. The precise dust temperature at which most of the CO is frozen out depends on the density and can be as low as 18 K for the adopted CO binding energy.

The shape of the distribution of  $\text{C}^{18}\text{O}$  and  $\text{C}^{17}\text{O}$  inside the disk appears different from that of CO (panels (c) and (d), Fig. 2.2), while the distribution of  $^{13}\text{C}\text{O}$  is similar to that of CO (panel (b), Fig. 2.2). For the two less abundant isotopologues the warm

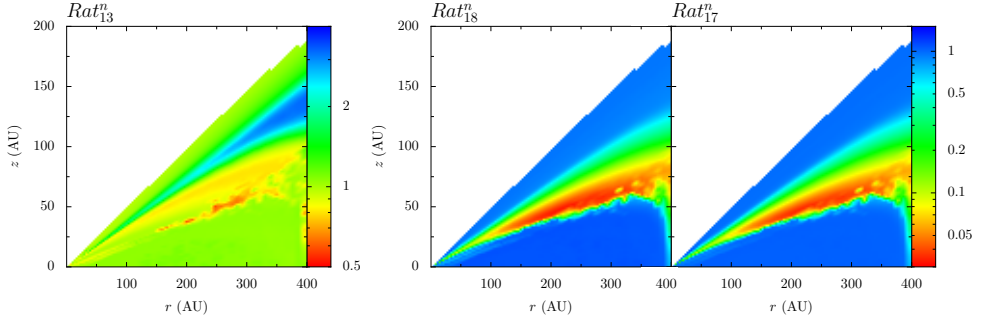


**Figure 2.3:** CO isotopologues abundance ratios obtained using the NOISO and the ISO chemical networks. The ratios are defined as follows:  $Rat_{13}^n = 77 \cdot \frac{n(^{13}\text{CO})_{\text{ISO}}}{n(\text{CO})_{\text{NOISO}}}$ ,  $Rat_{18}^n = 560 \cdot \frac{n(\text{C}^{18}\text{O})_{\text{ISO}}}{n(\text{CO})_{\text{NOISO}}}$  and  $Rat_{17}^n = 1792 \cdot \frac{n(\text{C}^{17}\text{O})_{\text{ISO}}}{n(\text{CO})_{\text{NOISO}}}$ . The plots show the results for a  $10^{-2} M_{\odot}$  disk around a T Tauri star, with  $f_{\text{large}} = 10^{-2}$ .

molecular layer is indeed much thinner and separated by a warm molecular finger at the midplane at small radii,  $R_i < 200$  AU. This difference in the molecular distribution is the effect of the isotope selective photodissociation and is highlighted in Fig. 2.3 through the abundance ratios:

$$Rat_{xy}^n = \frac{n(^x\text{C}^y\text{O})[^{12}\text{C}][^{16}\text{O}]}{n(^{12}\text{CO})[^x\text{C}][^y\text{O}]} \quad (2.6)$$

This indicates that the conventional way of deriving the CO isotopologue abundances by simply dividing the  $^{12}\text{CO}$  abundance by the isotope ratios is not accurate.

In Figure 2.3 the ratios of the abundances found using these two methods are presented, that is, the differences in the predictions whether or not the isotope-selective processes are taken into account. In the right-hand panels, the regions where  $\text{C}^{18}\text{O}$  and  $\text{C}^{17}\text{O}$  are not yet self-shielded, while  $^{12}\text{CO}$  is, blow-up clearly. In these regions the isotopologue ratios are lower by up to a factor of 40 compared with just rescaling the isotope ratios. These isotope-selective effects for the  $^{18}\text{O}$  and  $^{17}\text{O}$  species are also clearly seen when the values of  $Rat_{xy}^n$  for the total number of CO molecules summed over the whole disk are compared in Table 2.2.

Another way to present the isotopologue fractionation is through  $\mathcal{R}$ , the cumulative column density ratios normalized to  $^{12}\text{CO}$  and the isotopic ratios reported, as by Visser et al. (2009), for instance

$$\mathcal{R}(z) = \frac{N_z(^x\text{C}^y\text{O})[^{12}\text{C}][^{16}\text{O}]}{N_z(^{12}\text{CO})[^x\text{C}][^y\text{O}]}, \quad (2.7)$$

**Table 2.2:** Ratios of the total number of molecules  $Rat_{xy}^n$  in the gas summed over the entire disk obtained using the ISO and the NOISO networks for every model.

	$M_d [M_\odot]$	$f_{\text{large}}$	$Rat_{13}^n$	$Rat_{18}^n$	$Rat_{17}^n$
T Tau	$10^{-4}$	$10^{-2}$	0.95	0.20	0.22
		0.99	0.94	0.09	0.09
	$10^{-3}$	$10^{-2}$	0.93	0.55	0.58
		0.99	0.98	0.42	0.43
	$10^{-2}$	$10^{-2}$	0.95	0.75	0.79
		0.99	0.98	0.71	0.73
Herbig	$10^{-4}$	$10^{-2}$	0.95	0.23	0.24
		0.99	0.96	0.07	0.08
	$10^{-3}$	$10^{-2}$	0.94	0.45	0.49
		0.99	0.96	0.12	0.13
	$10^{-2}$	$10^{-2}$	0.94	0.77	0.84
		0.99	0.98	0.64	0.66

where  $[X]$  is the elemental abundance of isotope  $X$  and

$$N_z({}^x\text{C}^y\text{O})(z) = \int_z^{z_{\text{surf}}} n({}^x\text{C}^y\text{O}) dz', \quad (2.8)$$

is the column density, integrated from the surface of the disk ( $z_{\text{surf}}$ ) down to the height  $z$ .

Figure 2.4 shows  $\mathcal{R}$  as function of disk height through a vertical cut at a radius of 150 AU for the three isotopologues in two representative models. Consistent with Visser et al. (2009), for  $\text{C}^{18}\text{O}$  and  $\text{C}^{17}\text{O}$   $\mathcal{R}$  is found to be constant around unity, until it dips strongly at intermediate heights. There  $\mathcal{R}$  perceptibly drops because  $^{12}\text{CO}$  is already self-shielded and survives the photodissociation, while UV photons still dissociate  $\text{C}^{18}\text{O}$  and  $\text{C}^{17}\text{O}$ . This is the region where isotope-selective effects are most detectable. If only small grains are present in the disk (upper panel of Fig. 2.4), the temperature at which CO can freeze out ( $T_{\text{dust}} \lesssim 20$  K) is reached below  $z = 10$  AU, where the cumulative ratios are back close to the elemental isotope ratios ( $\mathcal{R} \sim 1$ ). On the other hand, if large grains are considered (lower panel), this threshold shifts to 25 AU, just in the region where isotope-selective dissociation is most efficient. For heights lower than 25 AU the tiny amount of  $\text{C}^{18}\text{O}$  and  $\text{C}^{17}\text{O}$  remaining in the gas phase does not add to the column density, so  $\mathcal{R}$  is effectively frozen at around 0.2 for both isotopologues.  $^{13}\text{CO}$ , on the other hand, has less fractionation in both models.  $\mathcal{R}$ , however, increases by a factor of three at intermediate heights (around  $z=40$

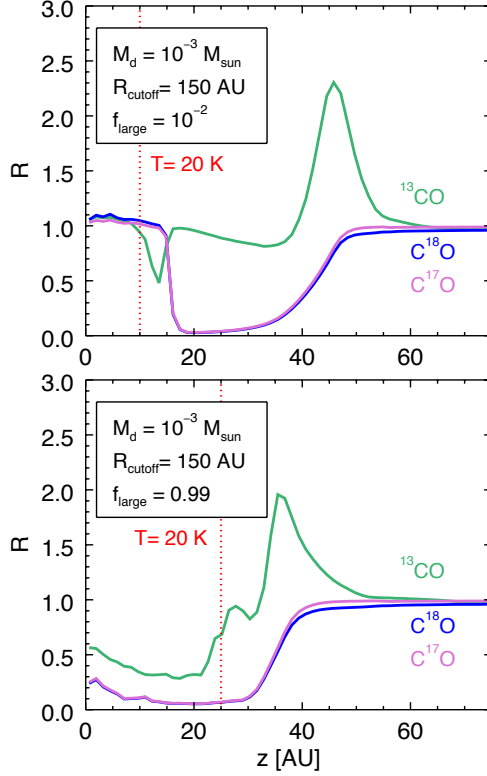


**Figure 2.4:** Cumulative column density ratios normalized to  $^{12}\text{CO}$  and the isotopic ratios (see eq. 2.7) shown as a function of height for a vertical cut through the disk at a radius of 150 AU. In the top panel we show a  $10^{-3} M_{\odot}$  disk around a T Tauri star with  $f = 10^{-2}$  (only small grains), while in the bottom panel the settling parameter is  $f_{\text{large}} = 0.99$ . The dotted red lines indicate where the temperature reaches 20 K, below which CO starts to freeze out.

---

AU) for this isotopologue as a result of gas-phase reactions. For each isotopologue, isotope-selective effects are maximized if mm-sized grains are present in the disk, as we discuss in Sect. 2.3.2 in more detail.

A negligible fraction of CO is in solid CO in our models, in particular for the warm Herbig disks. Only the more massive cold disks around T Tauri stars have a solid CO fraction similar to that of gaseous CO. Overall, a large portion of oxygen is locked up in water ice in the models. In particular, the excess  $^{18}\text{O}$  and  $^{17}\text{O}$  produced by the isotope-selective photodissociation is turned into water ice, which has a much higher binding energy and thus remains on the grains even in warm disks. If this water ice subsequently comes into contact with solids that drift inwards, this may explain the anomalous  $^{18}\text{O}$  and  $^{17}\text{O}$  isotope ratios found in meteorites (Lyons & Young 2005; Visser et al. 2009).

### 2.3.2 Line fluxes

While the 2D representations of molecular abundances shown in Figs. 2.2 and 2.3 are useful for understanding the chemical and physical structures of the disk, line fluxes are a better proxy for quantifying the observable effects given by the isotope-selective processes. In Fig. 3.3.2 we present the radial intensity ratios of the  $J=3-2$  line for  $^{13}\text{CO}$ ,  $\text{C}^{18}\text{O}$ , and  $\text{C}^{17}\text{O}$  obtained with the NOISO and ISO networks. Spectral-image cubes were obtained with DALI from the solution of the radiative transfer equation, assuming the disk is at a distance of 100 pc. The derived line intensities were not convolved with any observational beam. For  $^{13}\text{CO}$  the line intensities obtained with the two networks are very similar, leading to line ratios within a factor of two. On the other hand, for  $\text{C}^{18}\text{O}$  and  $\text{C}^{17}\text{O}$  the line intensity ratios obtained with the two networks differ by up to a factor of 40. This means that an analysis that does not consider isotope-selective effects would lead to an overprediction of the line intensity of the two less abundant isotopologues at radii around 100 AU. Using the NOISO network would overpredict the  $\text{C}^{18}\text{O}$  and  $\text{C}^{17}\text{O}$  lines intensities by up to a factor of 40.

#### Dependence on the parameters

It is interesting to determine how the observables depend on the variation of the parameters listed in Sect. 2.2.4. The focus is in particular on the line intensity ratios found for  $\text{C}^{18}\text{O}$  and  $\text{C}^{17}\text{O}$ , where the effects are more prominent.

When the dust composition is left unchanged and the disk mass is increased from  $M_{\text{d}} = 10^{-4}M_{\odot}$  to  $M_{\text{d}} = 10^{-2}M_{\odot}$ , the region where the isotope-selective photodissociation is most effective shifts toward the outer regions. The peak of the intensity ratios between the ISO and NOISO networks is located there (second and third panels of Fig. 3.3.2). They are defined as  $\text{Rat}_{13}^{\text{I}} = I[^{13}\text{CO}]_{\text{NOISO}} / I[^{13}\text{CO}]_{\text{ISO}}$ ,

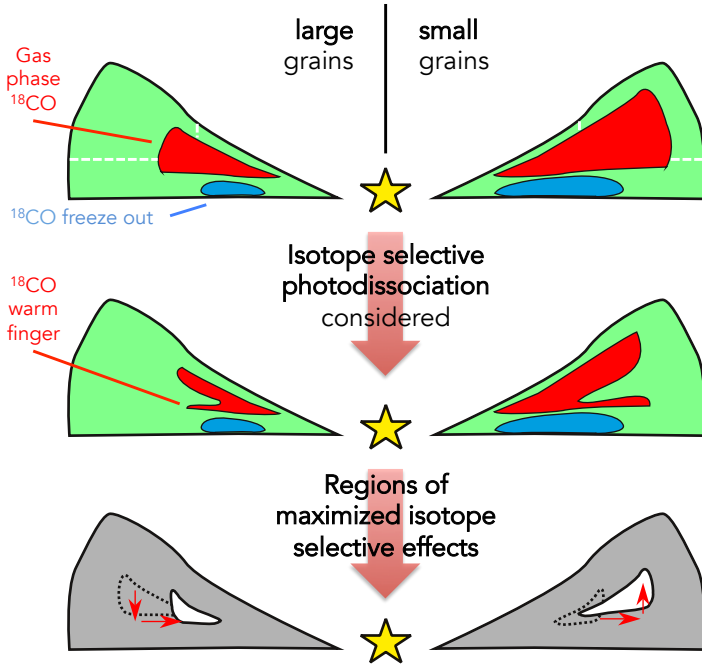


**Figure 2.5:** Sketch of the 2D abundances of  $C^{18}O$  in one quadrant of the disk. On the left-hand side mm-sized grains are present in the disk ( $f_{\text{large}}=0.99$ ), while on the right just (sub)  $\mu\text{m}$ -sized grains are considered ( $f_{\text{large}}=10^{-2}$ ). In the upper panel the 2D abundance predicted by the NOISO network (i.e., not considering isotope selective photodissociation) is plotted, in the middle panel that inferred by the ISO network, i.e., with an isotopologue selective treatment of isotopologues. The red regions show where CO isotopologues are in the molecular phase, while the blue regions are where they are frozen onto grains. The regions where the two predictions differ more are those in which isotope-selective processes are strongest; they are highlighted in the lower panel by the white shapes. The black dotted contours and the red arrows show the difference between ISO and NOISO. Since small grains are more efficient in shielding from photodissociating photons,  $C^{18}O$  can survive in the gas phase at greater heights and farther out (white dotted lines in the upper panel). Accordingly, the white regions that show the difference between ISO and NOISO in the lower panel also shift upward and outward in the case of small grains.

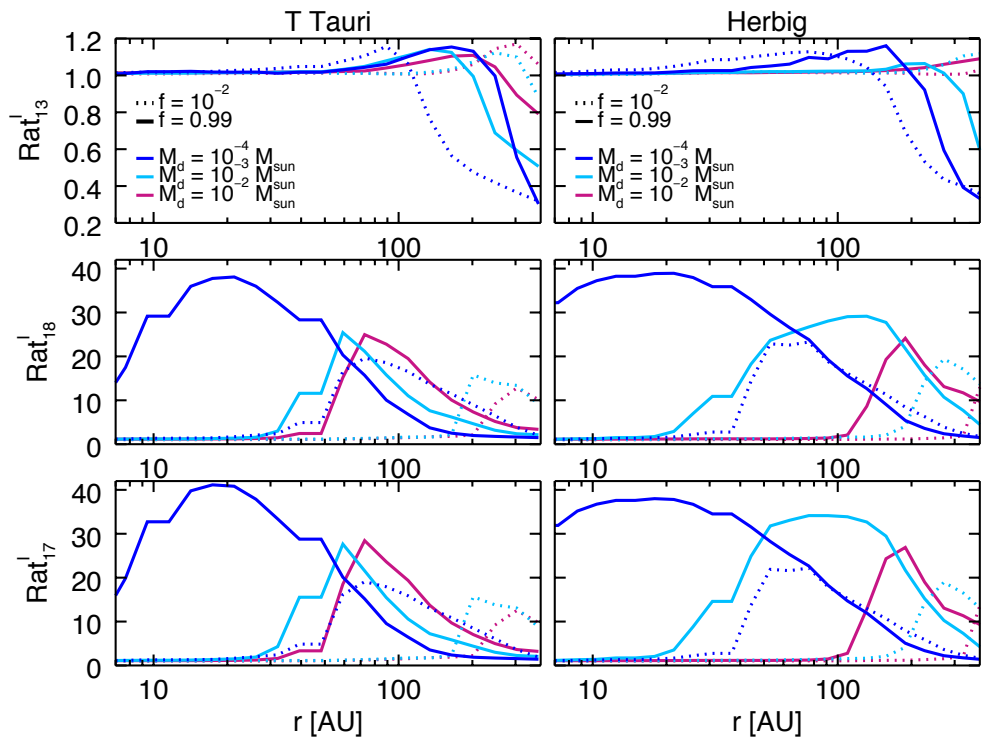


**Figure 2.6:** Ratios of CO isotopologues line intensity ( $J=3-2$ ) obtained with the NOISO and ISO networks as a function of the disk radius.  $\text{Rat}_{13}^I = I[\text{C}^{13}\text{CO}]_{\text{NOISO}}/I[\text{C}^{13}\text{CO}]_{\text{ISO}}$ ,  $\text{Rat}_{18}^I = I[\text{C}^{18}\text{O}]_{\text{NOISO}}/I[\text{C}^{18}\text{O}]_{\text{ISO}}$  and  $\text{Rat}_{17}^I = I[\text{C}^{17}\text{O}]_{\text{NOISO}}/I[\text{C}^{17}\text{O}]_{\text{ISO}}$  were defined. Dotted lines refer to models where  $f = 10^{-2}$ , solid lines to  $f_{\text{large}} = 0.99$ . Different colors indicate models with different disk masses:  $M_d = 10^{-4} M_\odot$  in blue,  $M_d = 10^{-3} M_\odot$  in light blue and  $M_d = 10^{-2} M_\odot$  in purple. Models with T Tauri stars are shown in the left panels, those with Herbig stars in the right panels.

$\text{Rat}_{18}^{\text{I}} = \text{I}[\text{C}^{18}\text{O}]_{\text{NOISO}} / \text{I}[\text{C}^{18}\text{O}]_{\text{ISO}}$  and  $\text{Rat}_{17}^{\text{I}} = \text{I}[\text{C}^{17}\text{O}]_{\text{NOISO}} / \text{I}[\text{C}^{17}\text{O}]_{\text{ISO}}$ . At higher masses the column densities at which CO UV-lines saturate are reached earlier: CO and its isotopologues can therefore survive at larger radii and heights and the observable effects of isotope-selective photodissociation come from the outer regions. Higher mass disks also have colder deeper regions and thus more CO freeze-out onto dust grains in the midplane.

A similar and even more substantial shift toward larger radii is seen by considering two models with the same disk mass, but with different dust composition. Submicron-sized particles are much more efficient than mm-sized grains in shielding FUV photodissociating photons, therefore the observable effects of isotope-selective photodissociations come from outer regions. This behavior is sketched in Fig. 2.5 where it is shown that the CO emitting region shifts deeper into the disk and inward with grain growth, as found previously by Jonkheid et al. (2004) and Aikawa & Nomura (2006).

The magnitude of the isotope-selective effects is lower in the case of small grains, however. The peak in line intensity ratios is a factor of 2 lower than for large grains. The explanation is in the location of the freeze out zone. For large grains the region where less abundant CO isotopologues are highly fractionated partially coincides with the freeze-out zone (see Fig. 2.4). For  $T_{\text{dust}} \lesssim 20$  K almost all CO molecules are frozen onto grains, except for a small fraction that is photodesorbed by FUV radiation, and the tiny fraction that remains in the gas phase cannot substantially enhance the line intensity.

The last parameter to consider is the spectrum of the central star. In Fig. 3.3.2 the line intensity ratios obtained considering a T Tauri star and a Herbig star are presented. There is no substantial difference in the peak values of the ratios, but their location depends on the stellar spectrum. For low-mass disks the peak for both T Tauri and Herbig disks is in the inner region, while for high-mass disks the Herbig emission peaks at larger radii. For example, for the model with the highest mass,  $M_{\text{d}} = 10^{-2} M_{\odot}$ , and with large grains,  $f_{\text{large}} = 0.99$ , the peak shifts drastically outward at  $\approx 200$  AU for a Herbig star. This shift is caused by the fact that Herbig stars have more CO-dissociating UV photons ( $\lambda < 1100$  Å), than T Tauri stars.

### 2.3.3 Line optical depth

$\text{C}^{18}\text{O}$  is frequently used as a mass tracer because of its low abundance. Compared with more abundant isotopologues such as  $^{12}\text{CO}$  and  $^{13}\text{CO}$ , its detection allows probing regions closer to the midplane and thus the bulk of the disk mass.  $\text{C}^{18}\text{O}$  is a good mass tracer as long as its lines are optically thin, which may not always be the case. Then  $\text{C}^{17}\text{O}$ , being rarer than  $\text{C}^{18}\text{O}$ , can be used to probe the regions where the optical depth is greater than unity.



---

One way to investigate line optical thickness is to compare the line intensity radial profile with the column density radial profile. For optically thin emission, they should indeed follow the same trend, since column density counts the total number of molecules at a given column. If the line intensity radial profile does not follow that of the column density, this is a signature of an opacity effect.

In Fig. 2.7 column density radial profiles are compared with line intensity radial profiles for models with a T Tauri star and with a Herbig star as central objects. Column densities are shown in black, while line intensities are shown in red for  $C^{18}O$  and in light blue for  $C^{17}O$ . Except for the very inner and dense regions, both isotopologues are optically thin throughout the entire disk. This is true in particular for the  $10^{-4}M_{\odot}$  disks, but not completely for the massive  $10^{-2}M_{\odot}$  T Tauri disk.

It is interesting to note that in Fig. 2.7 in the outer regions, that is for  $r > 200$  AU, the column densities obtained with different models do not scale linearly with mass. This depends on the amount of  $C^{18}O$  and  $C^{17}O$  frozen onto grains, which varies for the different models. In Fig. 2.8 the  $C^{18}O$  and the total ( $H + 2H_2$ ) cumulative column densities (Eq. 2.8) are shown for a cut at  $r = 300$  AU. The total cumulative column densities are divided by a factor  $10^{-9}$ . For  $z = 0$ , that is where the column densities are integrated from the surface up to the midplane, the total cumulative column density scales linearly with mass as expected, but that of  $C^{18}O$  does not, because of the different freeze-out zones.

## 2.4 Discussion

To properly compare model predictions with data, one needs to convolve output images with the same beam as used for observations. Whether or not the isotope-selective effects presented in previous sections can indeed be detected may vary with different beam sizes. Moreover, estimates of the total disk masses may be affected by this choice. Below we discuss this problem and provide estimates of the magnitude of this effect in determining disk masses.

### 2.4.1 Beam convolutions

To investigate the sensitivities of mass estimates on isotope selective effects, the output images obtained by implementing the ISO and NOISO network were convolved with different observational beams. Four beam sizes were adopted for the convolution:  $0.1''$ ,  $0.5''$ ,  $1.0''$ , and  $3.0''$ . The smallest are useful to simulate high-resolution observations (e.g., ALMA observations), while the largest are used to compare the models with lower resolution observations (e.g., SMA observations) or disk-integrated (single-dish) measurements.

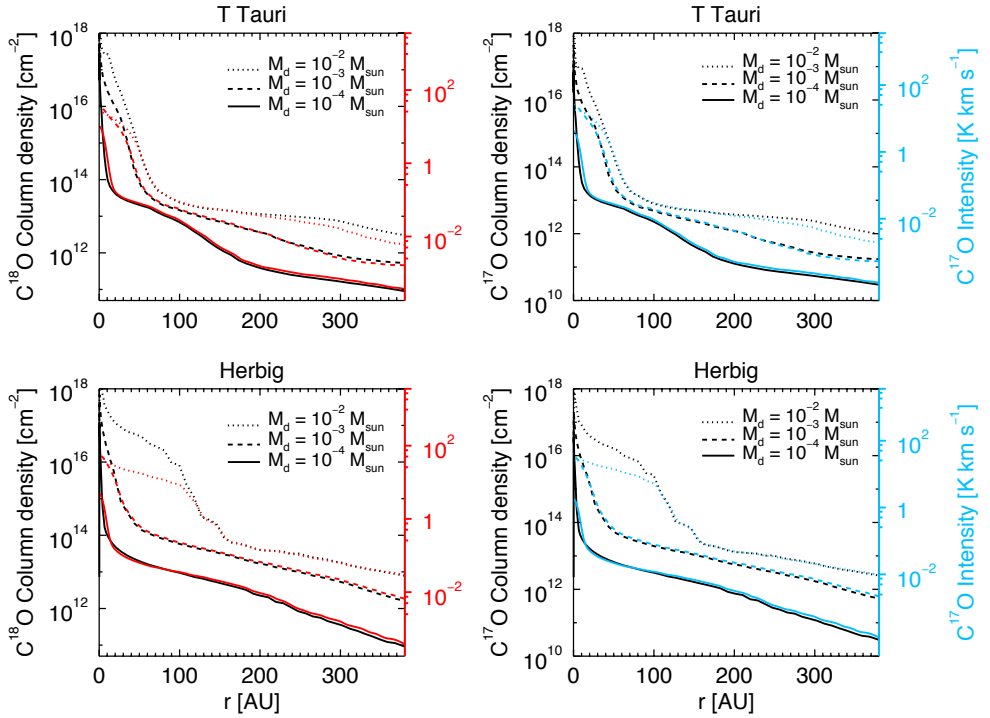


**Figure 2.7:** Column density radial profiles of  $\text{C}^{18}\text{O}$  and  $\text{C}^{17}\text{O}$  compared with beam-convolved line intensity ( $J=3-2$ ) radial profiles. Different line styles represent models with various disk masses; column densities in black,  $\text{C}^{18}\text{O}$  and  $\text{C}^{17}\text{O}$  line intensities in red and in blue, convolved with a  $0.1''$  beam. Models with a central T Tauri star are presented in the left panels, those with a Herbig star in the right panels. Only models with  $f_{\text{large}} = 0.99$  are shown.

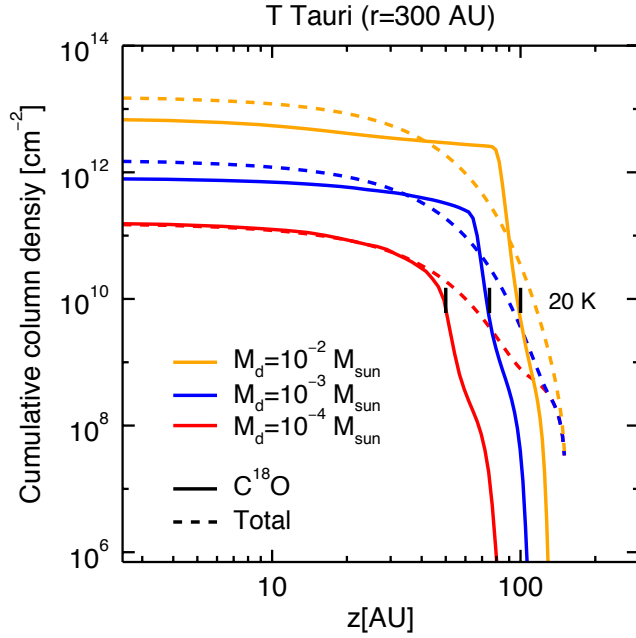


**Figure 2.8:** Cumulative column density as a function of the disk height integrating from the surface to the midplane in a disk radial cut ( $r = 300$  AU). Only T Tauri models with  $f_{\text{large}}=0.99$  are shown. Different line colors represent models with various disk masses. Dotted lines show the scaled total gas cumulative column density (see text), solid lines that of  $\text{C}^{18}\text{O}$ . The black lines show where the dust temperature is lower than 20 K for the different disk models, i.e., where CO freeze-out becomes important.

---

In Fig.3.6 radial distributions of  $C^{18}O$  line intensity obtained with different beam convolutions are presented for one of the T Tauri disk models located at 100 pc. Different colors refer to various beam sizes, while the line style shows whether isotope-selective effects are taken into account or not: a solid line is used if they are considered (ISO network), a dotted line otherwise (NOISO network). The predictions obtained with the two chemical networks always differ, but they do so in diverse ways if different beam sizes are adopted. In the extreme case of the 3'' beam, the NOISO network overproduces the disk-integrated  $C^{18}O$  line intensity by a factor of 5. On the other hand, if a very narrow beam is used for the convolution, that is, a 0.1'' beam, the line intensities are the same at very small radii for the two models; but at larger distances the NOISO network overestimates the line intensity, but not always by the same factor. Such a narrow beam allows resolving substructures that are smeared out by a larger beam. As expected, the regions of the disk where line intensity ratios of ISO and NOISO are high are the same as those for which the unconvolved line intensities obtained with the two networks differ most (see Fig. 3.3.2).

## 2.4.2 Mass estimates

The question to answer now is how much disk mass estimates may vary if a proper treatment of CO isotopologues is adopted. Unfortunately,  $^{13}CO$ , the isotopologue less affected by isotopologue selective processes, becomes optically thick at substantial heights from the midplane, and is thus not a good mass tracer (Fig. 2.10, top). Therefore just  $C^{18}O$  and  $C^{17}O$  can be considered for mass estimates.

For spatially resolved observations (0.1''-1''), the difference between the line intensities obtained with the NOISO and ISO networks varies through the disk (see Fig. 3.6). This is because isotope selective processes have different influence in different regions of the disk. Therefore, as our analysis concluded, no simple scaling relation can be given, but a full thermochemical model needs to be run to estimate the correct disk mass.

On the other hand, in the extreme case of a 3'' observational beam, where the disk substructures are not resolved, the bulk of the disk-integrated line intensity is obtained. In Fig. 2.10 the integrated line intensities obtained with disk masses  $M_d = 10^{-4}, 10^{-3}$  and  $10^{-2}M_\odot$  are shown, for the NOISO and the ISO network. The red line relates the intensity values obtained for the three disk masses with the NOISO network, while the blue line shows those with the ISO network. The dotted lines indicate the different masses inferred by the two networks, and thus the factor by which the total disk mass is underestimated if isotope-selective processes are neglected. Both grain growth level and variation in the stellar spectrum are investigated. The inferred masses, both considering isotope selective processes and not considering them, are presented in Table 2.3, together with their ratios. In practice, a

---

given  $C^{18}O$  and  $C^{17}O$  line intensity is observed and plots such as those in Fig. 2.10 can then be used to draw a horizontal line and read off the disk masses.

The grid of models presented in this paper explores only a few parameters, and it is not possible to draw a general correction rule; we stress that the values in Table 2.3 are only indicative and may well reproduce extreme cases. On the other hand, it is possible to find trends in the results. For a given  $C^{18}O$  and  $C^{17}O$  intensity, the total disk mass is always underestimated if the NOISO network is used, that is, if isotope-selective effects are not properly considered. The underestimates are higher if mm-sized grains are present in the disk (i.e., where photodissociation is most efficient) and for a T Tauri star as central object, whose disk is cold. Moreover, the results differ by a larger factor if more massive disks are considered, such as disks with masses that range from  $10^{-3}M_{\odot}$  to  $10^{-2}M_{\odot}$ .

Williams & Best (2014) used a simple parametric approach to infer disk masses from their  $^{13}CO$  and  $C^{18}O$  data assuming constant isotopologue abundance ratios in those regions of the disk where CO is not photodissociated or frozen out. Effects of isotope selective photodissociation are treated by decreasing the  $C^{18}O/CO$  abundance ratio by an additional constant factor of 3 throughout the disk. Although our mini-grid is much smaller than that of Williams & Best (2014), we tend to find higher  $^{13}CO$  and lower  $C^{18}O$  intensities by up to a factor of a few for the same disk mass, especially for the models with large grains at the low mass end. A more complete parameter study of our full chemical models is needed for proper comparison.

### 2.4.3 TW Hya

TW Hya is one of the best-studied protoplanetary disks, being the closest T Tauri system, at a distance of  $54 \pm 6$  pc from Earth (van Leeuwen 2007). In addition, it is the only case in which the fundamental rotational transition of HD has been detected with the *Herschel Space Observatory* (Bergin et al. 2013). Observations of HD emission lines provide an independent disk mass determination, assuming that the HD distribution follows that of  $H_2$ . From these observations Bergin et al. (2013) determined a total disk mass larger than  $5 \cdot 10^{-2}M_{\odot}$ . Favre et al. (2013) also reported spatial integrated  $C^{18}O$  ( $2 - 1$ ) observations of TW Hya with SMA. From their analysis an underestimate of the disk mass by a factor between 3 and 100 was found. In their modeling they do not treat isotope selective photodissociation in a self-consistent way and concluded instead that the carbon abundance is low.

For the model in our grid that best represents the TW Hya characteristics (T Tauri star, large grains,  $M_d = 10^{-2}M_{\odot}$ ), a mass correction factor of at least 20 is found (see Table 2.3). This demonstrates that accounting for isotope selective processes might mitigate the disagreement in mass determinations. The spatial resolution of the SMA data of 100–150 AU is just in the regime where the effects are strongest. A more accurate modeling of TW Hya implementing the full isotope selective photodissociation

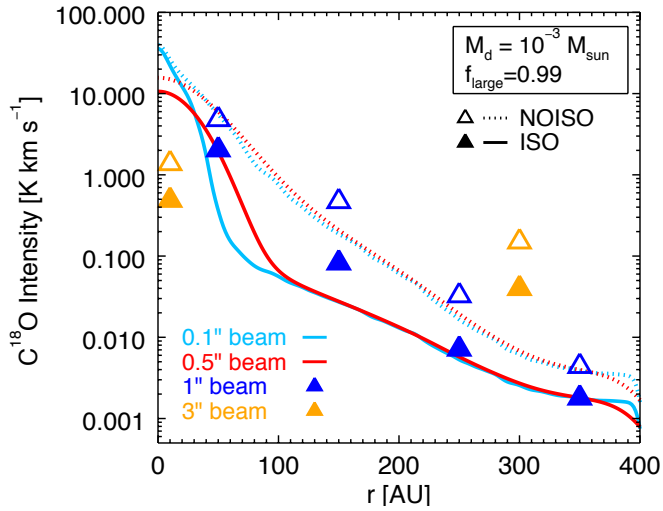


**Figure 2.9:** Radial profiles of the  $C^{18}O$  line intensity ( $J=3-2$ ) considering different observational beams for a particular disk model (T Tauri star,  $M_{\text{disk}} = 10^{-3} M_{\odot}$ ,  $f_{\text{small}} = 0.99$ ). Different colors show different choices of the observational beam size. Solid lines represent the intensities obtained considering the isotope-selective processes (ISO network), dotted lines show the results when an approximative analysis is carried out (NOISO network). For the 0.1'' and 0.5'' beam, full lines are presented, whereas for the 1'' and 3'' beam they are binned at the spatial resolution. For the 3'' beam, only the disk-integrated value (or the value that just resolves the outer disk) is shown.

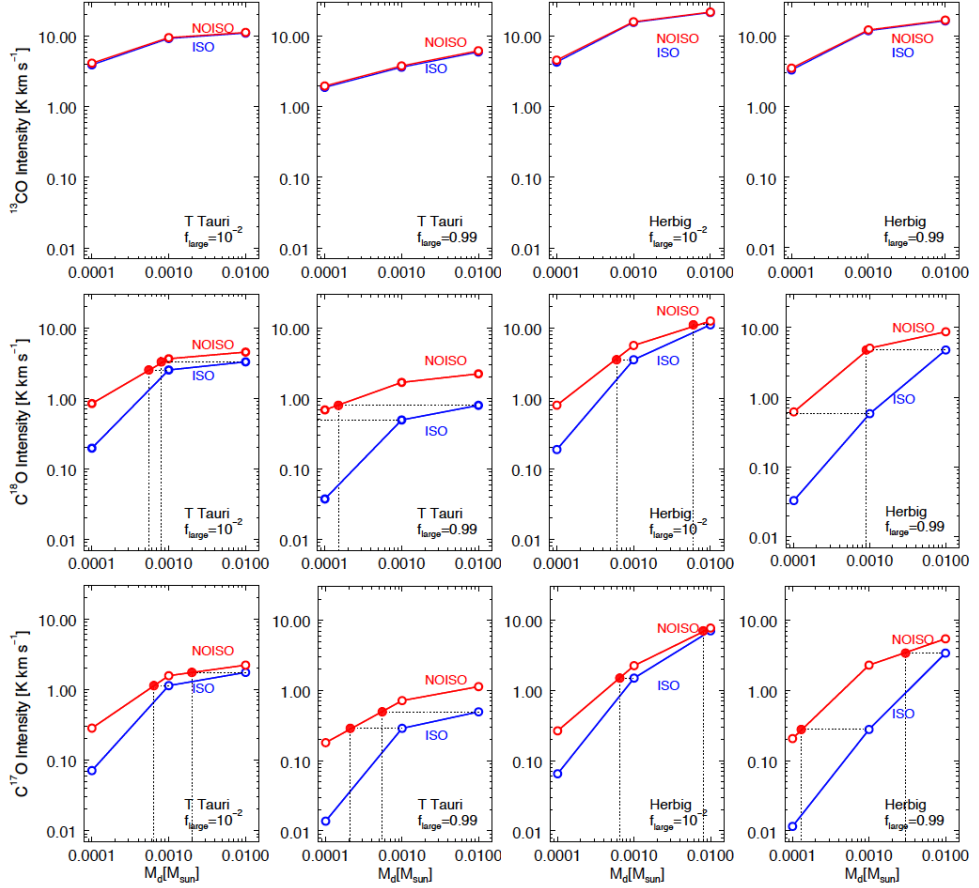


**Figure 2.10:** Disk-integrated  $^{13}\text{CO}$  (top),  $\text{C}^{18}\text{O}$  (middle), and  $\text{C}^{17}\text{O}$  (bottom) line intensities ( $J=3-2$ ) obtained with disk masses  $M_d = 10^{-4}, 10^{-3}, 10^{-2} M_{\odot}$  are shown as a function of the disk mass. The beam size is  $3''$ . The red line relates the intensity values obtained for the three disk masses with the NOISO network, while the blue line shows those with the ISO network. Dotted lines indicate by which factor the total disk mass is underestimated if no isotope-selective processes are considered. Results are presented for  $f_{\text{large}} = 10^{-2}, 0.99$  and for T Tauri and Herbig disks.

**Table 2.3:** Disk mass estimates obtained from a given observation of  $C^{18}O$  or  $C^{17}O$  without and with isotope selective photodissociation. The inferred disk masses are obtained with the disk-integrated line intensities given as outputs with the NOISO and ISO networks (see Fig. 2.10). The ratios between these two estimates are also reported for all the disk models. These correction factors should be applied to mass estimates that are obtained ignoring isotope-selective photodissociation.

	True $M_d [M_\odot]$		Inferred NOISO $M_d [M_\odot]$		Ratio( $M_{\text{True}}/M_{\text{NOISO}}$ )	
	small	large	small	large	small	large
	T Tauri		T Tauri		T Tauri	
$C^{18}O$	$10^{-3}$	$10^{-3}$	$5.5 \cdot 10^{-4}$	$5 \cdot 10^{-5}$	1.8	20
	$10^{-2}$	$10^{-2}$	$8 \cdot 10^{-4}$	$1.5 \cdot 10^{-4}$	12.5	67
$C^{17}O$	$10^{-3}$	$10^{-3}$	$6.4 \cdot 10^{-4}$	$2.1 \cdot 10^{-4}$	1.6	4.8
	$10^{-2}$	$10^{-2}$	$2 \cdot 10^{-3}$	$5.5 \cdot 10^{-4}$	5	20
	Herbig		Herbig		Herbig	
$C^{18}O$	$10^{-3}$	$10^{-3}$	$6 \cdot 10^{-4}$	$10^{-4}$	1.7	10
	$10^{-2}$	$10^{-2}$	$6 \cdot 10^{-3}$	$9 \cdot 10^{-4}$	1.7	11
$C^{17}O$	$10^{-3}$	$10^{-3}$	$6.5 \cdot 10^{-4}$	$1.3 \cdot 10^{-4}$	1.5	7.8
	$10^{-2}$	$10^{-2}$	$8 \cdot 10^{-3}$	$3 \cdot 10^{-3}$	1.3	3.3



---

using the same disk model as in Favre et al. (2013), Bergin et al. (2013) and Cleeves et al. (2014) with the observed stellar UV spectrum is needed to support this claim.

## 2.5 Summary and conclusions

We presented a detailed treatment of CO isotope selective photodissociation in a complete disk model for the first time. A full thermo-chemical model was used to which less abundant CO isotopologues were added into the chemical network as independent species, and the corresponding self-shielding factors were implemented. Abundances and line intensities were obtained as outputs for a grid of disk models, with and without isotope-selective photodissociation. The main conclusions are listed below.

- When CO isotope selective photodissociation is considered, the abundances of CO isotopologues are affected. In particular, there are regions in the disk where  $C^{18}O$  and  $C^{17}O$  show an underabundance with the respect to  $^{12}CO$  when compared with the overall elemental abundance ratios.
- The CO isotopologues line intensity ratios vary if isotope selective photodissociation is properly considered. The line intensity ratios are overestimated by up to a factor of 40 at certain disk radii, when isotope selective processes are not included into the modeling.
- A consequence of these results is that the disk mass can be underestimated by up to almost two orders of magnitude if a single line is observed and isotope selective effects are not properly taken into account. The effects are strongest for cold disks with large grains where the isotope selective effects are strongest close to the freeze-out zone, i.e., the same region of the disk from which most of the  $C^{18}O$  and  $C^{17}O$  emission arises. Moreover, the situation is worse for single-dish data or for low spatial resolution interferometry, which just resolves the outer disk.
- A preliminary comparison was made between the results presented here and TW Hya. The discrepancy in mass determination observed for this object may be explained by implementing isotope selective photodissociation in a self-consistent manner. More detailed modeling of the object is still needed, however.

In the future we will model TW Hya and other disks in more detail. In addition, a wider set of parameters will be explored in a larger grid of models, to provide mass estimate corrections for all kinds of disks when multiple lines are observed.

---

## Acknowledgements

The authors are grateful to Ruud Visser, Ilse Cleeves, Catherine Walsh, Mihkel Kama, and Leonardo Testi for useful discussions and comments. Astrochemistry in Leiden is supported by the Netherlands Research School for Astronomy (NOVA), by a Royal Netherlands Academy of Arts and Sciences (KNAW) professor prize, and by the European Union A-ERC grant 291141 CHEMPLAN.



# 3

## DETERMINING PROTOPLANETARY DISK GAS MASSES FROM CO ISOTOPOLOGUES LINE OBSERVATIONS

---

A. Miotello, E. F. van Dishoeck, M. Kama, and S. Bruderer, *Determining protoplanetary disk gas masses from CO isotopologues line observations*, 2016, *A&A*, 594, A85

---

**Abstract** – Despite intensive studies of protoplanetary disks, there is still no reliable way to determine their total (gas+dust) mass and their surface density distribution, quantities that are crucial for describing both the structure and the evolution of disks up to the formation of planets. The goal of this work is to use less-abundant CO isotopologues, such as  $^{13}\text{CO}$ ,  $\text{C}^{18}\text{O}$  and  $\text{C}^{17}\text{O}$ , detection of which is routine for ALMA, to infer the gas mass of disks. Isotope-selective effects need to be taken into account in the analysis, because they can significantly modify CO isotopologues' line intensities. CO isotope-selective photodissociation has been implemented in the physical-chemical code DALI (Dust And Lines) and more than 800 disk models have been run for a range of disk and stellar parameters. Dust and gas temperature structures have been computed self-consistently, together with a chemical calculation of the main atomic and molecular species. Both disk structure and stellar parameters have been investigated by varying the parameters in the grid of models. Total fluxes have been ray-traced for different CO isotopologues and for various low  $J$ -transitions for different inclinations. A combination of  $^{13}\text{CO}$  and  $\text{C}^{18}\text{O}$  total intensities allows inference of the total disk mass, although with non-negligible uncertainties. These can be overcome by employing spatially resolved observations, that is the disk's radial extent and inclination. Comparison with parametric models shows differences at the level of a factor of a few, especially for extremely low and high disk masses. Finally, total line intensities for different CO isotopologue and for various low- $J$  transitions are provided and are fitted to simple formulae. The effects of a lower gas-phase carbon abundance and different gas-to-dust ratios are investigated as well, and comparison with other tracers is made. Disk masses can be determined within a factor of a few by comparing CO isotopologue lines observations with the simulated line fluxes provided in this paper, modulo the uncertainties in the volatile elemental abundances.<sup>1</sup>

---

<sup>1</sup>Tables A.4 and A.5 are only available in electronic form at the CDS via anonymous ftp to cdsarc.u-strasbg.fr (130.79.128.5) or via <http://cdsweb.u-strasbg.fr/cgi-bin/qcat?J/A+A/>

---

### 3.1 Introduction

Protoplanetary disks are known to be the birth places of planets, but the process of grain growth, and ultimately planetesimal formation depends sensitively on the physical structure of gas in disks (see e.g., Armitage 2011, for a review). This structure is still poorly constrained from observations (e.g., Williams & Cieza 2011). In particular, there is not yet a reliable way for determining the total disk mass (gas + dust) and its radial distribution, which is one of the crucial parameters needed to describe disks' structure and evolution.

The traditional way of measuring disk masses has been through the detection of the cold dust, which dominates disk emission at millimeter wavelengths and is readily observed (e.g., Beckwith et al. 1990; Natta et al. 2004; Ricci et al. 2010; Testi et al. 2014). The dust component typically accounts for only 1% of the total disk mass, as the bulk of it is in the molecular gas. A conversion factor of 100 is generally taken for translating from dust to gas mass. However, as recent observations have shown, often the dust distribution does not follow that of the gas (e.g., Panić & Hogerheijde 2009; Andrews et al. 2012; Casassus et al. 2013; van der Marel et al. 2013; Walsh et al. 2014; Perez et al. 2015). In addition, major assumptions on dust particle size, shape, and composition need to be made in order to convert dust emission into dust mass. Finally, as a result of disk evolution, the gas-to-dust ratio may deviate significantly from 100 (Gorti & Hollenbach 2009; Alexander et al. 2014). In order to overcome these uncertainties, a direct measurement of molecular gas is preferred in order to determine the total gas mass, its spatial distribution and that of the gas-to-dust ratio of protoplanetary disks.

Ideally, one would like to directly trace molecular hydrogen ( $\text{H}_2$ ), the most abundant species, whose rotational lines are, however, difficult to detect. This molecule has no permanent dipole moment, requires higher temperatures for excitation and emits at wavelengths where the dust is optically thick. A solution comes from the detection of the less abundant isotopologue HD, whose far-infrared transitions were covered with the *Herschel* space observatory. Observations of HD lines have been published only for the closest protoplanetary disk, the well known TW Hya disk (Bergin et al. 2013), and no current facility is sensitive enough to detect HD in disks not covered by *Herschel*. These limitations lead to the need of other gas-mass tracers.

The second most abundant molecule, carbon monoxide (CO), is on the other hand readily detectable through its pure rotational lines at millimeter (mm-) wavelengths. However the main isotopologue,  $^{12}\text{CO}$ , becomes optically thick at low column densities and only traces the surfaces of protoplanetary disks. Thus, in order to trace the bulk of the mass, one needs to observe less-abundant CO isotopologues such as  $^{13}\text{CO}$  and  $\text{C}^{18}\text{O}$ , that become optically thick much deeper and trace the gas down to the midplane of the disk (van Zadelhoff et al. 2001; Dartois et al. 2003). Recently

---

Williams & Best (2014) have shown that through a combination of observations of multiple CO isotopologues (e.g.,  $^{13}\text{CO}$  and  $\text{C}^{18}\text{O}$ ) it is possible to determine disk gas masses with a grid of parametric models, even if the disk properties are not known. These models do not model chemistry, however, but use a parametrized temperature structure and CO abundance with fixed  $^{12}\text{C}/^{13}\text{C}$  and  $^{16}\text{O}/^{18}\text{O}$  ratios.

Although the CO chemistry is well studied and easily implemented in chemical models of disks (e.g., Aikawa et al. 2002; Hollenbach et al. 2005; Gorti & Hollenbach 2009; Nomura et al. 2009; Woitke et al. 2009), this is not the case for isotope-selective processes (Visser et al. 2009), which may affect the correct determination of disk masses. Miotello et al. (2014) have implemented isotope-selective photodissociation in a thermo-chemical and physical code, DALI (Dust And Lines, Bruderer et al. 2012; Bruderer 2013), exploring a set of parameters in a small grid of disk models. This study shows that isotope-selective processes may significantly affect CO isotopologues abundances, line emission and, accordingly, the determination of disk masses, especially as inferred from  $\text{C}^{18}\text{O}$  and  $\text{C}^{17}\text{O}$  alone.

In this paper we expand on Miotello et al. (2014b) and provide conversion factors to go from CO isotopologue line fluxes to the disk mass. A larger grid of disk models, 840 in total, is presented. After running a thermo-chemical calculation including isotope-selective photodissociation, CO isotopologues line intensities have been ray-traced for all models and lines are provided in Appendix 3.A and in electronic tables. These values can be used to infer disk masses, in particular if information about surface density distributions is derived from spatially resolved CO isotopologues observations. We also compare with alternative gas mass tracers such as the atomic fine structure lines (e.g. Kamp et al. 2011; Dent et al. 2013; Woitke et al. 2016).

## 3.2 Model

In this work, 2D disk models have been run to relate gas mass to CO isotopologues emission. Our models are computed using the physical-chemical code DALI, extensively tested with benchmark test problems (Bruderer et al. 2012; Bruderer 2013) and against observations (Bruderer et al. 2012; Fedele et al. 2013; Bruderer et al. 2014). The inputs needed by the code are the disk density structure and the stellar spectrum, which provides the central source of heating and dissociating radiation. First, the continuum radiative transfer is solved with a 2D Monte Carlo method which calculates the dust temperature  $T_{\text{dust}}$  and local continuum radiation field from UV to mm wavelengths. The following step is the determination of the chemical composition of the gas, obtained by a time-dependent chemical network simulation: the abundances of the main atoms and molecules are computed and subsequently the molecular excitation is obtained through a non-LTE calculation. Then the gas tem-

perature  $T_{\text{gas}}$  is obtained from the balance between heating and cooling processes. Since both the chemistry and the molecular excitation depend on  $T_{\text{gas}}$ , the problem is solved iteratively until a self-consistent solution is found. Finally, spectral image cubes are created with a raytracer.

As in Miotello et al. (2014b), we have included a complete treatment of isotope-selective processes. In the chemical network different isotopologues are taken as independent species (e.g.  $^{12}\text{CO}$ ,  $^{13}\text{CO}$ ,  $\text{C}^{18}\text{O}$ , and  $\text{C}^{17}\text{O}$ ) and reactions which regulate the abundance of one isotopolog over the other are included. Mutual (from H,  $\text{H}_2$ , CO) and self-shielding factors for different CO isotopologues from Visser et al. (2009) have been implemented in the chemical calculation.

### 3.2.1 Physical structure

In our models the disk density structure is parametrized by a power-law function, following the prescription proposed by Andrews et al. (2011). Physically this represents a viscously evolving disk, where the viscosity is expressed by  $\nu \propto R^\gamma$  (Lynden-Bell & Pringle 1974; Hartmann et al. 1998). The surface density follows:

$$\Sigma_{\text{gas}} = \Sigma_c \left( \frac{R}{R_c} \right)^{-\gamma} \exp \left[ - \left( \frac{R}{R_c} \right)^{2-\gamma} \right], \quad (3.1)$$

where  $R_c$  is the critical radius and  $\Sigma_c$  is the critical surface density. A fixed gas-to-dust ratio equal to 100 is employed to set the relation between the gas and the dust surface densities.

The vertical density structure follows a Gaussian with scale height angle  $h = h_c(R/R_c)^\psi$ . For the dust settling, two populations of grains are considered, small (0.005 - 1  $\mu\text{m}$ ) and large (1 - 1000  $\mu\text{m}$ ) (D'Alessio et al. 2006). The scale height is  $h$  for the the small grains and  $\chi h$  for the large ones, where  $0 < \chi \leq 1$ . The fraction of surface density distributed to the small and large population is  $(1 - f_{\text{large}})\Sigma_{\text{dust}}$  and  $f_{\text{large}}\Sigma_{\text{dust}}$ , respectively. In Miotello et al. (2014b) the ratio of large to small grains was varied:  $f_{\text{large}} = 0.99$  was chosen in order to simulate a mixture of large and small grains (most of the dust mass in large grains) and  $f_{\text{large}} = 10^{-2}$  was set for the situation of only small grains (only 1% of dust mass in large grains). Since small grains are much more efficient in absorbing UV radiation, the output CO isotopologues abundances and lines were different in the two cases. However, no significant differences were found between the case of  $f_{\text{large}} = 0.9$  and of  $f_{\text{large}}$  between 0.1 and 0.99. Since grains are expected to grow to mm-sizes in protoplanetary disks (e.g., Testi et al. 2003; Rodmann et al. 2006; Lommen et al. 2009; Ricci et al. 2010), for this work we assume only one case,  $f_{\text{large}} = 0.9$ . In contrast with Miotello et al. (2014b), the gas vertical density structure is coupled only to the small grains distribution. The gas-to-dust ratio is enforced on the total column of gas and dust (both small and large



---

grain populations).

Other parameters of the model are the stellar radiation field and the cosmic-ray ionization rate. Particularly important is the FUV (6 -13.6 eV) part of the stellar radiation field. In order to study the effects of different amounts of FUV radiation compared with the bolometric luminosity, the stellar spectrum is assumed to be a black-body at a given temperature  $T_{\text{eff}}$  with excess UV due to accretion. The X-ray spectrum is taken to be a thermal spectrum of  $7 \times 10^7$  K within 1 - 100 keV and the X-ray luminosity in this band  $L_X = 10^{30}$  erg s<sup>-1</sup>. As discussed in Bruderer (2013), the X-ray luminosity is of minor importance for the intensity of CO pure rotational lines which are the focus in this work. The cosmic-ray ionization rate is set to  $5 \times 10^{-17}$  s<sup>-1</sup>. We account for the interstellar UV radiation field and the cosmic microwave background as external sources of radiation.

The calculation is carried out on 75 cells in the radial direction and 60 in the vertical direction. The spectral grid of the continuum radiative transfer extends from 912 Å to 3 mm in 58 wavelength-bins. The wavelength dependence of the photodissociation and photo-ionization cross sections is taken into account using data summarized in van Dishoeck et al. (2006).

The chemistry is solved in a time-dependent manner, up to a chemical age of 1 Myr. The main difference to the steady-state solution is that carbon is not converted into methane (CH<sub>4</sub>) close to the mid-plane, since the time-scale of these reactions is longer than  $> 10$  Myr and thus unlikely to proceed in disks. CO line intensity results are not sensitive to this choice of age for values between 0.5-5 Myr. As in Miotello et al. (2014b) we run models both with isotope-selective processes switched on (ISO network) or off (NOISO network). The NOISO models do not include isotopologues in their chemical network and for the calculation of line fluxes, for example by <sup>13</sup>CO, the abundance is scaled by a constant factor given by the ISM isotope-ratio [<sup>13</sup>C]/[<sup>12</sup>C].

### 3.2.2 Chemical network

Our chemical reaction network is a reduced version of the ISO network presented by Miotello et al. (2014b), which is based on the UMIST 06 network (Woodall et al. 2007; Bruderer et al. 2012; Bruderer 2013). It includes H<sub>2</sub> formation on dust, freeze-out, thermal and non-thermal desorption, hydrogenation of simple species on ices, gas-phase reactions, photodissociation, X-ray and cosmic-ray induced reactions, PAH/small grain charge exchange/hydrogenation, and reactions with vibrationally excited H<sub>2</sub>. The details of the implementation of these reactions are reported in Appendix A.3.1 of Bruderer et al. (2012), while the implementation of CO isotope-selective processes is discussed in Miotello et al. (2014b). Specifically, a binding energy of 855 K was used for pure CO ice (Bisschop et al. 2006). The elemental abundances are also the same as those in Bruderer et al. (2012). The isotope ratios are

---

taken to be  $[^{12}\text{C}]/[^{13}\text{C}]=77$ ,  $[^{16}\text{O}]/[^{18}\text{O}]=560$  and  $[^{16}\text{O}]/[^{17}\text{O}]=1792$  (Wilson & Rood 1994).

Since CO is the main carbon-bearing species in protoplanetary disks, its abundance is strictly related to that of atomic carbon. As shown in Bruderer et al. (2012), Favre et al. (2013), Bergin et al. (2014), Du et al. (2015) and Kama et al. (2016b), some protoplanetary disk observations show evidence for carbon and/or oxygen depletion. So, CO isotopologue line intensities may be fainter because carbon is locked in more complex organics (see e.g., Bergin et al. 2014). In order to quantitatively explore the effects of carbon depletion on CO isotopologues line intensities, a small set of models has been run with a reduced initial carbon abundance. The standard value assumed for the whole grid,  $X_{\text{C}} = \text{C}/\text{H} = 1.35 \times 10^{-4}$ , has been reduced by factors of three and ten. Accordingly, the initial atomic abundance of  $^{13}\text{C}$  has been reduced by the same factors. These results and a more detailed discussion about the effects of carbon depletion on CO isotopologues lines are reported in Sec. 3.4.4 and in Appendix 3.B.

In order to be able to run a significantly larger number of models in a feasible amount of time, the ISO chemical network presented in Miotello et al. (2014b) has been reduced. It was possible to identify which species and reactions channels did not have an impact on CO chemistry, after running some test models with different versions of the chemical network. In particular, sulfur chemistry was found to have negligible influence on the CO chemistry. Accordingly, all sulfur-bearing molecules were removed by the list of the accounted species. Sulfur atoms and other metals like Si, Mg and Fe, are kept in the chemical network for allowing charge transfer. The simplifications applied to the chemical network do not bring significant variations in CO isotopologues abundance distributions and modify their resulting line intensities by less than 1%.

Finally, the total number of species has been reduced from 276 to 185 and the number of the reactions from 9755 to 5755. Since the time consumed is driven mainly by the number of the species in the chemical network, this reduction allows us to explore a much larger set of parameters, discussed in Sec. 3.2.3. From now on, we will refer to this chemical network such as the ISO network; all models have also been run without accounting for isotope-selective processes, using the NOISO network presented in Miotello et al. (2014b).

### 3.2.3 Grid of models

The physical structure of protoplanetary disks is difficult to constrain from observations without significant degeneracy in model parameter combination. In particular the vertical structure has been constrained only in few cases directly by observations (e.g., Rosenfeld et al. 2013). On the other hand, the structure of a disk may strongly affect the location and the intensity of the molecular emission. We explore to what

---

extent CO isotopologues lines trace  $M_{\text{disk}}$  by varying the radial and the vertical structure of the disk.

**Radial structure.** In a disk model the surface density distribution sets how the bulk of the gas mass is radially distributed inside the disk. Varying the values of different parameters in Eq. (5.1) influences the simulated line intensities. For exploring different scenarios, the following parameters have been varied:

- i.* The critical radius  $R_c$  has been assumed to be 30 au, 60 au and 200 au, in order to simulate disks with different radial extents. At  $R > R_c$  the exponential controls the surface density distribution. Indirectly,  $R_c$  regulates the disk outer radius.
- ii.* The power-law index  $\gamma$  determines the disk radial size, too. This parameter mainly determines how the mass is distributed along the radial extent of the disk. Shallower power-laws allow the bulk of the mass to be further out in the disk. In this paper  $\gamma$  is taken to be 0.8, 1.0, and 1.5.

These ranges of  $R_c$  and  $\gamma$  cover those found observationally by Andrews et al. (2012). Very extended disks with  $R_c = 200$  au are, however, expected to be extreme cases.

**Vertical structure.** From a modeling point of view, different vertical structures can strongly affect the disk temperature structure and the chemistry. Changes in the temperature structure affect the molecular composition and thus alter the emitting CO column density.

- i.* The scale height  $h_c$ , defined by  $h = h_c(R/R_c)^\psi$ , regulates the vertical extent of the disk. In this grid of models  $h_c$  is allowed to be either 0.1 or 0.2.
- ii.* The flaring angle  $\psi$  indicates how much the disk spreads in the vertical direction and thus how much direct stellar radiation it is able to intercept. Also  $\psi$  has been taken to have two values, 0.1 and 0.2 rad.

**Mass and radiation field.** Finally, the total disk mass is the main parameter governing CO isotopologues column densities and line intensities. At the same time, the amount of photodissociating photons plays an important role for the survival of CO isotopologues. In order to explore different combinations of column densities and FUV fluxes, disk masses and stellar spectra have been varied.

- 
- i.* The total disk mass has been covered for seven values in a realistic range:  $M_{\text{disk}} = 10^{-5}, 10^{-4}, 5 \times 10^{-4}, 10^{-3}, 5 \times 10^{-3}, 10^{-2}, 10^{-1} M_{\odot}$ .
- ii.* The stellar flux has been assumed to be a black body with an effective temperature  $T_{\text{eff}} = 4000$  K or  $T_{\text{eff}} = 10000$  K to simulate either a T Tauri or a Herbig star, as in Miotello et al. (2014b). Excess UV radiation due to accretion is taken into account for T Tauri stars as follows. The gravitational potential energy of accreted mass is assumed to be released with 100% efficiency as blackbody emission with  $T=10000$  K. The mass accretion rate is taken to be  $10^{-8} M_{\odot} \text{ yr}^{-1}$  and the luminosity is assumed to be emitted uniformly over the stellar surface. An accretion rate of  $10^{-8} M_{\odot} \text{ yr}^{-1}$  is the typical value measured in classical Class II disks (Hartmann et al. 1998; Mohanty et al. 2005; Herczeg & Hillenbrand 2008; Alcalá et al. 2014; Manara et al. 2016a) and lack of significant accretion variability was found for these kinds of objects (Costigan et al. 2014). This results in  $L_{\text{FUV}}/L_{\text{bol}} = 1.5 \cdot 10^{-2}$  for the T Tauri and  $L_{\text{FUV}}/L_{\text{bol}} = 7.8 \cdot 10^{-2}$  for the Herbig stars. The interstellar radiation field is also included.

Finally, two values for the inclination angle  $i$  have been chosen for the ray-tracing,  $10^{\circ}$  and  $80^{\circ}$ . Line luminosities are not expected to vary significantly for intermediate inclinations, i.e., up to  $70^{\circ}$  (Beckwith et al. 1990). The results obtained for  $i = 10^{\circ}$  can be considered for the analysis of typical disks. On the other hand, line intensities are extremely reduced in the rare case of an edge-on disk, that is, with an inclination close to  $90^{\circ}$ . In order to account for such objects, disk models with  $i = 80^{\circ}$  have been run. For the ray-tracing all the modeled disks are assumed to be at a distance of 100 pc from Earth.

All parameters explored with this grid of models are summarized in Table 3.1. The gas-to-dust ratio is generally kept fixed to 100 because it is not in the scope of this paper to compare dust-based and gas-based disk mass determinations. However, this parameter can and should be set as variable when interpreting combined continuum and line observations and some initial exploration of the effects of lowering the gas-to-dust ratio are presented below. We note that one can study these effects by either keeping the gas mass or the dust mass constant. Here the former approach is taken: keeping the gas mass fixed. Other studies have explored the sensitivities of line intensities by keeping the dust mass fixed and changing the gas mass (e.g., Bruderer et al. 2012; Kama et al. 2016a; Woitke et al. 2016).

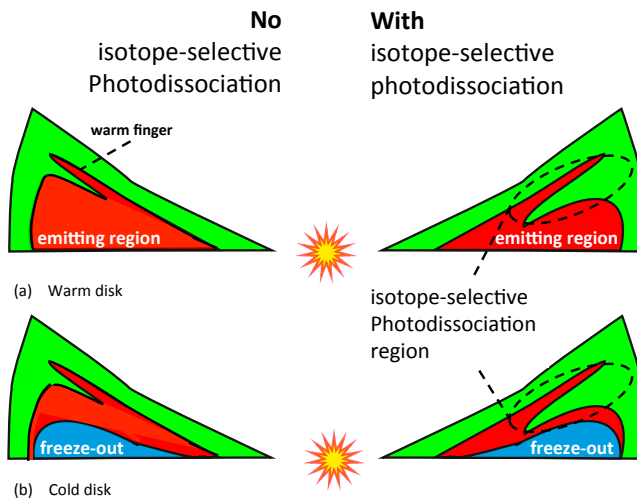


**Figure 3.1:** Sketch of a section of a disk. On the left hand side the region in red shows where CO isotopologues are expected to survive, if isotope-selective dissociation is not included. On the right hand side isotope-selective effects are included and the emitting region in red is reduced. Panel (a) shows the case of a warm disk, where CO isotopologues do not freeze-out anywhere in the disk, while panel (b) shows the case of a colder disk where freeze-out occurs in the midplane. The combination of freeze-out and isotope-selective photodissociation (panel (b), right hand side) drastically reduces CO isotopologues emission.

---

**Table 3.1:** Parameters of the disk models.

Parameter	Range
<i>Chemistry</i>	
Chemical network	ISO / NOISO
Chemical age	1 Myr
[C]/[H]	$1.35 \times 10^{-4}$
[PAH]	$10^{-2}$ ISM abundance
<i>Physical structure</i>	
$\gamma$	0.8, 1, 1.5
$\psi$	0.1, 0.2
$h_c$	0.1, 0.2 rad
$R_c$	30, 60, 200 au
$M_{\text{gas}}$	$10^{-5}, 10^{-4}, 5 \times 10^{-4}, 10^{-3},$ $5 \times 10^{-3}, 10^{-2}, 10^{-1} M_{\odot}$
Gas-to-dust ratio	100, 10, 1
$f_{\text{large}}$	0.9
$\chi$	1
$i$	$10^{\circ}, 80^{\circ}$
<i>Stellar spectrum</i>	
$T_{\text{eff}}$	4000 K +Accretion UV, 10000 K
$L_{\text{bol}}$	1, 10 $L_{\odot}$
$L_X$	$10^{30} \text{ erg s}^{-1}$
<i>Dust properties</i>	
Dust	0.005-1 $\mu\text{m}$ (small) 1-1000 $\mu\text{m}$ (large)

## 3.3 Results

### 3.3.1 Abundances

Photodissociation is the main process that regulates the abundance of gas phase CO in the emitting layer of disks and it is also the main isotope-selective process (see Visser et al. 2009, and references therein). The UV absorption lines, that initiate the dissociation process, can become optically thick and CO can shield itself from photodissociating radiation. For the main isotopologue,  $^{12}\text{CO}$ , UV absorption lines become optically thick even at the surface of the molecular layer in disks. On the other hand, less abundant isotopologues (e.g.,  $^{13}\text{CO}$ ,  $\text{C}^{18}\text{O}$  and  $\text{C}^{17}\text{O}$ ) shield themselves at higher column densities, that is deeper in the disk and closer to the midplane. As

shown in Miotello et al. (2014b), this results in a region where  $^{12}\text{CO}$  is self-shielded and able to survive, while less abundant isotopologues are still photodissociated. In these regions the rarer isotopologues (e.g.,  $\text{C}^{18}\text{O}$ ) are underabundant when compared to the correspondent ISM isotopic ratio ( $[\text{C}^{18}\text{O}]/[\text{C}^{16}\text{O}]$ ), that is usually adopted for predicting CO isotopologue abundances.

Fig. 3.1 shows a sketch of a disk section. On the left hand side the red regions show where CO isotopologues survive if isotope-selective dissociation is not included. On the right hand side isotope-selective effects are included and the emitting region in red is reduced. Panel (a) shows the case of a warm disk, where CO isotopologues do not freeze-out anywhere in the disk, while panel (b) shows the case of a colder disk where freeze-out occurs in the midplane. The combination of freeze-out and isotope-selective photodissociation (panel (b), right hand side) drastically reduces CO isotopologues column densities. Warmer disks, generally found around Herbig stars, are, however, also exposed to stronger UV fluxes compared with T Tauri disks. This causes photodissociation to be more efficient in Herbig disks and, accordingly, CO isotopologue abundances are strongly decreased. A more quantitative discussion on the competition between temperature effects and UV irradiation is presented in Sec. 3.3.2.

Comparison of models with the same disk parameters but run alternatively with the ISO and the NOISO network show that isotope-selective photodissociation has more effects on  $\text{C}^{18}\text{O}$  and  $\text{C}^{17}\text{O}$  abundances, than on  $^{13}\text{CO}$  survival.  $\text{C}^{18}\text{O}$  and  $\text{C}^{17}\text{O}$  present regions of significant underabundance (more than one order of magnitude) if isotope-selected processes are implemented in the models, while  $^{13}\text{CO}$  shows a slight overabundance of a factor of two (see Figs. 3 and 6 in Miotello et al. 2014b).  $\text{C}^{18}\text{O}$  and  $\text{C}^{17}\text{O}$  behave in an almost identical manner, therefore  $\text{C}^{17}\text{O}$  results are omitted in the following discussion. On the other hand,  $\text{C}^{17}\text{O}$  integrated line intensities are reported in Table 3.6.

### 3.3.2 Line intensities

#### Line intensities and disk masses

The results from our model show that a combination of disk spatially integrated  $^{13}\text{CO}$  and  $\text{C}^{18}\text{O}$  observations allow to assign a value for the total disk gas mass for a given carbon abundance. This result is similar to that found in Williams & Best (2014), with important differences described in Sec. 3.4.1. Fig. 3.2 presents the  $J = 2 - 1$  transitions of  $^{13}\text{CO}$  vs  $\text{C}^{18}\text{O}$  for the entire grid of models with colors indicating the different disk masses. It is seen that the points in this diagram show a clear disk mass segregation of the results, no matter which parameters are assumed in the disk models. This is particularly true for low-mass disks,  $M_{\text{disk}} = 10^{-5} - 10^{-3} M_{\odot}$ , while in the higher mass regime the separation becomes less clear. Here disk mass

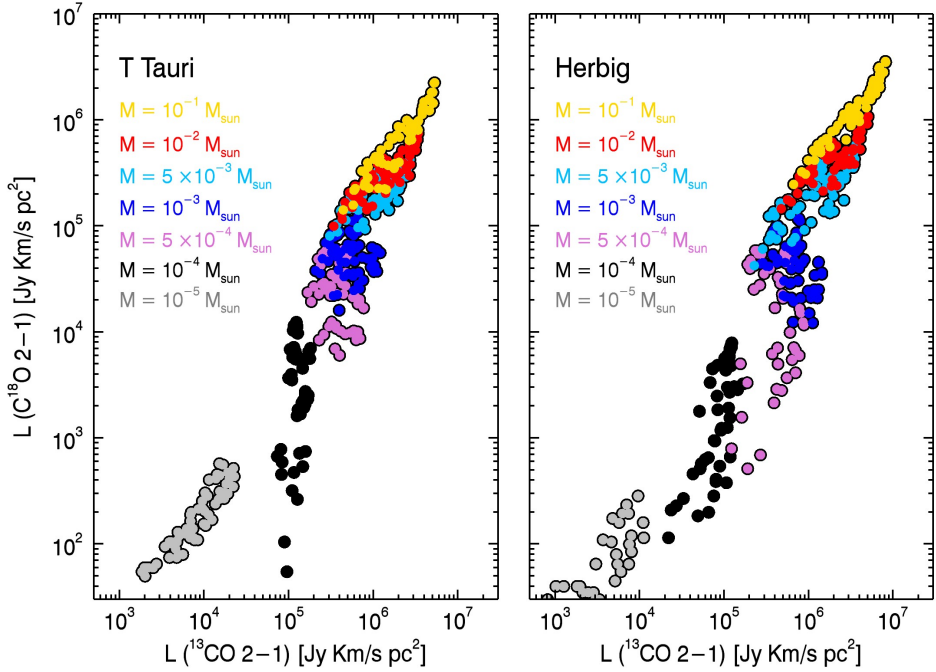


**Figure 3.2:** Line luminosity of  $C^{18}O$  vs  $^{13}CO$  ( $J = 2 - 1$ ) obtained implementing isotope-selective processes. Different colors represent models with different disk gas masses. The scatter of the points is due to the exploration of various disk parameters ( $\gamma$ ,  $R_c$ ,  $\psi$ ,  $h_c$ , and  $i$ ). Models shown in the left panel represent T Tauri disks, while those in the right panel represent Herbig disks, all located at a distance of 100 pc.



determinations are degenerate up to two orders of magnitude. This is caused by the high level of CO freeze-out in more massive disks. Only a small fraction of CO is left in the gas-phase in the outer disk and increasing the disk mass does not add much emission, defining an upper threshold for CO isotopologues line intensities. Accordingly, warmer Herbig disks (right panel of Fig. 3.2) present a lower level of freeze-out and reach higher line luminosities. In Fig. 3.2 results for all models are reported, while in the following plots some of them (those with  $M_{\text{disk}} = 5 \times 10^{-4}$  and  $5 \times 10^{-3} M_{\odot}$ ) are removed to better visualize the trends. Also, for all disk models transitions of different CO isotopologues up to  $J = 6 - 5$  are ray-traced for different disk inclinations, and are reported in Appendix 3.A.

The trends are similar for higher  $J$  transitions. As shown in Fig. 3.11, the scatter is, however, enhanced compared with that found for  $J = 2 - 1$  line intensities (Fig. 3.2). Higher  $J$  transitions, such as  $J = 6 - 5$ , indeed trace warmer gas in upper disk layers that are more sensitive to disk structure, while lower transitions are excited where most of the gas disk mass lies. Accordingly, lower  $J$  transitions of less abundant CO isotopologues are better mass tracers.

It is possible to determine how line intensities depend on the disk mass by computing the medians of the  $^{13}\text{CO}$  and  $\text{C}^{18}\text{O}$   $J = 2 - 1$  line intensities obtained by models in different disk mass bins. These trends are presented in Fig. 3.3, both for T Tauri and Herbig disks. For high-mass disks ( $M_{\text{disk}} > 10^{-3}$ ), line intensities do not increase linearly with mass, but tend to converge to a constant value. As discussed above, this is caused by the high level of CO freeze-out in more massive disks. Accordingly, this convergent trend occurs earlier (i.e., at lower disk masses) for colder T Tauri disks, than for warmer Herbig disks.

The median values of the line luminosities for models with  $i = 10^\circ$  are reported in Table 3.2 together with their standard deviations. The  $^{13}\text{CO}$  and  $\text{C}^{18}\text{O}$   $J = 2 - 1$  line luminosities can be expressed by fit functions of the disk mass:

$$L_y = \begin{cases} A_y + B_y \cdot M_{\text{disk}} & M_{\text{disk}} \leq M_{\text{tr}} \\ C_y + D_y \cdot \log_{10}(M_{\text{disk}}) & M_{\text{disk}} > M_{\text{tr}}, \end{cases} \quad (3.2)$$

where  $y = 13$  or  $18$ , for  $^{13}\text{CO}$  and  $\text{C}^{18}\text{O}$  respectively. For low mass disks the line luminosity has a linear dependence on the disk mass, while for more massive disks the trend is logarithmic. The transition point  $M_{\text{tr}}$  is different for the two isotopologues because  $^{13}\text{CO}$  becomes optically thick at lower column densities than  $\text{C}^{18}\text{O}$ . The polynomial coefficients  $A_y$ ,  $B_y$ ,  $C_y$ , and  $D_y$ , as well as the transition masses  $M_{\text{tr}}$  are reported in Table 4.2.

Finally it is worth investigating how the implementation of isotope-selective effects changes the obtained line intensities. Results for both T Tauri and Herbig disk models obtained with the NOISO network are reported in Sect. 3.4.1. The ratios NOISO/ISO of the  $^{13}\text{CO}$  and  $\text{C}^{18}\text{O}$  median  $J = 2 - 1$  line luminosities for each disk

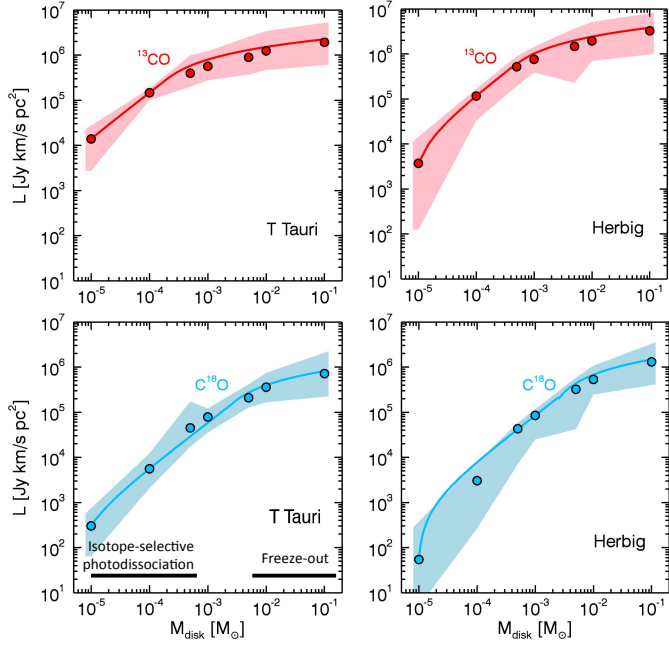


**Figure 3.3:** Median of the  $^{13}\text{CO}$  (in red) and  $\text{C}^{18}\text{O}$  (in blue)  $J = 2 - 1$  line intensities in different mass bins for models with  $i = 10^\circ$  are presented with filled circles. Solid lines show the fit functions presented in Eq. 4.3. Results for T Tauri disks are shown in the left panel, while those for Herbig disks in the right panel. The filled regions show the maximum range of the line luminosities obtained with different models.

mass bin can be used to quantify this behavior. The ratios are presented in Table 3.2 together with the standard deviations of the line luminosities for different mass bins. We see that if isotope selective effects are not implemented in the models  $\text{C}^{18}\text{O}$  lines are overestimated, in particular in the low mass regime. A similar behavior is found for the less abundant isotopologue  $\text{C}^{17}\text{O}$ . On the other hand,  $^{13}\text{CO}$  line intensities are slightly underestimated by the NOISO network, except for very low mass disks ( $M_{\text{disk}} = 10^{-5} M_\odot$ ) where they are slightly overestimated. Finally, we find that isotope-selective effects are more effective for Herbig than for T Tauri disks, in particular in the low mass regime (see fifth column of Table 3.2).

**Table 3.2:** Median CO isotopologues line luminosities,  $L_I$  in Jy km/s pc<sup>2</sup>, obtained implementing isotope-selective photodissociation (ISO network) together with their standard deviations (first and third columns). The second and the fourth columns list the medians of luminosity ratios, obtained by dividing the results from the simple NOISO and ISO networks. Results for both T Tauri and Herbig disks are reported.

$M_{\text{disk}}[M_{\odot}]$	<sup>13</sup> CO (2-1)		C <sup>18</sup> O (2-1)	
	$L_I$	$L_N/L_I$	$L_I$	$L_N/L_I$
T Tauri				
$10^{-5}$	$1.4 \pm 0.5 \cdot 10^4$	1.4	$3.0 \pm 1.3 \cdot 10^2$	14
$10^{-4}$	$1.5 \pm 0.4 \cdot 10^5$	0.7	$5.6 \pm 2.3 \cdot 10^3$	4.3
$10^{-3}$	$5.6 \pm 2.6 \cdot 10^5$	0.4	$7.5 \pm 2.9 \cdot 10^4$	0.9
$10^{-2}$	$1.2 \pm 0.7 \cdot 10^6$	0.4	$3.6 \pm 1.9 \cdot 10^5$	0.9
$10^{-1}$	$1.9 \pm 1.0 \cdot 10^6$	0.4	$7.2 \pm 3.8 \cdot 10^5$	0.4
Herbig				
$10^{-5}$	$3.7 \pm 3.4 \cdot 10^3$	3.3	$5.4 \pm 4.1 \cdot 10^1$	29
$10^{-4}$	$1.2 \pm 0.5 \cdot 10^5$	1.4	$3.0 \pm 2.7 \cdot 10^3$	18
$10^{-3}$	$7.6 \pm 2.8 \cdot 10^5$	0.7	$8.5 \pm 2.6 \cdot 10^4$	2.3
$10^{-2}$	$1.9 \pm 0.6 \cdot 10^6$	0.5	$5.3 \pm 2.1 \cdot 10^5$	0.6
$10^{-1}$	$3.3 \pm 1.7 \cdot 10^6$	0.5	$1.3 \pm 0.4 \cdot 10^6$	0.5

### Line ratios

An alternative way to present the results is to plot the ratios of C<sup>18</sup>O/<sup>13</sup>CO  $J = 2 - 1$  line intensities,  $L_{18}/L_{13}$ , as functions of the disk mass (see Fig. 3.4). Line ratios obtained by disk models with same  $R_c$  show a clear trend with disk mass, as shown in Fig. 3.4. Therefore, if  $R_c$  can be determined by spatially resolved observations these trends can be employed for determining the disk gas mass with lower uncertainties. More precisely, as done for line luminosities, the line ratios  $L_{18}/L_{13}$  for models with  $i = 10^\circ$  can be fitted by functions of the disk mass,

$$L_{18}/L_{13} = \begin{cases} A_{R_c} + B_{R_c} \cdot M_{\text{disk}} & M_{\text{disk}} \leq M_{\text{tr}} \\ C_{R_c} + D_{R_c} \cdot \log_{10}(M_{\text{disk}}) & M_{\text{disk}} > M_{\text{tr}}. \end{cases} \quad (3.3)$$

The coefficients  $A_{R_c}$ ,  $B_{R_c}$ ,  $C_{R_c}$ , and  $D_{R_c}$  vary for different values of  $R_c$  and are listed in Table 3.4. Similarly to Eq. 4.3, the transition from the linear to the logarithmic dependence of the line ratios on the disk mass varies for different values of  $R_c$ . The values for the transition masses  $M_{\text{tr}}$  are reported in Table 3.4. If  $R_c$  is known, the degeneracy in disk mass determinations, shown by the shaded regions in Fig. 3.3, is

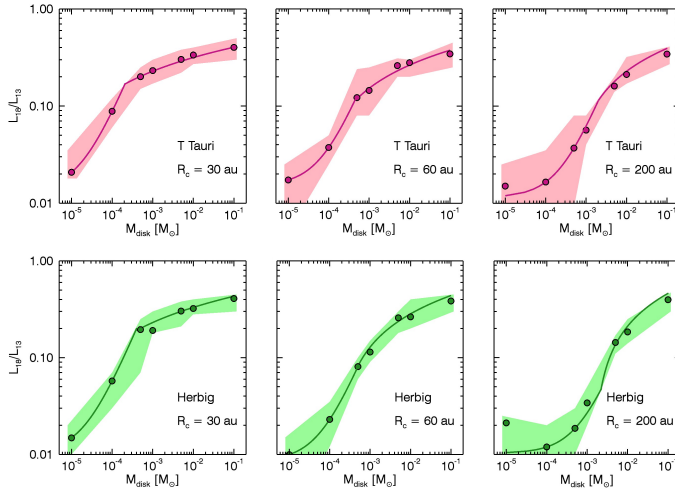


**Figure 3.4:** Line ratios of  $\text{C}^{18}\text{O}/^{13}\text{CO}$  ( $J = 2 - 1$ ), defined as  $L_{18}/L_{13}$ , as function of disk masses for models where  $i = 10^\circ$ . The top panels report the results for T Tauri disk models and lower panels those for Herbig disk models. Left, middle and right panels present results for models with respectively  $R_c = 30$  au,  $R_c = 60$  au, and  $R_c = 200$  au. Each point reports the result for the median line ratio in each mass bin. The continuous solid lines show the fit function reported in Eq. (3.3). The filled regions show the standard deviation from the median values.

reduced by a factor between two and five.

### Dependence on disk and stellar parameters

It is interesting to investigate how CO isotopologues line intensities depend on some disk parameters (see Fig. 3.10). From an observational point of view the radial disk extent can be constrained with spatially resolved data. In this context the first parameter to check is the critical radius  $R_c$ . Line intensities for models with different values of  $R_c$  are compared in the upper panels of Fig. 3.10 for the case of T Tauri disks. Very extended disks ( $R_c = 200$  au, see panel c) have lower  $\text{C}^{18}\text{O}$  and  $^{13}\text{CO}$  line intensities than more compact disks ( $R_c = 30$  au, see panel a) in the low mass regime. Keeping  $M_{\text{disk}}$  unchanged, more extended disks have lower column densities at each radius and FUV photons can penetrate easier. As a consequence the gas temperature is higher, the photodissociating radiation field is stronger and CO isotopologues are more efficiently dissociated and less abundant. These effects are illustrated in Fig. 3.5, which shows  $\text{C}^{18}\text{O}$  abundances and column densities as func-

---

tions of radius for two disks with  $R_c = 30$  and 200 au, respectively.

On the other hand, in the high mass regime ( $M_{\text{disk}} = 10^{-1}M_{\odot}$ ) more extended disks show higher line luminosities than more compact disks. Given the high column densities, CO isotopologues can shield themselves and survive to high abundances at larger radii, if the disk is more extended. The bulk of the emission comes from the outer regions. This holds true in particular for  $^{13}\text{CO}$  line emission which is optically thick.

A second parameter to explore is  $\gamma$ , the power-law index of the surface density distribution. Models with different  $\gamma$  values are presented separately in the lower panels of Fig. 3.10. The line luminosities produced by models with  $\gamma = 0.8$  and  $\gamma = 1$  are almost indistinguishable, while differences can be found comparing these with models with  $\gamma = 1.5$ . In particular in the intermediate disk mass regime, models for  $\gamma = 0.8, 1$  show three different populations that reflect models with different  $R_c$  values. This effect is less clear for models with  $\gamma = 1.5$ .

Finally, it is interesting to investigate how much the central star influences the CO isotopologues emission in the disk. Models with the same physical disk parameters, but irradiated by a T Tauri-like and a Herbig-like star are presented in Fig. 3.2 (respectively in the left and in the right panel) and in Fig. 3.3. For the Herbig disks, the derived line intensities are higher for more massive disks and lower for less massive disks compared with those obtained for the T Tauri disks. Since Herbig disks are warmer, less material is frozen-out onto grains in the higher mass regime and can contribute to the total emission enhancing the line luminosity. Also, the higher temperatures enhance the moderately optically thick  $^{13}\text{CO}$  lines. On the other hand, the strong UV flux coming from the Herbig star is very efficient in photodissociating CO isotopologue molecules for lower mass disks ( $M_{\text{disk}} = 10^{-4}, 10^{-5}M_{\odot}$ ) where the column densities are not high enough for shielding the photons. This combination of high UV field and low column densities reduces the line luminosities, thus they are lower than those from T Tauri disks.

### Dependence on gas-to-dust ratio

To test the sensitivity of the results to the gas-to-dust ratio for a fixed gas mass, we ran two T Tauri disk models ( $R_c = 60$  au,  $\gamma = 1$ ,  $\psi = 0.2$ ,  $h_c = 0.2$ ,  $M_{\text{disk}} = 10^{-4}, 10^{-2}M_{\odot}$ ) with reduced gas-to-dust ratios of ten and one. The ray-traced  $J = 3-2$  line intensities for CO isotopologues are presented in Fig. 3.12 as functions of the gas-to-dust ratio, normalized to the value at gas-to-dust=100. For the  $10^{-4}M_{\odot}$  disk the optically thin  $\text{C}^{18}\text{O}$  intensities increase by a factor of 3.5 if the gas-to-dust ratio is lowered by a factor of 100. This can be understood by the fact that if the dust mass is enhanced for a fixed gas mass, the FUV flux will be more efficiently attenuated. Accordingly CO and its isotopologues survive more easily and their lines are brighter for low gas-to-dust ratios, especially if their emission is optically thin. In addition,

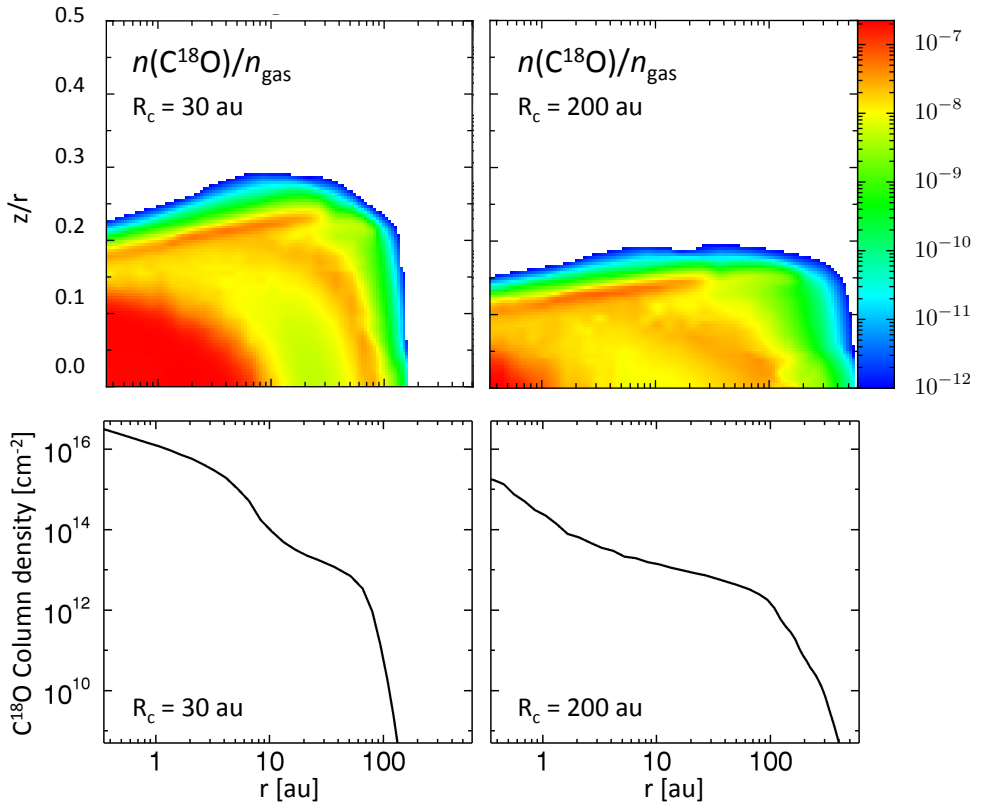


**Figure 3.5:** Abundances of  $\text{C}^{18}\text{O}$  (top panels) and column densities (lower panels) for models with different critical radii:  $R_c = 30$  au in the left panels and  $R_c = 200$  au in the right panels. For these particular T Tauri models the disk parameters are fixed to:  $M_{\text{disk}} = 10^{-5} M_{\odot}$ ,  $\gamma = 0.8$ ,  $h_c = 0.1$ , and  $\psi = 0.1$ .

---

if the dust opacity dominates over the line mutual shielding, isotope-selective processes are minimized. The  $^{13}\text{CO}$  and  $^{12}\text{CO}$  emission on the other hand stay the same within 30% because they are more optically thick. There are also small temperature differences of order 20% between the models in the emitting layer which can affect their line intensities.

For the  $10^{-2}M_{\odot}$  disk the trend is opposite: line intensities decrease if the gas-to-dust ratio is lowered for all three isotopologues. This happens because the dust column densities are increased to the point that the dust becomes optically thick to CO isotopologues emission. Therefore reducing the gas-to-dust ratio for large disk masses, that is, adding more dust, results in a larger fraction of gaseous CO not contributing to the line emission.

Overall, it is important to note that the variations in the CO isotopologues line fluxes are small for these two test cases, that is, a factor of a few or less over two orders of magnitude in gas-to-dust ratios, keeping the gas mass fixed. This variation is much smaller than if the dust mass is kept fixed but the gas mass is changed (Bruderer et al. 2012; Kama et al. 2016a; Woitke et al. 2016). Thus, the CO isotopologue line fluxes remain a robust tracer of the gas mass, even for low gas-to-dust ratios.

### Spatially resolved lines

Spatially integrated CO isotopologues line intensities are needed for determining the total disk gas content, with special attention to not losing the weak emission coming from the outer disk. However, as discussed above, disk mass determinations are degenerate since they depend on various parameters. Spatially resolved lines may help in breaking this degeneracy, constraining some of the disk parameters usually fixed by the model inputs.

The disk's spatial extent is the most straightforward characteristic that spatially resolved observations can constrain. This allows determination of  $R_c$  and  $\gamma$ . From an observational point of view, this is done by plotting spatially resolved optically thin line intensities as a function of the disk radial extent (i.e., distance from the central star). In this context,  $\text{C}^{18}\text{O}$  and  $^{13}\text{CO}$  are good tracers of the surface density, being optically thin and detectable by ALMA. For example, Fig. 3.6 shows the radial profile of  $^{13}\text{CO}$  and  $\text{C}^{18}\text{O}$   $J = 2 - 1$  lines for four models where  $\psi = 0.1$ ,  $h_c = 0.1$ ,  $M_{\text{disk}} = 10^{-3}M_{\odot}$  and  $R_c$  and  $\gamma$  assume different values. The modeled line intensities have been convolved with a  $0.5''$  beam in order to simulate typical moderate angular resolution ALMA observations. We can see that the maximum radial extent of the  $^{13}\text{CO}$  emission is clearly different if  $R_c = 30$  au or if  $R_c = 200$  au, although deep integrations are needed

Furthermore, the power-law spectral index of the surface density distribution may be constrained by spatially resolved observations. As shown by the purple line in Fig. 3.6, with an integration of around 2 hours and an angular resolution of  $0.2''$

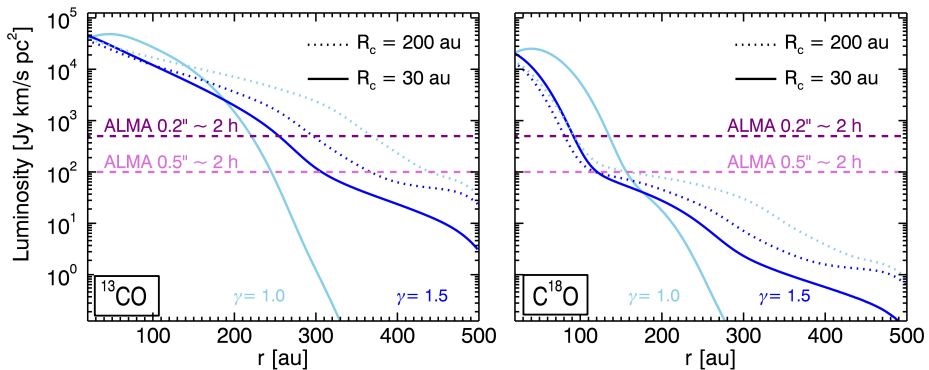


**Figure 3.6:** Radial profile of  $^{13}\text{CO}$  and  $\text{C}^{18}\text{O}$   $J = 2 - 1$  lines for four T Tauri models where  $\psi = 0.1$ ,  $h_c = 0.1$ ,  $M_{\text{disk}} = 10^{-3} M_{\odot}$  and  $R_c$  and  $\gamma$  assume different values. Models with  $\gamma = 1.5$  are presented in dark blue, while those with  $\gamma = 1.0$  are shown in light blue. Solid lines displays models with  $R_c = 30$  au and dotted lines represents those with  $R_c = 200$  au. These line profiles are obtained assuming a distance of 100 pc, an inclination angle  $i = 10^\circ$ , and by convolving the output images by a  $0.5''$  beam. The horizontal dashed lines show the typical ALMA sensitivity for an integration time of 1.84 hours on source for a  $0.2''$  beam (purple line) and for a  $0.5''$  beam (pink line), given a spectral resolution of 1.3 km/s.

it is possible to discriminate between a power-law index  $\gamma = 1.0$  and  $\gamma = 1.5$  with  $^{13}\text{CO}$  line emission.

## 3.4 Discussion

### 3.4.1 Comparison with parametric models

A large grid of parametric models has been run by Williams & Best (2014) to simulate a CO isotopologues survey for a sample of protoplanetary disks. The work presented here has been partially inspired by their paper and is designed to have results that could be easily compared with those by Williams & Best (2014).

The main differences between the two approaches are in how the gas temperature structure is defined and how the CO isotopologues survival is determined. Williams & Best (2014) do not calculate the temperature structure and do not run any chemical model. The gas temperature profile is purely parametric, but guided by theory and observations and is a combination of midplane and disk atmosphere temperatures, both assumed to be radial power-laws. This temperature parametrization avoids any assumption about stellar properties and interstellar irradiation. In order to ac-



---

count both for CO freeze-out and photodissociation, gas phase CO is abundant at a constant (ISM-like) abundance for temperatures higher than 20 K and for column densities higher than  $1.3 \times 10^{21} \text{H}_2 \text{ cm}^{-2}$ , as inspired by van Zadelhoff et al. (2001); Visser et al. (2009). Also less abundant CO isotopologues assume ISM-like abundances, corrected for a fixed  $^{13}\text{C}/^{12}\text{C}$  and  $^{18}\text{O}/^{16}\text{O}$  ratio. Isotope-selective photodissociation is accounted for empirically by decreasing the  $\text{C}^{18}\text{O}$  abundance by an additional factor of three. On the other side, as in Miotello et al. (2014b), the models presented in this paper use a star-like irradiation source for determining the disk dust and gas temperature. Also, a full chemical calculation is run to obtain both a self-consistent gas temperature distribution and atomic and molecular abundances.

### NOISO models

First, it is important to compare the two sets of models where isotope-selective processes have not been implemented. This allows us to find differences due only to different methodologies, before analyzing those caused by the effects of isotope-selective photodissociation. For this reason we refer to the line intensities obtained without reducing the  $\text{C}^{18}\text{O}$  abundances by a factor of three in Williams & Best (2014) and compare them with those obtained with the NOISO network.

Both sets of results are presented in Fig 3.7 (panel a): small dots show Williams & Best (2014) models and solid lines outline the regions covered by the NOISO models. While the Williams & Best (2014) models present a clear mass segregation, our model results are more degenerate, in particular for disk masses between  $10^{-3}$  and  $10^{-1} M_{\odot}$ . This difference is caused by a temperature effect. The higher mass disks presented in our grid are generally colder than those obtained by Williams & Best (2014), even if a  $40 L_{\odot}$  Herbig star is taken. As the disk mass increases, the column densities are enhanced too, deeper regions are colder and a larger fraction of CO is frozen out onto grains. The emitting fraction of CO (isotopologues) is strongly reduced and the line luminosities do not scale linearly with disk mass anymore, in particular for optically thin lines (i.e.,  $\text{C}^{18}\text{O}$  lines). By contrast, our NOISO line intensities are up to one order of magnitude higher at the low disk mass end. This is because only few NOISO models with disk masses of  $10^{-4} M_{\odot}$  are cold enough to cover the same range of very low line luminosity populated by Williams & Best (2014) results. Summarizing, Williams & Best (2014) parameterize a wider range of temperatures than in our models and consequently they find a wider range of CO luminosities. For the stellar and disk parameters assumed in this paper, the NOISO models do not reproduce the extreme (both cold and hot) temperature distributions assumed by Williams & Best (2014).

Even though the uncertainties in the gas temperature determination are not important for low- $J$  CO lines (they come from regions in the disk where  $T_{\text{gas}}$  is cou-

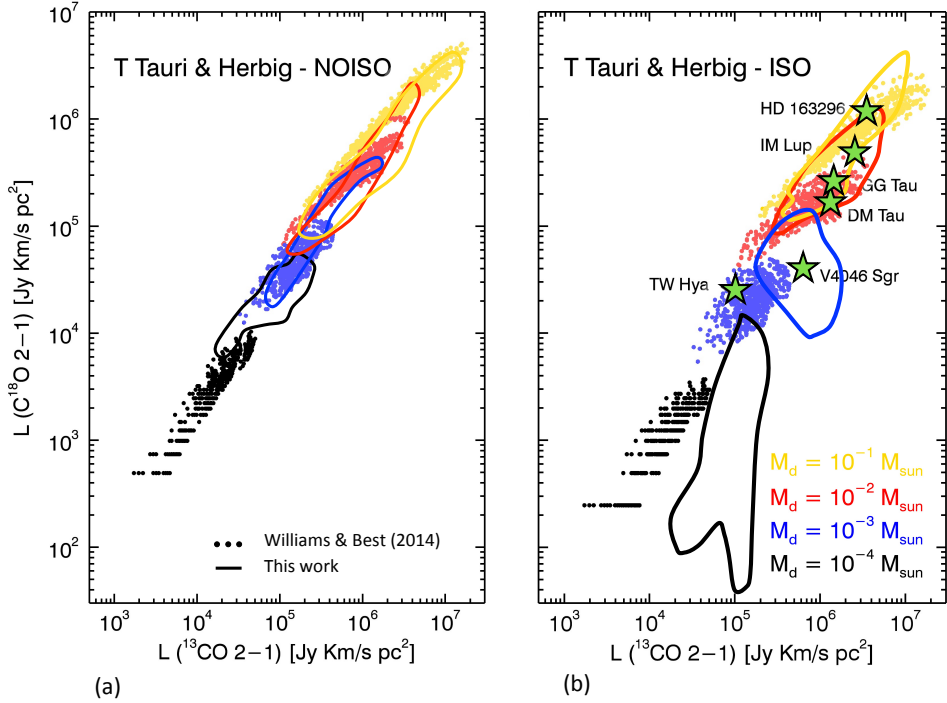


**Figure 3.7:** Line luminosities of  $C^{18}O$  vs  $^{13}CO$ . Different colors represent models with different disk gas masses. Small dots show the results by Williams & Best (2014) and the solid lines outline the regions covered by our model results. Panel (a) shows models where isotope-selective processes are not considered (NOISO). Panel (b) reports models where isotope-selective processes are implemented (ISO) and models by Williams & Best (2014) where the  $C^{18}O$  abundance has been reduced by a factor of three. Observations of six well studied disks are indicated by the green stars.

pled to  $T_{\text{dust}}$ ), there is a direct connection between the disk structure and the emitted lines. For example, high- $J$  CO lines are detected primarily in flared disks (Meeus et al. 2013) and can only be reproduced if  $T_{\text{gas}}$  and  $T_{\text{dust}}$  are decoupled (Bruderer et al. 2012). This aspect is faded out when assuming the same temperature parametrization for all disk structures. Therefore the physical-chemical approach is an improvement compared with the parametric modeling method.

## ISO models

As shown in panel (b) of Fig. 3.7, the implementation of isotope-selective effects in the models affects differently the line luminosities for different disk masses. Less massive disks are more heavily affected than more massive disks, where freeze-out dominates. More precisely, the ISO  $^{13}\text{CO}$  line luminosities are similar to those obtained with the NOISO network, while  $\text{C}^{18}\text{O}$  lines are less bright, in particular for low mass disks ( $M_{\text{disk}}$  between  $10^{-4}$  and  $10^{-3}M_{\odot}$ ). Williams & Best (2014) assume instead a constant reduction of a factor 3 of  $\text{C}^{18}\text{O}$  abundances in each mass bin in order to empirically consider isotope-selective effects. Comparing the two sets of models, a factor of three reduction for  $\text{C}^{18}\text{O}$  reproduces well the line luminosities for very high mass disks ( $M_{\text{d}} = 10^{-1}M_{\odot}$ ), but not for lower mass disks, where an additional factor of four would need to be applied. In addition, Williams & Best (2014) models do not show such a large degeneracy in the mass determination of very massive disks, as that shown by the ISO models.

The difference between the two sets of models may be explained also through application to existing data. Observed line luminosities of six well-studied disks reported by Williams & Best (2014) are presented in panel (b) of Fig. 3.7. In the lower mass regime, where isotope-selective photodissociation is more effective, only two disks are reported (V4046 Sgr and TW Hya) so the comparison is not well representative. For V4046 Sgr there is agreement between the mass derivations obtained by the two grids of models, that is,  $M_{\text{disk}} \approx 10^{-3}M_{\odot}$ . The TW Hya lines are instead just outside the grid of models presented in this paper, while Williams & Best (2014) obtain a mass of  $\sim 10^{-3}M_{\odot}$ . TW Hya is however a peculiar disk, for which a high level of carbon depletion has to be assumed in order to reach agreement with the derived mass from HD observations (Bergin et al. 2013; Favre et al. 2013; Kama et al. 2016b). This particular disk will be treated in detail in a future paper. Turning now to the higher mass regime, DM Tau and GG Tau are found to have  $\sim 10^{-2}M_{\odot}$  disk masses by Williams & Best (2014), while the ISO models give values that are degenerate by at least one order of magnitude: their mass could be between  $10^{-2}M_{\odot}$  and  $10^{-1}M_{\odot}$ . Finally, the mass of the HD163296 disk is  $10^{-1}M_{\odot}$  following Williams & Best (2014), while the ISO models indicate a mass range between  $10^{-2}M_{\odot}$  and  $10^{-1}M_{\odot}$ .

---

### 3.4.2 Analysis of CO isotopologues observations

One of the main goals of this paper is to provide outputs that can be employed by the community for analyzing CO isotopologue observations accounting for isotope-selective processes. For this reason integrated line intensities have been computed and tabulated for various isotopologues and different low- $J$  transitions (see Appendix 3.A).

Comparing the observed line intensities with the simulated intensities listed in Table 3.6, one can find the closest models predictions to the observations and the total disk mass can be constrained, assuming a range of other disk parameters such as  $R_c$ ,  $\gamma$ ,  $h_c$ , and  $\psi$ . Surely, the larger the number of different isotopologues and transitions the more secure the inferred values, although even a single line can be used as a mass tracer in the optically thin regime (Fig. 3).

Knowledge about some disk and stellar parameters helps in identifying the “best-fit” model. Knowing the stellar luminosity and type narrows down to either the T Tauri or the Herbig disk models. Spatially resolved observations could help in constraining  $R_c$  and  $\gamma$ , as explained in Sect. 3.3.2 and shown in Fig. 3.6. Finally, any information available about the vertical structure of the disk, for example from infrared data, assist constraining the range of scale-height values or flaring angles.

Table 3.6 also reports the continuum fluxes at  $870 \mu\text{m}$ . These are computed assuming a dust opacity  $\kappa_\nu = 4.2 \text{ cm}^2\text{g}^{-1}$  at  $\lambda = 870 \mu\text{m}$ . Dust mass derivations based on these fluxes will therefore scale directly with the chosen dust opacity and on the fixed gas-to-dust ratio, set to 100.

The significant computation time of the models presented in this paper does not allow us to highly populate the grid. However, a comparison of observed integrated line intensities with our models will allow improved disk mass derivations, accounting for CO isotope-selective photodissociation and temperature structures.

### 3.4.3 Complementary tracers: [OI], [CI], and [CII]

A comparison with complementary disk gas mass tracers is presented in this section. In particular, we present model results for the atomic oxygen and atomic and ionized carbon fine-structure transitions. As shown in Fig. 3.8, the median luminosities of [OI], [CI], and [CII] lines increase only slowly with disk masses. The luminosities vary from a factor of a few to two order of magnitude over a range of five orders of magnitudes in disk masses. In contrast, Fig. 3.3 shows an increase of CO isotopologues line luminosities of at least four orders of magnitudes over the same range of disk masses. This comparison illustrates that CO isotopologues emission is much more sensitive to total disk mass variations than [OI], [CI], and [CII]. For example [OI]  $63 \mu\text{m}$  line intensities increase by a factor of a few in our grid, in agreement with what found by Woitke et al. (2016) using the PRODIMO code (Fig. 13). Earlier stud-

ies using the same code (Kamp et al. 2010, 2011) find that [OI] 63  $\mu\text{m}$  line intensities increase by few orders of magnitude over the same range of masses. The reason for the difference between these two results obtained with PRODIMO is not clear.

The [OI]  $^3P_1 - ^3P_2$  ( $\lambda = 63.2\mu\text{m}$ ) line has a high flux in protoplanetary disks. The *Herschel* open time key program GASPS (Dent et al. 2013) has detected this line in the majority of the observed T Tauri disks. Given its high excitation energy (227 K), [OI] 63  $\mu\text{m}$  line arises from the surface layers of the disk, above the CO low- $J$  emission regions. For this reason, [OI] is more sensitive to temperature variations than total mass variations. The bulk of the mass resides in much deeper regions of the outer disks, where column densities are higher and CO low- $J$  lines arise from. Accordingly [OI] lines are more sensitive to the disk vertical structure and may help in constraining the scale height and the flaring angle and in reducing the degeneracy in CO-based disk mass determinations. As shown in Fig. 3.13, in our models median [OI] lines are up to one order of magnitude brighter for flared disks ( $h_c = 0.2$ ,  $\psi = 0.2$ ) than for flat disks ( $h_c = 0.1$ ,  $\psi = 0.1$ ).

While CO is the main gaseous carbon carrier in the warm molecular layer, neutral and ionized atomic carbon  $\text{C}^0$  and  $\text{C}^+$  ([CI], and [CII] when line emission is concerned) become the main reservoirs in the UV-irradiated disk surface. The optically thin lines of these species are a direct probe of the carbon abundance in the disk surface (Kama et al. 2016a,b). However, [CI] cannot be observed from the ground and the data from *Herschel* may be contaminated by extended emission (Fedele et al. 2013; Dent et al. 2013). [CI]  $^3P_1 - ^3P_0$  emission at 492 GHz and [CI]  $^3P_2 - ^3P_1$  emission at 809 GHz has recently been unambiguously detected with the *Atacama Pathfinder EXperiment* (APEX) telescope in several disks, and used to constrain the gas-phase carbon abundance, since it is not sensitive to the temperature structure (Kama et al. 2016a,b).

### 3.4.4 Effects of lower carbon abundance

The abundance of CO and its isotopologues depends on the total abundance of elemental gas-phase carbon, which may be lower than in the ISM ( $[\text{C}]/[\text{H}]_{\text{ISM}} = 1.35 \times 10^{-4}$ ) as suggested by recent observations and analyses (e.g., Bruderer et al. 2012; Favre et al. 2013; Kama et al. 2016a,b). Thus, there is a degeneracy between the carbon abundance and the total gas mass inferred from CO isotopologues. To quantify this effect, we ran ten T Tauri disk models with a reduced initial carbon abundance. The standard value assumed for the whole grid,  $X_{\text{C}} = [\text{C}]/[\text{H}]_{\text{ISM}} = 1.35 \times 10^{-4}$ , has been reduced by factors of three and ten. The total abundance of  $^{13}\text{C}$  has been reduced by the same factors. The other disk model parameters are kept at  $R_c = 60$  au,  $\gamma=0.8$ ,  $h_c=0.1$ ,  $\psi=0.1$ , and  $M_{\text{disk}} = 10^{-5}, 10^{-4}, 10^{-3}, 10^{-2}, 10^{-1} M_{\odot}$ . Both the oxygen and the PAHs abundances are kept as in the large grid models (see Table 3.8 and Table 3.1).

---

The results are shown in Fig. 4.5.2 and quantified in Appendix 3.B. As expected, both the  $^{13}\text{CO}$  and  $\text{C}^{18}\text{O}$  line intensities are reduced if the initial carbon abundance is lowered. For the more massive disks, the reduction is larger for the more optically thin  $\text{C}^{18}\text{O}$  than for  $^{13}\text{CO}$  lines. This difference decreases for the lower-mass disks, where both lines scale more linearly with  $[\text{C}]/[\text{H}]_{\text{gas}}$ . This trend is similar to that resulting from a reduction in disk mass, as shown in Fig. 3.2. This is to be expected from the direct dependence of CO isotopolog abundances on both  $[\text{C}]/[\text{H}]_{\text{gas}}$  and the total gas mass.

An underabundance of gas-phase carbon could show up as extended scatter in Fig. 3.2, especially along the  $\text{C}^{18}\text{O}$  axis which owing to its optically thin lines is expected to be more directly sensitive to the number of available carbon atoms. The behaviour of  $\text{C}^{18}\text{O}$  emission with carbon abundance is shown for a subset of models in Fig. 3.9, panels (a) and (c). We also investigated whether ratios of different- $J$  transitions of a single isotopologue,  $\text{C}^{18}\text{O}$ , can brake the abundance-mass degeneracy. Panel (b) and (d) of Fig. 3.9 present the model  $\text{C}^{18}\text{O } J = 1-0/6-5$  and  $J = 2-1/6-5$  line luminosity ratios as a function of the disk mass for different carbon abundances. These four figures demonstrate that the relations are more complex than simply linear: in some regimes  $\text{C}^{18}\text{O}$  scales sub-linearly, in others super-linearly with carbon abundance. The explanation for these trends is further discussed in Appendix 3.B.

Concluding, a combination of different CO isotopologues (e.g.,  $^{13}\text{CO}$  and  $\text{C}^{18}\text{O}$ ) and various  $J$  transitions (e.g.,  $\text{C}^{18}\text{O } J = 2-1$  and  $J = 6-5$ ) together with [CI] observations would provide stronger observational constraints on the total disk gas mass, because this could also provide some indication on the level of carbon depletion. This result has to be seen as indicative, however, because the models with a lower carbon abundances presented here only cover a small range of disk parameters. A more extended grid of models is needed to quantify the predictions on line ratios between various  $J$ -transitions of the same isotopolog.

### 3.5 Summary and Conclusion

We presented a grid of 840 disk models where CO isotope-selective photodissociation has been treated in a complete way. A full thermo-chemical model was run and abundances and line intensities were obtained as outputs. The main conclusions are listed below.

- When CO isotope selective photodissociation is considered, the abundances of CO isotopologues are affected. In particular, there are regions in the disk where  $\text{C}^{18}\text{O}$  and  $\text{C}^{17}\text{O}$  show an underabundance of more than one order of magnitude with respect to  $^{12}\text{CO}$  when compared with the overall elemental abundance ratios.  $^{13}\text{CO}$  line intensities are instead slightly enhanced (Miotello et al. 2014b).

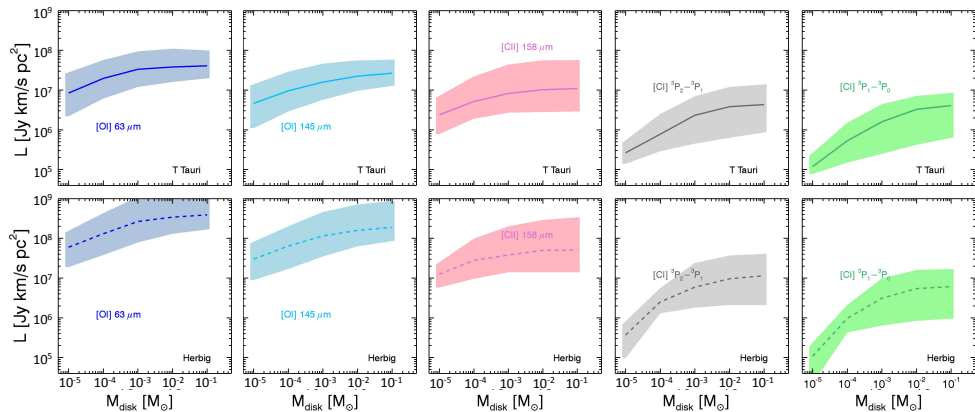


**Figure 3.8:** Median luminosities for [OI], [CI], and [CII] lines as a function of disk mass. Each line transition is shown by a differently colored line. Solid lines show T Tauri disk models (top panels), while dashed lines present Herbig disk models (bottom panels). The filled regions show the maximum range of the line luminosities obtained with different models.

- Observations of more than one CO-isotopologue, such as  $^{13}\text{CO}$  and  $\text{C}^{18}\text{O}$ , can be employed for determining disk total masses. There is however some degeneracy, of order one order of magnitude, for disks more massive than  $10^{-3}M_{\odot}$ . In the low-mass optically thin regime, where the line intensities scale linearly with disk mass,  $^{13}\text{CO}$  or  $\text{C}^{18}\text{O}$  alone can be employed as mass tracers and simple fit relations are presented. These species remain robust gas-mass tracers even for much lower gas-to-dust ratios.
- Constraining  $R_c$  and  $\gamma$  with spatially resolved line observations reduces the degeneracy in disk mass determinations by a factor between two and five.
- Comparison of results of our grid with parametric models shows that our  $^{13}\text{CO}$  and  $\text{C}^{18}\text{O}$  line intensities computed with the NOISO network are up to one order of magnitude higher at the low disk mass end than those obtained by Williams & Best (2014). Moreover, in our models isotope-selective effect are dependent on disk mass: the factor of 3 reduction for  $\text{C}^{18}\text{O}$  assumed by Williams & Best (2014) does not reproduce the line intensities for masses lower than  $10^{-3}M_{\odot}$ , where an additional factor of four would need to be applied.
- CO isotopologues emission is more sensitive to total disk mass variations than that of [OI], [CI], and [CII]. These lines can in fact be employed to constrain the disk vertical structure.

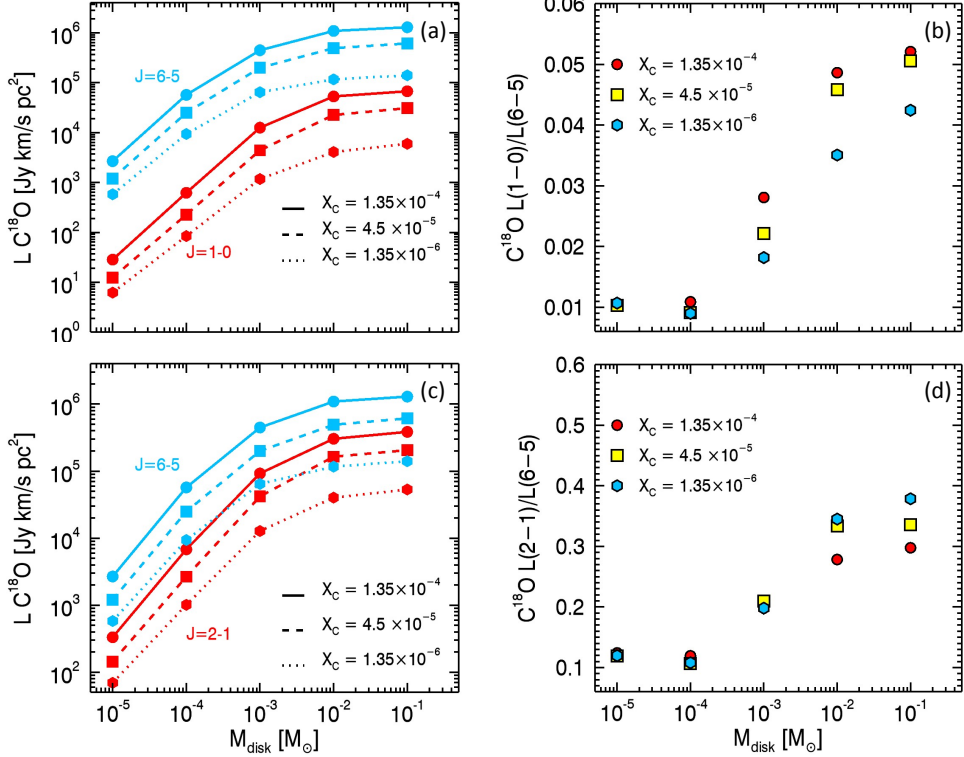


**Figure 3.9:** Results of T Tauri disk models with carbon abundances reduced by factors of three and ten. Panel (a) shows  $C^{18}O$   $J = 1 - 0$  and  $J = 6 - 5$  line luminosities as a function of the disk mass (respectively in red and blue), and panel (c) the  $C^{18}O$   $J = 2 - 1$  and  $J = 6 - 5$  line luminosities. The models with ISM-like carbon abundances are shown by the solid lines, those with a factor of 3 of carbon depletion by the dashed lines and those with a factor of 10 depletion by the dotted lines. Panel (b) shows  $C^{18}O$   $J = 1 - 0/J = 6 - 5$  line luminosity ratios as a function of the disk mass, and panel (d) the  $J = 2 - 1/J = 6 - 5$  ratios. The models with ISM-like carbon abundances are shown by the red circles, those with a factor of 3 of carbon depletion by yellow squares and those with a factor of 10 depletion by the blue hexagons. Model disk parameters:  $R_c = 60$  au,  $\gamma=0.8$ ,  $h_c=0.1$ ,  $\psi=0.1$ , and  $M_{\text{disk}} = 10^{-5}, 10^{-4}, 10^{-3}, 10^{-2}, 10^{-1} M_{\odot}$ .



- The degeneracy with carbon abundance has been investigated for a small set of models. [CI] observations give some indication on the level of carbon depletion and provide stronger constraints on the disk mass determination if combined with CO isotopologues observations.
- Finally, different CO isotopologues total fluxes for various low- $J$  transitions are provided in Appendix A. They can be used for the analysis of CO isotopologue observations, taking into account the isotope-selective effects.

## Acknowledgements

The authors are grateful to Jonathan Williams, Catherine Walsh, Paolo Cazzoletti, Leonardo Testi and the anonymous referee for useful discussions and comments. Astrochemistry in Leiden is supported by the Netherlands Research School for Astronomy (NOVA), by a Royal Netherlands Academy of Arts and Sciences (KNAW) professor prize, and by the European Union A-ERC grant 291141 CHEMPLAN.

## 3.A Additional tables and figures

**Table 3.3:** Polynomial coefficients  $A_y$ ,  $B_y$ ,  $C_y$ , and  $D_y$ , in Eq. (4.3)

	T Tauri	Herbig
$A_{13}$	$-8.954 \cdot 10^2$	$-8.746 \cdot 10^4$
$B_{13}$	$1.477 \cdot 10^9$	$1.245 \cdot 10^9$
$C_{13}$	$2.954 \cdot 10^6$	$5.214 \cdot 10^6$
$D_{13}$	$7.201 \cdot 10^5$	$1.402 \cdot 10^6$
$M_{\text{tr}}[M_{\odot}]$	$2 \cdot 10^{-4}$	$5 \cdot 10^{-4}$
$A_{18}$	$-2.852 \cdot 10^2$	$-8.026 \cdot 10^2$
$B_{18}$	$5.875 \cdot 10^7$	$8.571 \cdot 10^7$
$C_{18}$	$1.235 \cdot 10^6$	$2.276 \cdot 10^6$
$D_{18}$	$4.180 \cdot 10^5$	$8.001 \cdot 10^5$
$M_{\text{tr}}[M_{\odot}]$	$2.5 \cdot 10^{-3}$	$2.5 \cdot 10^{-3}$

Tables 4.2 and 3.4 report the polynomial coefficients  $A^{13}$  and  $A^{18}$  for  $L_{13}$  and  $L_{18}$  in Eq. (4.3) and the polynomial coefficients  $A_{R_c}$  for  $L_{18}/L_{13}$  in Eq. (3.3).

Table 3.6 reports  $^{12}\text{CO}$ ,  $^{13}\text{CO}$ ,  $\text{C}^{18}\text{O}$ ,  $\text{C}^{17}\text{O}$  and [CI] total fluxes (in K km/s) simulated by the models presented in this paper. The fluxes are computed assuming a distance of 100 pc and a beam size of  $10''$ . CO isotopologues fluxes are computed for

**Table 3.4:** Polynomial coefficients  $A_{R_c}$ ,  $B_{R_c}$ ,  $C_{R_c}$ , and  $D_{R_c}$  in Eq. (3.3).

	T Tauri	Herbig
$A_{30}$	$1.329 \cdot 10^{-2}$	$1.008 \cdot 10^{-2}$
$B_{30}$	$7.503 \cdot 10^2$	$4.730 \cdot 10^2$
$C_{30}$	$4.901 \cdot 10^{-1}$	$5.305 \cdot 10^{-1}$
$D_{30}$	$8.724 \cdot 10^{-2}$	$1.000 \cdot 10^{-1}$
$M_{\text{tr}}[M_{\odot}]$	$2 \cdot 10^{-4}$	$4 \cdot 10^{-4}$
$A_{60}$	$1.511 \cdot 10^{-2}$	$8.492 \cdot 10^{-3}$
$B_{60}$	$2.234 \cdot 10^2$	$1.448 \cdot 10^2$
$C_{60}$	$4.873 \cdot 10^{-1}$	$5.934 \cdot 10^{-1}$
$D_{60}$	$1.117 \cdot 10^{-1}$	$1.550 \cdot 10^{-1}$
$M_{\text{tr}}[M_{\odot}]$	$5 \cdot 10^{-4}$	$5 \cdot 10^{-4}$
$A_{200}$	$1.141 \cdot 10^{-2}$	$1.026 \cdot 10^{-2}$
$B_{200}$	$5.104 \cdot 10^1$	$1.662 \cdot 10^1$
$C_{200}$	$5.561 \cdot 10^{-1}$	$7.109 \cdot 10^{-1}$
$D_{200}$	$1.640 \cdot 10^{-1}$	$2.250 \cdot 10^{-1}$
$M_{\text{tr}}[M_{\odot}]$	$2 \cdot 10^{-3}$	$2 \cdot 10^{-3}$

four molecular line transitions ( $J = 1 - 0$ ,  $J = 2 - 1$ ,  $J = 3 - 2$ ,  $J = 6 - 5$ ) and for two disk inclination angles ( $i = 10^\circ, 80^\circ$ ). This table, together with the analogue one for Herbig disk models, is provided on-line in ascii format.

Table. A.4 reports the list of all the species considered in the ISO chemical network.

Finally, additional figures are also reported in this appendix. Fig. 3.10 shows  $\text{C}^{18}\text{O}$  vs  $^{13}\text{CO}$  ( $J = 2 - 1$ ) line luminosity obtained varying different disk parameters, such as  $R_c$  and  $\gamma$ . Fig. 3.11 shows  $\text{C}^{18}\text{O}$  vs  $^{13}\text{CO}$  ( $J = 6 - 5$ ) line luminosity obtained implementing isotope-selective processes. Fig. 3.13 shows the median luminosities for [OI] lines as a function of disk mass for flat ( $h_c = 0.1$ ,  $\psi = 0.1$ ) and flared ( $h_c = 0.2$ ,  $\psi = 0.2$ ) disk models. Fig. 3.12 presents CO isotopologues line intensities as a function of gas-to-dust ratio. The same T Tauri disk model ( $R_c = 60$  au,  $\gamma = 1$ ,  $\psi = 0.2$ ,  $h_c = 0.2$ ,  $M_{\text{disk}} = 10^{-4}M_{\odot}$ ) has been run with gas-to-dust mass ratios of 100, 10 and 1.

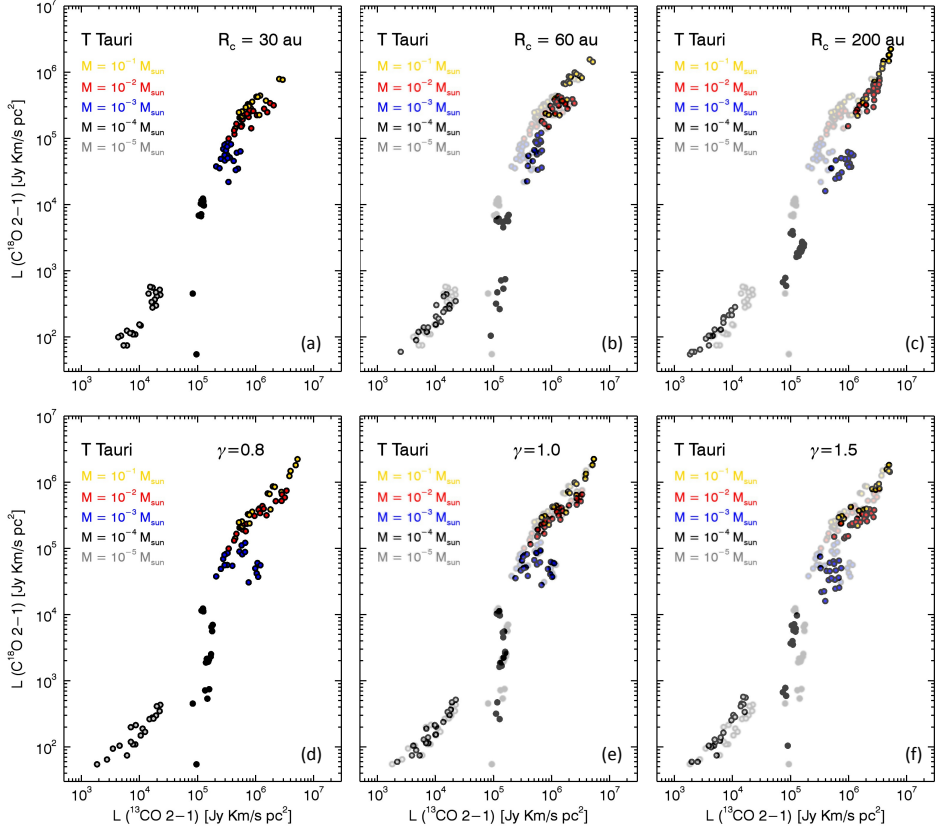


**Figure 3.10:** Line luminosity of  $C^{18}O$  vs  $^{13}CO$  ( $J = 2 - 1$ ) obtained implementing isotope-selective processes. Different colors represent models with different disk gas masses. In the upper panels models with different values for  $R_c$  are presented separately. In the lower panels models with different values for  $\gamma$  are shown separately. Models displayed in panel (a) and (d) are also reported in gray in panels (b,c) and (e,f) respectively in order to facilitate the comparison.

**Table 3.5:** Species contained in the ISO chemical network.  $H_2^*$  refers to vibrationally excited  $H_2$ ;  $PAH^0$ ,  $PAH^+$  and  $PAH^-$  are neutral, positively and negatively charged PAHs, while  $PAH:H$  denotes hydrogenate PAHs; JX refers to species frozen-out onto dust grains.

H	He	C	$^{13}C$	N
O	$^{17}O$	$^{18}O$	Mg	Si
S	Fe	$H_2$	$H_2^*$	CH
$^{13}CH$	$CH_2$	$^{13}CH_2$	NH	$CH_3$
$^{13}CH_3$	$NH_2$	$CH_4$	$^{13}CH_4$	OH
$^{17}OH$	$^{18}OH$	$NH_3$	$H_2O$	$H_2^{17}O$
$H_2^{18}O$	CO	$C^{17}O$	$C^{18}O$	$^{13}CO$
$^{13}C^{17}O$	$^{13}C^{18}O$	HCN	$H^{13}CN$	HCO
$HC^{17}O$	$HC^{18}O$	$H^{13}CO$	$H^{13}C^{17}O$	$H^{13}C^{18}O$
NO	$N^{17}O$	$N^{18}O$	$H_2CO$	$H_2C^{17}O$
$H_2C^{18}O$	$H_2^{13}CO$	$H_2^{13}C^{17}O$	$H_2^{13}C^{18}O$	$O_2$
$O^{17}O$	$O^{18}O$	$CO_2$	$CO^{17}O$	$CO^{18}O$
$^{13}CO_2$	$^{13}CO^{17}O$	$^{13}CO^{18}O$	CN	$^{13}CN$
$N_2$	SiH	SiO	$Si^{17}O$	$Si^{18}O$
$H^+$	$H^-$	$H_2^+$	$H_3^+$	$He^+$
$HCO^+$	$HC^{17}O^+$	$HC^{18}O^+$	$H^{13}CO^+$	$H^{13}C^{17}O^+$
$H^{13}C^{18}O^+$	C+	$^{13}C^+$	CH+	$^{13}CH^+$
$N^+$	$CH_2^+$	$^{13}CH_2^+$	NH+	$CH_3^+$
$^{13}CH_3^+$	O+	$^{17}O^+$	$^{18}O^+$	$NH_2^+$
$CH_4^+$	$^{13}CH_4^+$	OH+	$^{17}OH^+$	$^{18}OH^+$
$NH_3^+$	$CH_5^+$	$^{13}CH_5^+$	$H_2O^+$	$H_2^{17}O^+$
$H_2^{18}O^+$	$H_3O^+$	$H_3^{17}O^+$	$H_3^{18}O^+$	$Mg^+$
CN+	$^{13}CN^+$	HCN+	$H^{13}CN^+$	Si+
CO+	$C^{17}O^+$	$C^{18}O^+$	$^{13}CO^+$	$^{13}C^{18}O^+$
HCNH+	$H^{13}CNH^+$	SiH+	NO+	$N^{17}O^+$
$N^{18}O^+$	$SiH_2^+$	S+	$O_2^+$	$O^{17}O^+$
$O^{18}O^+$	SiO+	$Si^{17}O^+$	$Si^{18}O^+$	$CO_2^+$
$CO^{17}O^+$	$CO^{18}O^+$	$^{13}CO_2^+$	$^{13}CO^{17}O^+$	$^{13}CO^{18}O^+$
Fe+	SiOH+	$Si^{17}OH^+$	$Si^{18}OH^+$	$HN_2^+$
$e^-$	$PAH^0$	$PAH^+$	$PAH^-$	$PAH:H$
JC	$J^{13}C$	JN	JO	$J^{17}O$
$J^{18}O$	JCH	$J^{13}CH$	JCH <sub>2</sub>	$J^{13}CH_2$
JNH	JCH <sub>3</sub>	$J^{13}CH_3$	JNH <sub>2</sub>	JCH <sub>4</sub>
$J^{13}CH_4$	JOH	$J^{17}OH$	$J^{18}OH$	JNH <sub>3</sub>
JH <sub>2</sub> O	$JH_2^{17}O$	$JH_2^{18}O$	JCO	$JC^{17}O$
$JC^{18}O$	$J^{13}CO$	$J^{13}C^{17}O$	$J^{13}C^{18}O$	JCO <sub>2</sub>
$JCO^{17}O$	$JCO^{18}O$	$J^{13}CO_2$	$J^{13}CO^{17}O$	$J^{13}CO^{18}O$

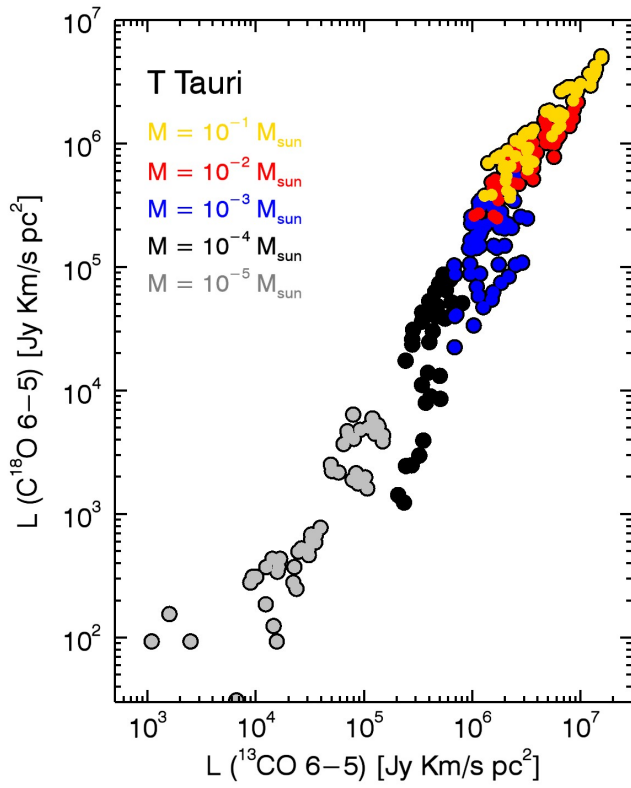


**Figure 3.11:**  $\text{C}^{18}\text{O}$  vs  $^{13}\text{CO}$  ( $J = 6-5$ ) line luminosity obtained implementing isotope-selective processes. Different colors represent models with different disk gas masses.

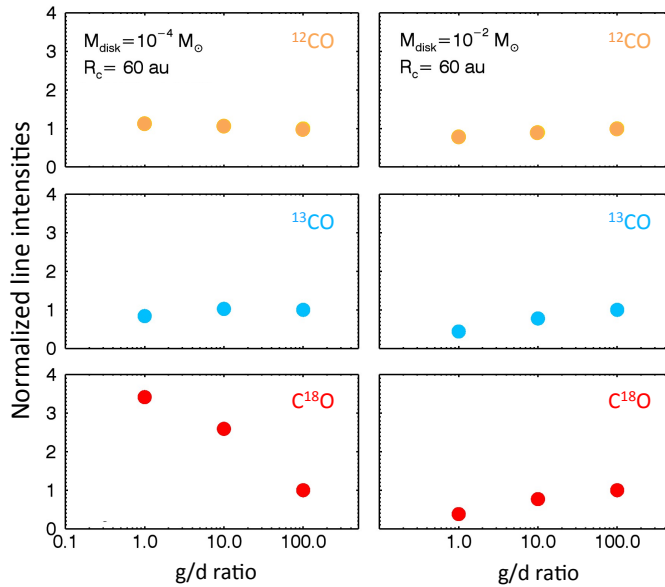


**Figure 3.12:** CO isotopologues line intensities normalized by the intensity for gas-to-dust=100 as a function of gas-to-dust ratio. Keeping the gas mass fixed, two T Tauri disk models ( $R_c = 60$  au,  $\gamma = 1$ ,  $\psi = 0.2$ ,  $h_c = 0.2$ ,  $M_{\text{disk}} = 10^{-4}, 10^{-2} M_{\odot}$ ) have been run with gas-to-dust mass ratios of 100, 10 and 1. Orange, blue and red circles show respectively  $^{12}\text{CO}$ ,  $^{13}\text{CO}$ , and  $\text{C}^{18}\text{O}$  lines.

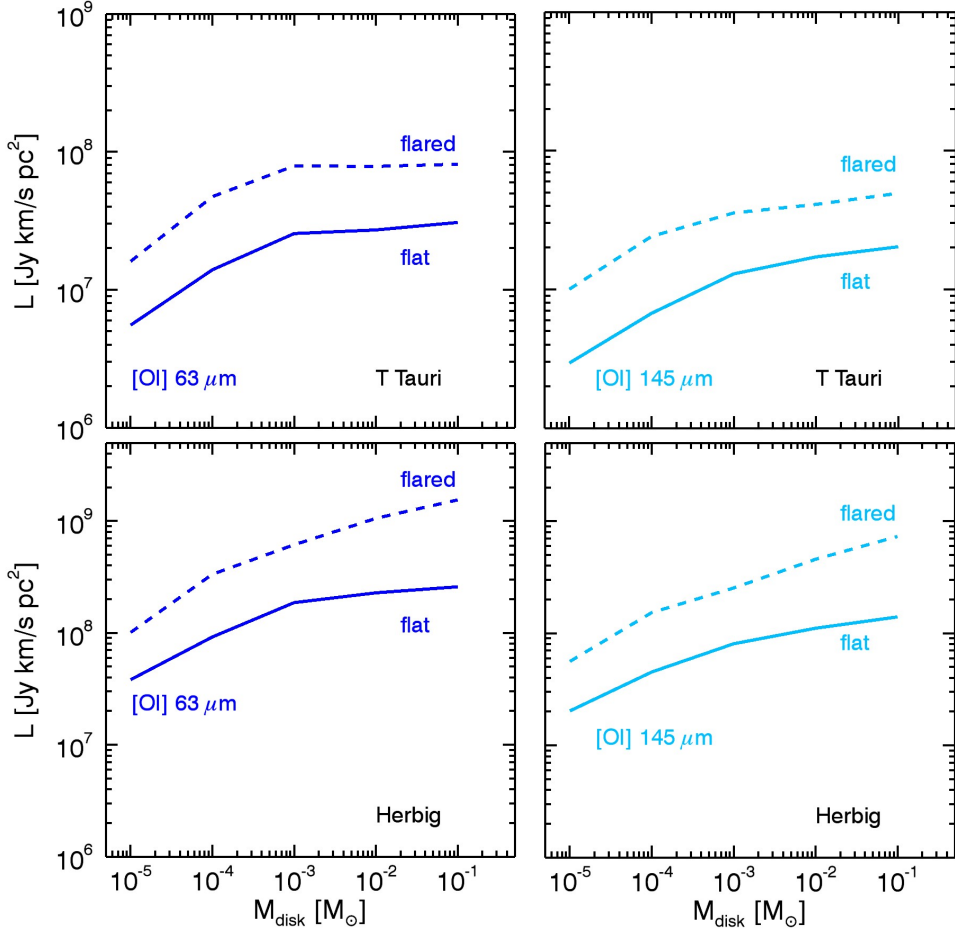


**Figure 3.13:** Median luminosities for [OI] lines as a function of disk mass for flat ( $h_c = 0.1$ ,  $\psi = 0.1$ ) and flared ( $h_c = 0.2$ ,  $\psi = 0.2$ ) disks, shown by the solid and the dashed lines respectively. T Tauri disk models are shown in upper panels and Herbig models are presented in the lower panels.

**Table 3.6:** Parameters assumed for each T Tauri disk model in our large grid (first five columns) and continuum emission at  $870 \mu\text{m}$  in K,  $^{12}\text{CO}$ ,  $^{13}\text{CO}$ ,  $\text{C}^{18}\text{O}$ ,  $\text{C}^{17}\text{O}$  and [CI] total fluxes simulated by these models, expressed in K km/s (remaining columns). The fluxes are computed assuming a distance of 100 pc and a beam size of  $10''$ . CO isotopologues fluxes are computed for four molecular line transitions ( $J = 1 - 0$ ,  $J = 2 - 1$ ,  $J = 3 - 2$ ,  $J = 6 - 5$ ) and for two disk inclination angles ( $i = 10^\circ, 80^\circ$ ). The full table is only available in electronic format.

$R_c$	$\gamma$	$h_c$	$\psi$	$M_{\text{disk}}$	$I[870\mu\text{m}]_{10}$	$I[^{12}\text{CO}]_{10}^{1-0}$	...	$I[^{13}\text{CO}]_{80}^{2-1}$	...	$I[\text{C}^{18}\text{O}]_{10}^{3-2}$	...	$I[\text{C}^{17}\text{O}]_{80}^{6-5}$
30.0	0.8	0.1	0.1	$10^{-5}$	$1.50^{(-4)}$	$3.16^{(-1)}$		$2.21^{(-2)}$		$1.46^{(-3)}$		$3.00^{(-5)}$
30.0	0.8	0.1	0.1	$10^{-4}$	$1.01^{(-3)}$	$7.27^{(-1)}$		$1.66^{(-1)}$		$2.95^{(-2)}$		...
...												



**Table 3.7:** Parameters assumed for each Herbig disk model in our large grid (first five columns) and continuum emission at  $870\ \mu\text{m}$  in K,  $^{12}\text{CO}$ ,  $^{13}\text{CO}$ ,  $\text{C}^{18}\text{O}$ ,  $\text{C}^{17}\text{O}$  and [CI] total fluxes simulated by these models, expressed in K km/s (remaining columns). The fluxes are computed assuming a distance of 100 pc and a beam size of  $10''$ . CO isotopologues fluxes are computed for four molecular line transitions ( $J = 1 - 0$ ,  $J = 2 - 1$ ,  $J = 3 - 2$ ,  $J = 6 - 5$ ) and for two disk inclination angles ( $i = 10^\circ$ ,  $80^\circ$ ). The full table is only available in electronic format.

$R_c$	$\gamma$	$h_c$	$\psi$	$M_{\text{disk}}$	$I[870\mu\text{m}]_{10}$	$I[^{12}\text{CO}]_{10}^{1-0}$	...	$I[^{13}\text{CO}]_{80}^{2-1}$	...	$I[\text{C}^{18}\text{O}]_{10}^{3-2}$	...	$I[\text{C}^{17}\text{O}]_{80}^{6-5}$
30.0	0.8	0.1	0.1	$10^{-5}$	...	...		...		...		...
30.0	0.8	0.1	0.1	$10^{-4}$	...	...		...		...		...
...												

### 3.B Effects of carbon depletion on CO isotopologue line intensities

The elemental composition assumed at the start of the calculation for the 800 models presented in this work is the same as in Miotello et al. (2014b) and is reported in Table 3.8. In this section, the impact of carbon depletion on CO isotopologues line luminosities is further quantified. Ten disk models have been run with carbon abundances reduced by factors of 3 and 10 compared with the total gas-phase elemental carbon abundance ( $[C]/[H]_{\text{gas}} = 1.35 \times 10^{-4}$ , both in the ISO and the NOISO networks). By averaging the change of fluxes seen in these models, we define a reduction factor,  $\Lambda$ , for the CO isotopolog line intensities. More specifically, if the carbon abundance is reduced by a factor of three or ten the CO isotopologues line luminosity are defined respectively as  $L(^{13}\text{CO})_3$  and  $L(\text{C}^{18}\text{O})_3$ ,  $L(^{13}\text{CO})_{10}$  and  $L(\text{C}^{18}\text{O})_{10}$ . The line luminosities obtained with a fiducial ISM-like carbon abundance are instead defined as:  $L(^{13}\text{CO})$  and  $L(\text{C}^{18}\text{O})$ . They are related to each other as follows:

$$\begin{aligned}
 L(^{13}\text{CO}) &= \Lambda_3^{13} \cdot L(^{13}\text{CO})_3, \\
 L(\text{C}^{18}\text{O}) &= \Lambda_3^{18} \cdot L(\text{C}^{18}\text{O})_3, \\
 L(^{13}\text{CO}) &= \Lambda_{10}^{13} \cdot L(^{13}\text{CO})_{10}, \\
 L(\text{C}^{18}\text{O}) &= \Lambda_{10}^{18} \cdot L(\text{C}^{18}\text{O})_{10},
 \end{aligned}
 \tag{3.4}$$

where the reduction factors  $\Lambda$  are reported in Table 3.9. In practice, if the carbon abundance is reduced by factors 3 or 10, CO isotopologues line luminosities are lowered by factors of  $\Lambda_3$  or  $\Lambda_{10}$ . The superscripts 13 and 18 stand for  $^{13}\text{CO}$  and  $\text{C}^{18}\text{O}$  line luminosities.

Figures 3.9 and 4.5.2 show the resulting  $\text{C}^{18}\text{O}$  and [CI] line intensities for various carbon abundances. It is seen, also from Table 3.9, that  $\text{C}^{18}\text{O}$  line intensities scale sub-linearly with the level of carbon depletion, i.e., the relative intensity decrease is smaller than the relative elemental abundance change. This reflects the fact that the  $\text{C}^{18}\text{O}$  abundances scale sub-linearly with the level of carbon depletion in the outer disk, and super-linearly in other regions. This in turn is due to the competing effects of self-shielding and dust opacity, which can be illustrated as follows.

Fig. 3.15 shows the ratios of  $\text{C}^{18}\text{O}$  abundance obtained with a depleted level of carbon and with an ISM-like C abundance, rescaled by the level of carbon depletion. If the  $\text{C}^{18}\text{O}$  abundance scaled linearly with carbon depletion, the ratio should be equal to unity everywhere (color: medium blue). Where the ratio is higher than unity (colors: from light blue to red), the  $\text{C}^{18}\text{O}$  abundance changes more slowly than the elemental carbon abundance. These regions are just below the  $A_V = 1$  surface. The carbon depletion decreases the  $\text{C}^{18}\text{O}$  abundance such that the dust opacity begins to protect  $\text{C}^{18}\text{O}$  from photodissociation before self-shielding becomes important. These

**Table 3.8:** Elemental composition assumed for the calculation.  $a(b)$  means  $a \times 10^b$ .

Element	Number fraction
H	1
He	7.59(-2)
C	1.35(-4)*
<sup>13</sup> C	1.75(-3)
N	2.14(-5)
O	2.88(-4)
<sup>17</sup> O	1.61(-7)
<sup>18</sup> O	5.14(-7)
Mg	4.17(-7)
Si	7.94(-6)
S	1.91(-6)
Fe	4.27(-7)

\* C abundance has been reduced by factors of 3 and 10 for ten disk models (See App. B).

regions contribute significantly to the  $J = 2 - 1$  lines, while the  $J = 6 - 5$  originates closer to the star, where the described effect is less important. As a consequence the line luminosity ratios of  $C^{18}O$   $J = 2 - 1$  over  $J = 6 - 5$  transitions vary for different levels of carbon depletion, as shown in panel (d) of Fig. 3.9. Models with a ISM-like carbon abundance have lower 2-1/6-5 line luminosity ratios than those with lower carbon abundance.

On the other hand, we see in Fig. 3.15 that there are regions where the  $C^{18}O$  abundance changes faster than the elemental carbon abundance (color: dark blue). These regions contribute significantly to the  $J = 1 - 0$  lines. As a consequence the line luminosity ratios of  $C^{18}O$   $J = 1 - 0$  over  $J = 6 - 5$  transitions vary for different levels of carbon depletion, as shown in panel (b) of Fig. 3.9. Models with a ISM-like carbon abundance have higher 1-0/6-5 line luminosity ratios than those with lower carbon abundance. In both cases (sub-linear and super-linear dependence on the carbon depletion) the effect on the line ratio is larger for higher mass disks ( $M_{\text{disk}} = 10^{-1}M_{\odot}$ ).

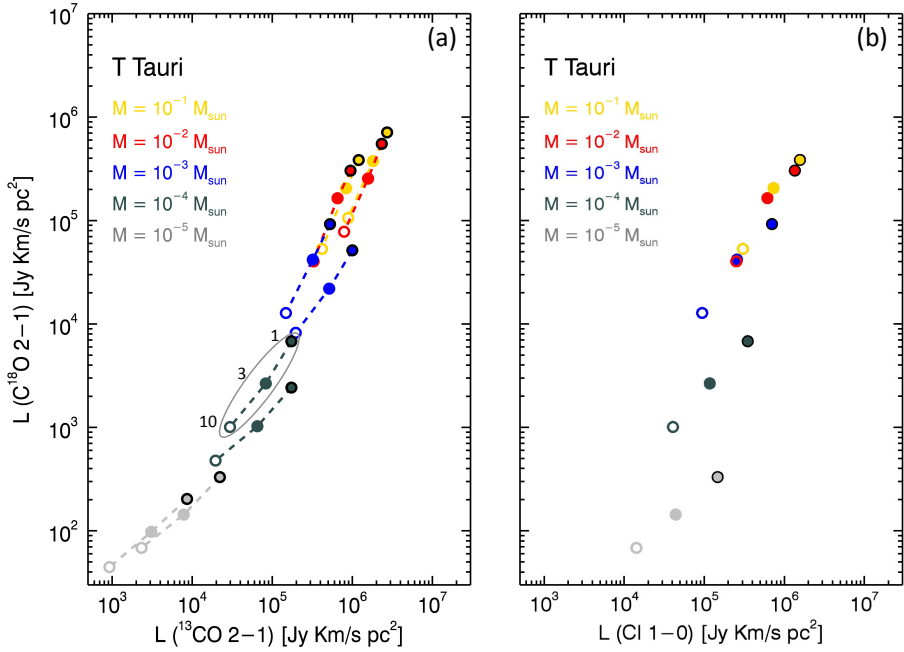


**Figure 3.14:** Line luminosity of  $C^{18}O$  vs  $^{13}CO$  ( $J = 2 - 1$ ) (panel a) and  $C^{18}O$  vs  $[CI]$  ( $J = 1 - 0$ ) (panel b) for ten models, run also with a reduced initial atomic C and  $^{13}C$  abundances. The standard value,  $X_C = [C]/[H] = 1.35 \times 10^{-4}$ , has been reduced by factors of 3 and 10. The models with ISM-like carbon abundances are shown by the outlined symbols, those with a factor of 3 of carbon depletion by the filled symbols and those with a factor of 10 depletion by the unfilled symbols.

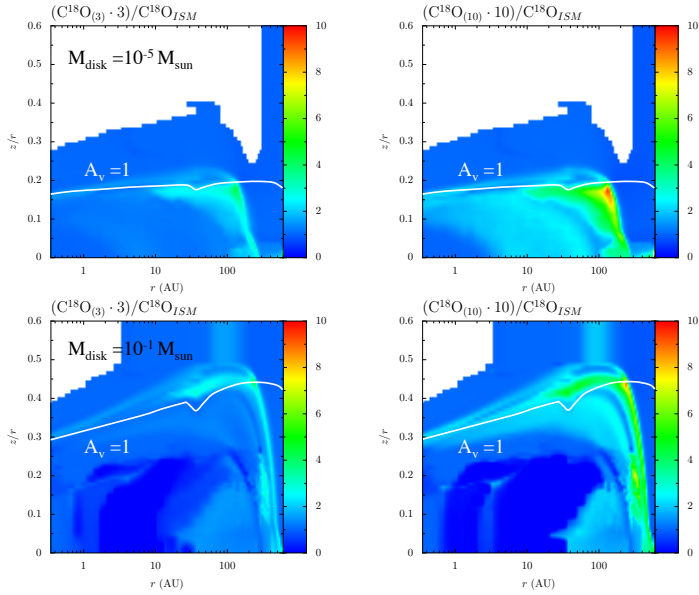


**Figure 3.15:** Ratios of  $C^{18}O$  abundance obtained with a depleted level of carbon and with an ISM-like C abundance, rescaled by the level of carbon depletion. Where the ratio is higher than unity (colors from light blue to red), the  $C^{18}O$  abundance changes more slowly than the elemental carbon abundance. Upper panels show a  $10^{-5} M_{\odot}$  T Tauri disk model, bottom panels show a  $10^{-1} M_{\odot}$  T Tauri disk model. Other disk parameters are:  $R_c = 60$  au,  $\gamma=0.8$ ,  $h_c=0.1$ , and  $\psi=0.1$ . The white solid line describes the  $A_V = 1$  surface, where photodissociating photons are mainly absorbed by the dust.

**Table 3.9:** Carbon depletion reduction factors that relates CO isotopologues line luminosities (for three transitions:  $J = 2 - 1, 1 - 0, 6 - 5$ ) obtained with ISM-like or reduced carbon abundances. In practice, if the carbon abundance is reduced by factors 3 or 10, CO isotopologues line luminosities are lowered by factors of  $\Lambda_3$  or  $\Lambda_{10}$ . The superscripts 13 and 18 stand for  $^{13}\text{CO}$  and  $\text{C}^{18}\text{O}$ .

$M_{\text{disk}} [M_{\odot}]$	$10^{-5}$	$10^{-4}$	$10^{-3}$	$10^{-2}$	$10^{-1}$
	$J = 2 - 1$				
$\Lambda_3^{13}$	1.5	1.2	1.1	1.2	1.1
$\Lambda_3^{18}$	1.0	0.9	1.8	1.3	1.7
$\Lambda_{10}^{13}$	4.9	3.4	3.1	3.9	2.3
$\Lambda_{10}^{18}$	2.0	2.5	5.2	5.3	5.2
	$J = 3 - 2$				
$\Lambda_3^{13}$	3.2	2.3	1.9	2.2	1.9
$\Lambda_3^{18}$	2.3	1.7	2.9	2.3	2.7
$\Lambda_{10}^{13}$	10.3	6.5	4.5	6.8	3.6
$\Lambda_{10}^{18}$	4.5	3.7	7.9	4.5	7.8
	$J = 6 - 5$				
$\Lambda_3^{13}$	13.8	7.1	4.7	5.1	4.7
$\Lambda_3^{18}$	6.1	3.4	4.1	5.3	4.7
$\Lambda_{10}^{13}$	40.1	20.6	10.4	14.2	10.4
$\Lambda_{10}^{18}$	10.2	10.2	13.4	18.4	16.7



# 4

## LUPUS DISKS WITH FAINT CO ISOTOPOLOGUES: LOW GAS/DUST OR HIGH CARBON DEPLETION?

---

A. Miotello, E. F. van Dishoeck, J. P. Williams, M. Ansdell, G. Guidi, M. Hogerheijde, C. F. Manara, M. Tazzari, L. Testi, N. van der Marel, and S. van Terwisga, *Lupus disks with faint CO isotopologues: low gas/dust or high carbon depletion?*, 2017, *A&A*, 599, A113



---

**Abstract** – An era has started in which gas and dust can be observed independently in protoplanetary disks, thanks to the recent surveys with the Atacama Large Millimeter/sub-millimeter Array (ALMA). The first near-complete high-resolution disk survey in both dust and gas in a single star-forming region has been carried out in Lupus, finding surprisingly low gas-to-dust ratios. The goal of this work is to fully exploit CO isotopologue observations in Lupus, comparing them with physical-chemical model results, in order to obtain gas masses for a large number of disks and compare gas and dust properties. We have employed the grid of physical-chemical models presented previously to analyze continuum and CO isotopologue ( $^{13}\text{CO } J = 3 - 2$  and  $\text{C}^{18}\text{O } J = 3 - 2$ ) observations of Lupus disks, including isotope-selective processes and freeze-out. We also employed the ALMA  $^{13}\text{CO}$ -only detections to calculate disk gas masses for a total of 34 sources, which expands the sample of 10 disks reported earlier, where  $\text{C}^{18}\text{O}$  was also detected. We confirm that overall gas-masses are very low, often lower than  $1M_J$ , when volatile carbon is not depleted. Accordingly, global gas-to-dust ratios are much lower than the expected interstellar-medium value of 100, which is predominantly between 1 and 10. Low CO-based gas masses and gas-to-dust ratios may indicate rapid loss of gas, or alternatively chemical evolution, for example, through sequestering of carbon from CO to more complex molecules, or carbon locked up in larger bodies. Current ALMA observations of  $^{13}\text{CO}$  and continuum emission cannot distinguish between these two hypotheses. We have simulated both scenarios, but chemical model results do not allow us to rule out one of the two, pointing to the need to calibrate CO-based masses with other tracers. Assuming that all Lupus disks have evolved mainly as a result of viscous processes over the past few Myr, the previously observed correlation between the current mass accretion rate and dust mass implies a constant gas-to-dust ratio, which is close to 100 based on the observed  $M_{\text{disk}}/\dot{M}_{\text{acc}}$  ratio. This in turn points to a scenario in which carbon depletion is responsible for the low luminosities of the CO isotopologue line.

---

## 4.1 Introduction

Protoplanetary disks have been extensively studied in the past decades with infrared (IR) surveys (Haisch et al. 2001; Hernández et al. 2007; Evans et al. 2009). Furthermore, several attempts have been carried out to study the structure and bulk content of disks independently in gas and dust (see, e.g., Thi et al. 2001; Panić et al. 2008; Panić & Hogerheijde 2009; Andrews et al. 2012; Boneberg et al. 2016; Andrews 2015, as a review). However, these studies have been limited to small, not statistically significant samples of mostly Herbig disks, often with partially unresolved and limited-sensitivity observations. The Atacama Large Millimeter/sub-millimeter Array (ALMA) now has the sensitivity and resolving power needed to image large numbers of disks in continuum and molecular lines in a modest amount of time. The first near-complete survey of protoplanetary disks in both dust and gas with ALMA in a single star-forming region has been carried out in Lupus (Ansdell et al. 2016). For the first time, about 80 disks in the same region have been observed at a resolution of  $0.3''$  (22 – 30 au radius for a distance of 150 – 200 pc). At the same time, the unprecedented sensitivity of ALMA allowed detection of a fraction of these disks in the faint CO isotopologue lines with just one minute observations per source. Moreover, stellar properties and mass accretion rates have been estimated from VLT/X-Shooter spectra for the same sample, allowing us to build a complete picture for the Lupus sources (Alcalá et al. 2014; Manara et al. 2016b; Alcalá et al. 2017). More recently, other star-forming regions have been surveyed with similar aims by ALMA, such as Chameleon I (Pascucci et al. 2016) and the more evolved Upper Scorpius region (Barenfeld et al. 2016). An era has started in which gas and dust can be observed independently in protoplanetary disks.

Together with the physical structure of the gas, the total gas mass is one of the crucial properties needed to describe the disk evolution. Starting from the process of grain-growth, planetesimal formation sensitively depends on the physical structure of the gaseous disk (see, e.g., Armitage 2011, for a review). For this reason, it is crucial to directly observe the bulk of the gas in protoplanetary disks. CO lines are commonly used to estimate the total disk gas mass. In particular, less abundant CO isotopologues, which become optically thick deeper in the disk than  $^{12}\text{CO}$ , can trace the bulk gas mass present in the molecular layer (van Zadelhoff et al. 2001; Dartois et al. 2003).

The main caveat when employing CO isotopologues as mass tracers is related to the conversion of the observed CO mass into total gas mass. There are various arguments why CO/H<sub>2</sub> is lower than the canonical value of  $10^{-4}$  (Aikawa et al. 1997) when averaged over the entire disk, as indicated by early observations (Dutrey et al. 1997). Processes such as CO photodissociation in the upper layers and freeze-out in the disk midplane have been identified as the main cause (van Zadelhoff et al.

---

2001; Aikawa et al. 2002), and these processes are well understood from a molecular physics point of view. They are included in all recent physical-chemical disk models (Hollenbach et al. 2005; Gorti & Hollenbach 2009; Nomura et al. 2009; Woitke et al. 2009; Bruderer et al. 2012; Bruderer 2013). When less abundant CO isotopologues are involved, the well-understood process of isotope-selective photodissociation, which destroys relatively more  $C^{18}O$ , needs to be taken into account (Visser et al. 2009; Miotello et al. 2014b, 2016).

Williams & Best (2014) have shown that by combining multiple CO isotopologues, such as  $^{13}CO$  and  $C^{18}O$ , and accounting in a parametrized way for photodissociation and freeze-out, it is possible to estimate disk gas masses, regardless of the disk properties. Traditionally, then a constant interstellar medium (ISM)-like overall volatile carbon abundance is used to calculate the total  $H_2$  mass ( $X_C = [C]/[H] = 1.35 \times 10^{-4}$ ). This assumption may be incorrect, however, as high levels of carbon depletion have been inferred for at least one disk. This is the case of TW Hya, the closest and probably best-studied disk, for which the fundamental rotational transition of hydrogen deuteride (HD) has been observed by the *Herschel Space Observatory* (Bergin et al. 2013). Comparing these data with SMA  $C^{18}O$  data, Favre et al. (2013) found that a carbon depletion of two orders of magnitude was needed in order to recover the HD-based disk mass determination from  $C^{18}O$ . This result has been confirmed by physical-chemical modeling of the source, which was able to reproduce, among other lines, spatially resolved ALMA data and atomic carbon lines (Kama et al. 2016b; Schwarz et al. 2016). This result is interpreted as chemical evolution, that is, carbon has been turned from CO into more complex species either in the gas or in the ice (Aikawa et al. 1996; Bergin et al. 2014; Drozdovskaya et al. 2015; Eistrup et al. 2016), or alternatively, as a grain growth effect, carbon has been locked up in large icy bodies that no longer participate in the gas-phase chemistry (Du et al. 2015; Kama et al. 2016b), resulting in less bright CO lines. This hints at the possible existence of a class of disks where CO is not the main carbon reservoir.

In this paper we apply the detailed modeling technique developed by Miotello et al. (2016) to the ALMA  $^{13}CO$  and  $C^{18}O$  Lupus observations. Our modeling procedure allows us to also employ the  $^{13}CO$ -only detections to provide a disk gas mass determinations for a total of 34 disks, which extends and refines the initial analysis presented in Ansdell et al. (2016) for only 10 disks, for which both  $^{13}CO$  and  $C^{18}O$  lines are available. Our derived gas masses are generally very low, often lower than the mass of Jupiter, consistent with Ansdell et al. (2016). This translates into very low global gas-to-dust ratios that often approach unity (Sect. 5.4). Low CO-based gas masses and gas-to-dust ratios may indicate rapid disk evolution, which is usually taken to be a loss of gas. An alternative is that the CO abundance may be low, as discussed above. Since current data cannot distinguish between these scenarios, we have simulated both of them, but model results do not allow us to rule out one of the two. Future ALMA observations of more complex tracers are needed to calibrate

---

CO-based masses. Alternatively, Manara et al. (2016b) and Rosotti et al. (2017) have proposed a method that allows tracing the gaseous disk component independently of chemistry by exploiting the availability of dust disk mass and mass accretion rate measurement. The implications of these data are discussed in Sect. 4.5.3.

## 4.2 ALMA observations

Lupus is one of the youngest ( $3 \pm 2$  Myr; Alcalá et al. 2014) and closest complexes and is composed of four main star-forming regions (Lupus I-IV, see Comerón 2008, for a review). Lupus III is located at a distance of  $\sim 200$  pc to the Sun, while Lupus I, II, and IV are at  $\sim 150$  pc.

The sample employed for this paper was observed in the Cycle 2 *Lupus ALMA Disk Survey*, it is composed of 88 objects with  $0.1 < M_*/M_\odot < 2.84$  and is presented in detail by Ansdell et al. (2016). The observations were obtained on 2015 June 14 and 15. The disks were observed in continuum (890  $\mu\text{m}$ ) and CO isotopologue line emission ( $^{13}\text{CO}$  and  $\text{C}^{18}\text{O}$  3-2 transitions). More details on the observational settings and data reduction are presented in Ansdell et al. (2016). Of the 88 targets, 34 were detected in  $^{13}\text{CO}$ , while only 10 were detected in  $\text{C}^{18}\text{O}$  at more than a  $3\sigma$  level.

## 4.3 Model

The observed CO isotopologue fluxes were compared with the model results presented in Miotello et al. (2016). These models are computed with the physical-chemical code DALI, which has been tested extensively with benchmark test problems (Bruderer et al. 2012; Bruderer 2013) and against observations (Bruderer et al. 2012; Fedele et al. 2013; Bruderer et al. 2014). The dust temperature,  $T_{\text{dust}}$ , and local continuum radiation field from UV to mm wavelengths are calculated by a 2D Monte Carlo method, given an input disk density structure and a stellar spectrum. Then the chemical composition is obtained with a time-dependent chemical network simulation (1 Myr). Finally, the gas temperature,  $T_{\text{gas}}$ , is obtained from an iterative balance between heating and cooling processes until a self-consistent solution is found, and the non-LTE excitation of the molecules is computed. The final outputs are spectral image cubes created with a raytracer. As in Miotello et al. (2014b) and in Miotello et al. (2016), a complete treatment of CO isotope-selective processes is included.

The grid by Miotello et al. (2016) is composed of around 800 disk models that have been run for a range of realistic disk and stellar parameters. Disk masses varied between  $10^{-5}M_\odot$  and  $10^{-1}M_\odot$ , and stellar luminosities were set to  $1 L_\odot$  (plus excess UV for mass accretion rates of  $10^{-8}M_\odot \text{yr}^{-1}$ ) for T Tauri disks and  $10 L_\odot$  for Herbig disks (see Table 1 in Miotello et al. 2016). Coupling of the UV excess to an

---

accretion rate is merely a convenient prescription to obtain a value for the UV luminosity, which controls the thermal and chemical structure of the gas, including the number of CO dissociating photons (Kama et al. 2016). It should not be taken here as a measure for disk evolution timescales. A consistent description of the accretion process and disk evolution is beyond the scope of our models. Line luminosities for different CO isotopologues and transitions have been ray traced. The majority of Lupus sources detected in both CO isotopologues have stellar luminosity  $L_*$  between  $0.1 L_\odot$  and  $1 L_\odot$  (Alcalá et al. 2017). As a check, a smaller grid of T Tauri disk models with  $L_* = 0.1 L_\odot$  and excess UV for mass accretion rates of  $10^{-8} M_\odot \text{ yr}^{-1}$ , which generates about  $0.2 L_\odot$  of UV accretion luminosity, was run to reproduce the extreme cases. However, we found that CO isotopologue line luminosities are reduced only up to 25%. As this is well within the uncertainties on the CO-based gas mass derivations by Miotello et al. (2016), the original grid of T Tauri disk models with  $L_* = 1 L_\odot$  was used for the analysis.

## 4.4 Results

### 4.4.1 Dust masses revisited

Continuum observations at sub-mm wavelengths are traditionally employed to trace large (mm-sized) grains that are present in the cold midplane of disks. Since the bulk of the dust mass is expected to be retained in large grains, their thermal emission is generally used to derive disk dust masses, following

$$M_{\text{dust}} = \frac{F_\nu d^2}{\kappa_\nu B_\nu(T_{\text{dust}})}. \quad (4.1)$$

The sub-mm flux  $F_\nu$  is directly related to the dust mass  $M_{\text{dust}}$  under the assumption that the emission is optically thin and in the Rayleigh-Jeans regime (Beckwith et al. 1990). Equation 4.1 has been employed by Ansdell et al. (2016) to derive dust masses for the Lupus disks, assuming a dust opacity  $\kappa_\nu = 3.4 \text{ cm}^2 \text{ g}^{-1}$  at 340 GHz and a characteristic dust temperature  $T_{\text{dust}} = 20 \text{ K}$ . This first-order analysis does not account for the effects of disk inclination and temperature variation on the spatially integrated dust emission. However, the inclination angle  $i$  has been derived for many of the Lupus disks from continuum data by Ansdell et al. (2016) and (Tazzari et al. 2017).

In this work we exploit the results obtained by Miotello et al. (2016) with DALI continuum radiative transfer to estimate Lupus disks dust masses, accounting for the disk inclination and temperature structure. The assumed dust opacity,  $\kappa_\nu = 4.3 \text{ cm}^2 \text{ g}^{-1}$  at 340 GHz, is the standard value in DALI (Weingartner & Draine 2001; Bruderer 2013) and is slightly higher than that used by Ansdell et al. (2016). Our

models assume that the dust surface density distribution follows a radial power-law with an exponential taper and a Gaussian distribution in the vertical direction. Two dust populations are considered: large (mm-sized) grains are settled toward the midplane, and small (sub- $\mu\text{m}$  to  $\mu\text{m}$ -sized) grains are coupled to the gas and present in the disk atmosphere (see Miotello et al. 2016, for more detail). Finally, grain-growth and migration are not included in the models, except in an ad hoc fashion by including small and large grains.

The continuum and line emission obtained with the disk models presented in Miotello et al. (2016) were both ray-traced assuming disk inclinations of  $10^\circ$  and  $80^\circ$ . Submillimeter fluxes are not expected to vary significantly for intermediate inclinations, that is, up to  $70^\circ$  (Beckwith et al. 1990). On the other hand, line intensities and dust emission are extremely modified in the rarer case of edge-on disks, that is, with an inclination close to  $90^\circ$ . Lupus disks with  $i < 70^\circ$  or with unknown inclination are compared with models where  $i = 10^\circ$ , elsewhere we employ models with  $i = 80^\circ$ .

The medians of the simulated continuum luminosities at  $890 \mu\text{m}$  can be calculated for different dust masses (Fig. 4.1). They can be fitted by simple functions of the disk dust mass and be employed to estimate Lupus disk masses. In particular, the continuum luminosity at  $890 \mu\text{m}$   $L_{0.9\text{mm}}$  can be expressed by

$$L_{0.9\text{mm}} = \begin{cases} a + b \cdot M_{\text{dust}}^c & M_{\text{dust}} < M_{\text{tr}} \\ d + e \cdot M_{\text{dust}}^f & M_{\text{dust}} > M_{\text{tr}}. \end{cases} \quad (4.2)$$

The coefficients  $a, b, c, d, e, f$ , and  $M_{\text{tr}}$  are reported in Table 4.1 for disk inclinations of both  $10^\circ$  and  $80^\circ$ . For dust masses below the transition mass  $M_{\text{tr}}$  the dependence is linear, while for higher masses it is sublinear. This reflects the fact that the dust emission becomes optically thick for high enough dust masses, even at  $890 \mu\text{m}$ . This occurs at lower masses for edge-on disks, as the high inclination enhances the dust column density.

**Table 4.1:** Polynomial coefficients  $a, b, c, d, e, f$ , and  $M_{\text{tr}}$ , in Eq. (4.2)

	$i = 10^\circ$	$i = 80^\circ$
$a$	17	10
$b$	$5 \cdot 10^8$	$10^9$
$c$	0.95	1.0
$d$	76	40
$e$	$1.3 \cdot 10^7$	$2.2 \cdot 10^6$
$f$	0.6	0.5
$M_{\text{tr}}[M_\odot]$	$3 \cdot 10^{-5}$	$5 \cdot 10^{-6}$

The Lupus disk dust masses derived in this work are generally a factor of a few

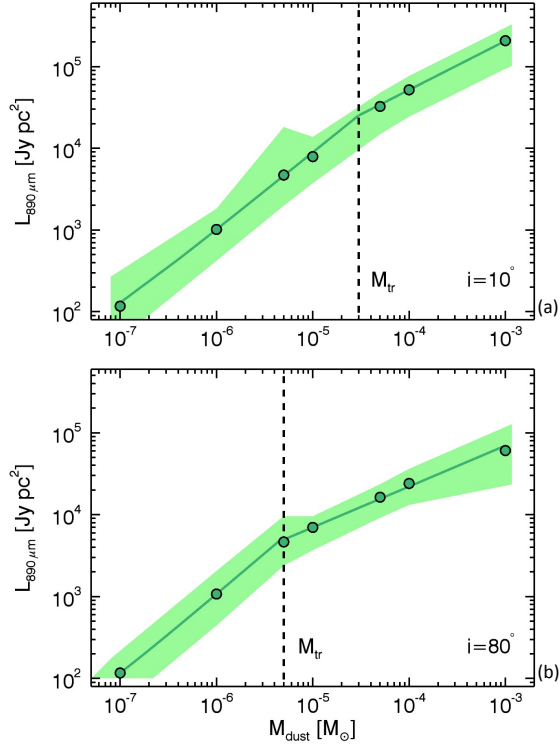


**Figure 4.1:** Medians of the simulated T Tauri continuum luminosities at  $890 \mu\text{m}$  for different mass bins, presented by the green dots for disk inclinations of  $10^\circ$  and  $80^\circ$  in panel (a) and (b), respectively. The solid lines show the fit function of the  $890 \mu\text{m}$  continuum luminosity as a function of the disk mass (see Eq. 4.2). The dotted black lines present the transition mass between the two dependencies of the luminosity on the mass expressed in Eq. 4.2. The colored bands show the maximum and minimum simulated continuum luminosities for the different mass bins.

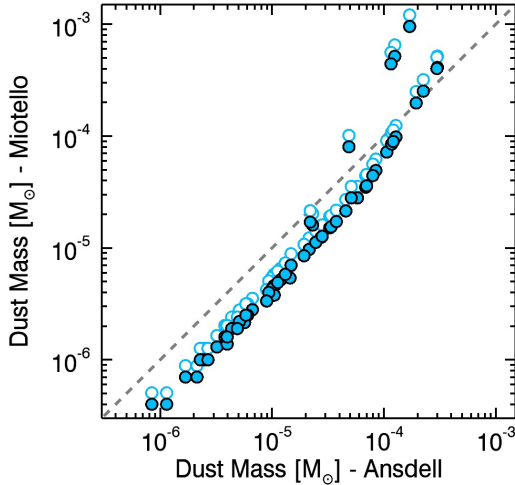


**Figure 4.2:** Disk dust masses derived in this work compared with the dust masses obtained by Ansdell et al. (2016). Full symbols show the current model results. Empty circles present mass estimates corrected for the dust opacity difference at 340 GHz between the two studies.

lower than the estimates given by Ansdell et al. (2016) (see Fig. 4.2). In particular, between  $5 \cdot 10^{-7} M_{\odot}$  and  $3 \cdot 10^{-5} M_{\odot}$ , dust masses derived by Ansdell et al. (2016) are a factor of 2.2 higher than those estimated by this analysis (1.7 if we correct for the dust opacity difference at 340 GHz). For disks with dust masses higher than  $M_{\text{tr}} = 3 \times 10^{-5} M_{\odot}$ , the derivations obtained with the two methods become similar because the emission becomes marginally optically thick. This effect is only considered by our models and leads to higher mass determinations. Finally, a bimodality can be seen in Fig. 4.2, with six points being displaced from the main trend. These represent the highly inclined disks ( $i > 70^{\circ}$ ) with dust masses higher than  $M_{\text{tr}} = 5 \times 10^{-6} M_{\odot}$ . For the most massive of these sources, the dust masses derived in this work are generally a factor of a few higher than the estimates given by Ansdell et al. (2016). The dust masses derived for the highly inclined disks are  $M_{\text{dust}} = 9.6 \cdot 10^{-4}$ ,  $5.2 \cdot 10^{-4}$ ,  $4.4 \cdot 10^{-4}$ ,  $8.0 \cdot 10^{-5}$ ,  $1.7 \cdot 10^{-5}$ ,  $1.6 \cdot 10^{-5}$ ,  $7.0 \cdot 10^{-6}$ ,  $3.4 \cdot 10^{-6}$ , and  $2.2 \cdot 10^{-6} M_{\odot}$  for J16083070-3828268, MY Lup, J16070854-3914075, Sz 133, J16090141-3925119, Sz 84, Sz 74, J16102955-3922144, and J16070384-3911113, respectively.



---

#### 4.4.2 Gas masses

Measuring disk gas masses is essential for understanding disk evolution up to the formation of planetary systems. The aim of this analysis is to employ the CO isotopologue lines observed in Lupus for deriving gas masses for a statistically significant number of disks. The  $^{13}\text{CO}$  and  $\text{C}^{18}\text{O}$  model results shown by Miotello et al. (2016) can be presented in the same way as done by Williams & Best (2014) and be compared with Lupus observations (Fig. 4.3). As explained by Miotello et al. (2016), the two sets of model results differ throughout the whole disk mass range because of a temperature effect. Williams & Best (2014) find a wider range of CO luminosities because they parameterize a wider range of temperatures than Miotello et al. (2016) find in their models. Miotello and collaborators compute the disk temperature structure through full radiative transfer. Furthermore, the divergence is maximized in the lower mass regime where the implementation of isotope-selective processes reduces  $\text{C}^{18}\text{O}$  line intensities compared with the results by Williams & Best (2014). The same disk mass model results cover a limited region of the line luminosity-luminosity space. Lupus disks that are detected in both isotopologues are presented in Fig. 4.3 with green stars, while  $\text{C}^{18}\text{O}$  non-detections are shown with white circles as upper limits on the  $y$  direction. This plot can only be used to derive disk masses when  $\text{C}^{18}\text{O}$  is also detected. For Lupus, this is the case for only 10 sources. Four of them are not reproduced by any of our models, presenting either lower  $^{13}\text{CO}$  and regular  $\text{C}^{18}\text{O}$  luminosities, or regular  $^{13}\text{CO}$  and higher  $\text{C}^{18}\text{O}$  luminosities (see Fig. 4.3). This shows that the current model grid may not apply to all disks, but a source-by-source detailed modeling may be needed. Knowledge about disk properties such as the radial extent and vertical structure would help to predict the line fluxes with higher confidence.

For disks that have been detected in  $^{13}\text{CO}$ , but not in  $\text{C}^{18}\text{O}$  (henceforth,  $^{13}\text{CO}$ -only detections),  $^{13}\text{CO}$  alone can only be employed as a mass tracer when its emission is optically thin. Similarly to Miotello et al. (2016), the median of the  $^{13}\text{CO}$  and  $\text{C}^{18}\text{O}$   $J = 3 - 2$  simulated line luminosities, rather than  $J = 2 - 1$ , are expressed by fit functions of the disk mass:

$$L_y = \begin{cases} A_y + B_y \cdot M_{\text{gas}} & M_{\text{gas}} \leq M_{\text{tr}} \\ C_y + D_y \cdot \log_{10}(M_{\text{gas}}) & M_{\text{gas}} > M_{\text{tr}}, \end{cases} \quad (4.3)$$

where  $y = 13$  or  $18$ , for  $^{13}\text{CO}$  and  $\text{C}^{18}\text{O}$ , respectively. For low-mass disks, the line luminosity has a linear dependence on the disk mass, while for more massive disks the trend is logarithmic because of the optical depth. The transition point  $M_{\text{tr}}$  is different for the two isotopologues because  $^{13}\text{CO}$  becomes optically thick at lower column densities than  $\text{C}^{18}\text{O}$ . The polynomial coefficients  $A_y$ ,  $B_y$ ,  $C_y$ , and  $D_y$ , as well as the transition masses  $M_{\text{tr}}$ , are reported in Table 4.2 for disk models with

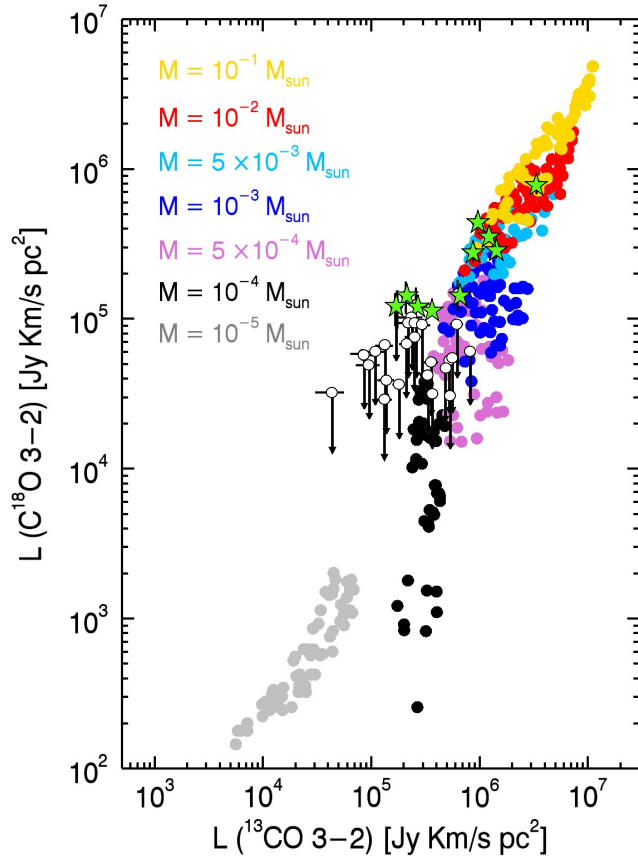


**Figure 4.3:**  $C^{18}O$  (3-2) vs  $^{13}CO$  (3-2) line luminosities. The color-coded dots show the line luminosities simulated by the T Tauri models in the Miotello et al. (2016) grid. The Lupus observations are overlotted. The disks detected in both isotopologues are shown with green stars, while the  $C^{18}O$  non detections are presented with empty circles.

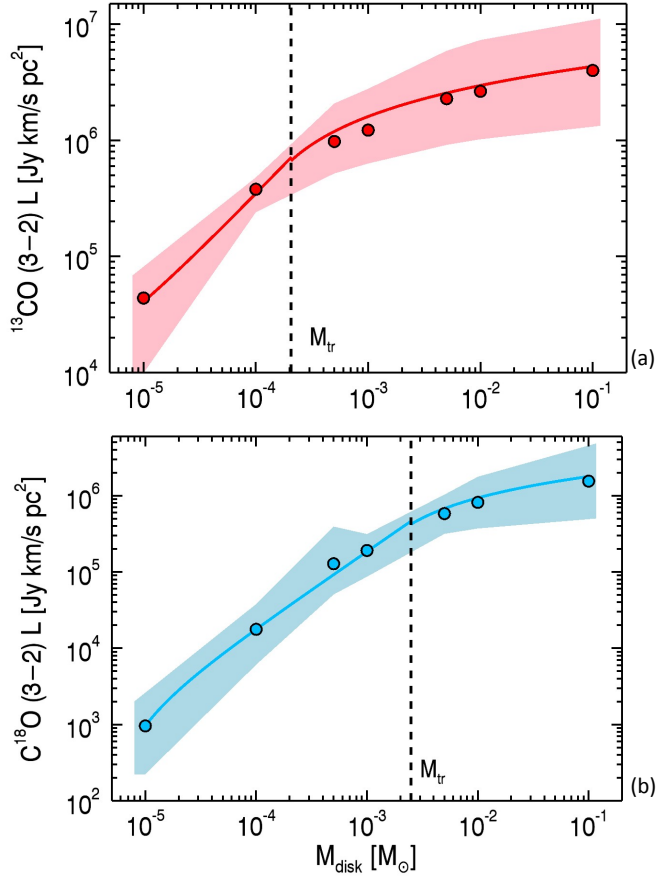


**Figure 4.4:** Medians of the  $^{13}\text{CO}$  (3-2) and  $\text{C}^{18}\text{O}$  (3-2) simulated T Tauri line luminosities for different mass bins, presented with red and blue dots in panel (a) and (b), respectively ( $i = 10^\circ$ ). The red and blue lines show the fit function of the line luminosity as a function of disk mass. The dotted black lines present the transition mass between the linear and the logarithmic dependence of the line luminosity on the mass (see Eq. 4.3). The colored bands show the maximum and minimum simulated line luminosities for the different mass bins.

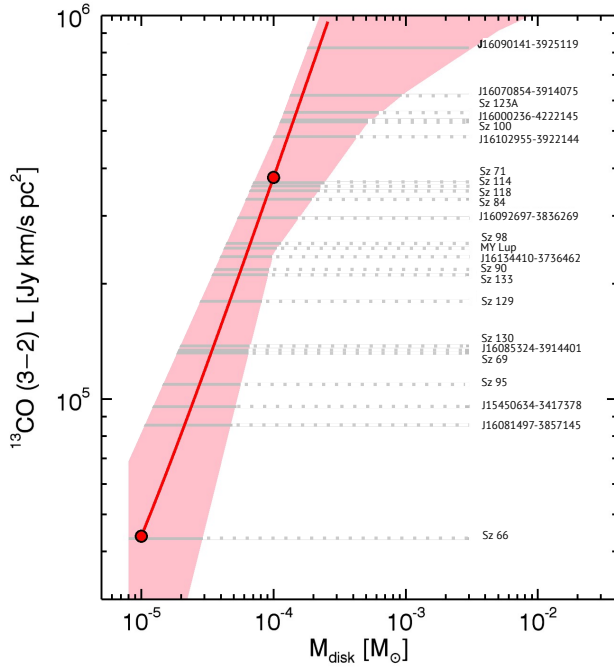


**Figure 4.5:** Zoom of Fig. 4 top: medians of the  $^{13}\text{CO}$  (3-2) simulated line luminosities for different mass bins, presented with red dots in the region where the luminosity dependence on mass is linear (see Eq. 4.3). The red line shows the fit function of the line luminosity as a function of disk mass. The  $^{13}\text{CO}$ -only detections are shown with gray dashed lines. The pink band shows the maximum and minimum simulated line luminosities.

inclination angle  $i = 10^\circ$  and  $i = 80^\circ$ . The fit functions are shown in Fig. 5.3.1 with red and blue lines for  $^{13}\text{CO}$  and  $\text{C}^{18}\text{O}$ , respectively.

Interestingly, all the  $^{13}\text{CO}$ -only detections fall in the region of panel (a) where the dependence is linear, that is, for  $M_{\text{disk}} < M_{\text{tr}}$  (Fig. 4.6). Accordingly, we can use the fit function presented in Eq. 4.3 to calculate the gas masses of these sources, as  $^{13}\text{CO}$  is optically thin for the observed range of luminosities, which is confirmed by the absence of  $\text{C}^{18}\text{O}$  emission. The uncertainties on the gas mass determinations are defined by the shadowed region in Fig. 4.5 (which is a zoom of Fig. 5.3.1), which covers the range of line luminosities simulated by the grid of models for different mass bins. Similarly, we can employ this line luminosity-mass relation to derive mass upper limits for disks that are undetected in both CO isotopologues. The disk mass determinations together with the calculated upper limits are presented in Table 4.3 and are shown in the middle panel of Fig. 4.6. Total gas masses are generally low, often lower than  $1 M_{\text{Jup}}$ . The implications of this result are discussed in Sect. 5.4.

**Table 4.2:** Polynomial coefficients  $A_y$ ,  $B_y$ ,  $C_y$ , and  $D_y$ , in Eq. (4.3)

	$i = 10^\circ$	$i = 80^\circ$
$A_{13}$	$6.707 \cdot 10^3$	$-1.182 \cdot 10^4$
$B_{13}$	$3.716 \cdot 10^9$	$3.110 \cdot 10^9$
$C_{13}$	$6.066 \cdot 10^6$	$5.945 \cdot 10^6$
$D_{13}$	$1.441 \cdot 10^6$	$1.460 \cdot 10^6$
$M_{\text{tr}}[M_\odot]$	$2 \cdot 10^{-4}$	$2 \cdot 10^{-4}$
$A_{18}$	$-9.006 \cdot 10^2$	$-7.972 \cdot 10^2$
$B_{18}$	$51.853 \cdot 10^8$	$1.120 \cdot 10^8$
$C_{18}$	$2.653 \cdot 10^6$	$2.581 \cdot 10^6$
$D_{18}$	$8.500 \cdot 10^5$	$8.900 \cdot 10^5$
$M_{\text{tr}}[M_\odot]$	$2.5 \cdot 10^{-3}$	$3.0 \cdot 10^{-3}$

## 4.5 Discussion

### 4.5.1 Gas-to-dust ratio

Dust masses were calculated for all Lupus disks detected in the continuum as described in Sect. 4.4.1. For the 34 sources for which at least one of the two CO isotopologues was detected, disk gas masses were derived as explained in Sect. 4.4.2. When we divide the gas masses by the newly determined dust masses, it is possible to obtain global gas-to-dust mass ratios. Figure 4.6 shows that these are often much lower than the expected ISM value of 100 and occasionally reach unity or lower.

---

Only full-disk models were employed for the mass determinations, but three disks in the Lupus sample show resolved dust cavities and three other sources show possible cavities with diameter  $\lesssim 0.4''$  (Ansdell et al. 2016). Moreover, six other disks are classified as transition disk candidates, but do not show cavities in the ALMA images (Merín et al. 2010; Romero et al. 2012; van der Marel et al. 2016; Bustamante et al. 2015). All these sources, presented with orange symbols in Fig. 4.6, are not properly described by our grid of full-disk models. However, these moderate-resolution Lupus data primarily trace the outer disks, which should be well represented by a full-disk model even for transitional disks. Therefore the calculated gas-to-dust ratios provide a first-order description of the disk properties in Lupus, including the transitional disks.

An alternative way to present the results is shown in Fig. 4.7. The global gas-to-dust ratios obtained for the sources detected in both gas and dust are shown in a histogram. Most of the disks, 23 out of 34, present gas-to-dust ratios lower than 10, with 13 of these sources showing ratios between 3 and 10.

Traditionally, disk masses are thought to be dominated by the gaseous component with ISM-like gas-to-dust ratios of 100 assumed to convert  $M_{\text{dust}}$  into total disk mass. Many disks in Lupus instead have lower measured gas-to-dust ratios, as shown in the bottom panel of Fig. 4.6. A similar result was found by Ansdell et al. (2016) with only 10 gas mass determinations, and this has been confirmed with a larger sample of 34 gas mass measurements. A possible interpretation is that Lupus disks are evolved and that the gas has been physically dissipated, while the large dust grains are still retained in the midplane. The finding of disks that are depleted in gas by a few Myr would place strong constraints on disk evolution and planet formation theories (Thommes et al. 2008; Lissauer et al. 2009; Levison et al. 2015), as discussed by Ansdell et al. (2016).

### 4.5.2 Carbon depletion vs low gas masses

An alternative interpretation of low CO-based gas masses and gas-to-dust ratios is that the CO abundance is low, for example, because of sequestering of carbon from CO to more complex molecules or because it is locked up into larger bodies (Aikawa et al. 1996; Bergin et al. 2014; Du et al. 2015; Eistrup et al. 2016; Kama et al. 2016b; Yu et al. 2016). However, current data cannot distinguish between these scenarios.

Clues on tracers to probe these two cases come from the well-studied TW Hya disk. In this unique case, HD far-infrared emission has been employed to independently determine an accurate gas mass (Bergin et al. 2013) and thereby calibrate the weak  $\text{C}^{18}\text{O}$  detection. These observations have been interpreted to imply a much lower abundance of CO, caused by carbon depletion of two orders of magnitude (Favre et al. 2013; Schwarz et al. 2016). This finding has been confirmed by an independent analysis, where other lines such as [CI], [CII], [OI],  $\text{C}_2\text{H}$ , and the CO ladder



---

have been fit self-consistently (Kama et al. 2016b). Unfortunately, no current facility is able to detect the fundamental HD transition in the Lupus disks. However, detection of more complex carbon-bearing species can help to distinguish between the two cases of gas-poor versus carbon-poor disks.

There is some debate about the mechanism(s) responsible for carbon depletion in protoplanetary disks. A possible explanation comes from gas-phase reactions initiated by X-ray and cosmic-ray ionization of He in the disk. The resulting He<sup>+</sup> atoms can react with gaseous CO and gradually extract the carbon, which can then be processed into more complex molecules that can freeze onto cold dust grains at higher temperatures than CO (Aikawa et al. 1997; Bruderer et al. 2012; Favre et al. 2013; Bergin et al. 2014; Kama et al. 2016b; Yu et al. 2016). Moreover, oxygen will also be removed from the gas by freeze-out of H<sub>2</sub>O, CO<sub>2</sub>, and CO, even more than carbon (Hogerheijde et al. 2011; Öberg et al. 2011; Walsh et al. 2015). Accordingly, a way to test the level of carbon depletion in disks is to compare observations of CO isotopologues with species such as C<sub>2</sub>H and c-C<sub>3</sub>H<sub>2</sub>, whose gas-phase abundances are sensitive to the gaseous carbon abundance and [C]/[O] ratio. Indeed, C<sub>2</sub>H is observed to have very strong emission in the TW Hya disk (Kastner et al. 2015) and is particularly strong when both elements are depleted, but gaseous [C]/[O]>1 (Kama et al. 2016b). If the difference in the global gas-to-dust ratios found in Lupus disks is due to different levels of carbon depletion, then this should be reflected in C<sub>2</sub>H and c-C<sub>3</sub>H<sub>2</sub> fluxes, and this may be tested by future ALMA observations. Alternatively, ice chemistry may be the fundamental process that turns CO into more complex organics, such as CH<sub>3</sub>OH, or into CO<sub>2</sub> and CH<sub>4</sub> ice (see, e.g., Fig. 3c in Eistrup et al. 2016). Finally, volatile elements, such as oxygen and carbon, may be locked up in large icy bodies in the midplane (Bergin et al. 2010; Ros & Johansen 2013; ?). These large pebbles cannot diffuse upward and participate in the gas-phase chemistry (see Du et al. 2015; Kama et al. 2016b). Such a process is most likely the cause of the underabundance of gas-phase water in disk atmospheres.

### Test models

From the modeling side, it is possible to simulate the two different scenarios (low gas-to-dust ratio or high carbon depletion) and to compare the predictions with the observations. As done by Miotello et al. (2016), the loss of gas is simulated by fixing the gas mass and increasing the dust mass, that is, by obtaining lower gas-to-dust ratios. The carbon depletion scenario is obtained by reducing the initial ISM-like carbon abundance by different levels. We define carbon depletion as  $\delta_C=1$  if the carbon over hydrogen ratio is set to the ISM-level,  $[C]/[H] = 1.35 \cdot 10^{-4}$ . We then assume higher values of carbon depletion  $\delta_C=0.1, 0.01$  if the abundance ratio is  $[C]/[H] = 1.35 \cdot 10^{-5}, 1.35 \cdot 10^{-6}$ , respectively.

Two interesting groups of sources can be identified in Fig. 4.6 for which the gas



mass is  $M_{\text{gas}} = 10^{-4}M_{\odot}$ , while the dust mass is either  $M_{\text{dust}} = 10^{-4}M_{\odot}$  (Sz71, Sz114, Sz129) or  $M_{\text{dust}} = 10^{-5}M_{\odot}$  (J16085324-3914401, Sz90). These five disks present similar  $^{13}\text{CO}$  emission, but different continuum fluxes. This may be interpreted as the first group of sources presenting a lower gas-to-dust ratio, or a higher level of carbon depletion. Four additional models were run with  $R_c = 30, 60$  au, fixing the gas mass  $M_{\text{gas}} = 10^{-4}M_{\odot}$  and increasing the dust mass from  $M_{\text{dust}} = 10^{-6}M_{\odot}$  to  $M_{\text{dust}} = 10^{-5}, 10^{-4}M_{\odot}$ , that is, with gas-to-dust ratios of 10 and 1 (see purple circles in Fig. 4.8). Moreover, another eight models were run with  $R_c = 30, 60$  au,  $M_{\text{dust}} = 10^{-5}, 10^{-4}M_{\odot}$ , gas-to-dust ratios of 100, but with initial carbon abundances reduced by a factor  $\delta_C=0.1, 0.01$  (see Fig. 4.8). Remarkably, for a fixed gas mass and  $\delta_C$ , the CO line intensities do not depend strongly on dust masses.

From comparing the results from the two sets of models presented in Fig. 4.8 with the observations, it is not possible to rule out one of the two scenarios, which indicates that we need to calibrate CO-based masses with other tracers. The first group of sources (Sz71, Sz114, and Sz129), bright in the continuum, but faint in CO emission, are well described either by models with gas-to-dust ratios equal to unity or with a carbon depletion of around two orders of magnitudes. The fluxes of the second set of disks (J16085324-3914401 and Sz90) are instead reproduced with less precision by models with a gas-to-dust ratio equal to 10, or with carbon depletion of about a factor of 10. Carbon depletion and gas dissipation processes may both playing a role, but it is not possible to estimate the relative importance.

### 4.5.3 Correlation between disk gas mass and stellar mass

Ansdell et al. (2016) found a positive correlation between  $M_{\text{gas}}$  and  $M_{\star}$  (computed by Alcalá et al. 2014, 2017), but were unable to produce a meaningful fit given the low number of disks detected in the two CO isotopologues and the large uncertainties on the gas mass determinations. This changes when the sample is enlarged from 10 to 34 sources. Using the Bayesian linear regression method (Kelly 2007), which accounts for the upper limits, we find a correlation with  $r = 0.74$  and a two-sided  $p$ -value of  $3 \cdot 10^{-2}$  for the null hypothesis that the slope of this correlation is zero. This is shown in Fig. 4.9, where the red line gives the Bayesian linear regression fit, which considers errors on both axes and is applied to detected and undetected targets. The slope of the correlation is 0.63 and the intercept is -3.92.

Ansdell et al. (2016) found a clear correlation between  $M_{\text{dust}}$  and  $M_{\star}$ . Furthermore, Manara et al. (2016b) found a linear relation between the mass accretion rate onto the central star and the disk mass inferred from the dust by combining ALMA and VLT/X-Shooter data (Alcalá et al. 2014, 2017). A relation between  $M_{\text{acc}}$  and  $M_{\text{disk}}$  has been theoretically predicted for viscously evolving disks (Hartmann et al. 1998), and it was found observationally in Lupus for the first time using dust masses to measure the bulk disk mass, which is equivalent to assume a constant gas-to-dust

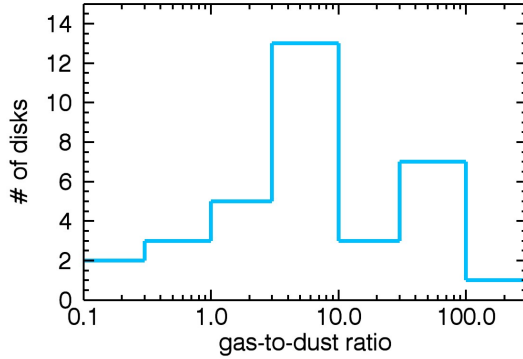


**Figure 4.7:** Histogram showing the number of disks presenting different levels of gas-to-dust ratio. Only sources detected in both continuum and line emission are considered.

ratio (Manara et al. 2016b). For a gas-to-dust ratio of 100, the ratio of  $M_{\text{disk}}/\dot{M}_{\text{acc}}$  is comparable with the age of the region, as expected for viscous disks and under the effect of other disk evolution processes (Jones et al. 2012; Rosotti et al. 2017). On the other hand, no correlation was found with disk masses derived from CO isotopologue lines by Ansdell et al. (2016). Even expanding the sample of gas masses to 34 sources, no correlation is found in this work. Furthermore, the ratio of  $M_{\text{disk}}/\dot{M}_{\text{acc}}$  when using  $M_{\text{disk}}$  derived from CO isotopologues is much lower than the age of the region. This is expected only in cases where external disturbances, such as external photoevaporation, play a major role in the evolution of disks (Rosotti et al. 2017). As this is probably not the case in the Lupus region, this method suggests that CO-based disk masses are generally underestimated.

When we assume that all Lupus disks have evolved mainly through viscous processes over the past few Myr, the observed correlation between the current mass accretion rate and dust mass found by Manara et al. (2016b) implies a constant gas-to-dust ratio, which is close to 100 based on the observed  $M_{\text{disk}}/\dot{M}_{\text{acc}}$  ratio. This in turn points to a scenario in which carbon-depletion mechanisms are in play and affect CO line emission. Moreover, the non-correlation found between mass accretion rate and CO-based gas masses implies that carbon is non-homogeneously depleted throughout the Lupus sample. This opens an interesting question on the stellar and disk properties that maximize the sequestering of carbon from gas-phase CO. As discussed in Sect. 4.5.2, if an anticorrelation of complementary gas tracers, such as  $\text{C}_2\text{H}$ , with CO lines were observed, then this would help in solving the controversy.

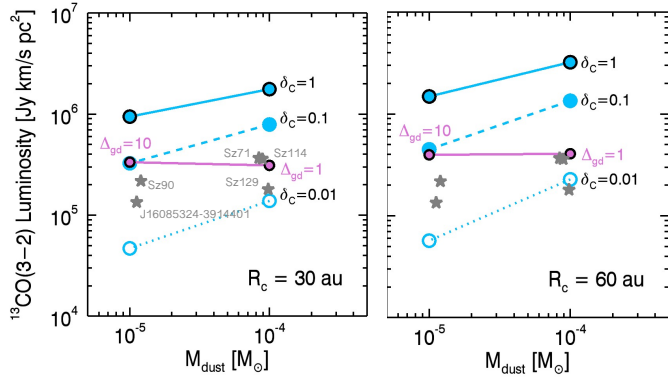


**Figure 4.8:**  $^{13}\text{CO}$  ( $J=3-2$ ) luminosity as a function of dust mass. Light blue circles present the simulated line luminosities with different levels of carbon depletion: no depletion ( $\delta_C = 1$ , black contoured circles), depletion by a factor of 10 ( $\delta_C = 0.1$ , filled light blue circles), and depletion by two orders of magnitude ( $\delta_C = 0.01$ , light blue empty circles). Purple circles present the simulated line luminosities obtained without carbon depletion, fixing the gas mass  $M_{\text{gas}} = 10^{-4} M_{\odot}$  and increasing the dust mass to  $M_{\text{dust}} = 10^{-5}, 10^{-4} M_{\odot}$ , accordingly with gas-to-dust ratios  $\Delta_{\text{gd}}=10, 1$ . A subsample of six Lupus sources is shown with gray stars. Models run with  $R_c = 30$  au and with  $R_c = 60$  au are shown in the left and right panels, respectively.

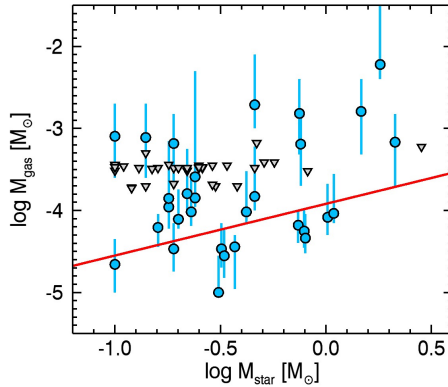


**Figure 4.9:** Disk gas mass as a function of stellar mass for Lupus disks. Gas non-detections are shown as upper limits with gray triangles. For the gas detections the error bars are reported. The red line gives the Bayesian linear regression fit (Kelly 2007).

---

## 4.6 Summary and conclusion

We have employed the grid of physical-chemical models presented in Miotello et al. (2016) to analyze continuum and CO isotopologue ALMA observations of Lupus disks (Ansdell et al. 2016). By also employing the  $^{13}\text{CO}$ -only detections in the optically thin regime, we calculated disk gas masses for a total of 34 sources, expanding the sample of 10 disks for which Ansdell et al. (2016) were able to derive gas masses. As previously found, overall, the gas masses are very low, often lower than  $M_{\text{Jup}}$ . Accordingly, global gas-to-dust ratios are much lower than the expected ISM-value of 100; they lie predominantly between 1 and 10. Low CO-based gas masses and gas-to-dust ratios may indicate rapid loss of gas, or alternatively, carbon depletion. The latter may occur through sequestering of carbon from CO that is either locked into large icy bodies in the midplane, or converted into more complex molecules by either gas-phase chemistry or ice chemistry (Aikawa et al. 1996; Bergin et al. 2014; Du et al. 2015; Eistrup et al. 2016; Kama et al. 2016b; Yu et al. 2016). However, current ALMA data alone cannot distinguish between these scenarios. We have simulated both of them, but model results did not allow us to rule out one of the two hypotheses, which means that we need to calibrate CO-based masses with other tracers. Alternatively, exploitation of disk mass and mass accretion rate measurements simultaneously available in protoplanetary disks can give insight into the nature of low CO-based masses (Manara et al. 2016b) and point to non-homogeneous carbon depletion throughout the Lupus sample.

## Acknowledgements

This paper makes use of the following ALMA data: ADS/JAO.ALMA#2013.1.00220.S. ALMA is a partnership of ESO (representing its member states), NSF (USA) and NINS (Japan), together with NRC (Canada), NSC and SIAA (Taiwan), and KASI (Republic of Korea), in cooperation with the Republic of Chile. The Joint ALMA Observatory is operated by ESO, AUI/ NRAO, and NAOJ. Astrochemistry in Leiden is supported by the Netherlands Research School for Astronomy (NOVA), by a Royal Netherlands Academy of Arts and Sciences (KNAW) professor prize, and by the European Union A-ERC grant 291141 CHEMPLAN. This work was partly supported by the Italian Ministero dell'Istruzione, Universita e Ricerca through the grant Progetti Premiali 2012-iALMA (CUP C52I13000140001). CFM gratefully acknowledges an ESA Research Fellowship. J.P.W. is supported by funding from the NSF and NASA through grants AST- 1208911 and NNX15AC92G.

**Table 4.3:** Disk mass determination for all the detected sources in Lupus. Upper limits on the disk mass are also reported. Notation:  $(^{-n})$  indicates  $10^{-n}$ .

Source name	$M_{\text{gas}}[M_{\odot}]$	$M_{\text{max}}[M_{\odot}]$	$M_{\text{min}}[M_{\odot}]$
Sz65	$6.435^{(-4)}$	$2.0^{(-4)}$	$1.5^{(-3)}$
Sz66	$1.000^{(-5)}$	$1.0^{(-5)}$	$2.8^{(-5)}$
J15430131-3409153	$<3.560^{(-4)}$	-	-
J15430227-3444059	$<3.060^{(-4)}$	-	-
J15445789-3423392	$<1.872^{(-4)}$	-	-
J15450634-3417378	$2.400^{(-5)}$	$1.3^{(-5)}$	$5.0^{(-5)}$
J15450887-3417333	$7.742^{(-4)}$	$2.5^{(-4)}$	$2.0^{(-3)}$
Sz68	$6.800^{(-4)}$	$2.0^{(-4)}$	$1.5^{(-3)}$
Sz69	$3.400^{(-5)}$	$1.8^{(-5)}$	$7.0^{(-5)}$
Sz71	$9.600^{(-5)}$	$7.0^{(-5)}$	$3.0^{(-4)}$
Sz72	$<1.965^{(-4)}$	-	-
Sz73	$<3.012^{(-4)}$	-	-
Sz74	$<2.055^{(-4)}$	-	-
Sz81	$<3.372^{(-4)}$	-	-
Sz83	$1.5162^{(-3)}$	$4.8^{(-4)}$	$4.0^{(-3)}$
Sz84	$1.100^{(-4)}$	$6.0^{(-5)}$	$2.2^{(-4)}$
Sz129	$4.600^{(-5)}$	$3.0^{(-5)}$	$9.0^{(-5)}$
J15592523-4235066	$<1.920^{(-4)}$	-	-
RYLup	$1.607^{(-3)}$	$4.8^{(-4)}$	$4.0^{(-3)}$
J16000060-4221567	$<2.102^{(-4)}$	-	-
J16000236-4222145	$1.420^{(-4)}$	$1.1^{(-4)}$	$7.0^{(-4)}$
J16002612-4153553	$<1.965^{(-4)}$	-	-
Sz130	$3.600^{(-5)}$	$1.1^{(-5)}$	$5.0^{(-5)}$
MYLup	$8.250^{(-5)}$	$5.0^{(-5)}$	$2.1^{(-4)}$
Sz131	$<1.965^{(-4)}$	-	-
J16011549-4152351	$2.374^{(-3)}$	$1.5^{(-3)}$	$5.0^{(-2)}$
Sz133	$7.250^{(-5)}$	$3.0^{(-5)}$	$9.0^{(-5)}$
Sz88A	$<3.860^{(-4)}$	-	-
Sz88B	$<3.292^{(-4)}$	-	-
J16070384-3911113	$8.022^{(-4)}$	$2.5^{(-4)}$	$2.0^{(-3)}$
J16070854-3914075	$2.025^{(-4)}$	$1.8^{(-4)}$	$4.0^{(-3)}$
Sz90	$5.600^{(-5)}$	$3.500^{(-5)}$	$1.0^{(-4)}$
J16073773-3921388	$3.455^{(-4)}$	-	-
Sz95	$2.800^{(-5)}$	$1.5^{(-5)}$	$6.0^{(-5)}$
J16075475-3915446	$<4.670^{(-4)}$	-	-
J16080017-3902595	$<3.292^{(-4)}$	-	-
J16080175-3912316	$<5.562^{(-4)}$	-	-
Sz96	$<3.292^{(-4)}$	-	-
J16081497-3857145	$2.200^{(-5)}$	$1.0^{(-5)}$	$4.5^{(-5)}$

---

	Sz97	$<3.535^{(-4)}$	-	-
	Sz98	$6.600^{(-5)}$	$4.0^{(-5)}$	$1.0^{(-4)}$
	Sz99	$<3.050^{(-4)}$	-	-
	Sz100	$1.400^{(-4)}$	$1.1^{(-4)}$	$7.0^{(-4)}$
	J160828.1-391310	$<3.050^{(-4)}$	-	-
	Sz103	$<3.292^{(-4)}$	-	-
	J16083070-3828268	$6.01^{(-3)}$	$4.0^{(-3)}$	$1.0^{(-1)}$
	Sz104	$<3.617^{(-4)}$	-	-
	J160831.1-385600	$5.400^{(-4)}$	-	-
	V856Sco	$<5.970^{(-4)}$	-	-
	Sz106	$<3.860^{(-4)}$	-	-
	Sz108B	$6.537^{(-4)}$	$2.0^{(-4)}$	$1.5^{(-3)}$
	J16084940-3905393	$<3.292^{(-4)}$	-	-
	V1192Sco	$<3.292^{(-4)}$	-	-
	Sz110	$<3.372^{(-4)}$	-	-
	J16085324-3914401	$3.400^{(-5)}$	$2.0^{(-5)}$	$7.0^{(-5)}$
	J16085373-3914367	$<3.617^{(-4)}$	-	-
	Sz111	$1.935^{(-3)}$	$1.0^{(-3)}$	$8.0^{(-3)}$
	J16085529-3848481	$<3.535^{(-4)}$	-	-
	Sz112	$<3.292^{(-4)}$	-	-
	Sz113	$<3.292^{(-4)}$	-	-
	J16085828-3907355	$<5.077^{(-4)}$	-	-
	J16085834-3907491	$<5.400^{(-4)}$	-	-
	J16090141-3925119	$2.575^{(-4)}$	$1.5^{(-4)}$	$5.0^{(-3)}$
	Sz114	$9.600^{(-5)}$	$6.5^{(-5)}$	$2.8^{(-4)}$
	Sz115	$<3.292^{(-4)}$	-	-
	J16091644-3904438	$<5.562^{(-4)}$	-	-
	J16092032-3904015	$<4.995^{(-4)}$	-	-
	J16092317-3904074	$<5.400^{(-4)}$	-	-
	J16092697-3836269	$7.800^{(-5)}$	$6.0^{(-5)}$	$1.8^{(-4)}$
	J160934.2-391513	$<5.562^{(-4)}$	-	-
	J16093928-3904316	$<5.400^{(-4)}$	-	-
	Sz117	$<3.535^{(-4)}$	-	-
	Sz118	$1.175^{(-4)}$	$7.0^{(-5)}$	$2.8^{(-4)}$
	J16095628-3859518	$<3.372^{(-4)}$	-	-
	J16100133-3906449	$<4.995^{(-4)}$	-	-
	J16101307-3846165	$<3.455^{(-4)}$	-	-
	J16101857-3836125	$<3.212^{(-4)}$	-	-
	J16101984-3836065	$<3.372^{(-4)}$	-	-
	J16102741-3902299	$<5.400^{(-4)}$	-	-
	J16102955-3922144	$1.600^{(-4)}$	$1.0^{(-4)}$	$5.6^{(-4)}$
	J16104536-3854547	$<5.725^{(-4)}$	-	-
	Sz123B	$<3.535^{(-4)}$	-	-
	Sz123A	$1.480^{(-4)}$	$1.0^{(-4)}$	$6.0^{(-4)}$

---

---

J16115979-3823383	$<3.212^{(-4)}$	-	-
J16120445-3809589	$<5.725^{(-4)}$	-	-
J16121120-3832197	$<5.645^{(-4)}$	-	-
J16124373-3815031	$<6.617^{(-4)}$	-	-
J16134410-3736462	$6.200^{(-5)}$	$3.6^{(-5)}$	$9.0^{(-5)}$

# 5

## PROBING PROTOPLANETARY DISK GAS SURFACE DENSITY DISTRIBUTION WITH $^{13}\text{CO}$ EMISSION

---

A. Miotello, S. Facchini, E. F. van Dishoeck, S. Bruderer, *Probing protoplanetary disk gas surface density distribution with  $^{13}\text{CO}$  emission*, in prep.



---

**Abstract** – How protoplanetary disks evolve is still an unsolved problem where different processes may be involved. Depending on the process, the disk gas surface density distribution  $\Sigma_{\text{gas}}$  may be very different which would have diverse implications for planet formation. Together with the total disk mass, it is key to constrain  $\Sigma_{\text{gas}}$  as function of disk radius  $R$  from observational measurements. In this work we investigate whether spatially resolved observations of rare CO isotopologues, such as  $^{13}\text{CO}$ , may be good tracers of the gas surface density distribution in disks. Physical-chemical disk models with different input  $\Sigma_{\text{gas}}(R)$  are run, taking into account CO freeze-out and isotope selective photodissociation. The input disk surface density profiles are compared with the simulated  $^{13}\text{CO}$  intensity radial profiles to check whether and where the two follow each other. For each combination of disk parameters, there is always an intermediate region in the disk where the slope of the  $^{13}\text{CO}$  radial emission profile and  $\Sigma_{\text{gas}}(R)$  coincide. In the inner part of the disk the line radial profile underestimates  $\Sigma_{\text{gas}}$ , as  $^{13}\text{CO}$  emission becomes optically thick. The same happens at large radii where the column densities become too low and  $^{13}\text{CO}$  is not able to efficiently self-shield. Moreover, the disk becomes too cold and a considerable fraction of  $^{13}\text{CO}$  is frozen out, thus it does not contribute to the line emission. If the gas surface density profile is a simple power-law of the radius, the input power-law index can be retrieved within a  $\sim 20\%$  uncertainty if one chooses the proper radial range. If instead  $\Sigma_{\text{gas}}(R)$  follows the self-similar solution for a viscously evolving disk, retrieving the input power-law index becomes challenging, in particular for less extended disks. An alternative approach is to fit the power-law index  $\gamma$  at a given line intensity contour, that is found to always correspond to the same  $\Sigma_{\text{gas}}$  contour.  $^{13}\text{CO}$  spatially resolved line radial profiles are promising to probe the disk surface density distribution, as they directly trace  $\Sigma_{\text{gas}}(R)$  profile at radii well resolvable by ALMA. There, chemical processes like freeze-out and isotope selective photodissociation are not affecting the emission assuming volatile carbon depletion does not change with radius, thus no chemical model is needed when interpreting the observations. However, identifying the proper radial range to fit requires some estimate of total disk mass.

---

## 5.1 Introduction

Protoplanetary disk evolution adds to the construction of the host young star and simultaneously provides the material for the formation of planets and large rocky bodies. Mass accretion onto the central star and planet formation are therefore connected processes where the gaseous and solid disk components play important and complementary roles (see Armitage 2015, for a review). It is generally assumed that gas is the main disk component accounting for 99% of its mass, while only 1% is in the form of dust. Furthermore the gaseous component is also what drives disk evolution and thus the disk structure at different stages. An open question is what the relative importance is of different mechanisms transporting the material onto the star and dispersing the disk within few Myr. Disk evolution leads to mass accretion onto the central star (Hartmann et al. 2016), but part of the disk content can be dissipated by high-energy radiation driven winds or magnetic torques (Alexander et al. 2014; Gorti et al. 2016; Bai et al. 2016) and external processes such as encounters (e.g. Clarke & Pringle 1993; Pfalzner et al. 2005) and external photoevaporation (e.g. Clarke 2007; Anderson et al. 2013; Facchini et al. 2016). Depending on which process is dominant, the disk structure will be considerably different. In particular this will impact the distribution of the gas as a function of the distance from the star, which is described by the surface density distribution,  $\Sigma_{\text{gas}}$ . Morbidelli & Raymond (2016) discuss the difference in the resulting disk structures between disk wind models and the standard viscously evolving  $\alpha$ -disk model. Suzuki et al. (2016) find that the inner disk can be heavily depleted as winds efficiently remove angular momentum from the disk and cause large accretion onto the star. On the other hand, a different disk wind model by Bai et al. (2016) predicts a surface density profile that scales inversely with the radius in the innermost 10 au, similarly to what is expected in the  $\alpha$ -disk case. Reliable observational measurements of  $\Sigma_{\text{gas}}$  as function of radius would therefore be key to understand disk evolution and the relative importance of different processes, as well as how planet formation occurs (Morbidelli & Raymond 2016).

Successful attempts have been made to constrain the disk dust surface density  $\Sigma_{\text{dust}}$  from high S/N spatially resolved mm-continuum observations. The thermal emission of mm-sized grains is largely optically thin in protoplanetary disks and allows to directly trace the column density of the bulk of the dust (e.g. Andrews 2015; Tazzari et al. 2017). Dust and gas surface densities, however, are not necessarily the same. Even though they are strongly coupled, different mechanisms are thought to affect their evolution, such as radial drift of millimeter-sized grains modifying the dust surface density on short timescales. This is the case e.g., in HD 163296 where the CO emission extends much further than the continuum dust emission (de Gregorio-Monsalvo et al. 2013; Isella et al. 2016), although the much higher optical depth of the

---

CO lines versus millimeter continuum also contributes significantly to this difference in appearance (Dutrey et al. 1998; Facchini et al. 2017). Another example comes from the Herbig disk HD 169142, where ALMA observations show that the dust appears to be concentrated in two rings between 20–35 au and 56–83 au, whereas gas seen in CO isotopologues is still present inside the dust cavity and gap (Fedele et al. 2017). More extreme examples are transitional disks with large cavities severely depleted in dust content, but less in gas, with gas cavities smaller than dust cavities (van der Marel et al. 2013, 2016; Bruderer et al. 2014; Zhang et al. 2014). Taken together, it is clear that gas and millimeter dust emission do not follow each other and that a more direct tracer of the gas surface density profile is needed.

The main gaseous component is molecular hydrogen ( $\text{H}_2$ ), whose emission lines at near- and mid-infrared wavelengths are very weak and are superposed on strong continuum emission (e.g. Thi et al. 2001; Pascucci et al. 2006). In contrast, carbon monoxide (CO) pure rotational transitions at millimeter wavelengths are readily detected (e.g. Dutrey et al. 1996; Thi et al. 2001; Dent et al. 2005; Panić et al. 2008). CO is the second-most abundant molecule, with a chemistry that is very well studied and implemented in physical-chemical codes. Owing to their optically thin emission lines, less abundant CO isotopologues are considered better tracers than  $^{12}\text{CO}$  of the gas column (Miotello et al. 2014b, 2016; Schwarz et al. 2016). This paper investigates whether spatially resolved observations of such lines may be good probes of the gas surface density distribution, once freeze-out and isotope selective photodissociation are taken into account.

Thanks to the unique sensitivity of ALMA, large surveys of disks in different star forming regions are being carried out to trace gas and dust simultaneously (Ansdell et al. 2016; Barenfeld et al. 2016; Eisner et al. 2016; Pascucci et al. 2016). In particular, CO isotopologues pure rotational lines have been targeted but lines are weaker than expected and at the short integration time of typically one minute the line data have low S/N. This may be interpreted as lack of gas due to fast disk dispersal, or as lack of volatile carbon that leads to faint CO lines (Favre et al. 2013; Ansdell et al. 2016; Schwarz et al. 2016; Miotello et al. 2017). As a consequence,  $^{13}\text{CO}$  lines are optically thin towards a larger part of the disk and become much better tracers of the gas columns than  $\text{C}^{18}\text{O}$  lines, which were thought to be preferred pre-ALMA, but are often undetected. Furthermore,  $^{13}\text{CO}$  is less affected by isotope selective photodissociation than  $\text{C}^{18}\text{O}$  (Miotello et al. 2014b). The focus of this paper is thus on  $^{13}\text{CO}$ , rather than on other isotopologues. Recently Zhang et al. (2017) have proposed the optically thin lines of  $^{13}\text{C}^{18}\text{O}$ , successfully detected in the TW Hya disk, to be a good probe of  $\Sigma_{\text{gas}}(R)$  at small radii. We briefly investigate this possibility from our modeling perspective using another low abundance isotopologue  $\text{C}^{17}\text{O}$ .

Williams & McPartland (2016) have presented a method to extract disk gas surface density profiles from  $^{13}\text{CO}$  ALMA observations. Assuming a self-similar density distribution as given by viscous evolution theory, the authors create a large

---

gallery of parametrized models, which they use to extract the disk parameters with a MCMC analysis. Although we share the same scientific question, this paper follows a different approach, i.e., we fit a power-law profile to our simulated  $^{13}\text{CO}$  radial profiles as if they were observations, in order to recover the power-law index  $\gamma$ . Our analysis shows that it may be difficult to infer both  $\gamma$  and the critical radius independently for small disks.

In Section 5.2, the physical-chemical modeling is presented. The results of the modeling investigation are presented in Section 5.3 and their implications are discussed in Section 5.4.

## 5.2 Modeling

### 5.2.1 DALI

The physical-chemical code DALI is used for the disk modeling (Dust And Lines, Bruderer et al. 2012; Bruderer 2013). DALI calculates the dust temperature,  $T_{\text{dust}}$ , and local continuum radiation field from UV to mm wavelengths with a 2D Monte Carlo method, given an input disk physical structure and a stellar spectrum as source of irradiation. Then a time-dependent (1 Myr) chemical network simulation is run. Subsequently, the gas temperature,  $T_{\text{gas}}$ , is calculated through an iterative balance between heating and cooling processes until a self-consistent solution is found and the non-LTE excitation of the molecules is computed. In this paper, the final outputs are spectral image cubes of CO isotopologues computed by a ray-tracer module. Throughout this paper, the  $J=3-2$  line is produced and analyzed, but results are similar for  $J=2-1$ .

DALI has been extensively tested and benchmarked against observations (Fedele et al. 2013) and a detailed description of the code is presented by Bruderer et al. (2012) and Bruderer (2013). For this work, a complete treatment of CO freeze-out and isotope-selective processes is included (for more detail, see Miotello et al. 2014b, 2016).

### 5.2.2 Grid of models

The disk surface density distribution is often parametrized by an exponentially tapered power-law function, following the prescription proposed by Andrews et al. (2011). Physically this represents a viscously evolving disk, where the viscosity is expressed by  $\nu \propto R^\gamma$  (Lynden-Bell & Pringle 1974; Hartmann et al. 1998). The self-

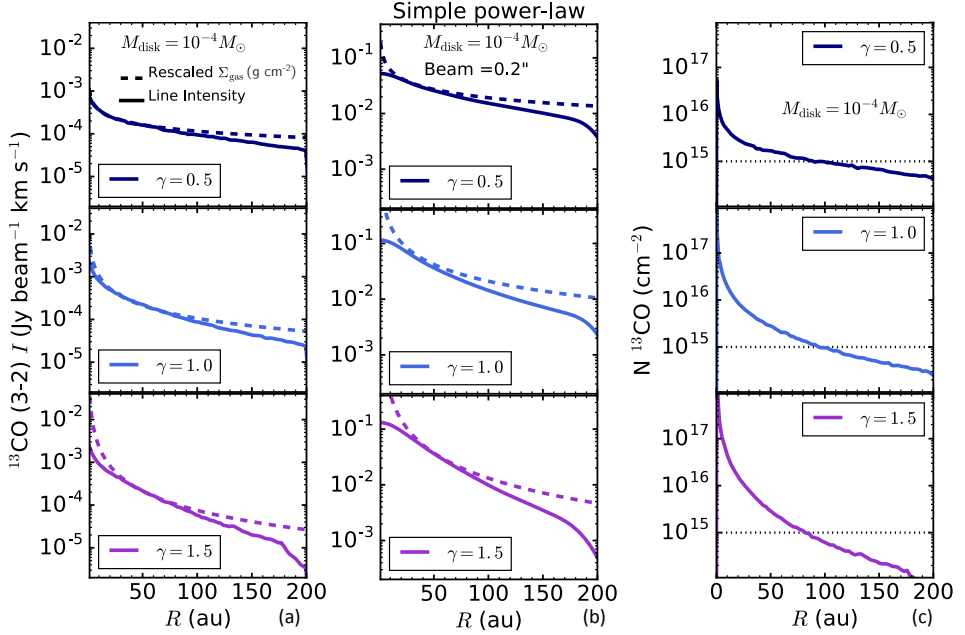


**Figure 5.1:** Panel *a* –  $^{13}\text{CO}$  line intensity radial profiles (solid lines) obtained with three representative disk models with input surface density distribution  $\Sigma_{\text{gas}}$  (dashed lines) chosen to be a simple power-law (see Eq. 5.2). The model parameters are  $R_{\text{out}} = 200$  au,  $M_{\text{disk}} = 10^{-4} M_{\odot}$  and  $\gamma = 0.8, 1, 1.5$  shown in dark blue, light blue, and purple respectively (top, middle, and bottom panels). No beam convolution is applied to the simulated images and a distance of 150 pc is assumed. Panel *b* –  $^{13}\text{CO}$  line intensity radial profiles compared with input surface density profiles as in panel *a*, but convolved with a  $0.2''$  beam. Panel *c* – Column densities of gas-phase  $^{13}\text{CO}$  calculated from the surface to the midplane shown as function of the disk radius for the three representative models with simple power-law surface density. The dotted black line indicates the column density at which CO self-shielding becomes inefficient ( $N = 10^{15} \text{ cm}^{-2}$ ).

similar surface profile is expressed by:

$$\Sigma_{\text{gas}} = \Sigma_c \left( \frac{R}{R_c} \right)^{-\gamma} \exp \left[ - \left( \frac{R}{R_c} \right)^{2-\gamma} \right], \quad (5.1)$$

where  $R_c$  is the critical radius and  $\Sigma_c$  is the surface density at the critical radius. This parametrization has often been employed to model disks with DALI (see e.g., Miotello et al. 2014b, 2016). Adopting an exponential taper to the power-law profile of the surface density distribution (see Eq. 5.1), as suggested by viscous evolution theory, has the inconvenience that the profile slope depends on two free parameters,  $R_c$  and  $\gamma$ , which can be difficult to disentangle. A simplification comes from the assumption that  $\Sigma_{\text{gas}}$  has a pure power-law dependence with radius. In this case the power-law index  $\gamma$  is left as a single free parameter:

$$\Sigma_{\text{gas}} = \begin{cases} \Sigma_c \left( \frac{R}{R_c} \right)^{-\gamma} & R \leq R_{\text{out}}, \\ 0 & R > R_{\text{out}}. \end{cases} \quad (5.2)$$

In this work both parametrizations have been employed to design the input density structures.

**Table 5.1:** Parameters of the disk models.

Parameter	Value	
	Self similar	Power-law
$\gamma$	0.8, 1, 1.5	0.5, 1, 1.5
$R_c$	30, 60, 200 au	–
$R_{\text{out}}$	500 au	100, 200 au
$M_{\text{gas}}$	$10^{-5}, 10^{-4},$ $10^{-3}, 10^{-2} M_{\odot}$	$10^{-5}, 10^{-4},$ $10^{-3}, 10^{-2} M_{\odot}$

First, some of the model results presented in Miotello et al. (2014b) using the self similar profile have been analyzed. The free parameters are then  $R_c$ ,  $\gamma$ , and  $M_{\text{disk}}$ , whose values are reported in column 2 of Table 5.1. A value for  $R_{\text{out}}$  is also reported, but this is simply needed for the simulation and does not have any effect on the disk structure, as the exponential cut-off truncates the disk at smaller radii. Parameters defining the disk vertical structure are reported in Table 1 of Miotello et al. (2014b) and simulate a medium-flared disk with large dust grains settled. From here on, such disk models where the input surface density distribution is set by Eq. 5.1 will be called *self-similar* disk models.

Additional models have then been run with the simple power-law surface density structure (see eq. 5.2). In this case the free parameters are  $R_{\text{out}}$ ,  $\gamma$ , and  $M_{\text{disk}}$  as

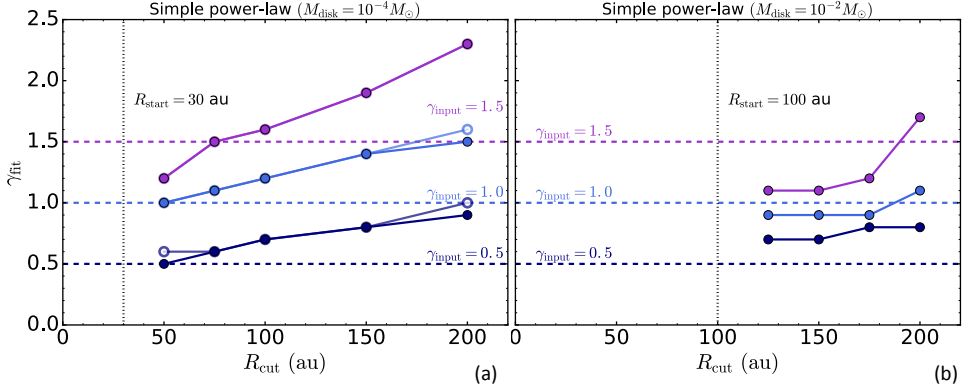


**Figure 5.2:** Results of the power-law fitting of the simulated  $^{13}\text{CO}$  line intensity profiles obtained with the simple power-law models ( $M_{\text{disk}} = 10^{-4} M_{\odot}$  and  $M_{\text{disk}} = 10^{-2} M_{\odot}$  in panel a and b respectively). The values of the fitted power-law index  $\gamma_{\text{fit}}$  are shown by the filled dots as a function of the radial range over which the fitting was carried out. The empty symbols in panel (a) show the fitted power-law index  $\gamma_{\text{fit}}$  when the simulated images are convolved with a  $0.2''$  beam. The model input power-law indexes are shown by the dashed lines. The dotted line shows the starting point of the fitting  $R_{\text{start}}$ .

shown in column 3 of Table 5.1. From here on, disk models where the input surface density distribution is set by Eq. 5.2 will be called *simple power-law* disk models.

In order to investigate different disk mass regimes and then compare with recent observations of CO isotopologues in protoplanetary disks (Ansdell et al. 2016), a range of models from less massive to high mass disks have been run (see Tab. 5.1). These observations also show moderately extended emission, therefore the outer radius in the models has been set to 200 au. The raytracing of all models presented here is carried out assuming the disk to be at a distance of 150 pc, representative of that of the nearby star-forming regions. Furthermore, the output synthetic images have either been left unconvolved or convolved with a moderate resolution beam of  $0.2''$ . In the first case, the resolution is that of the radial grid assumed for the simulation. The calculation is carried out on 75 cells in the radial direction (logarithmically spaced up to 30 au and then linearly spaced for a radial resolution of  $\sim 10$  au) and 60 in the vertical direction models (Miotello et al. 2014b). In the new models with the simple power-law surface density structure, a denser grid with 95 cells in the radial direction (improved radial resolution in the outer disk of  $\sim 3$  au) and 80 in the vertical direction was chosen. For the unconvolved images (see Sec. 5.3) a nominal beam size of  $0.01''$  is used, which corresponds to a resolution of  $\sim 1.5$  au at 150 pc.

---

## 5.3 Results

The first test is to compare the input disk surface density profiles for the DALI models with the simulated  $^{13}\text{CO}$  profiles, as if they were observed at infinite resolution, i.e. not convolved with any beam. However, the ray-tracing requires a beam, which we set to  $0.01''$  in order to be smaller than the physical grid resolution in our models. The results obtained in the two cases, where  $\Sigma_{\text{gas}}$  is parametrized by a simple power-law or following the self-similar solution are presented below.

### 5.3.1 Simple power-law

The input disk surface density profiles are compared with the simulated  $^{13}\text{CO}$  profiles for three representative models ( $M_{\text{disk}} = 10^{-4}M_{\odot}$ ,  $R_{\text{out}} = 200 \text{ au}$ ,  $\gamma = 0.8, 1, 1.5$ ) and are shown in panel (a) of Fig. 5.1. The surface density profiles (in  $\text{g cm}^{-2}$ ) have been rescaled by a constant factor in order to visually match the line intensity profiles. The disk can be divided in three regions: an inner part in which the  $^{13}\text{CO}$  radial profile underestimates  $\Sigma_{\text{gas}}$ , a central zone where the two coincide, and an outer region where the line emission drops and deviates from the surface density distribution (see case with  $\gamma = 1.5$ , for clarity). At small radii the divergence is caused by the fact that  $^{13}\text{CO}$  emission becomes optically thick as the columns are very high. At large radii the  $^{13}\text{CO}$  column densities become too low, lower than  $10^{15} \text{ cm}^{-2}$ , and  $^{13}\text{CO}$  is not able to efficiently self-shield (van Dishoeck & Black 1988; Visser et al. 2009).

There are two ways to further investigate these cases. The column densities of gas-phase  $^{13}\text{CO}$  calculated from the surface to the midplane are shown as function of the disk radius in panel (c) of Fig. 5.1 in blue, light blue and purple for models with  $\gamma = 0.8, 1, 1.5$  respectively. The column density can be compared with the line luminosity profiles presented in panel (a) of Fig. 5.1. The radius where the line luminosity profiles decrease and deviate from the surface density distribution is similar to that at which the  $^{13}\text{CO}$  column densities drop below  $10^{15} \text{ cm}^{-2}$ . This illustrates that inefficient CO self-shielding affects CO isotopologues intensity profiles and needs to be considered in the disk outer regions.

As reported in Table 5.1, less and more massive models have been run for the simple power-law case. We observe similar trends, but the radial location of the three regions described above are radially shifted to smaller or larger radii, depending on disk mass (see Fig. 5.8). Compared with the representative model with mass  $M_{\text{disk}} = 10^{-4}M_{\odot}$ , for  $M_{\text{disk}} = 10^{-5}M_{\odot}$  the simulated radial intensity profiles better follow  $\Sigma_{\text{gas}}$  at smaller radii as the line is less optically thick. On the other hand  $^{13}\text{CO}$  column densities smaller than  $N = 10^{15} \text{ cm}^{-2}$  are reached at smaller radii. The opposite happens for  $M_{\text{disk}} = 10^{-2}M_{\odot}$ , where the line emission is optically thick up



to almost 100 au, but CO self-shielding becomes inefficient much further out, around 200 au.

### Fitting of the surface density power-law index $\gamma$

We now address the question of whether it is possible to retrieve the underlying surface density power-law index  $\gamma$  by fitting the line intensity profiles. We refer to the power-law index used as input in DALI as  $\gamma_{\text{input}}$  and we label the fitted value  $\gamma_{\text{fit}}$ .

The fit of a power-law profile to the simulated intensity profiles is performed as a linear fit in the  $\log I$ - $\log R$  space. As it is clear from Fig. 5.1 that  $^{13}\text{CO}$  radial intensity profiles follow  $\Sigma_{\text{gas}}(R)$  only in a particular region, the fit is not carried out over the whole extent of the disk, but over a radial range that spans from  $R_{\text{start}}$  to  $R_{\text{cut}}$ . The starting point  $R_{\text{start}}$  is kept fixed and chosen to be just outside the inner region where the emission is optically thin, typically 30–40 au. The range of radii over which the fitting is performed is then varied by changing the value of  $R_{\text{cut}}$ .

The results of the fitting are presented in Fig. 5.2 for the single power-law case. The dashed lines illustrate the value of  $\gamma_{\text{input}}$ , while the colored dots show the value of  $\gamma_{\text{fit}}$  if different  $R_{\text{cut}}$  are chosen for the fitting. The starting radius for the fitting procedure  $R_{\text{start}}$  is indicated by the dotted vertical line.

For low mass disk models ( $M_{\text{disk}} = 10^{-4}M_{\odot}$ , panel a of Fig. 5.2), the power-law index  $\gamma_{\text{input}}$  can be retrieved within 20% of uncertainty in a range of radii that goes from 30 – 40 au to  $\sim 100$  au, the typical scales probed with ALMA. Furthermore, the retrieved  $\gamma_{\text{fit}}$  usually overestimates the input value, except for the  $\gamma = 1.5$  case. Fixing  $R_{\text{start}}$  to either 30 au or 40 au does not change qualitatively the outcome of the fit. For  $R_{\text{cut}}$  larger than 100 au, the fitted values deviate significantly from  $\gamma_{\text{input}}$  as one enters the region where self-shielding becomes inefficient and the intensity profiles deviate from  $\Sigma_{\text{gas}}$ . For higher mass disk models ( $M_{\text{disk}} = 10^{-2}M_{\odot}$ , panel b of Fig. 5.2) one needs to choose a larger  $R_{\text{start}}$  of 100 au, as  $^{13}\text{CO}$  is optically thick much further out than the low mass disk case. Furthermore, the uncertainties on  $\gamma_{\text{fit}}$  are larger.

In order to choose the correct radial range over which to perform the fit, one would need to know in which mass regime the observed disk is. More precisely, one would need to constrain the total  $^{13}\text{CO}$  gas mass. For faint observed  $^{13}\text{CO}$  fluxes, Miotello et al. (2016) have found a linear relation between line emission and total disk mass. This could be used to constrain  $M_{\text{disk}}$ . For brighter observed  $^{13}\text{CO}$  fluxes, this relation is less reliable and one could employ the dust masses obtained from continuum emission, multiplied by the canonical factor of 100. This would provide an upper limit to the disk mass (see Sec. 5.4 for discussion on carbon depletion). Another possibility is to combine  $^{13}\text{CO}$  and  $\text{C}^{18}\text{O}$  line fluxes (Miotello et al. 2016), if the latter are available from the same observation.

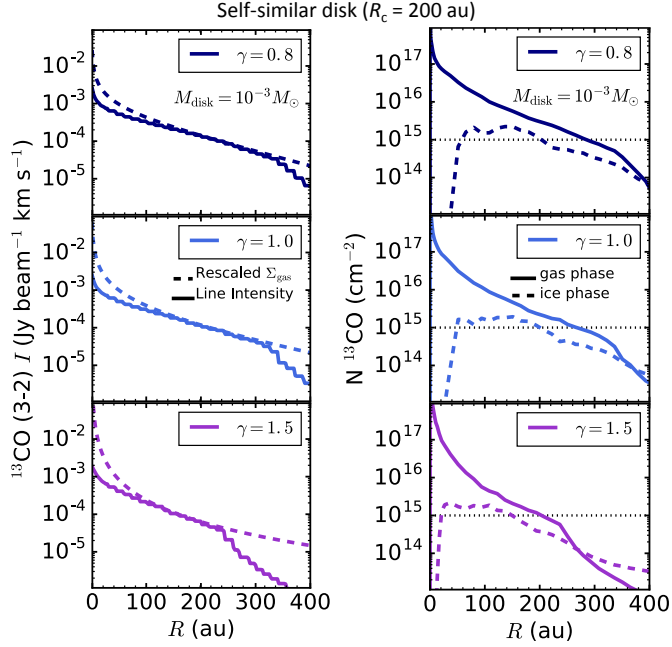


**Figure 5.3:** *Panel (a)* –  $^{13}\text{CO}$  line intensity radial profiles (solid lines) obtained with three representative disk models with input surface density distribution  $\Sigma_{\text{gas}}$  (dashed lines) given by the viscously evolving disk model (see Eq. 5.1). The model parameters are  $R_c = 200$  au,  $M_{\text{disk}} = 10^{-3} M_{\odot}$  and  $\gamma = 0.8, 1, 1.5$  shown in dark blue, light blue, and purple respectively (top, middle, and bottom panels). *Panel (b)* – Column densities of gas-phase (solid lines) and ice-phase (dashed lines)  $^{13}\text{CO}$  calculated from the surface to the midplane shown as function of the disk radius for the three representative self-similar disk models. The dotted black line indicates the column density at which CO self-shielding becomes inefficient ( $N = 10^{15} \text{ cm}^{-2}$ ).

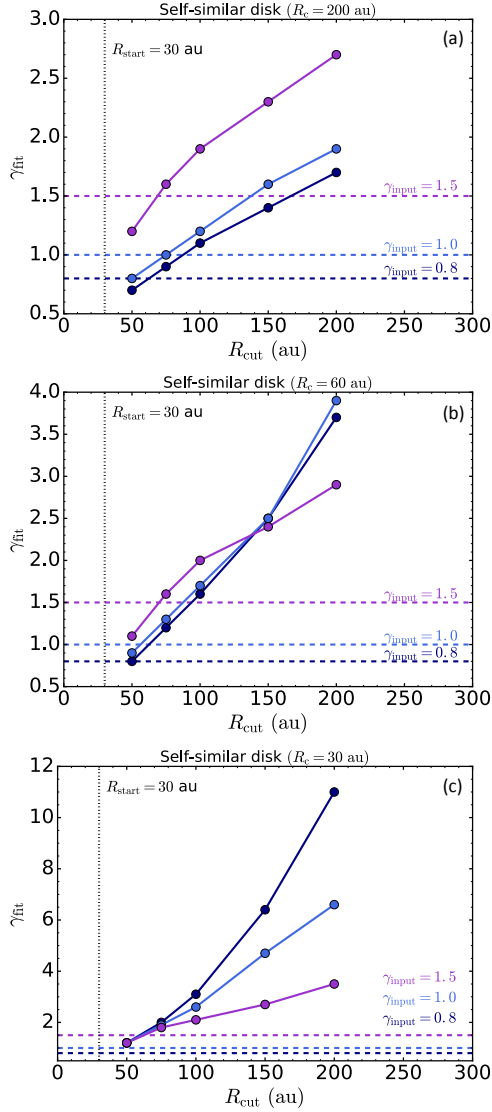


**Figure 5.4:** Results of the power-law fitting of the simulated  $^{13}\text{CO}$  line intensity profiles obtained with the self-similar disk models with  $M_{\text{disk}} = 10^{-1}M_{\odot}$ . The values of the fitted power-law index  $\gamma_{\text{fit}}$  are shown by the filled dots as a function of the radial range in which the fitting was carried out. The model input power-law indexes are shown by the dashed lines. The dotted line shows the starting point of the fitting  $R_{\text{start}}$ .

---

## Convolution with a beam

Finally, the simulated line intensity radial profiles need to be convolved with a synthesized beam to check how the trends are affected by this operation. Observations taken from recent ALMA disk surveys have moderate angular resolution, between  $0.2''$  and  $0.3''$ , corresponding to 30 – 40 au diameter at 150 pc (Ansdell et al. 2016, e.g.). To mimic such observations we convolve our simulated profiles with a  $0.2''$  beam. The convolved  $^{13}\text{CO}$  line intensity radial profiles are shown in panel b of Fig. 5.1.

As in Sec. 5.3.1, a power-law fitting of the convolved radial intensity profiles has been carried out. The starting point  $R_{\text{start}}$  has been fixed to 30 au and the results are shown in panel (a) of Fig. 5.2. The values of  $\gamma_{\text{fit}}$  do not qualitatively differ from those found with the unconvolved radial profiles, shown in panel (a) of Fig. 5.2. Even with a beam convolution of  $0.2''$  the power-law index can be retrieved to an accuracy of  $\sim 20\%$ , if the fit is carried out in a region that goes from  $\sim 30$  au to  $\sim 100$  au.

## 5.3.2 Self-similar disk models

Similar trends as those presented in Sec. 5.3.1 have been found also for the self-similar case. The input disk surface density profiles compared with the simulated  $^{13}\text{CO}$  profiles for three representative self-similar models ( $M_{\text{disk}} = 10^{-3}M_{\odot}$ ,  $R_{\text{c}} = 200$  au,  $\gamma = 0.8, 1, 1.5$ ) are shown in panel (a) of Fig. 5.3. The surface density profiles have been rescaled by a constant factor in the plots to visually match the line intensity profiles. As for the simple power-law case it is possible to identify three regions: the inner disk in which  $^{13}\text{CO}$  lines are optically thick and the emission profile is flatter than the  $\Sigma_{\text{gas}}$  profile, a central region in which the two profiles match, and the outer disk where the line intensity underestimates the surface density distribution.

In the self-similar models a secondary effect adds to inefficient CO self-shielding to reduce the emission in the outer disk. As shown in Fig. 5.7, the simple power-law representative model (panel b) for a less massive disk ( $M_{\text{disk}} = 10^{-4}M_{\odot}$ ) is warmer than the self-similar representative disk model (panel a,  $M_{\text{disk}} = 10^{-3}M_{\odot}$ ). In this second case, the dust temperature  $T_{\text{dust}}$  drops below 20 K in the midplane at radii larger than 50 au and a significant fraction of  $^{13}\text{CO}$  is frozen out, thus not contributing to the line emission (see panel a of Fig. 5.7). Moreover, the inner region where the emission lines are optically thick is smaller compared to the power-law case, and the radial range over which the line intensity profile follows  $\Sigma_{\text{gas}}$  is shifted toward smaller radii.

The column density, reported in panel b of Fig. 5.3, can be compared with the line intensity profiles presented in panel a. The radius where the line intensity profiles decrease and deviate from the surface density distribution is similar to that at which  $^{13}\text{CO}$  column densities drop below  $10^{15} \text{ cm}^{-2}$  (at  $\sim 300$  au for  $\gamma = 0.8$ ,  $\sim 250$  au for

$\gamma = 1.0$ , and  $\sim 200$  au for  $\gamma = 1.5$ ).

As for the simple power-law case, simulated  $^{13}\text{CO}$  radial intensity profiles have been fitted with a power-law to try and retrieve the power-law index  $\gamma_{\text{input}}$ . This procedure is applied to models where  $M_{\text{disk}} = 10^{-4}M_{\odot}$ , in order to directly compare with the results found in the simple power-law case, instead of  $M_{\text{disk}} = 10^{-3}M_{\odot}$ , as discussed above. The intensity profiles for the lower mass ( $M_{\text{disk}} = 10^{-4}M_{\odot}$ ) self-similar disk models are reported in Fig. 5.9 in Appendix 5.A. Fit parameters are much more unambiguous when fitting the intensity profiles obtained with the self-similar disk models. As shown in Fig. 5.4, the retrieved  $\gamma_{\text{fit}}$  significantly deviate from the original  $\gamma_{\text{input}}$ . If  $R_c$  is 200 au, it is still possible to distinguish  $\gamma_{\text{fit}}$  between models with different  $\gamma_{\text{input}}$  (panel a of Fig. 5.4). If instead  $R_c$  is smaller, i.e., 30 au or 60 au (panel b and c of Fig. 5.4 respectively), this is not true. The complication is given by the fact that for  $R > R_c$  the  $\Sigma_{\text{gas}}$  profile follows an exponential decline which, when fitted with a power-law, will give higher values for  $\gamma_{\text{fit}}$ . Those values are however unrelated to the value of  $\gamma_{\text{input}}$  that one would like to retrieve. On top of this, as already discussed, inefficient self-shielding adds to the steepness of the intensity profiles in the outer disk. Whether a simultaneous fit to both  $\gamma$  and  $R_c$  would provide better fits remains to be determined.

In summary, the obtained  $\gamma_{\text{fit}}$  has a poor relation with  $\gamma_{\text{input}}$  if the underlying surface density profile is given by a self-similar disk model.

### 5.3.3 Inner disk surface density profile from $\text{C}^{17}\text{O}$ line intensity radial profiles

Our models show that  $^{13}\text{CO}$  is not a good tracer of  $\Sigma_{\text{gas}}$  in the inner 30–40 au. Recently, Zhang et al. (2017) have used the rarer  $^{13}\text{C}^{18}\text{O}$  isotopologue to try determining the surface density profile in the inner regions of the well studied TW Hya disk. A rather low abundance CO isotopologue is  $\text{C}^{17}\text{O}$ , expected to be around 24 times more abundant than  $^{13}\text{C}^{18}\text{O}$  based on isotope ratios. We thus analyze the intensity profiles obtained for  $\text{C}^{17}\text{O}$  to check how they can be used to infer the surface density profile in the disk inner regions.

The simulated  $\text{C}^{17}\text{O}$  intensity profiles and column density profiles for six power-law disk models ( $R_{\text{out}} = 200$  au,  $M_{\text{disk}} = 10^{-4}, 10^{-2}M_{\odot}$  and  $\gamma = 0.8, 1, 1.5$ ) are presented in Fig. 5.6. For the  $10^{-4}M_{\odot}$  mass disk models, the intensity profiles follows the shape of  $\Sigma_{\text{gas}}$  in the very inner disk ( $R < 10$  au, see panel a of Fig. 5.6), apart for the steeper  $\gamma = 1.5$  model where optical thickness starts to play a role for  $R < 5$  au. On the other hand  $\text{C}^{17}\text{O}$  column densities drop below  $10^{15}\text{cm}^{-2}$  very early, at  $R < 10$  au. Thus, any information about  $\Sigma_{\text{gas}}$  from  $\text{C}^{17}\text{O}$  intensity profiles is lost for the outer disk regions.

The picture changes if the results of the more massive ( $M_{\text{disk}} = 10^{-2}M_{\odot}$ ) disk

model are analyzed.  $\text{C}^{17}\text{O}$  emission is optically thick out to 50 au, except for the model with  $\gamma = 0.5$ , where  $\Sigma_{\text{gas}}$  is less steep in the inner disk (see panel b in Fig. 5.6). Therefore  $\text{C}^{17}\text{O}$  is not a good tracer of the surface density distribution in the inner disk in massive disks. An even rarer CO isotopologue, as  $^{13}\text{C}^{18}\text{O}$ , should be used in these cases, as was done for TW Hya (Zhang et al. 2017).

As for  $^{13}\text{CO}$ , it is possible to fit the simulated intensity profiles with a power-law and check for which conditions  $\gamma_{\text{fit}}$  resembles  $\gamma_{\text{input}}$  well enough.

### 5.3.4 The “slope-pivot-region”

The fitting method of the surface density power-law index presented in Sec. 5.3.1 is not straightforward to be applied to observations, as this approach involves two free parameters,  $R_{\text{start}}$  and  $R_{\text{cut}}$ , and requires some prior knowledge on the disk total mass. On the other hand, the fact that there is a relation between the “slope-pivot-point” (see Fig. 5.5) where the surface density profile and  $^{13}\text{CO}$  radial intensity profile start to deviate due to optical depth and where CO self-shielding becomes inefficient provides information about the column densities. As a consequence the slope-pivot-point will always be around the same intensity, modulo temperature effects, which however are not significant for low- $J$  CO lines. One can then perform the fit of  $\gamma$  over the “slope-pivot-region” between the slope-pivot-point and the point where the  $^{13}\text{CO}$  column density is larger than  $10^{15} \text{ cm}^{-2}$ . Such radial region will always be around the same narrow range of line intensity.

More specifically, at the radius where  $\tau_{^{13}\text{CO}} = 1$ , the  $^{13}\text{CO}$  intensity is roughly  $1 \times 10^{-4} \text{ Jy beam}^{-1} \text{ km s}^{-1}$  (using a beam of  $0.01''^1$ , see Fig. 5.5). This results from the line intensity, which is controlled by a combination of the line opacity and the temperature. The intensity at the frequency  $\nu$  of a gas column with line opacity  $\tau_\nu$  and uniform temperature  $T$  is

$$I_\nu = B_\nu(T) \cdot (1 - e^{-\tau_\nu}) \quad (5.3)$$

where  $B_\nu(T)$  is the Planck function. Thus, for  $\tau_\nu = 1$ ,  $I_\nu$  depends only on the temperature. In the Rayleigh-Jeans approximation,  $I_\nu \propto T$ . Protoplanetary disks have strong gradients in physical conditions both in radial and vertical direction and thus cannot be taken as at uniform temperature. However, the bulk of the disks mass is close to the midplane, where the physical conditions change less than in the warm molecular layer of the upper disk (van Zadelhoff et al. 2001; Bruderer et al. 2012). Mass tracers such as  $^{13}\text{CO}$  trace mostly regions close to the midplane. In the midplane, the temperature is a weak function of the radius with  $T \sim r^{-q}$  with  $0 < q < 1$

<sup>1</sup>The line intensity varies by changing the beam size and can be rescaled using the relation in Appendix B of Bruderer (2013)

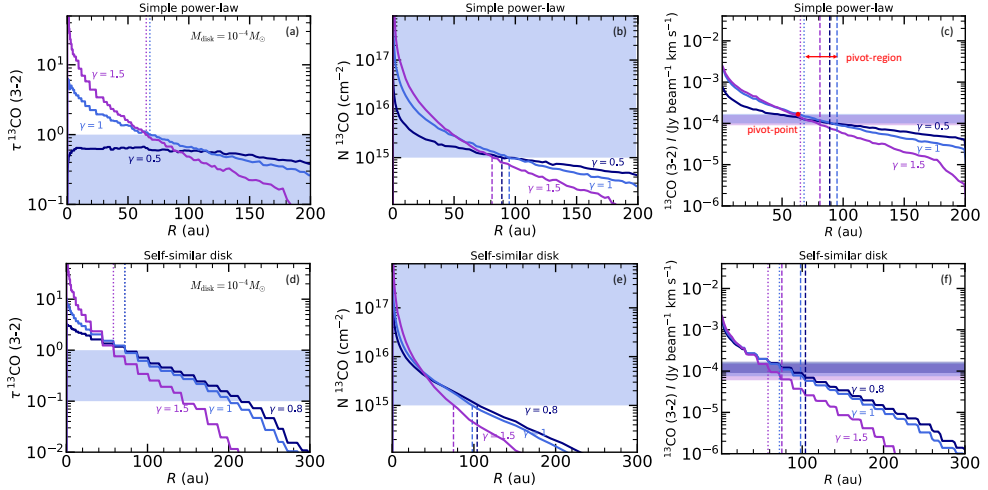


**Figure 5.5:** Total  $^{13}\text{CO}$  line optical depth  $\tau$  (panels a, and d),  $^{13}\text{CO}$  column density (panels b, and e), and  $^{13}\text{CO}$  intensity radial profiles for simple power-law disk models (top panels) and self-similar disk models (bottom panels). The total disk mass is set to  $M_{\text{disk}} = 10^{-4} M_{\odot}$ , and results obtained with different values of  $\gamma$  are presented with different colors. The shaded regions in panels (a) and (d) show the range where  $\tau < 1$ , which holds for radii larger than those shown by the dotted lines. The shaded region in panels (b) and (e) shows the region where  $^{13}\text{CO}$  column density are larger than  $10^{15} \text{ cm}^{-2}$ , i.e. for radii smaller than those shown by the dashed lines. The shaded regions (purple for  $\gamma = 1.5$ , light blue for  $\gamma = 1$  and dark blue for  $\gamma = 0.5$ ) in panels (c) and (f) show the range of  $^{13}\text{CO}$  line intensity for which the conditions  $\tau < 1$  and  $N^{13}\text{CO} > 10^{15} \text{ cm}^{-2}$  hold. The fit of  $\gamma$  is performed over the “slope-pivot-region” between the dotted and dashed lines (shown by the red arrow in panel (c) for  $\gamma = 1$ ).

1. In the simple power-law case the pivot-point is at radii between 60 and 100 au (see Fig. 5.5) and the temperature at the radius of the pivot point varies by less than a factor of two. Thus, the intensity also changes by less than a factor of two. This explains the similar intensity at the pivot-point. The explanation may also apply to other molecules with emission mostly from regions close to the midplane (e.g.  $^{12}\text{CO}$  or  $\text{C}^{18}\text{O}$ ).

We have compared our results in the simple power-law case and self-similar disk case, to test that one can always retrieve  $\gamma$  safely around the same range or line intensity. In Fig. 5.5 the  $^{13}\text{CO}$  emission radial profiles are compared with the total line optical depth  $\tau$  and the  $^{13}\text{CO}$  column density. The line emission can be used to trace the gas distribution if  $\tau < 1$  (shaded region in panels a, and d), i.e. for

---

radii larger than those shown by the dotted lines. On the other hand, the  $^{13}\text{CO}$  column density needs to be larger than  $10^{15} \text{ cm}^{-2}$  where the self shielding is effective (shaded region in panels b, and e), i.e. for radii smaller than those shown by the dashed lines. Combining these two requirements one is restricted to a radial range where the  $^{13}\text{CO}$  intensity is always around  $10^{-4} \text{ Jy beam}^{-1} \text{ km s}^{-1}$  (given an angular resolution of  $0.01''$ ), for each value of  $\gamma$  and no matter if the underlying  $\Sigma_{\text{gas}}$  is given by a simple power-law or a self-similar disk model. This means that, in practice, one would only need to measure the slope of the  $^{13}\text{CO}$  radial intensity at a given contour to retrieve the surface density slope (see shaded region in panels c, and f). The models presented in Fig. 5.5 have a total disk mass of  $10^{-4} M_{\odot}$  and therefore  $^{13}\text{CO}$  emission lines are still optically thin in the interested region of the disk. If the disk was more massive, for example with  $M_{\text{disk}} = 10^{-2} M_{\odot}$ , the same argument described above would be valid for less abundant CO isotopologues, e.g. for  $\text{C}^{17}\text{O}$  as shown in Fig. 5.10. Also for  $\text{C}^{17}\text{O}$ , one could retrieve  $\gamma$  by fitting the radial profile at a given contour at  $10^{-4} \text{ Jy beam}^{-1} \text{ km s}^{-1}$  (given an angular resolution of  $0.01''$ ).

This finding is promising as it relates the observable line intensity radial profile directly with the column density, with no need to know a priori the radial range for the fit of  $\gamma$  or disk mass. On the other hand, the observer would need good angular resolution and sensitivity to perform this fit at a given contour.

## 5.4 Discussion

The results presented in Sec. 5.3 indicate that constraining  $\Sigma_{\text{gas}}$  from spatially resolved observations of  $^{13}\text{CO}$  is a challenging task. However, if the underlying surface density distribution is a power-law, it is possible to constrain its steepness by fitting the emission coming from the correct portion of the disk, in particular at large enough distances from the star that the observed line is optically thin, but at small enough radii that photo-dissociation and freeze-out are not too significant. Moreover, in these intermediate regions, the radial gradient of gas temperature is small, and thus does not affect the gradient of the radial intensity profile of the  $^{13}\text{CO}$  line. From the models shown in this paper, it is possible to retrieve the dependence of the surface density of radius with good accuracy (20% on the power-law exponent) especially if one has an estimate of the  $^{13}\text{CO}$  total mass or if one has high enough resolution data to fit around the pivot-point-region at  $10^{-4} \text{ Jy beam}^{-1} \text{ km s}^{-1}$ .

However, in this approach there is the very strong assumption that the surface density is indeed a power law. If for example  $\Sigma_{\text{gas}}$  is set by viscous evolution, i.e. an exponential taper dominates for radii larger than a given  $R_c$ , determining the actual surface density profile is much more difficult. The main difficulty is due to the relatively narrow radial range where  $^{13}\text{CO}$  traces well the underlying surface density, where this radial range is limited by optical depth effects in the inner disk and in-



---

efficient self-shielding in the outer regions. Determining additional free parameters, as the characteristic radius of the self-similar profile, leads to a large degeneracy between the power-law index and the new parameters. To overcome the issue of  $^{13}\text{CO}$  being optically thick at small radii, one possibility is to probe  $\Sigma_{\text{gas}}$  in the inner disk by observing very optically thin isotopologues, such as  $\text{C}^{17}\text{O}$  and  $^{13}\text{C}^{18}\text{O}$ . The latter was successfully detected with ALMA in the closest and best studied protoplanetary disk, TW Hya, by Zhang et al. (2017). The inconveniences of this emission line are its faintness combined with the possibility that the continuum becomes optically thick shielding  $^{13}\text{C}^{18}\text{O}$  emission at very small radii. Moreover the gas temperature structure has a strong impact on the line emission in the inner disk, therefore possibly independent constraints of the thermal structure would be needed.

An alternative approach is to fit the power-law index  $\gamma$  at the slope-pivot-region as explained in Sec. 5.3.4. This allows a reliable estimate of  $\gamma$  both in the case of a simple power-law and self similar disk, by only fitting the intensity profile at the right intensity contour. High angular resolution and sensitivity are however needed.

An additional caveat is volatile carbon depletion, a process that may be happening in a large fraction of protoplanetary disks (Favre et al. 2013; Kama et al. 2016b; Schwarz et al. 2016; Miotello et al. 2017). The nature of this depletion process is not yet known, but it is possible that carbon is sequestered from CO into  $\text{CO}_2$  and more complex ice species in the outer disk and then drifted inward following the large dust grains. If this is true, one would expect a radially dependent decrease of CO abundances in the outer disk, on top of the reduction due to inefficient self-shielding and freeze-out. As the ices reach the inner disk then carbon should be liberated into gas phase and quickly return into CO, which would then present an increased emission (Du et al. 2015). This would introduce a new degree of degeneration in the employment of CO isotopologues as tracers of the disk surface density distribution. Interestingly, the expected enhancement of  $^{13}\text{C}^{18}\text{O}$  in the inner disk of TW Hya has not been found by Zhang et al. (2017), showing that much is still to be understood about volatile depletion in protoplanetary disks. If however carbon depletion is constant throughout the disk, especially around the pivot-region, this should not add major complications to retrieving the surface-density profile.

## 5.5 Summary and conclusion

In this work we have addressed the issue of determining the gas surface density distribution in protoplanetary disks by using resolved high signal-to-noise observations of  $^{13}\text{CO}$ . Simulated  $^{13}\text{CO}$  intensity radial profiles have been produced using the physical-chemical code DALI (Bruderer et al. 2012; Bruderer 2013), with two different input surface density profiles: a simple power-law with radius, and the self-similar solution given by viscously evolving disk theory. By comparing the input

---

$\Sigma_{\text{gas}}$  profiles with the output intensity profiles one always finds the following:

- $^{13}\text{CO}$  emission follows the slope of  $\Sigma_{\text{gas}}(R)$ , but only in a specific disk region. For very small radii the low- $J$   $^{13}\text{CO}$  lines become optically thick and underestimate the surface density, while in the outer disk this happens because the  $^{13}\text{CO}$  column density drops below  $10^{15} \text{ cm}^{-2}$  and self-shielding becomes inefficient.
- When fitting a power-law to the simulated intensity profiles, it is possible to recover the input power-law index  $\gamma_{\text{input}}$  only by performing the fit over the appropriate radial range. This holds in particular for simple power-law disk models, where  $\gamma_{\text{input}}$  can be retrieved within 20% uncertainty between 30–100 au, even when the profiles are convolved with a  $0.2''$  beam.
- In the self-similar case it is not possible to reliably retrieve  $\gamma_{\text{input}}$  by fitting a simple power-law to the intensity profile.
- Fitting the power-law index  $\gamma$  at the slope-pivot-region of the intensity profile allows a reliable estimate of  $\gamma$  both in the case of a simple power-law and self-similar disk. The slope-pivot-region is always located around  $10^{-4} \text{ Jy beam}^{-1} \text{ km s}^{-1}$ , given an angular resolution of  $0.01''$ .
- If carbon depletion were constant throughout the disk, this would not introduce an additional uncertainty in the employment of CO isotopologues as tracers of the disk surface density distribution.

$^{13}\text{C}^{18}\text{O}$  may be a better tracer of  $\Sigma_{\text{gas}}(R)$  in the inner regions for massive disks, circumventing the  $^{13}\text{CO}$  optical depth issue, as suggested by Zhang et al. (2017). For lower mass disks,  $\text{C}^{17}\text{O}$  and  $\text{C}^{18}\text{O}$  may be more appropriate. However, both dust optical depth and gas temperature may limit the analysis. Thus, combining observations of optically thin tracers with  $^{13}\text{CO}$  may be the best option after-all.

## Acknowledgements

Astrochemistry in Leiden is supported by the Netherlands Research School for Astronomy (NOVA), by a Royal Netherlands Academy of Arts and Sciences (KNAW) professor prize, and by the European Union A-ERC grant 291141 CHEMPLAN.

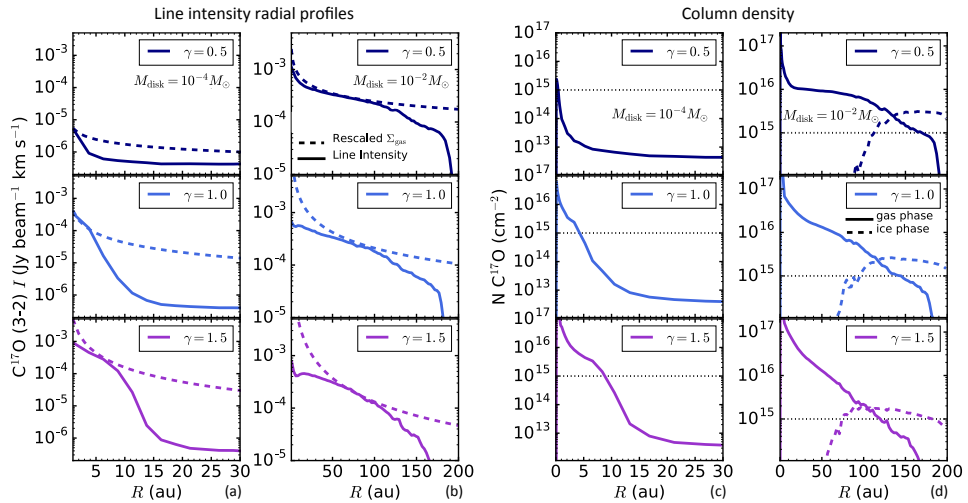


**Figure 5.6:** Panels (a) and (b) –  $\text{C}^{17}\text{O}$  line intensity radial profiles (solid lines) obtained with six disk models with input surface density distribution  $\Sigma_{\text{gas}}$  (dashed lines) chosen to be a simple power-law (see Eq. 5.2). The model parameters are  $R_{\text{out}} = 200$  au,  $M_{\text{disk}} = 10^{-4} M_{\odot}$  (left),  $10^{-2} M_{\odot}$  (right) and  $\gamma = 0.8, 1, 1.5$  shown in dark blue, light blue, and purple respectively (top, middle, and bottom panels). Panels (c) and (d) – Column densities of gas-phase (solid lines) and ice-phase (dashed lines) of  $\text{C}^{17}\text{O}$  calculated from the surface to the midplane shown as function of the disk radius for six models with simple power-law surface density ( $R_{\text{out}} = 200$  au,  $M_{\text{disk}} = 10^{-4}, 10^{-2} M_{\odot}$ ). Top, middle, and bottom panels represent the models with  $\gamma = 0.8, 1, 1.5$  respectively. The dotted black lines indicate the column density at which CO self-shielding becomes inefficient ( $N = 10^{15} \text{ cm}^{-2}$ ).

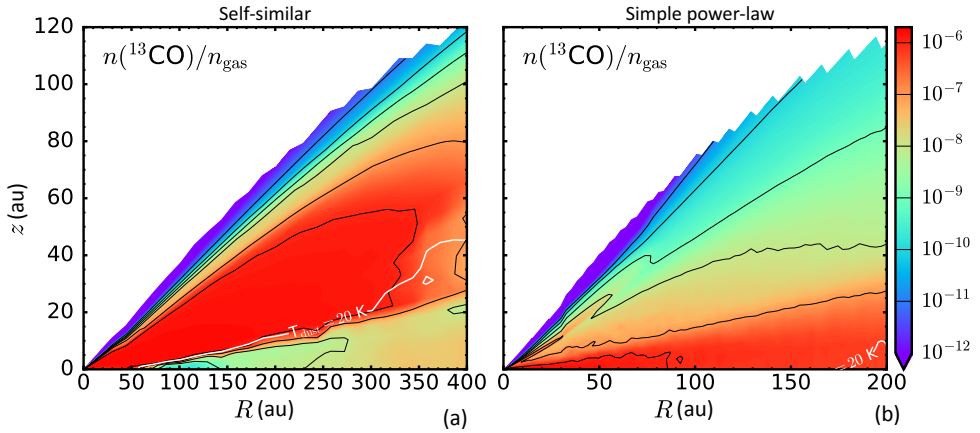


**Figure 5.7:** Abundance of  $^{13}\text{CO}$  in one quadrant the disk for two representative models. Panel (a) shows the self-similar disk model ( $R_c = 200$  au,  $M_{\text{disk}} = 10^{-3}M_{\odot}$  and  $\gamma = 1$ ); panel (b) shows the simple power-law disk model ( $R_{\text{out}} = 200$  au,  $M_{\text{disk}} = 10^{-4}M_{\odot}$  and  $\gamma = 1$ ). The white contours indicates the  $T_{\text{dust}}=20$  K surface below which CO freeze-out becomes important.

## 5.A Additional figures

Here some ancillary figures are reported.

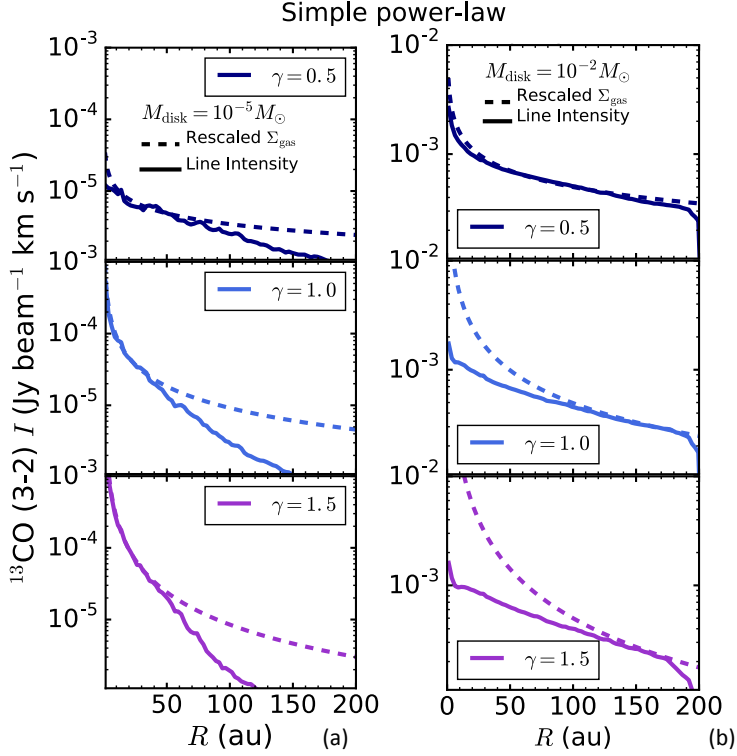


**Figure 5.8:**  $^{13}\text{CO}$  line intensity radial profiles (solid lines) obtained with input surface density distribution  $\Sigma_{\text{gas}}$  (dashed lines) given by the simple power-law disk models (see Eq. 5.1). The model parameters are  $M_{\text{disk}} = 10^{-5} M_{\odot}$  (panel a) and  $M_{\text{disk}} = 10^{-2} M_{\odot}$  (panel b),  $\gamma = 0.8, 1, 1.5$  shown in dark blue, light blue, and purple respectively (top, middle, and bottom panels).

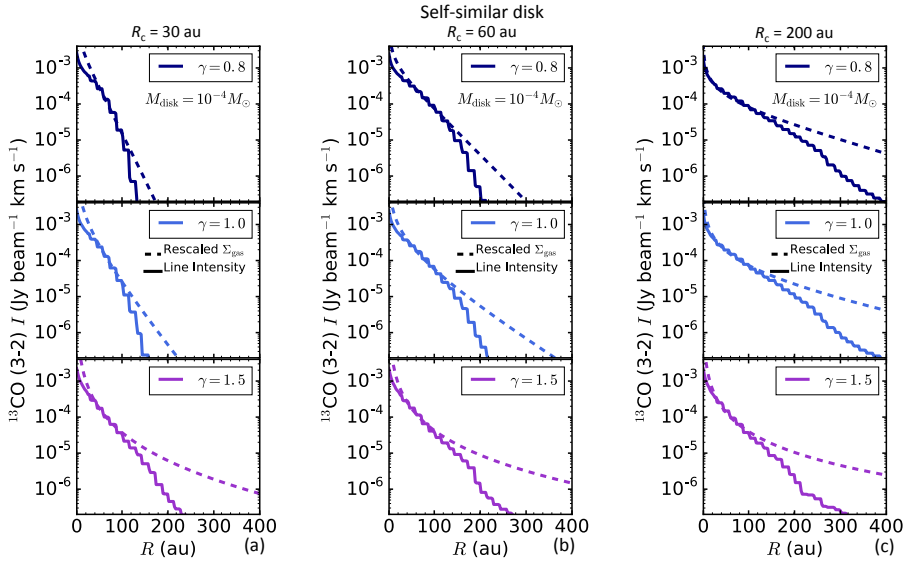


**Figure 5.9:**  $^{13}\text{CO}$  line intensity radial profiles (solid lines) obtained with input surface density distribution  $\Sigma_{\text{gas}}$  (dashed lines) given by the self-similar disk model (see Eq. 5.1). The model parameters are  $M_{\text{disk}} = 10^{-4} M_{\odot}$  and  $\gamma = 0.8, 1, 1.5$  shown in dark blue, light blue, and purple respectively (top, middle, and bottom panels). Model with  $R_c = 30, 60, 200$  au are presented in panel a, b, and c respectively.

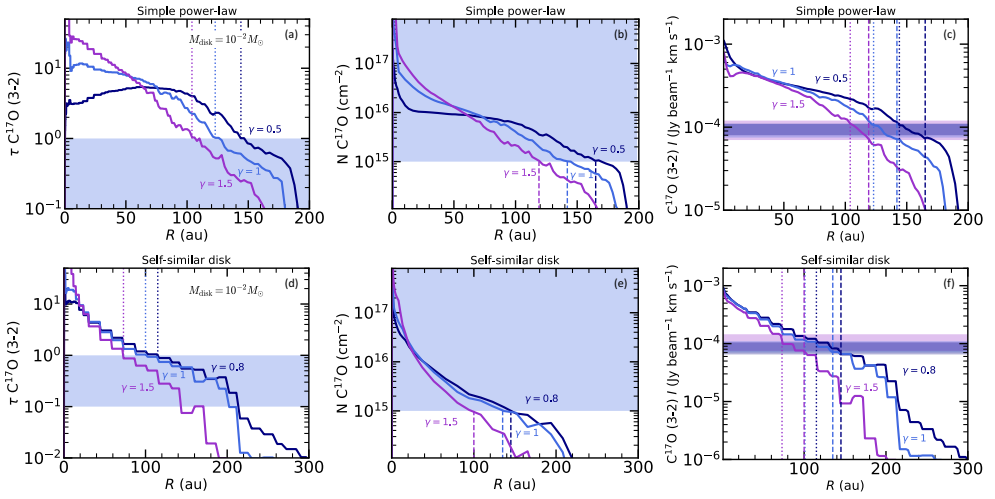


**Figure 5.10:** Total  $C^{17}O$  line optical depth  $\tau$  (panels a, and d),  $C^{17}O$  column density (panels b, and e), and  $C^{17}O$  intensity radial profiles for simple power-law disk models (top panels) and self-similar disk models (bottom panels). The total disk mass is set to  $M_{\text{disk}} = 10^{-2} M_{\odot}$ , and results obtained with different values of  $\gamma$  are presented with different colors. The shaded regions in panels (a) and (d) show the range where  $\tau < 1$ , which holds for radii larger than those shown by the dotted lines. The shaded region in panels (b) and (e) shows the region where  $C^{17}O$  column density are larger than  $10^{15} \text{ cm}^{-2}$ , i.e. for radii smaller than those shown by the dashed lines.

# 6

## HD FAR INFRARED EMISSION AS A MEASURE OF PROTOPLANETARY DISK MASS

---

L. Trapman, A. Miotello, M. Kama, E. F. van Dishoeck, and S. Bruderer, *HD far infrared emission as a measure of protoplanetary disk mass*, 2017, arXiv:1705.07671



---

**Abstract** – Protoplanetary disks around young stars are the sites of planet formation. While the dust mass can be estimated using standard methods, determining the gas mass - and thus the amount of material available to form giant planets - has proven to be very difficult. Hydrogen deuteride (HD) is a promising alternative to the commonly-used gas mass tracer, carbon monoxide. However, its potential has not yet been investigated with models incorporating both HD and CO isotopologue-specific chemistry, and its sensitivity to uncertainties in disk parameters has not yet been quantified. To examine the robustness of HD as tracer of the disk gas mass, specifically the effect of gas mass on the HD far infrared emission and its sensitivity to the vertical structure. Also, to provide requirements for future far-infrared missions such as SPICA. Deuterium chemistry reactions relevant for HD were implemented in the thermochemical code DALI and more than 160 disk models were run for a range of disk masses and vertical structures. The HD J=1-0 line intensity depends directly on the gas mass through a sublinear power law relation with a slope of  $\sim 0.8$ . Assuming no prior knowledge about the vertical structure of a disk and using only the HD 1-0 flux, gas masses can be estimated to within a factor of two for low mass disks ( $M_{\text{disk}} \leq 10^{-3} M_{\odot}$ ). For more massive disks, this uncertainty increases to more than an order of magnitude. Adding the HD 2-1 line or independent information about the vertical structure can reduce this uncertainty to a factor of  $\sim 3$  for all disk masses. For TW Hya, using the radial and vertical structure from Kama et al. (2016b) the observations constrain the gas mass to  $6 \cdot 10^{-3} M_{\odot} \leq M_{\text{disk}} \leq 9 \cdot 10^{-3} M_{\odot}$ . Future observations require a  $5\sigma$  sensitivity of  $1.8 \cdot 10^{-20} \text{ W m}^{-2}$  ( $2.5 \cdot 10^{-20} \text{ W m}^{-2}$ ) and a spectral resolving power  $R \geq 300$  (1000) to detect HD 1-0 (HD 2-1) for all disk masses above  $10^{-5} M_{\odot}$  with a line-to-continuum ratio  $\geq 0.01$ . These results show that HD can be used as an independent gas mass tracer with a relatively low uncertainty and should be considered as an important science goal for future far-infrared missions.

---

## 6.1 Introduction

One of the key properties for understanding the evolutionary path of disks and the formation of planets is the disk gas mass (e.g., Armitage 2015). Determining gas masses is no easy task. The main component of the gas, molecular hydrogen ( $\text{H}_2$ ), is difficult to observe. As a symmetric rotor,  $\text{H}_2$  has no electric dipole moment, limiting its rotational lines to quadrupole transitions ( $\Delta J = 2$ ). The  $J = 2$  level lies at 549.2 K, so in order to produce any appreciable  $\text{H}_2$  emission gas temperatures have to be at least 100 K (Thi et al. 2001; Carmona et al. 2011) which is much higher than the temperature of the bulk of the gas in the disk. In addition, these lines lie in the mid- and near-infrared (IR) where the continuum is bright, which further hampers the observations due to the high continuum optical depth and low line-to-continuum ratios. Even if detected, the  $\text{H}_2$  emission does not trace the bulk of the mass (e.g., Pascucci et al. 2013). This means that indirect tracers of the gas mass have to be used.

Historically, most of the disk mass estimates have been based on observations of the (sub-)millimeter (mm) emission of the dust grains (e.g., Beckwith et al. 1990; Dutrey et al. 1996; Mannings & Sargent 1997; Williams et al. 2005). In order to relate the observed flux to the mass of the emitting material, a mass opacity  $\kappa_\nu$  and a temperature  $T_{\text{dust}}$  have to be assumed (cf. Hildebrand 1983). To obtain the total (gas+dust) mass, the estimate of the dust mass has to be scaled up by the gas-to-dust mass ratio. Usually the interstellar medium (ISM) value of 100 is assumed, but it is unclear whether this is applicable to protoplanetary disks.

The gaseous component of the disk can be traced using carbon monoxide (CO), the second most abundant molecule in the disk, which is readily detected towards many protoplanetary disks (e.g., Dutrey et al. 1996; Thi et al. 2001; Dent et al. 2005; Panić et al. 2008; Williams & Best 2014). To derive a gas mass from CO observations, a relation has to be found between the amount of CO in the disk and the amount of  $\text{H}_2$ . In the simplest case where most of the available carbon is contained in gas-phase CO, the fractional abundance of CO is  $n(\text{CO})/n(\text{H}_2) \sim 2 \cdot 10^{-4}$ , in line with observations of warm dense clouds (e.g., Lacy et al. 1994).

In protoplanetary disks there are two processes that decrease the CO abundance below its maximum value (van Zadelhoff et al. 2001). In the upper layer of the disk, CO is being destroyed through photodissociation by ultraviolet (UV) photons. In the midplane, where temperatures are below  $\sim 20$  K, CO freezes out onto the dust grains. As a result of these non-linear processes, thermochemical models have to be used to relate CO observations to the total gas mass. These processes are well understood and they are implemented in current thermochemical models. However, studies that include these effects find that overall gas phase carbon must still be additionally depleted by a factor 10-100. This leads to low CO emission even for

---

massive disks (e.g., Bruderer et al. 2012; Favre et al. 2013; Du et al. 2015; Kama et al. 2016b; Bergin et al. 2016).

Several processes have been proposed to explain the underabundance of gas-phase carbon in regions where freeze-out is not important. A possible explanation could be grain growth, where carbon has been locked up in large icy bodies that no longer participate in the gas-phase chemistry (see, e.g., Bergin et al. 2010; Du et al. 2015; Bergin et al. 2016; Kama et al. 2016b). Another cause could be the conversion of CO into more complex species. This process can happen in the gas-phase through reactions between CO and  $\text{He}^+$ , which extracts atomic carbon that can then be used to construct more complex molecules. These molecules have higher freeze-out temperatures than CO and freeze out onto the cold grains, thus lowering the apparent carbon abundance (Aikawa et al. 1997; Favre et al. 2013; Bergin et al. 2014). Similarly, ice chemistry can play an important role in converting CO into more complex organics, such as  $\text{CH}_3\text{OH}$  or turning it into  $\text{CO}_2$  or  $\text{CH}_4$  ice (see, e.g., Figure 3c in Eistrup et al. 2016).

Due to its high abundance,  $^{12}\text{CO}$  becomes optically thick at the disk surface, meaning it does not trace the bulk of the mass. Instead, less abundant CO isotopologues such as  $^{13}\text{CO}$ ,  $\text{C}^{18}\text{O}$  and  $\text{C}^{17}\text{O}$  have to be used, which remain optically thin throughout the disk (van Zadelhoff et al. 2001; Dartois et al. 2003). Visser et al. (2009) and Miotello et al. (2014b) showed that  $\text{C}^{18}\text{O}/\text{C}^{16}\text{O}$  ratio is reduced beyond the  $^{18}\text{O}/^{16}\text{O}$  isotope ratio in disks due to isotope-selective photodissociation. Not taking this effect into account can change the estimated mass using  $\text{C}^{18}\text{O}$  up to one order of magnitude (Miotello et al. 2014b).

Using the *Herschel* Space Observatory, hydrogen deuteride (HD) has been detected towards TW Hya, DM Tau and GM Aur (Bergin et al. 2013; McClure et al. 2016). HD has been suggested as an alternative tracer of the disk gas mass. Because of their chemical similarities, the distribution of HD is expected to closely follow that of  $\text{H}_2$ . HD has a small dipole moment, so dipole transitions ( $\Delta J = 1$ ) are allowed. The difference between the energy needed to excite the first rotational level of HD ( $E/k_B \simeq 128.5$  K) and the energy needed to excite the second rotational level of  $\text{H}_2$  ( $E/k_B \simeq 549.2$  K), means that at a temperature of  $T \sim 20$  K the expected emission of HD is much larger than that of  $\text{H}_2$ .

The energetically lowest transition of HD,  $J=1-0$ , emits at  $112 \mu\text{m}$  (Müller et al. 2005). This places the transition in a wavelength range where the dust continuum is bright, the atmospheric opacity is high and the production of low-noise detectors is expensive. All these reasons combined make detecting HD a challenge. Even with *Herschel*, deep integrations were required to observe HD in disks. After the end of the *Herschel* mission, there are currently no far-IR observatories capable of detecting HD in disks. However, this may change with the advent of future far-IR missions such as the proposed SPICA mission (Nakagawa et al. 2014) and with the HIRMES instrument on SOFIA.

---

In this work, a simple HD chemistry is incorporated into the thermochemical code `Dust and Lines` (DALI, Bruderer et al. 2012; Bruderer 2013). In Section 6.2 a description of the code is given, including the deuterium chemistry that was implemented. A description of the models that were run is also given here. In Section 6.3 the dependence of the HD far-infrared emission on the disk gas mass is examined. In addition, the effect of other disk properties such as the vertical structure and the dust distribution on the HD emission is investigated. Furthermore, the results are examined in the light of possible future far-IR missions such as SPICA. The effect of prior knowledge of the disk vertical structure on the uncertainty of the HD based mass estimates is discussed in Section 6.4. Additionally, the models are compared to the current observations. Of particular interest is the protoplanetary disk of TW Hya ( $59.54 \pm 1.45$  pc, Astraatmadja & Bailer-Jones 2016), where the gas mass estimated using HD is more than one order of magnitude higher than the gas mass estimated using  $C^{18}O$  (Favre et al. 2013). Different studies have shown that the TW Hya disk seems genuinely depleted in volatile carbon and oxygen (e.g., Bergin et al. 2010, 2013, 2016; Hogerheijde et al. 2011; Favre et al. 2013; Du et al. 2015; Kama et al. 2016b). Recently, new observations of the CO isotopologues have become available (see, e.g., Schwarz et al. 2016). Therefore, the case of TW Hya is revisited using a combined HD and CO isotopologue analysis. The conclusions can be found in Section 6.5.

## 6.2 Model

The thermochemical code `Dust and Lines` (DALI) was used to calculate the line fluxes for the disk models (Bruderer et al. 2012; Bruderer 2013). DALI is a 2D physical-chemical code that for a given physical disk model calculates the thermal and chemical structure self-consistently. In addition to the disk density structure, a stellar spectrum has to be provided in order to determine the UV radiation field inside the disk. The computation proceeds through three steps. First the dust temperature structure and the internal radiation field (from UV- to mm-wavelengths) are determined by solving the continuum radiative transfer using a 2D Monte Carlo method. Next, the abundances of the molecular and atomic species at each point of the disk are obtained from the solution of the time-dependent chemistry. The atomic and molecular excitations are then computed using a non-LTE calculation. Given the excitation levels, the gas temperature is determined by balancing the heating and cooling processes. Due to the fact that both the chemistry and the excitations depend on temperature, the problem is solved iteratively until a self-consistent solution is found. Lastly, the model is ray-traced to construct spectral image cubes and line profiles. A more detailed description of the code can be found in Appendix A of Bruderer et al. (2012).

---

### 6.2.1 Density structure

The density structure used in the code follows the simple parametric model proposed by Andrews et al. (2011). This model is based on the assumption that the disk structure is determined by viscous accretion, where the viscosity goes as  $\nu \propto R^\gamma$  (Lynden-Bell & Pringle 1974; Hartmann et al. 1998). The resulting surface density is given by

$$\Sigma_{\text{gas}}(R) = \Sigma_c \left( \frac{R}{R_c} \right)^\gamma \exp \left[ - \left( \frac{R}{R_c} \right)^{2-\gamma} \right]. \quad (6.1)$$

Here  $\Sigma_c$  is the surface density at the characteristic radius  $R_c$ .

The vertical structure is given by a Gaussian density distribution, as motivated by hydrostatic equilibrium (Kenyon & Hartmann 1987)

$$n(R, z) = \frac{1}{\sqrt{2\pi}} \frac{1}{H} \exp \left[ - \frac{1}{2} \left( \frac{z}{H} \right)^2 \right] \quad (6.2)$$

$$= \frac{1}{\sqrt{2\pi}} \frac{1}{Rh} \exp \left[ - \frac{1}{2} \left( \frac{z/R}{h} \right)^2 \right], \quad (6.3)$$

where  $H = Rh$  is the physical height of the disk and the scale height angle  $h$  is parametrized by

$$h = h_c \left( \frac{R}{R_c} \right)^\psi. \quad (6.4)$$

Here  $h_c$  is the scale height at  $R_c$  and  $\psi$  is known as the flaring angle. Equation (6.4) is a representation for a physical disk, where the vertical structure is set by balancing gravity and the vertical pressure gradient at each point in the disk.

### 6.2.2 Dust settling

In order to include dust settling into the model, the dust grains are split into two populations:

- *small grains* (0.005-1  $\mu\text{m}$ ) are included with a (mass) fractional abundance  $1 - f_{\text{large}}$ . These are located throughout the vertical extent of the disk.
- *large grains* (1-10<sup>3</sup>  $\mu\text{m}$ ) are included with a fractional abundance  $f_{\text{large}}$ . They are limited to a vertical region with scale height  $\chi h$ ;  $\chi < 1$ , simulating the effect of dust settling.

Note that in the current version of DALI the gas surface density profile is only coupled to the density profile of the small grains, in contrast to earlier versions of DALI. The resulting disk structure is summarized in Figure 6.1.

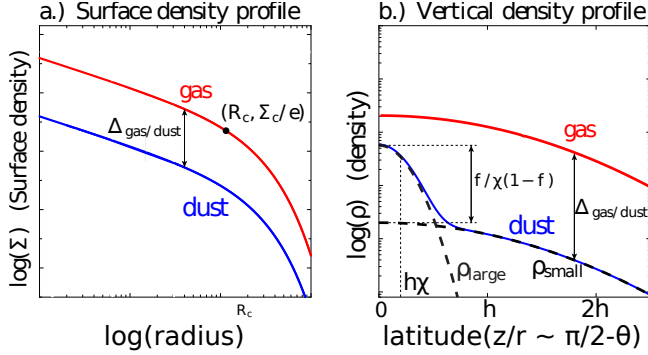


**Figure 6.1:** Gas and dust density structure assumed in DALI

A standard ISM dust composition is assumed for the dust opacities following Weingartner & Draine (2001), in line with Bruderer (2013) (see e.g. his Figure 2). The mass opacities for absorption at  $112 \mu\text{m}$  and  $56 \mu\text{m}$  for both dust grain populations are given in Table 6.1.

**Table 6.1:** Dust mass opacities

	wavelength [ $\mu\text{m}$ ]	$\kappa_{\text{abs.}}$ [ $\text{cm}^2 \text{g}^{-1}$ ]
small grains	112	29.9
	56	154
large grains	112	30.0
	56	46.3

### 6.2.3 Chemical network

For the models in this work the list of chemical species adopted in Miotello et al. (2014b) was extended to include HD, D,  $\text{HD}^+$  and  $\text{D}^+$  as separate species. By adding the element D to H, He,  $^{12}\text{C}$ ,  $^{13}\text{C}$ , N,  $^{16}\text{O}$ ,  $^{17}\text{O}$ ,  $^{18}\text{O}$ , Mg, Si, S and Fe, the total number of species was increased to 280. The reaction types included are  $\text{H}_2$  and HD formation on dust, freeze-out, thermal and non-thermal desorption, hydrogenation of simple species on ices, gas-phase reactions, photodissociation, X-ray and cosmic-ray induced reactions, PAH/small grain charge exchange/hydrogenation, and reactions with  $\text{H}_2^*$  (vibrationally excited  $\text{H}_2$ ). The details of the implementation of these reactions are described in Appendix A.3.1 of Bruderer et al. (2012).

To properly simulate HD integrated line fluxes, simple deuterium chemistry has

been added to the chemical network. The only D-bearing species considered for the chemical calculation are D, D<sup>+</sup>, HD, and HD<sup>+</sup>. Accordingly, the important reactions regulating their abundances have been included, with rate coefficients from Roberts & Millar (2000); Walmsley et al. (2004). Photodissociation of HD was included following Glover & Jappsen (2007). The photodissociation rate for a radiation field with a flat spectrum is given by Eq. 51 in Glover & Jappsen (2007):

$$R_{\text{diss,HD}} = 1.5 \times 10^{-9} I(\nu) \text{ s}^{-1}. \quad (6.5)$$

Here  $I(\nu)$  is the mean intensity of the radiation field. Note that the prefactor has units such that the photodissociation rate has units [s<sup>-1</sup>].

HD self-shielding was also included in the model using the shielding function of H<sub>2</sub> but slightly shifted in wavelength. Finally HD formation onto grains and ion-exchange reactions with metals and PAHs have been included, with the same rate coefficients as that assumed for the analogue reactions with H instead of D. The reactions involving D-bearing species added in the chemical network are presented in Table 6.6 in Appendix 6.D.

## 6.2.4 Grid of models

As a basis for the models, the physical structure of the TW Hya disk from the Kama et al. (2016b) model is used. A combination of spatially and spectrally resolved and unresolved line fluxes, in combination with observations of the spectral energy distribution (SED), was used to constrain the parameters of their model, which can be found in Table 6.2. Note that Kama et al. (2016b) find a strongly flared vertical structure for TW Hya. Also, their model has a radially steeper temperature profile and smaller outer radius than the models of Cleeves et al. (2015).

In total, over a 160 models were run using DALL. The employed chemical network is the expanded version of that used by Miotello et al. (2014b), where simple deuterium chemistry has been considered (see Section 6.2.3). The input total disk masses are  $M_{\text{disk}} = [2.6 \cdot 10^{-5}, 2.6 \cdot 10^{-4}, 7.7 \cdot 10^{-4}, 2.6 \cdot 10^{-3}, 7.7 \cdot 10^{-3}, 2.3 \cdot 10^{-2}, 7.7 \cdot 10^{-2}, 2.6 \cdot 10^{-1}] M_{\odot}$ . For each mass, 20 models with different vertical structures were ran:  $h_c \in [0.05, 0.1, 0.2, 0.3]$ ,  $\psi \in [0.1, 0.2, 0.3, 0.4, 0.5]$  (cf. equation 6.4). The other parameters have been kept fixed to the values assumed by Kama et al. (2016b). For the overall carbon and oxygen abundances, typical ISM values of  $[C]/[H]_{\text{ISM}} = 1.35 \cdot 10^{-4}$ ,  $[O]/[H]_{\text{ISM}} = 2.88 \cdot 10^{-4}$  are used (Bruderer et al. 2012).

The stellar spectrum for TW Hya from Cleeves et al. (2015) was used as the central source of radiation. It closely resembles a 4000 K blackbody with a 10000 K blackbody component to represent the observed UV excess (following the prescription in Kama et al. 2016a, see also Figure 3 and Table 3 in Kama et al. 2016b).

The time-dependent chemistry is run for 1 Myr, which is less than the expected age for TW Hya, but the HD emission is not sensitive to the chemical age.

The overall deuterium abundance  $[D]/[H]$  of the gas in the disk has a direct impact on the HD fluxes. Prodanović et al. (2010) used observations of the atomic D and H lines in the diffuse ISM to find  $([D]/[H])_{\text{ISM}} \geq (2.0 \pm 0.1) \times 10^{-5}$  for the local ISM (i.e., within  $\sim 1 - 2$  kpc of the Sun). The uncertainties due to the error on the assumed  $[D]/[H]$  are much smaller than the spread in HD fluxes due to the disk structure. Note that for older star forming regions such as Orion the deuterium abundance is lower, due to the fact that a fraction of the deuterium has been burned up in the cores of stars (Wright et al. 1999; Howat et al. 2002).

**Table 6.2:** DALI parameters of the physical model.

Parameter	Range
<i>Chemistry</i>	
Chemical age	1 Myr
$[D]/[H]$	$2 \cdot 10^{-5}$
<i>Physical structure</i>	
$\gamma$	1.0
$\psi$	[0.1,0.2, <b>0.3</b> ,0.4,0.5]
$h_c$	[0.05, <b>0.1</b> ,0.2,0.3] rad
$R_c$	35 AU
$R_{\text{out}}$	200 AU
$M_{\text{disk}}$	$2.6 \cdot 10^{-5}$ , $2.6 \cdot 10^{-4}$ , $7.7 \cdot 10^{-4}$ , $2.6 \cdot 10^{-3}$ , $7.7 \cdot 10^{-3}$ , <b><math>2.3 \cdot 10^{-2}</math></b> , $7.7 \cdot 10^{-2}$ , $2.6 \cdot 10^{-1} M_{\odot}$
<i>Dust properties</i>	
Gas-to-dust ratio	200
$f_{\text{large}}$	0.99
$\chi$	0.2
$f_{\text{PAH}}$	0.001
<i>Stellar spectrum</i> <sup>1</sup>	
type	T Tauri
$L_X$	$10^{30} \text{ erg s}^{-1}$
$L_{\text{FUV}}$	$2.7 \cdot 10^{31} \text{ erg s}^{-1}$
$L_*$	$0.28 L_{\odot}$
$\zeta_{\text{cr}}$	$10^{-19} \text{ s}^{-1}$
<i>Observational geometry</i>	
$i$	$6^{\circ}$
$d$	140 pc

Bold numbers denote the best fit values for TW Hya from Kama et al. (2016b). The deuterium fraction was taken from Prodanović et al. (2010).<sup>1</sup> Spectrum of TW Hya (Cleeves et al. 2015).



---

## 6.3 Results

### 6.3.1 HD flux vs. disk gas mass

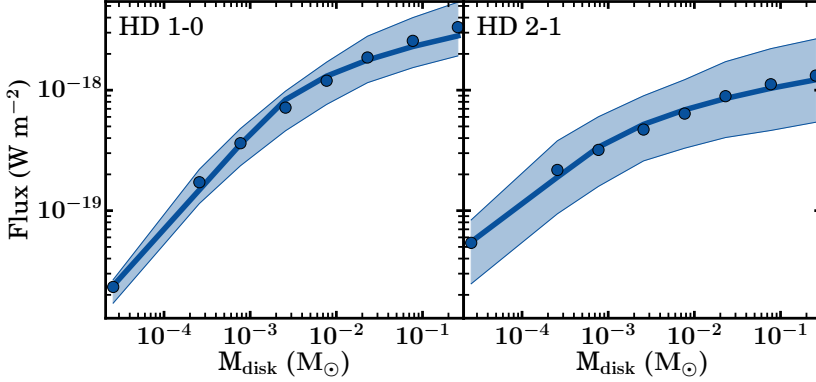


**Figure 6.2:** Left panel: Integrated line flux (calculated at 140 pc) of the HD 1-0 transition as a function of disk mass. The points show the median flux of the models in that mass bin. The blue shaded region shows fluxes between the 16<sup>th</sup> and 84<sup>th</sup> percentiles in the same mass bin. The blue line shows the fit of equation (6.6) using the values from Table 6.3. Right panel: Integrated line flux (calculated at 140 pc) of the HD 2-1 transition as function of disk mass.

The first step in investigating the viability of HD as a tracer of the disk gas mass is examining the behaviour of its emission under variation of the gas mass. This is presented in Figure 6.2, where the integrated HD 1-0 and 2-1 line fluxes are plotted as function of disk mass. In the left panel of Figure 6.2 the blue dots shows the median HD 1-0 flux for each disk mass, while the coloured region presents fluxes between the 16<sup>th</sup> and 84<sup>th</sup> percentiles in each mass bin. The HD 1-0 line flux increases with mass, following a linear dependence in log-log space for the low-mass disks ( $M_{\text{disk}} \leq 10^{-3} M_{\odot}$ ).

Towards the high mass regime, the relation flattens. There are two reasons for this change in behaviour. For disk masses above  $0.001 M_{\odot}$  the HD 1-0 line emission starts to become optically thick, which means that the HD emission no longer traces the full gas reservoir. In addition, high mass disks have larger densities, which decreases the gas temperature in the disk. Miotello et al. (2016) found a similar decrease in line luminosity for  $^{13}\text{CO}$  and  $\text{C}^{18}\text{O}$  for high mass disks, which they attributed to optical depth for  $^{13}\text{CO}$  and increased freeze-out for  $\text{C}^{18}\text{O}$ .

The right panel of Figure 6.2 shows that the flux-mass relation for the HD 2-1 line is flatter compared to HD 1-0. This is likely due to increased temperature depen-

dence of the HD 2-1 line, compared to the HD 1-0 line. The increased temperature dependence is reflected in the increased sensitivity of HD 2-1 to the vertical structure of the disk, as indicated by the large flux variations in each mass bin.

The behaviour of the flux-mass relation can be expressed with an analytical relation, such as:

$$F_{\text{HD}} = \begin{cases} A (M_{\text{disk}}/M_{\text{tr}})^\alpha, & \text{if } M_{\text{disk}} \leq M_{\text{tr}} \\ A + B \log_{10} (M_{\text{disk}}/M_{\text{tr}}), & \text{otherwise} \end{cases} \quad (6.6)$$

where  $M_{\text{tr}}$  is defined as the mass where the flux-mass relation starts to flatten.

This model was fitted to the median fluxes of both HD lines. The resulting coefficients can be found in Table 6.3. Note that the powerlaw slopes for both HD lines are sublinear. This is likely a result from the fact that the HD emission is produced by warm gas only.

**Table 6.3:** Fit coefficients of the HD flux-mass relation.

	HD 1-0	HD 2-1
$\alpha$	0.79	0.54
A	$5.44 \cdot 10^{-19}$	$2.83 \cdot 10^{-19}$
B	$9.95 \cdot 10^{-19}$	$3.50 \cdot 10^{-19}$
$M_{\text{tr}} (M_{\odot})$	$1.32 \cdot 10^{-3}$	$5.43 \cdot 10^{-4}$

Coefficients fitted to HD fluxes calculated at 140 pc. For a different distance  $d$ , the coefficients  $A$  and  $B$  scale as  $A' = (140/d)^2 \cdot A$ .

### 6.3.2 HD emitting layers

The 2D abundance of HD in a typical model is presented in Figure 6.3. This distribution is the outcome of the deuterium chemical calculation discussed in Section 6.2.3. Note that  $n(\text{HD})/n_{\text{gas}} = 2 \cdot 10^{-5}$  throughout most of the disk, indicating that all of the available deuterium is locked up in HD. The exceptions to this rule are in the upper layer of the disk, where HD is photodissociated and in an intermediate layer where HD abundance is decreased by a factor of  $\sim 2$ . This layer is due to a combination of chemical processes. It should be noted here that this layer is very thin and only covers a very small fraction of the HD emission area shown in Figure 6.3. Therefore the depletion in this layer has no relevant effect on the HD flux.

The solid blue lines in Figure 6.3 denote where 25% and 75% of the HD 1-0 emission is produced. This region is elevated above the midplane ( $0.1 \leq z/r \leq 0.25$ ),

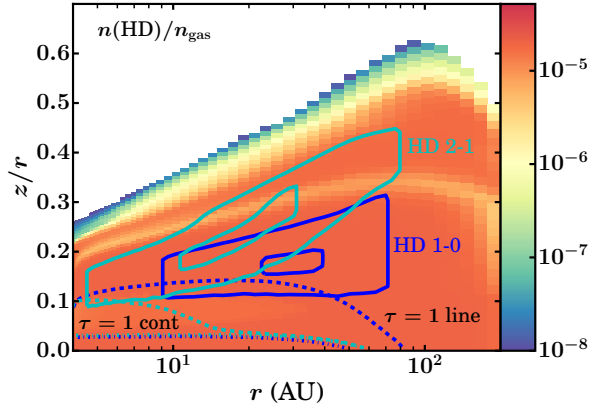


**Figure 6.3:** HD abundance structure for a disk model with  $M_{\text{disk}} = 2.3 \cdot 10^{-2} M_{\odot}$ ,  $\psi = 0.3$  and  $h_c = 0.1$ . Colour indicates the number density of HD with respect to the total gas density. The coloured lines correspond the HD 1-0 (blue) and HD 2-1 (light blue) respectively. Solid contours indicate where 25% and 75% of the emission originates from. The dashed (dashed-dotted) lines show the  $\tau = 1$  surface for the line and continuum opacity, respectively.

indicating that most of the HD 1-0 emission is produced by warm gas, with an average temperature of 30 – 70 K (cf. Figure 6.15). The emitting region extends radially from  $r_{\text{in}} \approx 9$  AU up to  $r_{\text{out}} \approx 70$  AU for  $M_{\text{disk}} = 2.3 \cdot 10^{-2} M_{\odot}$ . The inner and outer radii vary slightly vertical structure (cf. Figure 6.16). Figure 6.17 shows that when the disk gas mass is increased the emitting region shifts outward, from  $(r_{\text{in}}, r_{\text{out}}) \approx (1 \text{ AU}, 40 \text{ AU})$  for  $M_{\text{disk}} = 2.3 \cdot 10^{-5} M_{\odot}$  to  $(r_{\text{in}}, r_{\text{out}}) \approx (10 \text{ AU}, 100 \text{ AU})$  for  $M_{\text{disk}} = 2.3 \cdot 10^{-1} M_{\odot}$ . This is a result of the optically thick HD zone extending to larger radii as the gas mass increases.

The  $\tau = 1$  surfaces for the line and continuum optical depth are shown in dashed and dashed-dotted lines, respectively. They show that continuum optical depth has no effect on the line emission. This is likely due to the fact that most of the dust mass is in large grains, which are settled to the midplane in contrast with the models by Bergin et al. (2014). The dashed line shows that for this model with  $M_{\text{disk}} = 2.3 \cdot 10^{-2} M_{\odot}$ , the HD emission starts to become optically thick, which is in line with the flattening of the slope seen in Figure 6.2.

For the HD 2-1 emission, shown in light blue in Figure 6.3, the emission originates even higher up in the disk, where gas temperatures are in the range of 70 – 100 K (cf. Figure 6.15). The contour for the line optical depth show that the HD 2-1 emission starts to become optically thick in the inner part of the disk for  $M_{\text{disk}} = 2.3 \cdot 10^{-2} M_{\odot}$ .

### 6.3.3 Influence of the vertical structure

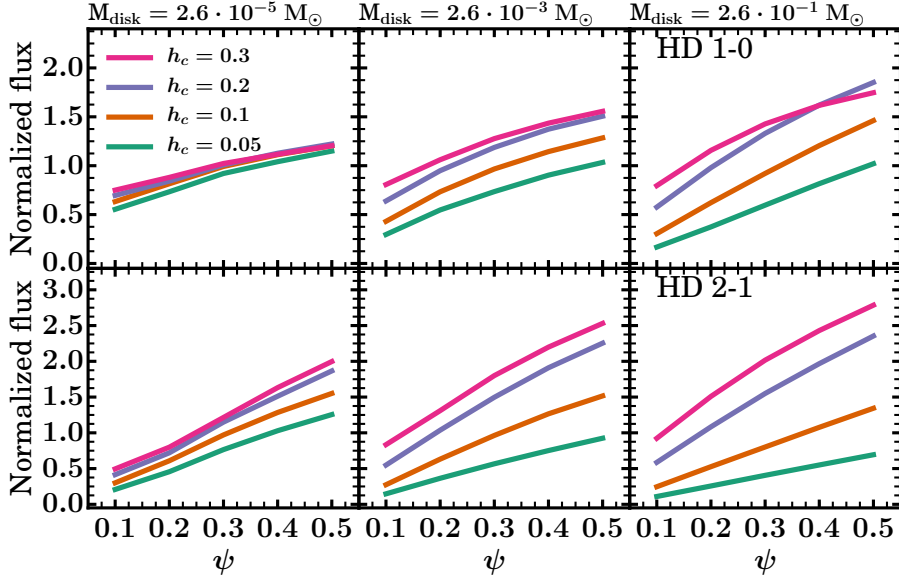


**Figure 6.4:** Integrated HD 1-0 (top) and HD 2-1 (bottom) line fluxes as function of flaring angle  $\psi$  for different scale heights  $h_c$ . The fluxes are normalized with respect to median flux of the models with the same disk mass (cf. Figure 6.2).

The strength of the HD emission depends on the amount of material and the temperature of the material. In protoplanetary disks the temperature structure is set by the vertical structure of the disk (Chiang & Goldreich 1997). The effect of the vertical structure on the HD 1-0 and 2-1 fluxes is presented in Figure 6.4. It shows the HD fluxes as function of the flaring angle  $\psi$  for different scale heights  $h_c$  (colours). This was done for three different mass bins ( $2.3 \cdot 10^{-5} M_{\odot}$ ,  $2.3 \cdot 10^{-3} M_{\odot}$  and  $2.3 \cdot 10^{-1} M_{\odot}$ ). The fluxes in each mass bin are normalized with respect to the median flux in the same bin (cf. the blue dots in Figure 6.2).

The normalized HD 1-0 integrated line fluxes are presented in top panels of Figure 6.4. It shows that the HD 1-0 flux increases with increasing  $\psi$ . The relation is roughly linear, with a slope that is independent of  $h_c$  and  $M_{\text{disk}}$ .

The spacing between the different  $h_c$  lines indicate that the HD 1-0 flux also increases systematically with  $h_c$ . The shape of the flux- $h_c$  relation depends only weakly on  $\psi$ . It does depend strongly on disk mass, with the influence of  $h_c$  on the flux increasing as function of disk mass.

For HD 2-1, presented in the bottom panels of Figure 6.4, the dependencies of the flux on  $h_c$  and  $\psi$  are stronger than those found for HD 1-0. The bulk of the HD 2-1 emission is produced by gas at temperatures of 70–100 K (cf. Figure 6.15). This gas is located higher up in the disk. As the optically thin HD 2-1 emission depends on both the temperature and the density, the location of the HD 2-1 emitting material varies strongly with vertical structure, as can be seen in Figure 6.16. This is in contrast to the HD 1-0 emitting material, which stays at roughly the same location, independent of the vertical structure.

Figure 6.4 shows that the maximum variation in flux due to the different vertical structure increases with disk mass, from  $0.75 \times$  the median flux for  $M_{\text{disk}} \sim 10^{-5} M_{\odot}$  up to  $1.9 \times$  the median flux for  $M_{\text{disk}} \sim 10^{-1} M_{\odot}$ . For the HD 2-1 integrated line flux, shown in the bottom panel of Figure 6.4, the maximum variation in flux is both larger than for HD 1-0 and is less dependent on disk mass. The maximum variation of the flux is  $1.9 \times$  the median flux for  $M_{\text{disk}} \sim 10^{-5} M_{\odot}$ , increasing to  $2.8 \times$  the median flux for  $M_{\text{disk}} \sim 10^{-1} M_{\odot}$ . As mentioned in Section 6.3.2, the regions where the HD lines are optically thick have larger outer radii as the gas mass is increased. On the one hand this pushes the HD emitting regions upwards to parts of the disk that are more sensitive to the vertical structure. On the other hand, the increased size of the optically thick HD zone means that, for massive disks, a larger mass fraction of HD will be much warmer as the vertical structure changes. The uncertainty in derived gas masses from HD due to vertical structure is further quantified in Section 6.4.1.

In the above models, the vertical structure is parametrized according to Equation (6.4). Another approach would be to calculate the vertical structure using hydrostatic equilibrium from the computed gas temperature structure. The effect of this approach on the HD fluxes is examined in Appendix 6.C and is found to be within the flux variations shown in Figure 6.4.

### 6.3.4 Influence of the large grains

For the models discussed in Section 6.2.4 only three parameters ( $M_{\text{disk}}$ ,  $\psi$  and  $h_c$ ) were varied. However, several other parameters may also affect the HD flux. Their role is investigated here. In particular, the large dust grains in the disk can affect the HD flux, both by affecting heating and by changing the optical depth of the dust at the wavelengths where HD emits. Two dust parameters are examined here: the mass fraction of the large grains  $f_{\text{large}}$  and the dust settling parameter of the large grains  $\chi$  (cf. Section 6.2.2). In both cases, the mass and vertical structure of the disk were fixed to the values from Kama et al. (2016b). The resulting HD 1-0 fluxes, normalized to the median flux of the  $M_{\text{disk}} = 2.3 \cdot 10^{-2} M_{\odot}$  mass bin, are shown in Figure 6.5.

Figure 6.5 shows that the HD 1-0 flux increases with dust settling (i.e., when the large grains are more settled towards the midplane). This can be understood by the fact the dust optical depth at a fixed height in the disk increases when the large grain

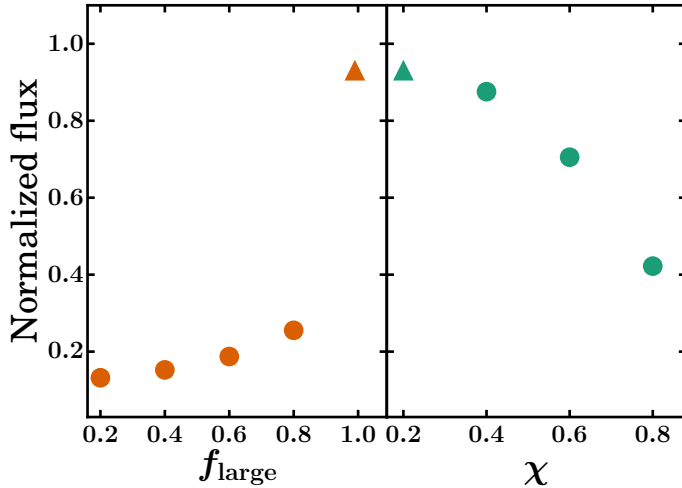


**Figure 6.5:** Integrated line flux of HD 1-0 as function of dust parameters for  $M_{\text{disk}} = 2.3 \cdot 10^{-2} M_{\odot}$ . Models with different  $f_{\text{large}}$  and  $\chi$  are shown in orange and green, respectively. The fluxes are normalized to the median flux of the  $M_{\text{disk}} = 2.3 \cdot 10^{-2} M_{\odot}$  mass bin. The triangular marker denotes the value of the parameter ( $f_{\text{large}}$  or  $\chi$ ) in the fiducial model of the TW Hya disk (Kama et al. 2016b, cf. Table 6.2).

population (cf. Section 6.2.2) is less settled. This is especially the case in the model for TW Hya, where most of the dust mass is in these grains.

A similarly large effect is found when the mass fraction of the large grains is changed. When  $f_{\text{large}}$  decreases, the amount of small grains increases significantly, which increases the opacity at  $112 \mu\text{m}$ .

Comparing these results with those from the previous section, it is clear that both the large grains and the vertical structure have similar effects on the HD 1-0 line flux. It should be noted however that both  $\chi$  and  $f_{\text{large}}$  are constrained by the spectral energy distribution (e.g., D’Alessio et al. 2001; Chiang et al. 2001), so their values cannot be chosen arbitrarily.

### 6.3.5 Influence of the gas-to-dust ratio

Deriving accurate gas-to-dust mass ratios has been one of the motivations for measuring the gas mass directly (e.g., Ansdell et al. 2016; Miotello et al. 2017). However, the gas-to-dust ratio could also affect the HD emission directly, e.g., by changing the coupling between the dust and the gas. If the effect is strong it may prevent accurate measurements of the gas-to-dust ratio using gas masses derived from HD emission.

For fixed gas mass of  $M_{\text{gas}} = 2.3 \cdot 10^{-2} M_{\odot}$ , Figure 6.6 presents the HD 1-0 fluxes as functions of increasing gas-to-dust ratio (and therefore decreasing dust mass). The fluxes are normalized with respect to the median flux of the  $M_{\text{disk}} = 2.3 \cdot 10^{-2} M_{\odot}$  mass bin.

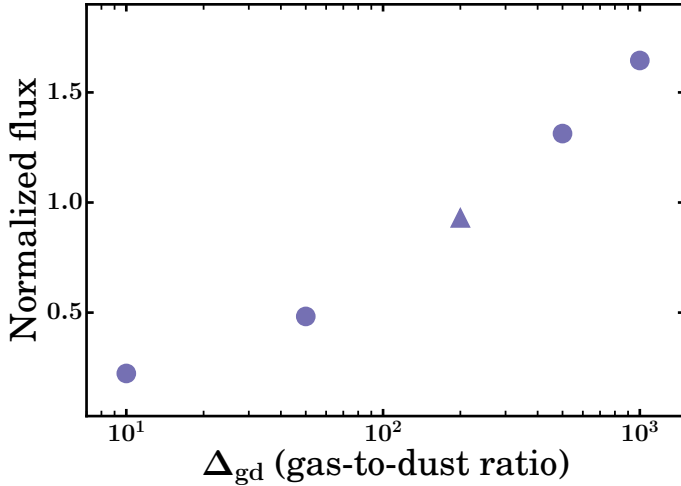


**Figure 6.6:** Integrated line flux of HD 1-0 as function of gas-to-dust mass ratio for fixed gas mass ( $M_{\text{gas}} = 2.3 \cdot 10^{-2} M_{\odot}$ ). The fluxes are normalized to the median flux of the  $M_{\text{disk}} = 2.3 \cdot 10^{-2} M_{\odot}$  mass bin. The triangular marker denotes the value of  $\Delta_{\text{gd}}$  in the fiducial model of the TW Hya disk (Kama et al. 2016b, cf. Table 6.2).

The figure shows that the HD 1-0 flux increases systematically with  $\Delta_{\text{gd}}$ . The primary reason for this is the decreased coupling between the gas and the dust for higher gas-to-dust ratios. As the gas in the HD emitting region is less efficient in cooling than the dust, this leads to slightly higher gas temperatures. Additionally, the increased dust mass for the models with a lower  $\Delta_{\text{gd}}$  enhances the dust opacities at the wavelengths where HD emits, which lowers the amount of observed line flux. However, inspection of the  $\tau_{\text{dust}} = 1$  surface at  $112 \mu\text{m}$  shows that the increase in opacity is relatively small.

### Determining gas-to-dust ratios using HD 1-0

Figure 6.6 shows that varying the gas-to-dust ratio by two orders of magnitude for a fixed gas mass only leads to a variation in the HD 1-0 line flux of  $\sim 1.5 \times$  the median flux. In this analysis the dust mass is assumed to be a free parameter. However, in practice the dust mass of the observed disks will be constrained, e.g., by observation

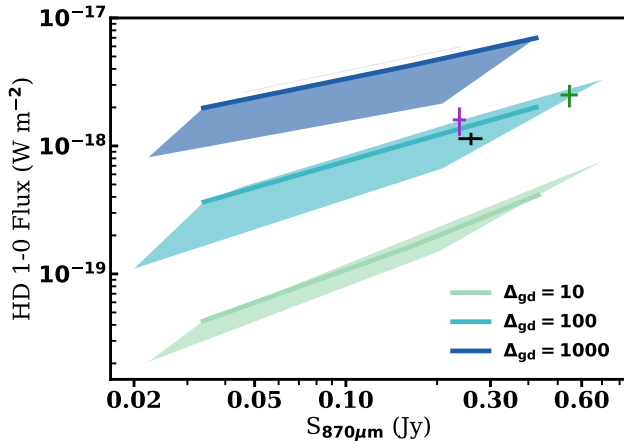


**Figure 6.7:** HD 1-0 integrated fluxes and 870  $\mu\text{m}$  continuum flux densities for the models described in Table 6.4. Colours indicate different gas-to-dust ratios, where the shaded region shows the flux variations due to different vertical structures. For each  $\Delta_{\text{gd}}$ , the coloured line shows models with  $(\psi, h_c) = (0.3, 0.1)$ . The crosses denote observations for TW Hya (black; Bergin et al. 2013; Andrews et al. 2012), DM Tau (purple; McClure et al. 2016; Andrews et al. 2013) and GM Aur (green; McClure et al. 2016; Andrews et al. 2013). Note that both the model fluxes and the observations were scaled to a distance of 140 pc.

of their millimeter-continuum fluxes. A comparison of HD 1-0 fluxes and millimeter continuum fluxes for models with different  $\Delta_{\text{gd}}$  is shown in Figure 6.7.

Here the HD emission is combined with the millimeter continuum emission of the dust to provide a method for estimating the gas-to-dust ratio from observations. For this purpose an additional set of 27 models was run, where the dust mass, gas-to-dust ratio and the vertical structure were varied (cf. Table 6.4). Figure 6.7 shows the HD 1-0 line flux, which traces the gas mass, plotted against the 870  $\mu\text{m}$  continuum flux, which traces the dust mass. The lack of overlap between models with different gas-to-dust ratios indicates that combined observations of HD and the dust continuum can be used to determine  $\Delta_{\text{gd}}$ . For the three disks for which HD 1-0 observations are available (i.e., TW Hya, DM Tau and GM Aur) gas-to-dust ratios are found to be  $\Delta_{\text{gd}} \sim 100$ , close to the ISM value. This would suggest that indeed the lower values found from similar measurements made using  $^{13}\text{CO}$  are due to an underabundance of volatile carbon (see Miotello et al. 2017 and references therein).



**Table 6.4:** Disk parameters for the fixed dust mass models.

Parameter	Range
<i>Dust masses</i>	
$M_{\text{dust}}$	$10^{-5}, 10^{-4}, 10^{-3} M_{\odot}$
<i>Gas-to-dust ratios</i>	
$\Delta_{\text{gd}}$	10, 100, 1000
<i>Gas masses<sup>1</sup></i>	
$M_{\text{gas}}$	$10^{-5} - 1 M_{\odot}$
<i>Vertical structure</i>	
$(\psi, h_c)$	(0.1, 0.1), (0.3, 0.1), (0.3, 0.3)

<sup>1</sup>:  $M_{\text{gas}}$  is determined from the combination of  $M_{\text{dust}}$  and  $\Delta_{\text{gd}}$ .

### 6.3.6 Line-to-Continuum ratios

As mentioned in the introduction, observing lines in the far-infrared is inherently difficult because the emission of the dust in protoplanetary disks peaks at  $\sim 100 \mu\text{m}$ . Superimposed on this bright continuum are the intrinsically weak far-infrared lines. As a result, the line-to-continuum ratio ( $L/C$ ) is a crucial ingredient for observing the HD levels.

The line-to-continuum ratio can be defined as:

$$L/C \equiv \frac{\int d\nu F_{\text{line}}}{\int d\nu F_{\text{cont}}} \simeq \frac{F_{\text{peak}}}{F_{\text{cont,bin}}}. \quad (6.7)$$

Here  $F_{\text{line}}$  and  $F_{\text{cont}}$  are the continuum subtracted line flux and continuum flux, respectively. The approximation holds if the line is narrow, such that the integrated line flux can be approximated by the total flux in the center-most frequency bin ( $F_{\text{peak}}$ ) times the bin width. In this case  $F_{\text{cont,bin}}$  is the continuum flux in the same bin.

Due to the difficulties in characterizing the noise properties of infrared detectors as well as cosmic ray impacts on the detector and electronics, the current best achievable signal-to-noise ratio (SNR) for these detectors is  $\sim 300$ . In the most optimal case, these detectors are able to distinguish variations at the level of  $\frac{1}{300} \equiv 0.0033$  of the source continuum flux. By requiring that the HD lines are detected at the  $3\sigma$  level, the SNR = 300 translates into a detection limit of  $L/C \geq 3 \cdot 0.0033 = 0.01$ , which can not be improved by longer integration times.

The spectral resolving power  $R = \lambda/\Delta\lambda$  of the instrument plays a crucial role in determining the  $L/C$ . As long as the line is unresolved, a higher  $R$  corresponds to a larger  $L/C$ , independent of the disk properties. This assumption is valid for the HD lines in protoplanetary disks, which are intrinsically narrow (FWHM  $\sim 5 \text{ km}$

$s^{-1}$  in the outer disk). As explained in the introduction there is currently no facility capable of observing HD rotational transitions in disks. However, this work and previous studies (e.g., Bergin et al. 2013; McClure et al. 2016) have shown that HD is a unique tracer of the total gas mass. This means that the possibility of observing HD should be included in the consideration for instruments on future FIR observatories, such as the proposed SPICA mission. To be able to detect HD, the detection limit of  $L/C \geq 0.01$  places a constraint on the requirements of the spectral resolving power of these future FIR missions.

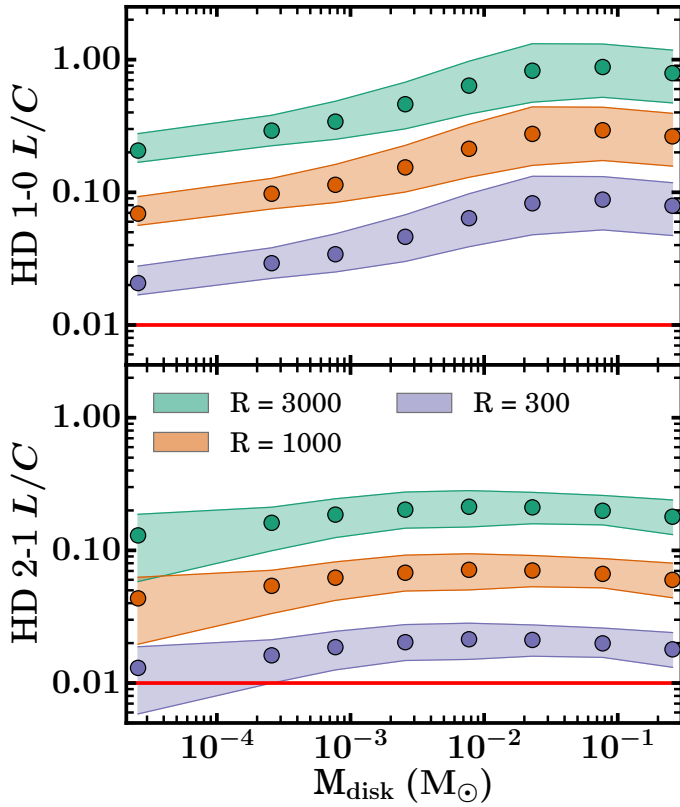


**Figure 6.8:** Line-to-continuum ratios of HD as function of  $M_{\text{disk}}$  for different spectral resolving powers. The points show the median  $L/C$  of the models in the mass bin. The shaded region shows the  $L/C$ s between the 16<sup>th</sup> and 84<sup>th</sup> percentile in each mass bin. The red line represents a  $3\sigma$  detection limit of  $L/C = 0.01$ , which is equivalent to assuming a SNR on the continuum of 300.

The top panel of Figure 6.8 shows  $L/C$  for HD 1-0 as function of disk mass for three different values of  $R$ . It is clear that the lower spectral resolving power mainly lowers the  $L/C$ . The current HD 1-0 detections with the *Herschel* PACS instrument are for  $R = 1000$  at  $112 \mu\text{m}$ . This figure demonstrates that future instruments, such as the SPICA SAFARI instrument (Roelfsema et al. 2014), need a resolving power of  $R \geq 300$  to detect HD 1-0 over the full mass range examined here, if a detection limit of  $L/C \geq 0.01$  (so S/N on the continuum of 300) is assumed. In the case of the HD 2-1 transition, shown in the bottom panel of Figure 6.8 a spectral resolving power of  $R \geq 1000$  is required to detect HD 2-1 towards all disk masses above  $10^{-5} M_{\odot}$ .

### 6.3.7 Sensitivities of future FIR missions

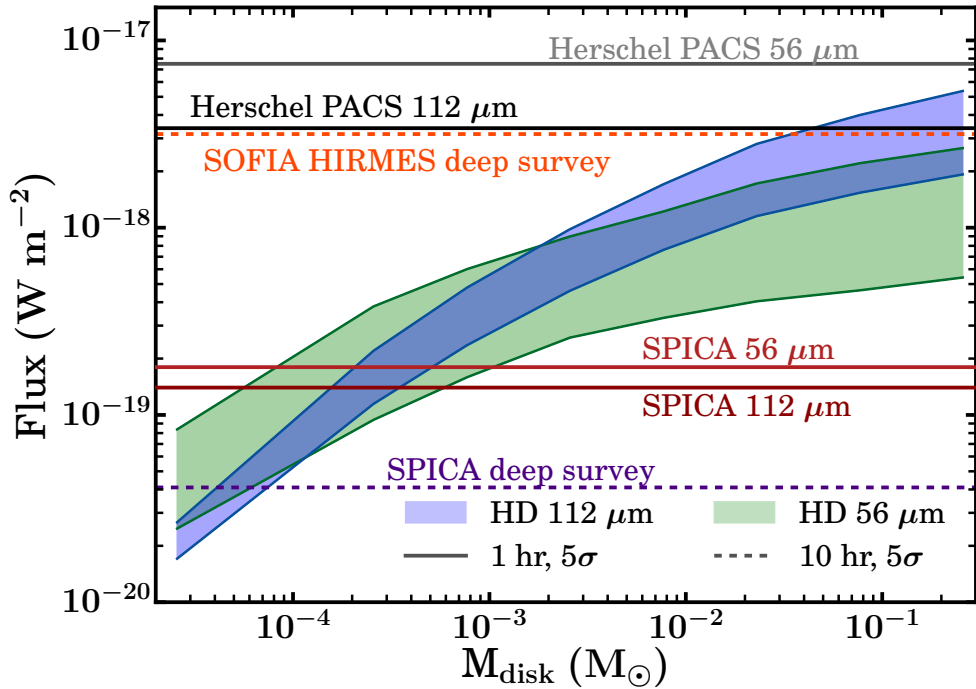


**Figure 6.9:** HD 1-0 (blue) and 2-1 (green) model fluxes (calculated at 140 pc) as function of disk gas mass (cf. Figure 6.2). The horizontal lines represent the  $5\sigma$  sensitivities for various instruments. The solid lines show the detection limit after 1 hr of integration. The dashed lines show the  $5\sigma$  sensitivity at  $112 \mu\text{m}$  after 10 hrs of integration (labeled ‘deep survey’).

In addition to good line-to-continuum ratios, future FIR missions also require

good sensitivities to be able to detect the HD rotational lines in protoplanetary disks. In Figure 6.9 the models presented in Figure 6.2 are compared to the sensitivities of two FIR instruments: the proposed SPICA SAFARI instrument (Roelfsema et al. 2014) and the recently approved HIRMES instrument for SOFIA (E. Bergin, priv. comm.). The fluxes in the figure have been calculated for a distance of 140 pc, in line with typical distances to the closest star forming regions. The sensitivity of the Herschel PACS instrument is also shown here. The  $5\sigma$  sensitivities after 1 hr of integration for SAFARI and Herschel PACS are shown in dark red and black respectively. The purple and orange lines represent the  $5\sigma$  sensitivities at  $112 \mu\text{m}$  after 10 hrs of integration for the SAFARI and HIRMES instruments, respectively. Figure 6.9 shows that the proposed SPICA SAFARI instrument will be able to detect HD 1-0 in disks with gas masses down to  $5 \cdot 10^{-4} M_{\odot} \approx 0.5 M_{\text{jup}}$ . If the integration time is increased to 10 hrs the mass sensitivity goes down to  $8 \cdot 10^{-5} M_{\odot} \approx 0.08 M_{\text{jup}}$ .

## 6.4 Discussion

### 6.4.1 Determining the disk gas mass

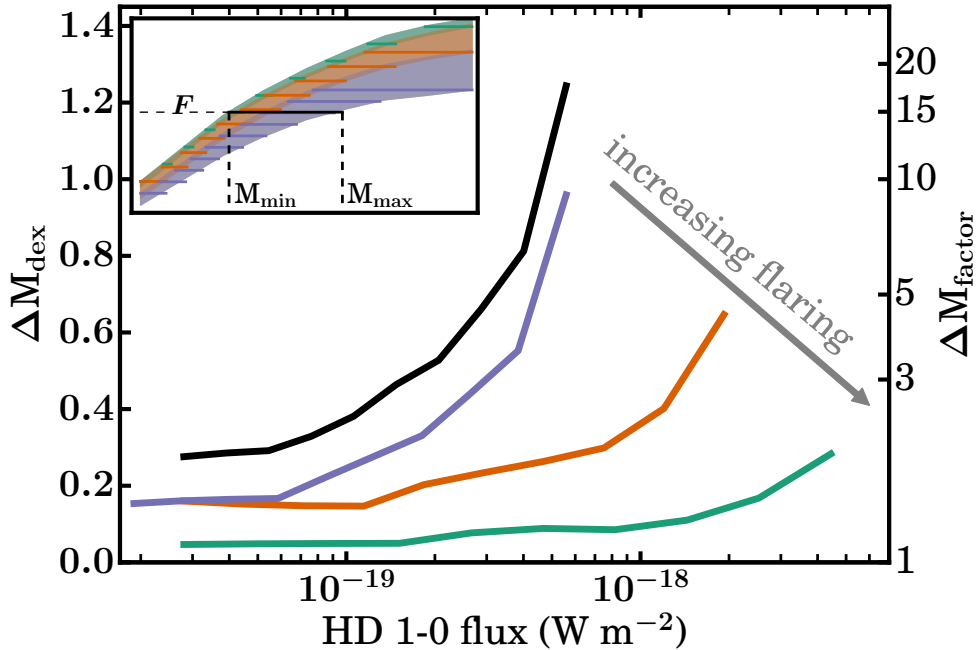
In Section 6.3.1 the behaviour of the HD emission under variation of the disk gas mass was discussed. Figure 6.2 shows that it is possible to constrain the gas mass using the HD 1-0 flux. However, the variations in the flux due to the uncertainties on vertical structure translate into uncertainties in the determined gas mass. In this section these uncertainties are quantified and the impact of complementary observations on these uncertainties is investigated.

Figure 6.2 shows that models with different combinations of disk gas masses and vertical structures can produce the same HD 1-0 flux. The difference between the minimum and the maximum disk mass, interpolated using the model fluxes shown in Figure 6.2, can be used to quantify the uncertainty on the gas mass estimates using the flux (cf. the small panel in Figure 6.10). Here the mass derivation uncertainty is defined as a factor of  $10^{\Delta M}$ , where:

$$\log_{10} \Delta M(F) = \frac{1}{2} |\log_{10} M_{\text{max}}(F) - \log_{10} M_{\text{min}}(F)|. \quad (6.8)$$

Here  $M_{\text{min}}(F)$ ,  $M_{\text{max}}(F)$  are the minimum and maximum disk masses that can produce a HD 1-0 flux  $F$ , given the range of vertical structures examined.

The calculated mass uncertainties as function of HD 1-0 flux are presented in Figure 6.10. For the full set of models introduced in Section 6.2.4 (cf. Table 6.2), shown in black,  $\Delta M$  increases with HD flux. The increase is steep, with  $\Delta M = 1$  dex at a HD flux of  $\sim 5 \cdot 10^{-19} \text{ W m}^{-2}$ , indicating that this flux corresponds to an estimated mass between  $10^{-3} M_{\odot}$  and  $10^{-1} M_{\odot}$ .



**Figure 6.10:** Calculated mass uncertainties (cf. Equation 6.8) as function of HD 1-0 flux. The left and right vertical axis are related via  $\Delta M_{\text{factor}} = 10^{\Delta M_{\text{dex}}}$ . The black line shows the result if the full set of models is used (cf. Table 6.2). The other three lines show results for “weakly flared” (purple), “intermediately flared” (orange) and “strongly flared” (light green) disks (see Table 6.5 for definitions for these subsets). The subsets are also shown in the top left panel, which shows a scaled version of Figure 6.2.

This estimate relies only on the HD 1-0 flux, without making any assumptions on the vertical structure of the disk. In practice, most disks will also have been observed at other wavelengths and with other chemical tracers. These can be used to put constraints on the vertical structure of the disk. This would in turn lead to lower  $\Delta M$ . If complementary observations can distinguish between “weakly flared” disks, “intermediately flared” disks and “strongly flared” disks (see Table 6.5 for the definitions), the uncertainties on the mass estimates can be significantly improved.

The top left panel of Figure 6.10 shows the three subsets with respect to the full set of models together with the mass uncertainties for each subset. For “intermediately flared” disks, shown in orange,  $\Delta M$  is significantly lower compared to the full set. Here the maximum mass uncertainty is  $\sim 0.65$  dex, meaning that the mass can be estimated within a factor of  $\sim 5$ .

---

**Table 6.5:** Definition vertical structure classification

	$\psi$	$h_c$
“weakly flared”	0.1-0.2	0.05-0.1
“intermediately flared”	0.3-0.5	0.05-0.1
	<b>or</b> <sup>1</sup>	
	0.1-0.2	0.2-0.3
“strongly flared”	0.3-0.5	0.2-0.3

<sup>1</sup> Note that “intermediately flared” disks is a joint set of two subsets of vertical structures.

For the “strongly flared” disks, shown in light green, the uncertainty is minimized, with  $\Delta M$  never becoming larger than 0.2 dex. As a result, masses for this subset can be estimated to within a factor of two.

The mass uncertainty for the “weakly flared” disks follows the uncertainty of the full sample, with  $\Delta M$  being  $\sim 0.1$  dex lower than for the full sample. For these ranges of  $h_c$  and  $\psi$  the HD flux is quite sensitive to the vertical structure, which results in variations in the flux comparable to those in the full set. However, a difference of 0.1 dex is still a factor of two improvement on the mass uncertainty.

## 6.4.2 HD 1-0 and HD 2-1 line fluxes

An interesting complementary observable is the HD 2-1 line emission. The main disk parameter determining the difference between the  $J = 1$  and  $J = 2$  level populations of HD is the gas temperature, which is largely set by the vertical structure. By combining observations of HD 2-1 and HD 1-0 this difference can be exploited to determine the disk mass with low uncertainty.

As shown in Figure 6.11, the different dependencies of HD 1-0 and HD 2-1 line fluxes on disk mass and vertical structure result in a clear mass segregation, independent of vertical structure. For disks with  $M_{\text{disk}} \geq 7.7 \cdot 10^{-3} M_{\odot}$  the mass bins start to overlap. As the bins differ by a factor of 3 in mass, the combination of two HD lines allow the gas mass to be determined to within a factor of  $\sim 3$ , provided that the observational uncertainties are small enough. To be able to determine the mass accurately across the whole mass range, the observational uncertainties have to decrease with increasing disk mass. This is not a too strict requirement as the observed line flux increases with disk mass, allowing for a more precise flux determination. The observations of HD 1-0 and HD 2-1 for TW Hya shown in Figure 6.11 will be discussed in Section 6.4.4.

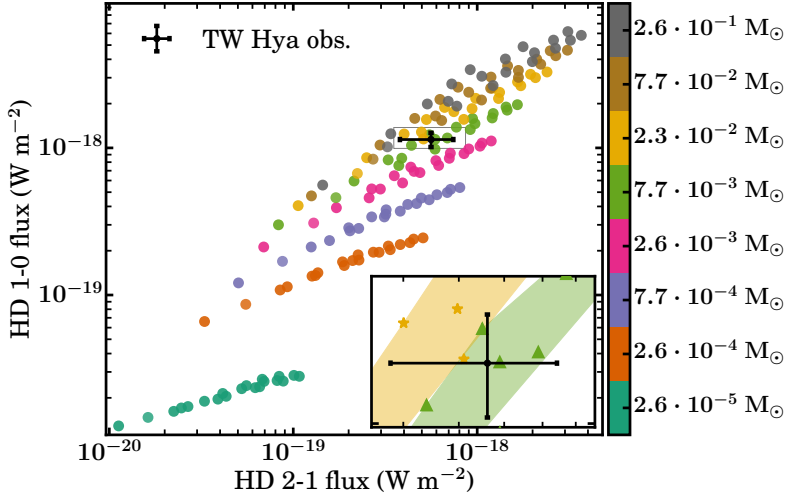


**Figure 6.11:** HD 1-0 and HD 2-1 integrated fluxes (calculated at 140 pc) for the models described in Section 6.2.4. The different colours indicate different disk masses. The observations for TW Hya are shown in black (Bergin et al. 2013; Kama et al. 2016b, D. Fedele, priv. comm.). The bottom right corner shows the region around the observations, where the shaded regions link models that are within the same mass bin.

### 6.4.3 Comparing models to observations

The HD 1-0 transition has been observed for three disks: TW Hya (Bergin et al. 2013), DM Tau and GM Aur (McClure et al. 2016). These observations are shown in Figure 6.12, which represents the high mass part of the left panel of Figure 6.2. The observed flux for TW Hya was scaled to a distance of 140 pc, to allow for comparison with the same models.

For DM Tau the lower limit on disk gas mass based on the HD 1-0 observation is  $M_{\text{disk}} \approx 4 \cdot 10^{-3} M_{\odot}$ . This correspond to a high, strongly flared vertical structure. If instead the median vertical structure is assumed, the estimated gas mass becomes  $M_{\text{disk}} \approx 1.5 \cdot 10^{-2} M_{\odot}$ . For GM Aur, a similar analysis gives a lower limit on the disk gas mass of  $M_{\text{disk}} \approx 1 \cdot 10^{-2} M_{\odot}$  for a high, strongly flared disk. Comparing the observed HD 1-0 flux to the medians, a gas mass of  $M_{\text{disk}} \approx 8 \cdot 10^{-2} M_{\odot}$  is found.

Both estimates based on the medians are in line with the results of McClure et al. (2016), who found gas masses of  $(1.0 - 4.5) \cdot 10^{-2}$  and  $(2.5 - 19.5) \cdot 10^{-2} M_{\odot}$  for DM Tau and GM Aur by modeling both the HD flux and the continuum SED.

The observations for TW Hya shown in Figure 6.12 will be discussed in Section 6.4.4.

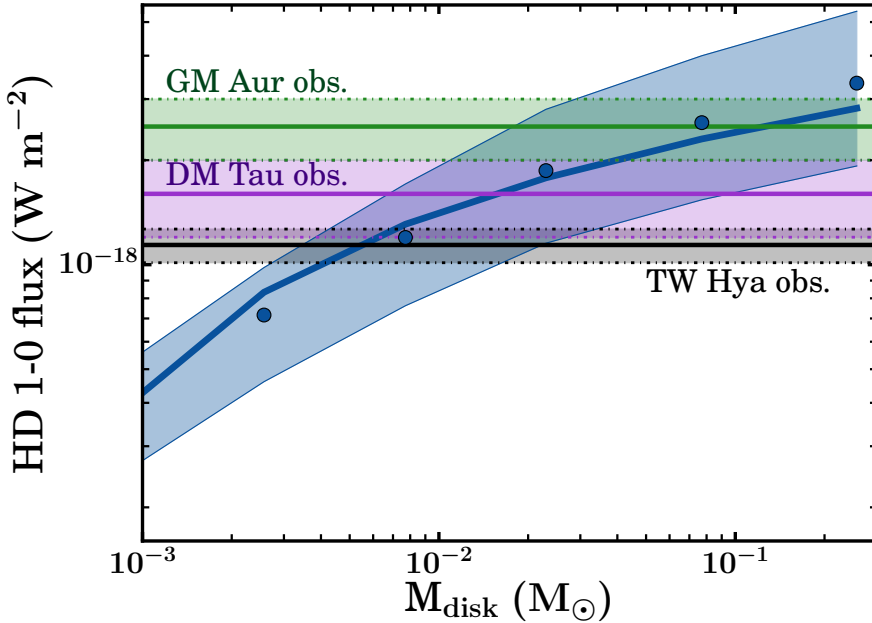


**Figure 6.12:** Integrated line flux (calculated at 140 pc) of the HD 1-0 transition as a function of disk mass, representing the high mass end of the left panel of Figure 6.2. The horizontal black solid line gives the observation of TW Hya, scaled to a distance of 140 pc, with the black shaded region representing the  $1\sigma$  uncertainties (Bergin et al. 2013). The observations for DM Tau and GM Aur (McClure et al. 2016) are shown in purple and green, respectively.

#### 6.4.4 Case study: TW Hya

The protoplanetary disk of TW Hya ( $59.54 \pm 1.45$  pc, Astraatmadja & Bailer-Jones 2016), one of the best-studied disks. Its disk gas mass has been estimated to be  $\geq 0.05 M_{\odot}$  using HD (Bergin et al. 2013). This estimate is an order of magnitude higher than a similar estimate of the gas mass using  $C^{18}O$  (Favre et al. 2013).

The observations of the HD 1-0 and 2-1 line fluxes for the TW Hya disk are presented in Figures 6.11 and 6.12. Comparing these observations to the models shows that the observed HD 1-0 flux for TW Hya places a lower limit of  $M_{\text{disk}} \approx 3 \cdot 10^{-3} M_{\odot}$  if high, strongly flared vertical structure is assumed. Using the radial and vertical structure from Kama et al. (2016b), the observations constrain the disk gas mass to  $6 \cdot 10^{-3} M_{\odot} \leq M_{\text{disk}} \leq 9 \cdot 10^{-3} M_{\odot}$ . A similar gas mass is found from combining the observations of HD 1-0 and HD 2-1 (cf. Figure 6.11), which favor a gas mass between  $7.7 \cdot 10^{-3} M_{\odot} \leq M_{\text{disk}} \leq 2.3 \cdot 10^{-2} M_{\odot}$ . Both estimates are lower than previous es-



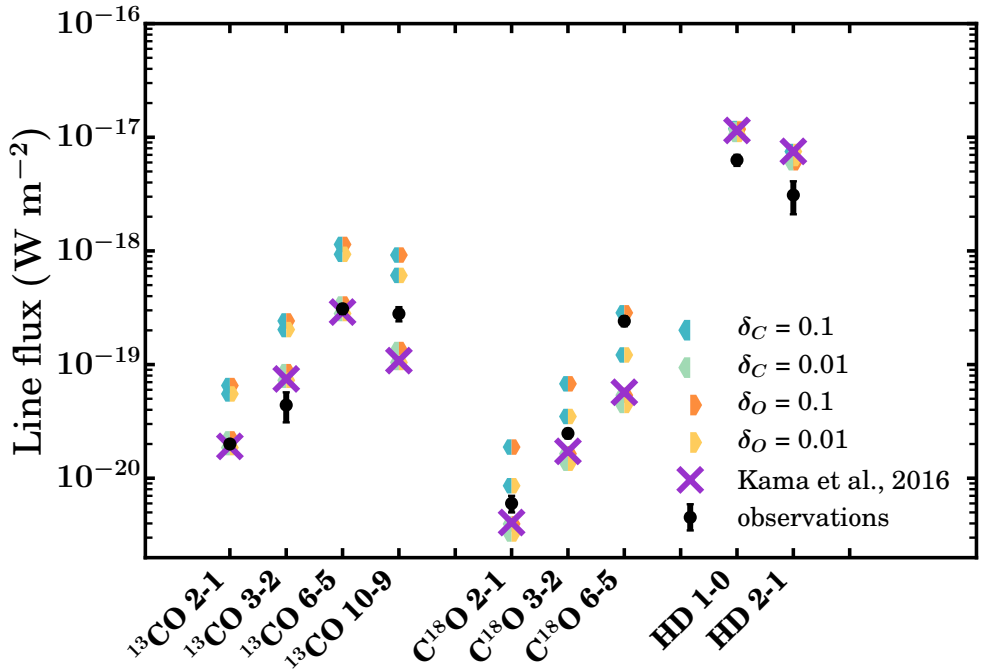


**Figure 6.13:** Integrated line fluxes from TW Hya models ( $M_{\text{disk}} = 2.3 \cdot 10^{-2} M_{\odot}$ ,  $\psi = 0.3$  and  $h_c = 0.1$ ) with different amounts of carbon depletion (hexagons; left side) and oxygen depletion (right side). The black bars show the observations for TW Hya (Schwarz et al. (2016); Kama et al. (2016b) and references therein). The purple crosses show the results from Kama et al. (2016b), recalculated for  $\delta_C = \delta_O = 0.01$ ,  $[D]/[H] = 2 \cdot 10^{-5}$  (cf. Section 6.4.4).

timates (e.g., Bergin et al. 2013; Kama et al. 2016b). Note that the estimates lie closer to the disk mass estimated from C<sup>18</sup>O observations (Favre et al. 2013), suggesting a smaller tension between the two.

Using models that include detailed modeling of the CO and H<sub>2</sub>O chemistry, studies found that the disk surrounding TW Hya is genuinely depleted in volatile carbon and oxygen (e.g., Bergin et al. 2010, 2013; Hogerheijde et al. 2011; Favre et al. 2013; Du et al. 2015). Recent observations of [CI], [CII], [OI], C<sub>2</sub>H and C<sub>3</sub>H<sub>2</sub> have reinforced this conclusion (Kama et al. 2016b; Bergin et al. 2016).

In their model, Kama et al. (2016b) incorporate the isotopes <sup>13</sup>C, <sup>17</sup>O, <sup>18</sup>O and D parametrically. In this section, their best fitting model ( $M_{\text{disk}} = 2.3 \cdot 10^{-2} M_{\odot}$ ,  $\psi = 0.3$  and  $h_c = 0.1$ ) is rerun using the extended chemical network that includes the deuterium and CO isotopologue selective chemistry following Miotello et al. (2014b). For these models, the carbon abundance was varied between the ISM abundance and two consecutive orders of underabundance, i.e.,  $X(\text{C}) \equiv [\text{C}]/[\text{H}] \in [1.35 \cdot 10^{-4}, 1.35 \cdot 10^{-5}, 1.35 \cdot 10^{-6}]$ . The same was done for the oxygen abundance,  $X(\text{O}) \in [2.88 \cdot 10^{-4}, 2.88 \cdot 10^{-5}, 2.88 \cdot 10^{-6}]$ . These underabundances are denoted using  $\delta_i \equiv X(i)/X(i)_{\text{ISM}}$ . Note that in order to match the hydrocarbon abundances Kama et al. (2016b) fine-tuned their final model to  $\delta_{\text{C}} = 0.01$  and  $\text{C}/\text{O} = 1.5$ , while the disk structure was unchanged from the best-fit fiducial model.

Figure 6.13 shows the resulting line fluxes for several rotational transitions of HD, <sup>13</sup>CO and C<sup>18</sup>O, similar to Figure 6 in Kama et al. (2016b). In the figure only the models with  $X(\text{C}, \text{O}) \sim 10^{-6}, 10^{-5}$  are shown. The full figure can be found in Appendix 6.E. It should be noted that HD abundance used in Kama et al. (2016b) ( $n(\text{HD})/n(\text{H}_2) = 1 \cdot 10^{-5}$ ) is a factor four lower than the maximal HD abundance of the models in this work ( $n(\text{HD})/n(\text{H}_2) = 4 \cdot 10^{-5}$ ). In order to compare the output of the chemical calculations to their parametric method, the HD line fluxes of their model were recalculated using the higher HD abundance. This accounts for the differences in the HD line fluxes seen here and those in Kama et al. (2016b). Similar steps were taken so that the  $\delta_{\text{C}} = \delta_{\text{O}} = 0.01$  model and the Kama et al. (2016b) model have the same oxygen and carbon abundances.

Starting with HD, one can see that the line fluxes from the models run here, which include the deuterium chemistry network, match the line fluxes from the model with the parametric HD within a few percent (8% and 15% for HD 1-0 and HD 2-1, respectively). This can be understood from the results in Section 6.3.2, which show that all the available deuterium is locked up in HD, thus mimicking the parametric approach used by Kama et al. (2016b). Note that all models overproduce the observed HD fluxes by a factor  $\sim 2$ , suggesting a slightly lower disk gas mass for TW Hya than used by Kama et al. (2016b).

For <sup>13</sup>C, there is again good agreement between the fluxes from Kama et al. (2016b) and the  $\delta_{\text{C}} = \delta_{\text{O}} = 0.01$  model (its CO isotopologue counterpart). This can be understood by reactions such as the ion-molecule reaction  $^{13}\text{C}^+ + ^{12}\text{CO} \rightleftharpoons$

---

$^{13}\text{CO} + ^{12}\text{C}^+ + 35 \text{ K}$ . The forward reaction direction of this reaction is favoured at low temperatures, leading to an increased  $^{13}\text{CO}$  abundance which balances out the additional decrease of  $^{13}\text{CO}$  due to isotope-selective photodissociation (Miotello et al. 2014b).

The line fluxes of  $\text{C}^{18}\text{O}$  of the  $\delta_{\text{C}} = \delta_{\text{O}} = 0.01$  model are systematically lower than the same lines from Kama et al. (2016b). This qualitatively agrees with previous results (e.g., Visser et al. 2009; Miotello et al. 2014b), but the effect is smaller than has been suggested. A possible explanation can be found in the gas mass of the disk. Miotello et al. (2014b, 2016) show that for disks with  $M_{\text{disk}} \geq 7 \cdot 10^{-3} M_{\odot}$  freeze-out is the dominant process affecting the  $\text{C}^{18}\text{O}$  flux, whereas isotope-selective photodissociation is more important for low mass disks (see, e.g., Fig. 3 in Miotello et al. 2016).

When the models are compared to the observations to determine the carbon and oxygen underabundance the results vary based on the tracer used. The  $^{13}\text{CO}$  observations point to  $\delta_{\text{C}} = 0.01$ , in line with the value found by Kama et al. (2016b). The observed  $^{13}\text{CO}$  10-9 flux and the observations for  $\text{C}^{18}\text{O}$  instead favour a lower underabundance of carbon, between  $\delta_{\text{C}} = 0.01$  and  $\delta_{\text{C}} = 0.1$ . For all CO isotopologue lines  $\delta_{\text{O}} = 0.01$  and  $\delta_{\text{O}} = 0.1$  fit the observations equally well. Combined with the lower gas mass estimates found for TW Hya, these results show that the inclusion of isotope-selective processes decreases underabundance of carbon needed to explain the observations to  $\delta_{\text{C}} \approx 0.1$ . It should be noted however that in this analysis only the CO isotopologues are considered, whereas the analysis in Kama et al. (2016b) also included observations of atomic carbon and atomic oxygen.

## 6.5 Conclusions

Accurately determining the amount of material in protoplanetary disks is crucial for understanding both the evolution of disks and the formation of planets in these disks. Recent observations of the rotational transitions of HD in protoplanetary disks (Bergin et al. 2013; McClure et al. 2016) have added a new possibility of tracing the disk gas mass. In this work, the robustness of HD as a tracer of the disk gas mass and its dependence on the vertical structure are investigated. The thermochemical code DALI (Bruderer et al. 2012; Bruderer 2013) was used to calculate the line fluxes for the disk models. The normal chemical network of DALI was expanded to include CO isotopologue selective chemistry, following Miotello et al. (2014b). A simple D chemistry network was also implemented in DALI. A series of models was run spreading a range of disk masses ( $M_{\text{disk}} \sim 10^{-5} - 10^{-1} M_{\odot}$ ) and vertical structures ( $h_c \sim 0.05 - 0.3$ ,  $\psi \sim 0.1 - 0.5$ ), with the large grains settled close to the midplane. From these models, the following observations can be made:

- The HD flux increases as a powerlaw for low mass disks ( $M_{\text{disk}} \leq 10^{-3} M_{\odot}$ ).

---

The fitted powerlaw indices are 0.8 for HD 1-0 (112  $\mu\text{m}$ ) and 0.5 for HD 2-1 (56  $\mu\text{m}$ ). These indices are less than 1.0 due to the dependence of the emission on the gas temperature. For high mass disks ( $M_{\text{disk}} > 10^{-3} M_{\odot}$ ) the HD flux scales with  $\log_{10} M_{\text{disk}}$ , which is a result of the increased line optical depth and decreased overall temperature of these disks.

- The maximum variation in HD 1-0 flux due to the different vertical structure increases with disk mass, from  $0.75 \times$  the median flux for  $M_{\text{disk}} \sim 10^{-5} M_{\odot}$  up to  $1.9 \times$  the median flux for  $M_{\text{disk}} \sim 10^{-1} M_{\odot}$ . The variation for HD 2-1 is both larger than for HD 1-0 and is less dependent on disk mass. The maximum variation of this flux is  $1.9 \times$  the median flux for  $M_{\text{disk}} \sim 10^{-5} M_{\odot}$ , increasing to  $2.8 \times$  the median flux for  $M_{\text{disk}} \sim 10^{-1} M_{\odot}$ .
- The influence of the large grain population on the HD flux is less than that of the vertical structure, approximately  $0.7 \times$  the median flux at  $M_{\text{disk}} = 2.3 \cdot 10^{-2} M_{\odot}$ .
- Without making assumptions on the vertical structure of the disk, the HD 1-0 flux can be used to estimate the disk gas mass to within a factor of  $\sim 3$  for low mass disks ( $M_{\text{disk}} \leq 10^{-3} M_{\odot}$ ). For more massive disks the uncertainty in the estimated mass increases to more than an order of magnitude.
- If complementary observations are employed to constrain the disk's flaring, the uncertainty on the gas mass can be reduced down to factor of 2, even for massive disks. Moreover, a combination of HD 1-0 and the HD 2-1 fluxes can be used to determine the disk gas mass to within a factor of 3, without making assumptions on the vertical structure.
- For DM Tau and GM Aur, gas mass estimates found by comparing the observed fluxes to the models agree with the results from McClure et al. (2016), confirming the high gas masses of these disks.
- For TW Hya, a gas mass between  $6 \cdot 10^{-3} M_{\odot} \leq M_{\text{disk}} \leq 9 \cdot 10^{-3} M_{\odot}$  is found if the best fit vertical structure from (Kama et al. 2016b) is assumed. This estimate agrees with the combination of HD 1-0 and HD 2-1 line fluxes, which favour a gas mass of  $7.7 \cdot 10^{-3} M_{\odot}$ .
- Detailed modeling of the TW Hya disk shows that the difference between HD- and CO-based gas masses is mitigated by including CO isotopologue selective

---

effects. A carbon underabundance of  $\sim 10$  with respect to the ISM can also explain the CO isotopologue observations.

In the interest of future far-infrared observatories, the line-to-continuum ratios for HD 1-0 and HD 2-1 were calculated for different spectral resolving power. If a maximum signal-to-noise on the continuum of 300 is assumed, it was shown that future far-IR missions need a spectral resolving power  $R \geq 300$  (equivalent to  $\Delta v \leq 500 \text{ km s}^{-1}$ ) to detect HD 1-0 for all disk masses. To detect HD 2-1 towards all models, a spectral resolving power of  $R \geq 1000$  (equivalent to  $\Delta v \leq 150 \text{ km s}^{-1}$ ) is required. Furthermore, a  $5\sigma$  sensitivity of  $1.8 \cdot 10^{-20} \text{ W m}^{-2}$  ( $2.5 \cdot 10^{-20} \text{ W m}^{-2}$ ) is required to detect HD 1-0 (2-1) in disks with gas mass  $\geq 3 \cdot 10^{-5} M_{\odot} \approx 0.03 M_{\text{jup}}$ . Both requirements can be met by proposed future missions such as SPICA.

## Acknowledgements

The authors would like to thank Inga Kamp and Ted Bergin for the useful discussions and for providing the details for the SPICA SAFARI and SOFIA HIRMES instruments. They also acknowledge Arthur Bosman for his support with the DALI code and Davide Fedele for providing the HD 2-1 line flux that was observed for TW Hya. Astrochemistry in Leiden is supported by the Netherlands Research School for Astronomy, by a Royal Netherlands Academy of Arts and Sciences (KNAW) professor prize, and by the European Union A-ERC grant 291141 CHEMPLAN.

## 6.A Abundance and temperature maps of TW Hya

In Figure 6.14 the abundance maps of  $^{13}\text{CO}$  and  $\text{C}^{18}\text{O}$  are shown for the TW Hya model ( $M_{\text{disk}} = 2.3 \cdot 10^{-2} M_{\odot}$ ,  $h_c = 0.1$ ,  $\psi = 0.3$  and  $\delta_C = \delta_O = 0.01$ .) The gas and dust temperature structures for the same model are shown in the panels of Figure 6.15.

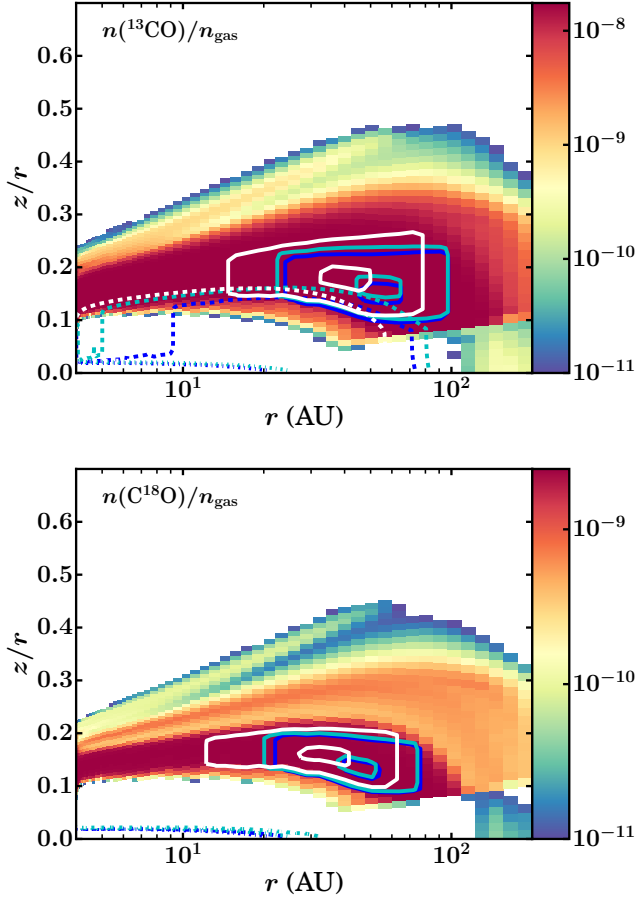


**Figure 6.14:** Maps of the  $^{13}\text{CO}$  (top) and  $\text{C}^{18}\text{O}$  (bottom) abundances. The coloured lines correspond to  $^{x}\text{C}^{y}\text{O}$  2-1 (blue), 3-2 (light blue) and 6-5 (white) respectively. The solid lines denote where 25% and 75% of the emission is produced. the dashed lines. The dashed lines show the  $\tau = 1$  surface for the line emission. The dashed-dotted lines show the  $\tau = 1$  surface for the continuum at the wavelength of the line.

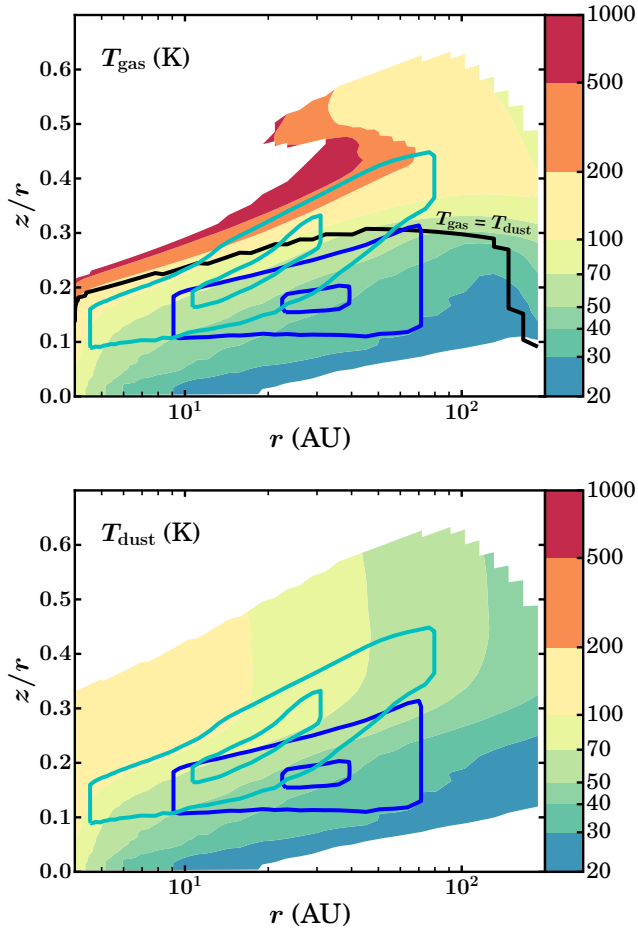
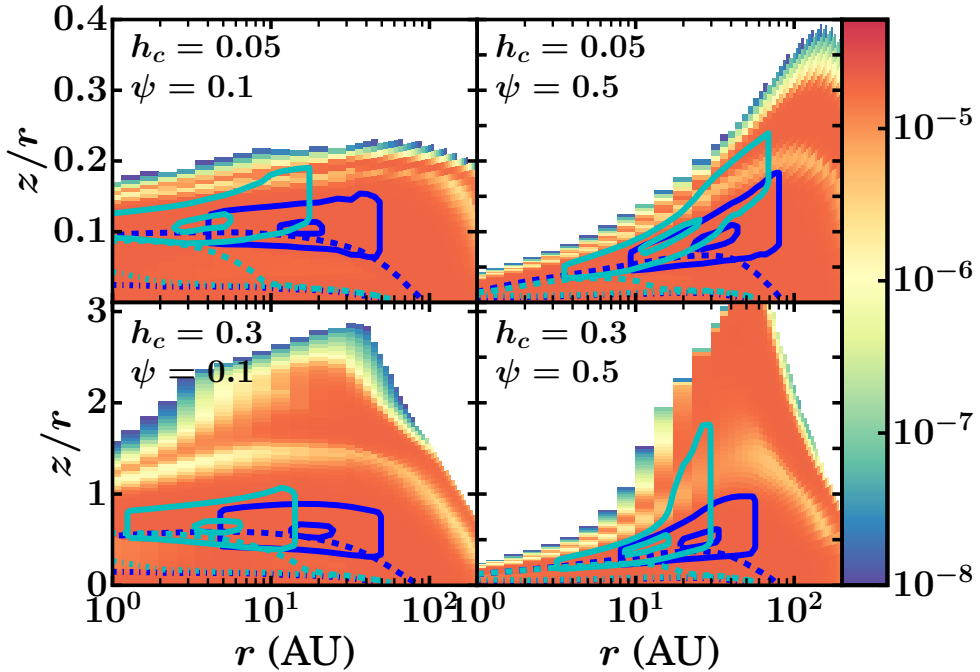


**Figure 6.15:** Maps of the gas temperature (top), dust temperature (bottom). The solid lines denote where 25% and 75% of the emission from HD 1-0 (blue) and HD 2-1 (light blue) originate from. The region below the black line in the top panel is where  $T_{\text{gas}} = T_{\text{dust}}$ .

## 6.B Abundance and emission maps of grid models

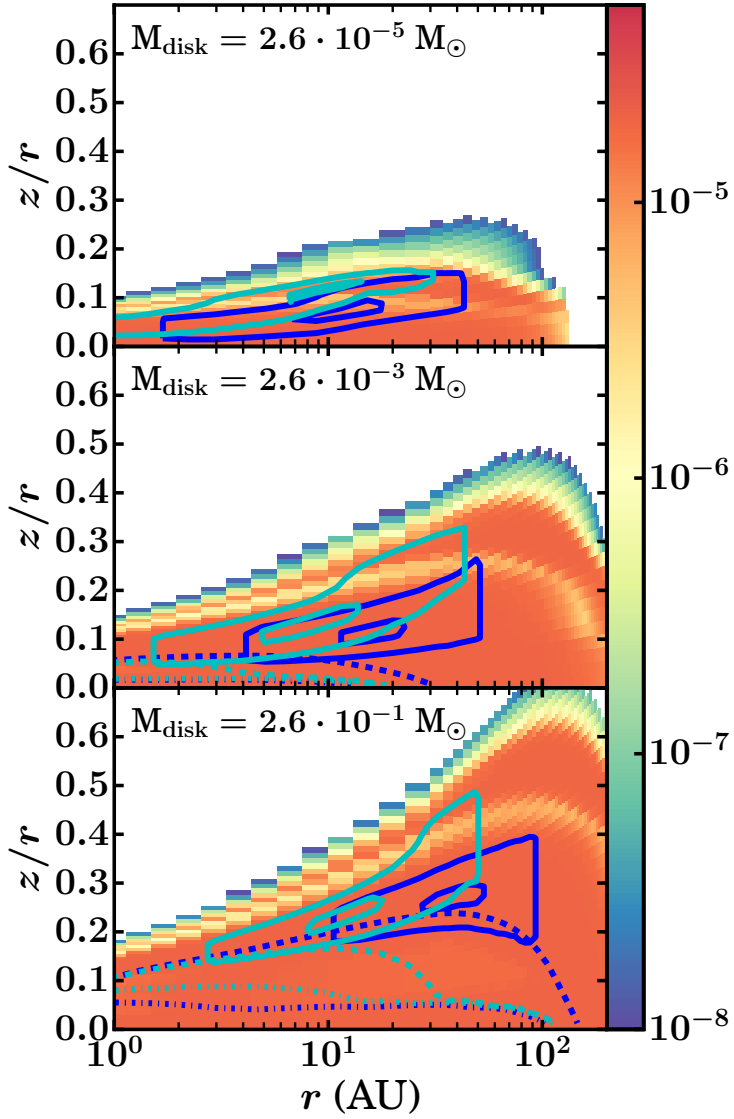
The HD abundance maps for several models with different vertical structures and disk masses are shown here. Figure 6.16 presents four models with different vertical structures:  $(h_c, \psi) = [0.05, 0.1], [0.05, 0.5], [0.3, 0.1], [0.3, 0.5]$ . These represent the most extreme cases in the grid. Note that the top and bottom rows in the figure have different vertical extents. Also note that the HD 1-0 emission (blue solid contours) originates from approximately the same horizontal region in all four models, between a few AU and several tens of AU.

Figure 6.17 presents the abundance maps for three disks with different disk masses:  $M_{\text{disk}} = [10^{-5}, 10^{-3}, 10^{-1}] M_{\odot}$ . Note that the height  $\tau = 1$  surface for the line optical depth (blue dashed line) increases with disk mass.



**Figure 6.16:** Maps of the HD abundance for four models with different vertical structures. Starting with the top left figure and continuing clockwise the vertical structure shown are  $(h_c, \psi) = [0.05, 0.1], [0.05, 0.5], [0.3, 0.1], [0.3, 0.5]$ . Note that the top and bottom row have different ranges on the vertical axis. The solid lines denote where 25% and 75% of the emission from HD 1-0 (blue) and HD 2-1 (light blue) originate from.





**Figure 6.17:** Maps of the HD abundance for three models with different disk masses:  $M_{\text{disk}} = [10^{-5}, 10^{-3}, 10^{-1}] M_{\odot}$ . The solid lines denote where 25% and 75% of the emission from HD 1-0 (blue) and HD 2-1 (light blue) originate from.

---

## 6.C Effects of including hydrostatic equilibrium

As shown in Figure 6.3, the HD emission originates from regions close to the disk surface. Accordingly, the HD emission will depend on the assumed disk vertical structure. In the models presented here the vertical structure is parametrized with a Gaussian (cf. Equation 6.2), to mimic a balance between gravitational force and pressure gradient, which in reality would depend on the temperature structure of the disk. Another possible approach is to the hydrostatic equilibrium to derive the vertical structure (e.g., Woitke et al. 2009). This results in a puffed-up inner rim, which shadows the outer disk from direct irradiation by the star. However, this may be a temporary feature that could be dispersed by e.g. stellar winds.

For completeness, we have investigated how the inclusion of hydrostatic equilibrium would affect the HD emission. The fiducial model described in Section 6.3.2 was rerun using eight iterations of the hydrostatic solver of DALI, where the temperature structure of the  $(n - 1)^{\text{th}}$  model is used to calculate the vertical structure of the  $n^{\text{th}}$  model. The resulting vertical structure is then used to recalculate the dust and gas temperatures, the chemistry and the HD emissions.

### 6.C.1 The hydrostatic solver

One way to obtain the vertical structure of the disk is to solve the equations of hydrostatic equilibrium. The hydrostatic equations in cylindrical geometry read (e.g. Hartmann 2000)

$$\rho \frac{v_\phi}{r} = \frac{dP}{dr} + \rho \frac{d\phi}{dr} \quad (6.9)$$

$$0 = \frac{dP}{dz} + \rho \frac{d\phi}{dz}, \quad (6.10)$$

where the velocities in the  $z$  and  $r$  direction are assumed to be 0. Without self-gravity, the gravitational potential by the star is

$$\phi = -\frac{GM_*}{(r^2 + z^2)^{1/2}}, \quad (6.11)$$

where  $M_*$  is the mass of the star.

Assuming that the pressure gradient in the  $r$  direction is negligible, the first hydrostatic equation yields the Keplerian velocity profile and the second hydrostatic equation can be solved independently for each radius. Instead of directly solving the equation for the density  $\rho$ , the equation can also be solved for pressure. The pressure and the density are related through  $P = c_s^2 \rho$ , where  $c_s$  is the sound speed

which depends on the gas temperature  $T_{\text{gas}}$  and therefore varies with height  $z$ . The differential equation for  $P$  reads

$$\frac{dP}{dz} = -\rho \frac{d\phi}{dz} \quad (6.12)$$

$$\frac{1}{P} \frac{dP}{dz} = -\frac{zGM_*}{c_s^2 (r^2 + z^2)^{3/2}}, \quad (6.13)$$

which is solved by

$$P(z) = c_s(z)^2 \rho(z) = C \exp\left(\int \frac{zGM_*}{c_s^2 (r^2 + z^2)^{3/2}} dz\right). \quad (6.14)$$

In the case of an isothermal disk, the above equation reduces to a Gaussian vertical density profile, as given in equation (6.2). The integration constant  $C$  in the above equation results from the normalization conditions for the vertical column density and should thus adjusted such that  $\int \rho(z) dz$  is preserved.

## 6.C.2 Comparing with parametrized vertical structure

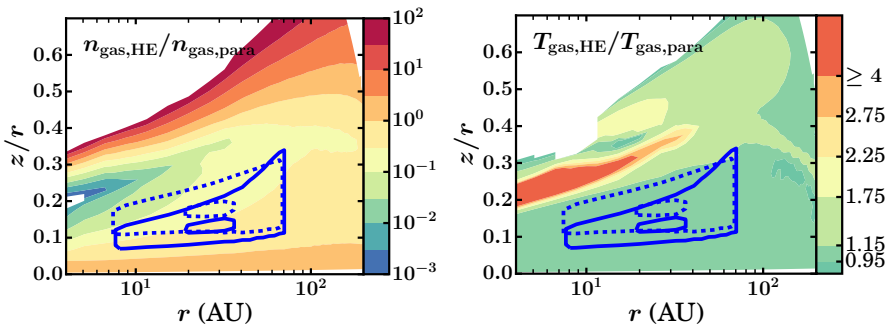


**Figure 6.18:** Maps of the density (left) and temperature (right) differences between the fiducial model (denoted ‘para’; Section 6.3.2) and the same model after eight iterations of the hydrostatic solver (denoted ‘HE’). Colour indicates the ratio of the densities or gas temperatures of the two models. The dashed blue lines show the HD 1-0 emitting region of the fiducial model. The solid blue lines show the HD 1-0 the 25% and 75% cumulative emission regions of the ‘HE’ model.

Figure 6.18 shows the effect of eight iterations of the hydrostatic solver on the density and gas temperature structure of the fiducial model ( $M_{\text{disk}} = 2.3 \cdot 10^{-2} M_{\odot}$ ,  $\psi = 0.3$

and  $h_c = 0.1$ , cf. Section 6.3.2). It also shows the regions where the HD 1-0 emission is produced before and after applying the hydrostatic solver. The top panel shows that the HD 1-0 emission has moved slightly towards the midplane for the hydrostatic model. This is likely the result of the decrease in height of the line optical depth surface. The bottom panel shows that the gas temperature in the HD 1-0 emitting region has changed by less than 5%.

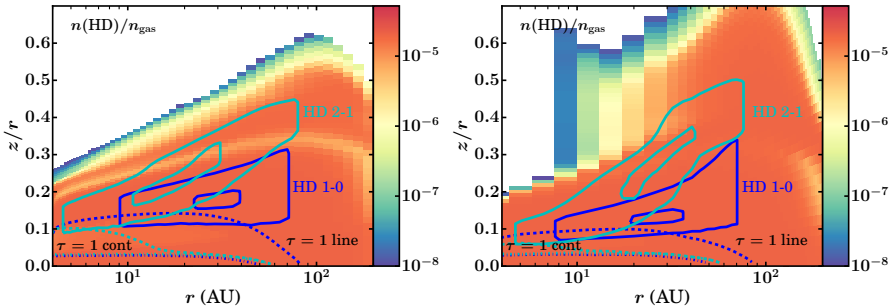


**Figure 6.19:** *Left panel:* HD abundance structure for a disk model with  $M_{\text{disk}} = 2.3 \cdot 10^{-2} M_{\odot}$ ,  $\psi = 0.3$  and  $h_c = 0.1$ , identical to Figure 6.3. Colour indicates the number density of HD with respect to the total gas density. The coloured lines correspond the HD 1-0 (blue) and HD 2-1 (light blue) respectively. Solid contours indicate where 25% and 75% of the emission originates from. The dashed (dashed-dotted) lines show the  $\tau = 1$  surface for the line and continuum opacity, respectively. *Right panel:* HD abundance structure of the same initial model, where the vertical structure is now determined by eight iterations of the hydrostatic solver of DALI.

The effect of the hydrostatic solver on the HD emitting regions is shown in Figure 6.19. While disk models obtained with the hydrostatic calculations are vertically more extended, the HD emitting regions have not extremely changed. This is also reflected in the integrated fluxes, which for the hydrostatic model are  $\sim 50\%$  (HD 1-0) and  $\sim 66\%$  (HD 2-1) lower compared to the model with the parametrized vertical structure. While this affects the inferred disk masses by a similar absolute factor, all the trends presented here should be robust. Also note that varying the parametric vertical structure changes the HD fluxes by a similar or larger factor (cf. Figure 6.4). The mass uncertainties calculated in Section 6.4.1 therefore remain unchanged.

## 6.D Deuterium chemistry

Table 6.6 list the reactions that were included in the deuterium chemical network. The rate coefficients were adapted from Roberts & Millar (2000); Walmsley et al.

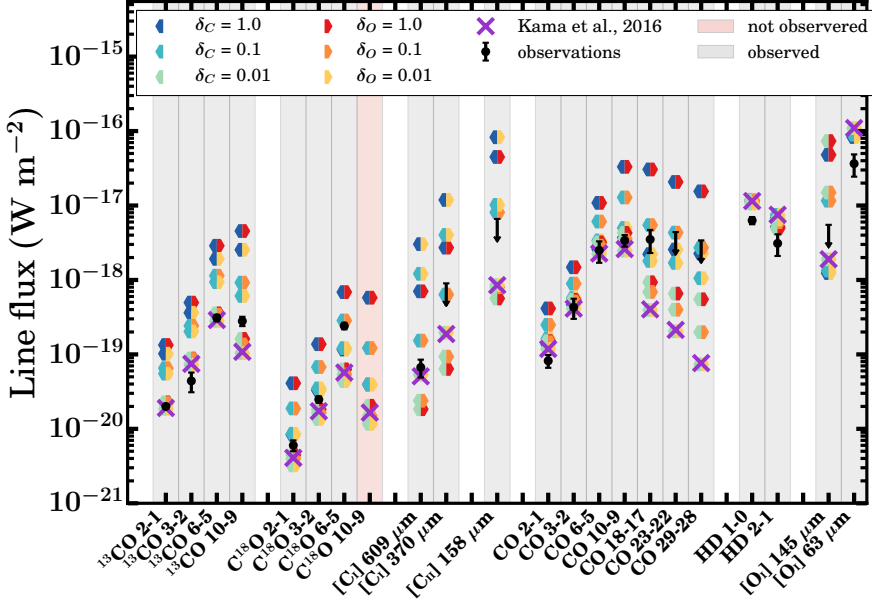


**Figure 6.20:** Integrated line fluxes from TW Hya models ( $M_{\text{disk}} = 2.3 \cdot 10^{-2} M_{\odot}$ ,  $\psi = 0.3$ ,  $h_c = 0.1$ ,  $d = 59.54$  pc (Astraatmadja & Bailer-Jones 2016)) with different amounts of carbon/oxygen underabundances. The x-axis shows the various modelled transitions. The black bars show the observations for TW Hya (Schwarz et al. 2016; Kama et al. 2016b and references therein). The purple crosses show the modelled line fluxes from the best fit model from Kama et al. (2016b) (with  $\delta_C = \delta_O = 0.01$ ). The coloured hexagons show the results from this work, with the left hand side showing the amount carbon underabundance (with respect to the ISM). The right hand side shows the amount of oxygen underabundance.

(2004) and Glover & Jappsen (2007). Where the rate coefficients were not known, the coefficients for the analogue reactions with H instead of D were used.

## 6.E Line fluxes of the TW Hya model

The extended version of Figure 6.13 is shown here. Its setup is similar to Figure 6 in Kama et al. (2016b). The fluxes and upper limits for the observations used can be found in Table B.1 in Kama et al. (2016b). The line fluxes of  $^{13}\text{CO}$  6-5,  $\text{C}^{18}\text{O}$  3-2 and  $\text{C}^{18}\text{O}$  6-5 were calculated from the data presented in Schwarz et al. (2016).

**Table 6.6:** Simple HD chemical network reactions and adopted rate coefficient.

Reaction	$\alpha$	$\beta$	$\gamma$	Ref.
$D^+ + H \rightarrow H^+ + D$	1.0(-9)	0.0(0)	0.0(0)	1,2
$D + H^+ \rightarrow H + D^+$	1.0(-9)	0.0(0)	4.1(1)	1,2
$D^+ + H_2 \rightarrow H^+ + HD$	2.1(-9)	0.0(0)	0.0(0)	1,2
$D^+ + H_2 \rightarrow H + HD^+$	1.75(-9)	9.8(-2)	0.0(0)	1,2
$HD + H^+ \rightarrow H_2 + D^+$	1.0(-9)	0.0(0)	6.345(2)	1,2
$HD^+ + H \rightarrow HD + H^+$	6.4(-10)	0.0(0)	0.0(0)	2
$H_2^+ + D \rightarrow H_2 + D^+$	6.4(-10)	0.0(0)	0.0(0)	2
$D + cr \rightarrow D^+ + e^-$	4.6(-20)	0.0(0)	0.0(0)	2
$HD + cr \rightarrow H + D^+ + e^-$	4.73(-20)	0.0(0)	0.0(0)	2
$HD + cr \rightarrow D + H^+ + e^-$	4.73(-20)	0.0(0)	0.0(0)	2
$HD + cr \rightarrow D + H$	5.99(-19)	0.0(0)	0.0(0)	2
$HD + cr \rightarrow D^+ + H^-$	8.4(-22)	0.0(0)	0.0(0)	2
$HD + cr \rightarrow HD^+ + e^-$	5.16(-18)	0.0(0)	0.0(0)	2
$HD^+ + H_2 \rightarrow H_3^+ + D$	5.25(-9)	0.0(0)	0.0(0)	2
$H_2^+ + HD \rightarrow H_3^+ + D$	5.25(-9)	0.0(0)	0.0(0)	2
$HD + He^+ \rightarrow He + H^+ + D$	5.5(-14)	-2.4(-1)	0.0(0)	2
$HD + He^+ \rightarrow He + D^+ + H$	5.5(-14)	-2.4(-1)	0.0(0)	2
$D^+ + H \rightarrow HD^+ + \gamma$	3.9(-19)	1.8(0)	0.0(0)	2
$H^+ + D \rightarrow HD^+ + \gamma$	3.9(-19)	1.8(0)	0.0(0)	2
$HD^+ + H \rightarrow H_2^+ + D$	1.0(-9)	0.0(0)	1.54(2)	2
$H_2^+ + D \rightarrow HD^+ + H$	1.0(-9)	0.0(0)	0.0(0)	2
$HD^+ + D \rightarrow HD^+ + D$	6.4(-10)	0.0(0)	0.0(0)	2
$HD^+ + e^- \rightarrow H + D$	3.4(-9)	-4.0(-1)	0.0(0)	2
$D^+ + e^- \rightarrow D + \gamma$	3.61(-12)	-7.5(-1)	0.0(0)	2
$H + D \rightarrow HD + \gamma$	3.0(-18)	5.0(-1)	0.0(0)	*
$D^+ + Mg \rightarrow D + Mg^+$	1.1(-9)	0.0(0)	0.0(0)	*
$D^+ + Si \rightarrow D + Si^+$	9.9(-10)	0.0(0)	0.0(0)	*
$D^+ + Fe \rightarrow D + Fe^+$	7.4(-9)	0.0(0)	0.0(0)	*
$D^+ + S \rightarrow D + S^+$	1.3(-9)	0.0(0)	0.0(0)	*
$D^+ + PAH \rightarrow D + PAH^+$	3.1(-8)	0.0(0)	0.0(0)	*
$D^+ + PAH^- \rightarrow D + PAH$	8.3(-7)	-5.0(-1)	0.0(0)	*
$HD^+ + PAH \rightarrow HD + PAH^+$	3.1(-8)	0.0(0)	0.0(0)	*
$HD^+ + PAH^- \rightarrow HD + PAH$	8.3(-7)	-5.0(-1)	0.0(0)	*

References: 1. Roberts & Millar (2000); 2. Walmsley et al. (2004);

\* Rate coefficients are the same as those for the analogue reactions with H instead of D.



# BIBLIOGRAPHY

- Adams, F. C., Hollenbach, D., Laughlin, G., & Gorti, U. 2004, *ApJ*, 611, 360
- Aikawa, Y., Miyama, S. M., Nakano, T., & Umebayashi, T. 1996, *ApJ*, 467, 684
- Aikawa, Y., Umebayashi, T., Nakano, T., & Miyama, S. M. 1997, *ApJL*, 486, L51
- Aikawa, Y., van Zadelhoff, G. J., van Dishoeck, E. F., & Herbst, E. 2002, *A&A*, 386, 622
- Aikawa, Y., & Nomura, H. 2006, *ApJ*, 642, 1152
- Akimkin, V., Zhukovska, S., Wiebe, D., et al. 2013, *ApJ*, 766, 8
- Alcalá, J. M., Natta, A., Manara, C. F., et al. 2014, *A&A*, 561, A2
- Alcalá, J. M., Manara, C. F., Natta, A., et al. 2017, *A&A*, 600, A20
- Alexander, R., Pascucci, I., Andrews, S., Armitage, P., & Cieza, L. 2014, *Protostars and Planets VI*, 475
- ALMA Partnership, Brogan, C. L., Pérez, L. M., et al. 2015, *ApJL*, 808, L3
- Anderson, K. R., Adams, F. C., & Calvet, N. 2013, *ApJ*, 774, 9
- André, P. 1995, *Ap&SS*, 224, 29
- André, P., Men'shchikov, A., Bontemps, S., et al. 2010, *A&A*, 518, L102
- Andrews, S. M., & Williams, J. P. 2005, *ApJ*, 631, 1134
- Andrews, S. M., Wilner, D. J., Espaillat, C., et al. 2011, *ApJ*, 732, 42
- Andrews, S. M., Wilner, D. J., Hughes, A. M., et al. 2012, *ApJ*, 744, 162
- Andrews, S. M., Rosenfeld, K. A., Kraus, A. L., & Wilner, D. J. 2013, *ApJ*, 771, 129
- Andrews, S. M. 2015, *PASP*, 127, 961
- Andrews, S. M., Wilner, D. J., Zhu, Z., et al. 2016, *ApJL*, 820, L40
- Ansdell, M., Williams, J. P., van der Marel, N., et al. 2016, [arXiv:1604.05719](https://arxiv.org/abs/1604.05719)
- Ansdell, M., Williams, J. P., Manara, C. F., et al. 2017, *AJ*, 153, 240
- Armitage, P. J. 2011, *ARAA*, 49, 195



- 
- Armitage, P. J., Simon, J. B., & Martin, R. G. 2013, *ApJL*, 778, L14
- Armitage, P. J. 2015, arXiv:1509.06382
- Astraatmadja, T. L., & Bailer-Jones, C. A. L. 2016, *ApJ*, 833, 119
- Bai, X.-N., Ye, J., Goodman, J., & Yuan, F. 2016, *ApJ*, 818, 152
- Bally, J., & Langer, W. D. 1982, *ApJ*, 255, 143
- Barenfeld, S. A., Carpenter, J. M., Ricci, L., & Isella, A. 2016, arXiv:1605.05772
- Bary, J. S., Weintraub, D. A., Shukla, S. J., Leisenring, J. M., & Kastner, J. H. 2008, *ApJ*, 678, 1088
- Beckwith, S. V. W., Sargent, A. I., Chini, R. S., & Guesten, R. 1990, *AJ*, 99, 924
- Bergin, E. A., Hogerheijde, M. R., Brinch, C., et al. 2010, *A&A*, 521, L33
- Bergin, E. A., Cleeves, L. I., Gorti, U., et al. 2013, *Nature*, 493, 644
- Bergin, E. A., Cleeves, L. I., Crockett, N., & Blake, G. 2014, arXiv:1405.7394
- Bergin, E. A., Du, F., Cleeves, L. I., et al. 2016, *ApJ*, 831, 101
- Birnstiel, T., Klahr, H., & Ercolano, B. 2012, *A&A*, 539, A148
- Bisschop, S. E., Fraser, H. J., Öberg, K. I., van Dishoeck, E. F., & Schlemmer, S. 2006, *A&A*, 449, 1297
- Bitner, M. A., Richter, M. J., Lacy, J. H., et al. 2008, *ApJ*, 688, 1326
- Blake, G. A., van Dishoeck, E. F., & Sargent, A. I. 1992, *ApJL*, 391, L99
- Boneberg, D. M., Panić, O., Haworth, T. J., Clarke, C. J., & Min, M. 2016, *MNRAS*, 461, 385
- Brittain, S. D., Najita, J. R., & Carr, J. S. 2009, *ApJ*, 702, 85
- Brown, J. M., Pontoppidan, K. M., van Dishoeck, E. F., et al. 2013, *ApJ*, 770, 94
- Bruderer, S., van Dishoeck, E. F., Doty, S. D., & Herczeg, G. J. 2012, *A&A*, 541, A91
- Bruderer, S. 2013, *A&A*, 559, A46
- Bruderer, S., van der Marel, N., van Dishoeck, E. F., & van Kempen, T. A. 2014, *A&A*, 562, A26
- Bustamante, I., Merín, B., Ribas, Á., et al. 2015, *A&A*, 578, A23
- Cacciani, P., & Ubachs, W. 2004, *Journal of Molecular Spectroscopy*, 225, 62
- Carmona, A., van den Ancker, M. E., Henning, T., et al. 2008, *A&A*, 477, 839
- Carmona, A., van der Plas, G., van den Ancker, M. E., et al. 2011, *A&A*, 533, A39
- Casassus, S., van der Plas, G., M, S. P., et al. 2013, *Nature*, 493, 191
- Chiang, E. I., & Goldreich, P. 1997, *ApJ*, 490, 368

- 
- Chiang, E. I., Joungh, M. K., Creech-Eakman, M. J., et al. 2001, *ApJ*, 547, 1077
- Clarke, C. J., & Pringle, J. E. 1993, *MNRAS*, 261, 190
- Clarke, C. J., Gendrin, A., & Sotomayor, M. 2001, *MNRAS*, 328, 485
- Clarke, C. J. 2007, *MNRAS*, 376, 1350
- Cleeves, L. I., Bergin, E. A., Alexander, C. M. O., et al. 2014, arXiv:1409.7398
- Cleeves, L. I., Bergin, E. A., Qi, C., Adams, F. C., & Öberg, K. I. 2015, *ApJ*, 799, 204
- Cleeves, L. I., Öberg, K. I., Wilner, D. J., et al. 2016, *ApJ*, 832, 110
- Comerón, F. 2008, *Handbook of Star Forming Regions*, Volume II, 5, 295
- Costigan, G., Vink, J. S., Scholz, A., Ray, T., & Testi, L. 2014, *MNRAS*, 440, 3444
- D'Alessio, P., Calvet, N., & Hartmann, L. 2001, *ApJ*, 553, 321
- D'Alessio, P., Calvet, N., Hartmann, L., Franco-Hernández, R., & Servín, H. 2006, *ApJ*, 638, 314
- Dartois, E., Dutrey, A., & Guilloteau, S. 2003, *A&A*, 399, 773
- de Gregorio-Monsalvo, I., Ménard, F., Dent, W., et al. 2013, *A&A*, 557, A133
- Dent, W. R. F., Greaves, J. S., & Coulson, I. M. 2005, *MNRAS*, 359, 663
- Dent, W. R. F., Thi, W. F., Kamp, I., et al. 2013, *PASP*, 125, 477
- Draine, B. T. 1978, *ApJS*, 36, 595
- Draine, B. T. 2006, *ApJ*, 636, 1114
- Drozdovskaya, M. N., Walsh, C., Visser, R., Harsono, D., & van Dishoeck, E. F. 2015, *MNRAS*, 451, 3836
- Du, F., Bergin, E. A., & Hogerheijde, M. R. 2015, *ApJL*, 807, L32
- Du, F., Bergin, E. A., Hogerheijde, M., et al. 2017, *ApJ*, 842, 98
- Dullemond, C. P., & Dominik, C. 2005, *A&A*, 434, 971
- Dunham, M. M., Allen, L. E., Evans, N. J., II, et al. 2015, *ApJS*, 220, 11
- Dutrey, A., Guilloteau, S., Duvert, G., et al. 1996, *A&A*, 309, 493
- Dutrey, A., Guilloteau, S., & Guelin, M. 1997, *A&A*, 317, L55
- Dutrey, A., Guilloteau, S., Prato, L., et al. 1998, *A&A*, 338, L63
- Dutrey, A., di Folco, E., Guilloteau, S., et al. 2014, *Nature*, 514, 600
- Eidelsberg, M., Benayoun, J. J., Viala, Y., et al. 1992, *A&A*, 265, 839
- Eisner, J. A., Bally, J. M., Ginsburg, A., & Sheehan, P. D. 2016, *ApJ*, 826, 16

- 
- Eistrup, C., Walsh, C., & van Dishoeck, E. F. 2016, *A&A*, 595, A83
- Evans, N. J., II, Dunham, M. M., Jørgensen, J. K., et al. 2009, *ApJS*, 181, 321-350
- Facchini, S., Clarke, C. J., & Bisbas, T. G. 2016, *MNRAS*, 457, 3593
- Facchini, S., Birnstiel, T., Bruderer, S., & van Dishoeck, E. F. 2017, *A&A*, 605, A16
- Favre, C., Cleeves, L. I., Bergin, E. A., Qi, C., & Blake, G. A. 2013, *ApJL*, 776, L38
- Fedele, D., van den Ancker, M. E., Henning, T., Jayawardhana, R., & Oliveira, J. M. 2010, *A&A*, 510, A72
- Fedele, D., Bruderer, S., van Dishoeck, E. F., et al. 2013, *ApJL*, 776, L3
- Fedele, D., Carney, M., Hogerheijde, M. R., et al. 2017, *A&A*, 600, A72
- Field, G. B., Somerville, W. B., & Dressler, K. 1966, *ARAA*, 4, 207
- Frerking, M. A., Langer, W. D., & Wilson, R. W. 1982, *ApJ*, 262, 590
- Glover, S. C. O., & Jappsen, A.-K. 2007, *ApJ*, 666, 1
- Goldsmith, P. F., Bergin, E. A., & Lis, D. C. 1997, *ApJ*, 491, 615
- Gorti, U., & Hollenbach, D. 2004, *ApJ*, 613, 424
- Gorti, U., & Hollenbach, D. 2009, *ApJ*, 690, 1539
- Gorti, U., Hollenbach, D., Najita, J., & Pascucci, I. 2011, *ApJ*, 735, 90
- Gorti, U., Liseau, R., Sándor, Z., & Clarke, C. 2016, *Space Sci. Rev.*, 205, 125
- Guilloteau, S., Dutrey, A., Piétu, V., & Boehler, Y. 2011, *A&A*, 529, A105
- Hacar, A., & Tafalla, M. 2011, *A&A*, 533, A34
- Hacar, A., Tafalla, M., Kauffmann, J., & Kovács, A. 2013, *A&A*, 554, A55
- Haisch, K. E., Jr., Greene, T. P., Barsony, M., & Ressler, M. 2001, *Bulletin of the American Astronomical Society*, 33, 04.10
- Harsono, D., Bruderer, S., & van Dishoeck, E. F. 2015, *A&A*, 582, A41
- Hartmann, L., & Kenyon, S. J. 1985, *ApJ*, 299, 462
- Hartmann, L., & Kenyon, S. J. 1987, *ApJ*, 312, 243
- Hartmann, L., Calvet, N., Gullbring, E., & D'Alessio, P. 1998, *ApJ*, 495, 385
- Hartmann, L. 2000, *Accretion processes in star formation*, Vol. 32 (Cambridge University Press)
- Hartmann, L., Herczeg, G., & Calvet, N. 2016, *ARAA*, 54, 135
- Hayashi, C. 1981, *Fundamental Problems in the Theory of Stellar Evolution*, 93, 113
- Helled, R., Bodenheimer, P., Podolak, M., et al. 2014, *Protostars and Planets VI*, 643

- 
- Herbst, E., & van Dishoeck, E. F. 2009, *ARAA*, 47, 427
- Hernández, J., Calvet, N., Briceño, C., et al. 2007, *ApJ*, 671, 1784
- Herczeg, G. J., & Hillenbrand, L. A. 2008, *ApJ*, 681, 594-625
- Hildebrand, R. H. 1983, *QJRAS*, 24, 267
- Hogerheijde, M. R., Bergin, E. A., Brinch, C., et al. 2011, *Science*, 334, 338
- Hollenbach, D., Gorti, U., Meyer, M., et al. 2005, *ApJ*, 631, 1180
- Howat, S. K. R., Timmermann, R., Geballe, T. R., Bertoldi, F., & Mountain, C. M. 2002, *ApJ*, 566, 905
- Hudson, R. D. 1971, *Reviews of Geophysics and Space Physics*, 9, 305
- Isella, A., Guidi, G., Testi, L., et al. 2016, *Physical Review Letters*, 117, 251101
- Izidoro, A., Morbidelli, A., Raymond, S. N., Hersant, F., & Pierens, A. 2015, *A&A*, 582, A99
- Johnstone, D., Hollenbach, D., & Bally, J. 1998, *ApJ*, 499, 758
- Jones, M. G., Pringle, J. E., & Alexander, R. D. 2012, *MNRAS*, 419, 925
- Jonkheid, B., Faas, F. G. A., van Zadelhoff, G.-J., & van Dishoeck, E. F. 2004, *A&A*, 428, 511
- Kama, M., Bruderer, S., Carney, M., et al. 2016, *A&A*, 588, A108
- Kama, M., Bruderer, S., van Dishoeck, E. F., et al. 2016, *A&A*, 592, A83
- Kamp, I., Tilling, I., Woitke, P., Thi, W.-F., & Hogerheijde, M. 2010, *A&A*, 510, A18
- Kamp, I., Woitke, P., Pinte, C., et al. 2011, *A&A*, 532, A85
- Kastner, J. H., Qi, C., Gorti, U., et al. 2015, *ApJ*, 806, 75
- Kelly, B. C. 2007, *ApJ*, 665, 1489
- Kennicutt, R. C., & Evans, N. J. 2012, *ARAA*, 50, 531
- Kenyon, S. J., & Hartmann, L. 1987, *ApJ*, 323, 714
- Kóspál, Á., Moór, A., Juhász, A., et al. 2013, *ApJ*, 776, 77
- Lacy, J. H., Knacke, R., Geballe, T. R., & Tokunaga, A. T. 1994, *ApJL*, 428, L69
- Lada, C. J. 1987, *Star Forming Regions*, 115, 1
- Langer, W. D., Graedel, T. E., Frerking, M. A., & Armentrout, P. B. 1984, *ApJ*, 277, 581
- Letzelter, C., Eidelsberg, M., Rostas, F., Breton, J., & Thieblemont, B. 1987, *Chemical Physics*, 114, 273
- Levison, H. F., Kretke, K. A., & Duncan, M. J. 2015, *Nature*, 524, 322
- Lissauer, J. J., Hubickyj, O., D'Angelo, G., & Bodenheimer, P. 2009, *Icarus*, 199, 338

- 
- Lommen, D., Maddison, S. T., Wright, C. M., et al. 2009, *A&A*, 495, 869
- Lynden-Bell, D., & Pringle, J. E. 1974, *MNRAS*, 168, 603
- Lyons, J. R., & Young, E. D. 2005, *Chondrites and the Protoplanetary Disk*, 341, 193
- Manara, C. F., Fedele, D., Herczeg, G. J., & Teixeira, P. S. 2016, *A&A*, 585, A136
- Manara, C. F., Rosotti, G., Testi, L., et al. 2016, *A&A*, 591, L3
- Mannings, V., & Sargent, A. I. 1997, *ApJ*, 490, 792
- Matsuo, T., Shibai, H., Ootsubo, T., & Tamura, M. 2007, *ApJ*, 662, 1282
- McClure, M. K., Bergin, E. A., Cleeves, L. I., et al. 2016, *ApJ*, 831, 167
- Meeus, G., Salyk, C., Bruderer, S., et al. 2013, *A&A*, 559, A84
- Merín, B., Brown, J. M., Oliveira, I., et al. 2010, *ApJ*, 718, 1200-1223
- Miotello, A., Testi, L., Lodato, G., et al. 2014, *A&A*, 567, A32
- Miotello, A., Bruderer, S., & van Dishoeck, E. F. 2014, *A&A*, 572, AA96
- Miotello, A., van Dishoeck, E. F., Kama, M., & Bruderer, S. 2016, *A&A*, 594, A85
- Miotello, A., van Dishoeck, E. F., Williams, J. P., et al. 2017, *A&A*, 599, A113
- Morbidelli, A., & Raymond, S. N. 2016, *Journal of Geophysical Research (Planets)*, 121, 1962
- Mohanty, S., Jayawardhana, R., & Basri, G. 2005, *ApJ*, 626, 498
- Müller, H. S. P., Schlöder, F., Stutzki, J., & Winnewisser, G. 2005, *Journal of Molecular Structure*, 742, 215
- Najita, J., Carr, J. S., & Mathieu, R. D. 2003, *ApJ*, 589, 931
- Nakagawa, T., Shibai, H., Onaka, T., et al. 2014, in *SPIE Astronomical Telescopes+ Instrumentation*, International Society for Optics and Photonics, 9143, 91431I
- Natta, A., Testi, L., Neri, R., Shepherd, D. S., & Wilner, D. J. 2004, *A&A*, 416, 179
- Nomura, H., Aikawa, Y., Nakagawa, Y., & Millar, T. J. 2009, *A&A*, 495, 183
- Öberg, K. I., Murray-Clay, R., & Bergin, E. A. 2011, *ApJL*, 743, L16
- O'dell, C. R., & Wen, Z. 1994, *ApJ*, 436, 194
- Ossenkopf, V., & Henning, T. 1994, *A&A*, 291, 943
- Owen, J. E., Ercolano, B., Clarke, C. J., & Alexander, R. D. 2010, *MNRAS*, 401, 1415
- Panić, O., Hogerheijde, M. R., Wilner, D., & Qi, C. 2008, *A&A*, 491, 219
- Panić, O., & Hogerheijde, M. R. 2009, *A&A*, 508, 707
- Pascucci, I., Gorti, U., Hollenbach, D., et al. 2006, *ApJ*, 651, 1177

---

Pascucci, I., Herczeg, G., Carr, J. S., & Bruderer, S. 2013, *ApJ*, 779, 178

Pascucci, I., Testi, L., Herczeg, G. J., et al. 2016, *ApJ*, 831, 125

Pérez, L. M., Carpenter, J. M., Chandler, C. J., et al. 2012, *ApJL*, 760, L17

Perez, S., Casassus, S., Ménard, F., et al. 2015, *ApJ*, 798, 85

Pfalzner, S., Vogel, P., Scharwächter, J., & Olczak, C. 2005, *A&A*, 437, 967

Pinilla, P., Birnstiel, T., Ricci, L., et al. 2012, *A&A*, 538, A114

Pollack, J. B., Hollenbach, D., Beckwith, S., et al. 1994, *ApJ*, 421, 615

Pollack, J. B., Hubickyj, O., Bodenheimer, P., et al. 1996, *Icarus*, 124, 62

Pontoppidan, K. M., Blake, G. A., van Dishoeck, E. F., et al. 2008, *ApJ*, 684, 1323

Prodanović, T., Steigman, G., & Fields, B. D. 2010, *MNRAS*, 406, 1108

Regály, Z., Juhász, A., Sándor, Z., & Dullemond, C. P. 2012, *MNRAS*, 419, 1701

Ricci, L., Testi, L., Natta, A., et al. 2010, *A&A*, 512, A15

Roberts, H., & Millar, T. J. 2000, *A&A*, 364, 780

Rodmann, J., Henning, T., Chandler, C. J., Mundy, L. G., & Wilner, D. J. 2006, *A&A*, 446, 211

Roelfsema, P., Giard, M., Najarro, F., et al. 2014, *Proc. SPIE*, 9143, 91431K

Röllig, M., & Ossenkopf, V. 2013, *A&A*, 550, A56

Romero, G. A., Schreiber, M. R., Cieza, L. A., et al. 2012, *ApJ*, 749, 79

Ros, K., & Johansen, A. 2013, *A&A*, 552, A137

Rosenfeld, K. A., Andrews, S. M., Hughes, A. M., Wilner, D. J., & Qi, C. 2013, *ApJ*, 774, 16

Rosotti, G. P., Clarke, C. J., Manara, C. F., & Facchini, S. 2017, *MNRAS*, 468, 1631

Sargent, A. I., & Beckwith, S. 1987, *ApJ*, 323, 294

Schoonenberg, D., & Ormel, C. W. 2017, *A&A*, 602, A21

Schwarz, K. R., Bergin, E. A., Cleeves, L. I., et al. 2016, *ApJ*, 823, 91

Shakura, N. I., & Sunyaev, R. A. 1973, *A&A*, 24, 337

Shirley, Y. L., Huard, T. L., Pontoppidan, K. M., et al. 2011, *ApJ*, 728, 143

Smith, D., & Adams, N. G. 1980, *ApJ*, 242, 424

Smith, B. A., & Terrile, R. J. 1984, *Science*, 226, 1421

Strom, K. M., Strom, S. E., Edwards, S., Cabrit, S., & Skrutskie, M. F. 1989, *AJ*, 97, 1451

---

Suzuki, T. K., Ogihara, M., Morbidelli, A., Crida, A., & Guillot, T. 2016, *A&A*, 596, A74

Tazzari, M., Testi, L., Ercolano, B., et al. 2016, *A&A*, 588, A53

Tazzari, M., Testi, L., Natta, A., et al. 2017, arXiv:1707.01499

Testi, L., Natta, A., Shepherd, D. S., & Wilner, D. J. 2003, *A&A*, 403, 323

Testi, L., Birnstiel, T., Ricci, L., et al. 2014, *Protostars and Planets VI*, astro-ph/1402.1354

Thi, W. F., Blake, G. A., van Dishoeck, E. F., et al. 2001, *Nature*, 409, 60

Thommes, E. W., Matsumura, S., & Rasio, F. A. 2008, *Science*, 321, 814

Trapman, L., Miotello, A., Kama, M., van Dishoeck, E. F., & Bruderer, S. 2017, arXiv:1705.07671

Turner, N. J., Fromang, S., Gammie, C., et al. 2014, *Protostars and Planets VI*, 411

van Dishoeck, E. F., & Black, J. H. 1988, *ApJ*, 334, 771

van Dishoeck, E. F., Jonkheid, B., & van Hemert, M. C. 2006, *Faraday Discussions*, 133, 231

van der Marel, N., van Dishoeck, E. F., Bruderer, S., et al. 2013, *Science*, 340, 1199

van der Marel, N., van Dishoeck, E. F., Bruderer, S., Pérez, L., & Isella, A. 2015, *A&A*, 579, A106

van der Marel, N., van Dishoeck, E. F., Bruderer, S., et al. 2016, *A&A*, 585, A58

van der Plas, G., van den Ancker, M. E., Acke, B., et al. 2009, *A&A*, 500, 1137

van Leeuwen, F. 2007, *A&A*, 474, 653

van Zadelhoff, G.-J., van Dishoeck, E. F., Thi, W.-F., & Blake, G. A. 2001, *A&A*, 377, 566

Varnière, P., & Tagger, M. 2006, *A&A*, 446, L13

Viala, Y. P., Letzelter, C., Eidelsberg, M., & Rostas, F. 1988, *A&A*, 193, 265

Visser, R., van Dishoeck, E. F., & Black, J. H. 2009, *A&A*, 503, 323

Walmsley, C. M., Flower, D. R., & Pineau des Forêts, G. 2004, *A&A*, 418, 1035

Walsh, K. J., Morbidelli, A., Raymond, S. N., O'Brien, D. P., & Mandell, A. M. 2011, *Nature*, 475, 206

Walsh, C., Juhász, A., Pinilla, P., et al. 2014, *ApJL*, 791, L6

Walsh, C., Nomura, H., & van Dishoeck, E. 2015, *A&A*, 582, A88

Watson, W. D., Anicich, V. G., & Huntress, W. T., Jr. 1976, *ApJL*, 205, L165

Weidenschilling, S. J. 1977, *MNRAS*, 180, 57

Weingartner, J. C., & Draine, B. T. 2001, *ApJ*, 548, 296

Whipple, F. L. 1972, *From Plasma to Planet*, 211

- 
- Willacy, K., & Woods, P. M. 2009, *ApJ*, 703, 479
- Williams, J. P., Andrews, S. M., & Wilner, D. J. 2005, *ApJ*, 634, 495
- Williams, J. P., & Cieza, L. A. 2011, *ARAA*, 49, 67
- Williams, J. P., & Best, W. M. J. 2014, *ApJ*, 788, 59
- Williams, J. P., & McPartland, C. 2016, *ApJ*, 830, 32
- Wilson, T. L., & Rood, R. 1994, *ARAA*, 32, 191
- Woitke, P., Kamp, I., & Thi, W.-F. 2009, *A&A*, 501, 383
- Woitke, P., Pinte, C., Tilling, I., et al. 2010, *MNRAS*, 405, L26
- Woitke, P., Min, M., Pinte, C., et al. 2016, *A&A*, 586, A103
- Wolcott-Green, J., & Haiman, Z. 2011, *MNRAS*, 412, 2603
- Woodall, J., Agúndez, M., Markwick-Kemper, A. J., & Millar, T. J. 2007, *A&A*, 466, 1197
- Woods, P. M., & Willacy, K. 2009, *ApJ*, 693, 1360
- Wright, C. M., van Dishoeck, E. F., Cox, P., Sidher, S. D., & Kessler, M. F. 1999, *ApJL*, 515, L29
- Wynn-Williams, C. G. 1982, *ARAA*, 20, 587
- Yu, M., Willacy, K., Dodson-Robinson, S. E., Turner, N. J., & Evans, N. J., II 2016, *ApJ*, 822, 53
- Zhang, X., Liu, B., Lin, D. N. C., & Li, H. 2014, *ApJ*, 797, 20
- Zhang, K., Bergin, E. A., Blake, G. A., Cleeves, L. I., & Schwarz, K. R. 2017, *Nature Astronomy*, 1, 0130
- Zhu, Z., Nelson, R. P., Hartmann, L., Espaillat, C., & Calvet, N. 2011, *ApJ*, 729, 47





# SAMENVATTING

*De kosmos zit in ons.  
We zijn gemaakt van sterrenstof.  
We zijn een manier voor het heelal om zichzelf te kennen.*  
Carl Sagan

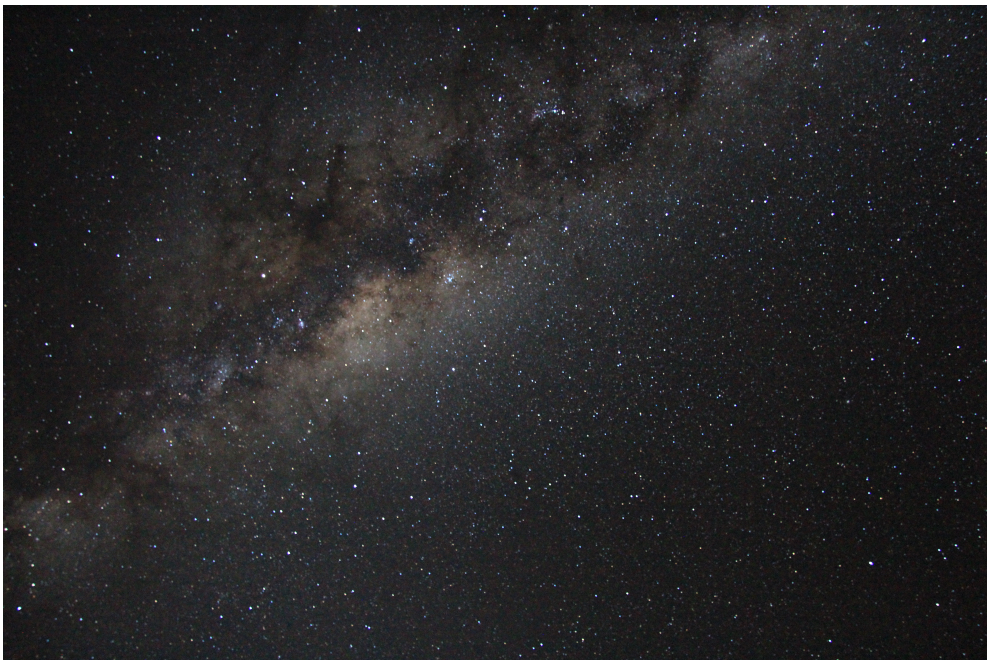


**Figure 7.1:** Foto van het galactisch centrum en de Melkweg – vol met donkere stofwolken – vanaf Cerro Paranal tijdens nieuwe maan op 26 maart 2017 (foto genomen door de auteur met een spiegelreflexcamera, belichting 30 sec).

---

Sinds het begin van de mensheid heeft men omhoog gekeken naar de nachtelijke hemel en zich verwonderd over de betekenis van zo'n majestieuze voorstelling (Fig. 7.1). Oude beschavingen over de hele wereld, van Egypte tot China en van Oceanië tot Zuid-Amerika, kenden mythen en legendes over de sterrenbeelden en nevelachtige objecten die ze aan de hemel zagen. Ook gedurende onze Europese geschiedenis zijn vele dichters, schilders en kunstenaars geïnspireerd geweest door hemelse verschijnselen. De verbazing over de nachtelijke hemel is altijd hand in hand gegaan met het verlangen om de relatie tussen mensheid en universum te begrijpen. Zelfs nu de wetenschap en technologie verder ontwikkeld zijn, en we de fysische en chemische structuur van astronomische objecten kunnen verklaren, blijft deze vraag ons bezig houden. De wetenschap heeft onthuld dat de verbinding tussen de cosmos en ons bestaan veel inniger is dan de wildste pre-wetenschappelijke voorstellingen. Onze kennis over het sterrenstelsel waarin wij ons bevinden vertelt ons bijvoorbeeld dat alle verschijnselen in de Melkweg, van zwarte gaten en ontplofende supernovae tot de exacte locatie van ons zonnestelsel, hebben samengewerkt om te zorgen dat leven kon evolueren tot hoe wij dat nu kennen. Daarnaast kunnen we door de groeiende populatie van ontdekte exoplaneten hun eigenschappen vergelijken met die van ons eigen planetenstelsel. Ondanks het grote aantal bekende planetenstelsels lijkt de inrichting van ons eigen zonnestelsel erg "speciaal" te zijn. Uit omvangrijke studies naar exoplaneten blijkt dat een zon-Jupiter systeem maar in één op duizend planetenstelsels wordt waargenomen. Maar aan de andere kant voorspellen theoretische modellen dat Jupiter een fundamentele rol heeft gespeeld in de evolutie van ons zonnestelsel.

## Vorming van sterren en protoplanetaire schijven

De vraag over onze oorsprong is gecentreerd rond de vorming van sterren en planeten. Hoe vormen sterren en de planeten die om hen heen draaien? Wat zijn de beginvoorwaarden om een planetenstelsel zoals het onze te vormen? Welke rol speelt de fysische structuur en de chemische samenstelling van deze stelsels in wording?

De vorming van sterren begint op grote schaal met het ontstaan van filamenten in gigantische moleculaire wolken. Waarnemingen hebben laten zien dat deze filamenten langgestrekte structuren zijn waarin zich in het algemeen tientallen kleinere draadvormingstructuren vormen. Deze draden vallen uiteindelijk uiteen in kernen met zeer hoge dichtheden die we *pre-stellaire kernen* noemen, omdat ze waarschijnlijk instorten om één of meerdere sterren te vormen. Tijdens dit ineenstorten wordt er een draaiende schijfvormige structuur gevormd zodat het hoekmoment behouden blijft. Via deze schijf beweegt materiaal naar binnen om uiteindelijk in de groeiende protoster te vallen (Fig. 7.2). We noemen het een *protoplanetaire schijf* omdat het de plaats is waar planeten, zoals de aarde en de andere planeten in ons zonnestelsel,

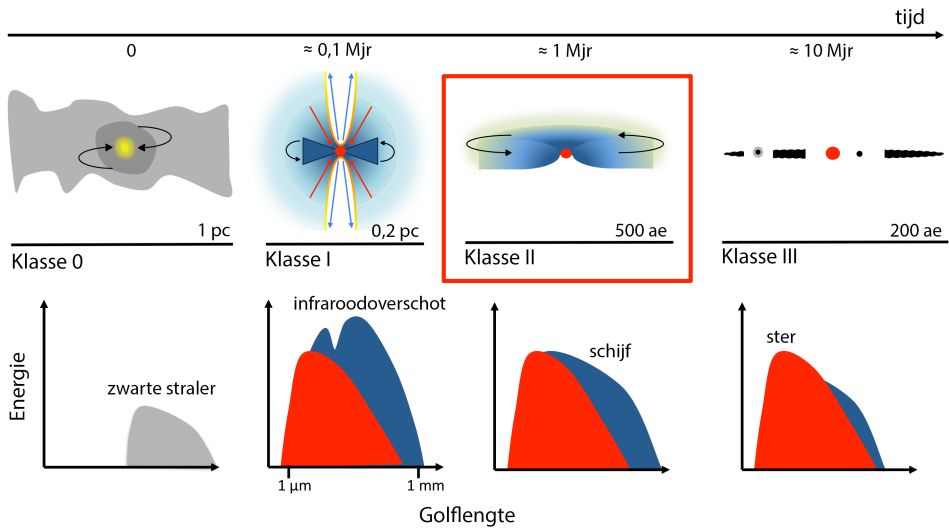


**Figure 7.2:** Illustratie van de vorming van een ster en daaromheen draaiende planeten. De verschillende evolutionaire stadia zijn weergegeven in de bovenste rij. De onderste rij laat de bijbehorende waarneembare kenmerken zien in de vorm van schematische Spectrale Energie Diagrammen (SEDs). Dit proefschrift richt zich op het Klasse II stadium.

gevormd worden.

Protoplanetaire schijven evolueren van een beginstadium waarin ze nog omhuld worden door een grote hoeveelheid gas en stof (Klasse 0 en Klasse I objecten) naar een meer typerende fase waarin ze veel gas herbergen en het omhulsel verdwenen is (Klasse II). In het volgende stadium bevatten ze nog maar weinig gas en moeten grotere lichamen zoals planeten en asteroiden al gevormd zijn (Klasse III). Zoals te zien in de illustratie in Fig. 7.2 worden de diverse evolutionaire stadia gekenmerkt door verschillen in de vorm van hun Spectrale Energie Diagram (SED). Dit proefschrift richt zich op het modeleren van het gas in protoplanetaire schijven tijdens de gasrijke Klasse II fase en het vergelijken van deze resultaten met spiksplinternieuwe waarnemingen van gas en stof in schijven gedaan met de Atacama Large Millimeter/submillimeter Array (ALMA, zie Fig. 7.3).

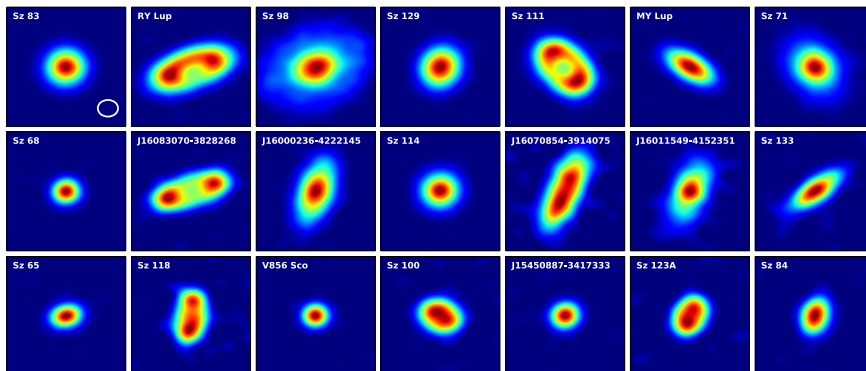


**Figure 7.3:** Compositie van protoplanetaire schijven die met ALMA zijn waargenomen in het stervormingsgebied Lupus en die illustratief zijn voor de grote variëteit aan type schijven. De afbeeldingen laten de thermische straling zien bij een golflengte van  $890 \mu\text{m}$ . Deze straling wordt uitgezonden door stofdeeltjes in de schijf die een grootte hebben van enkele millimeters. Figuur door M. Ansdell.

### Openstaande vragen omtrent protoplanetaire schijven

De totale massa is een fundamentele eigenschap van een schijf, want het bepaalt niet alleen zijn structuur en evolutie, maar ook de kenmerken van het planetenstelsel dat uiteindelijk gevormd wordt. Desondanks is het nog niet gelukt om de massa's van schijven met grote zekerheid af te leiden uit waarnemingen. Schijven bestaan uit gas en stof, en hoewel het gas 99% van de massa uitmaakt, is het het stof dat grotendeels bepaalt wat voor straling uitgezonden wordt. Daar komt nog bij dat het merendeel van het stof bestaat uit deeltjes van enkele millimeters die niet noodzakelijkerwijs goed gemengd zijn met het gas. Om deze redenen zou de massa van het gas en stof dus apart gemeten moeten worden. Verwacht wordt dat het grootste gedeelte van de schijfmassa bestaat uit moleculair waterstof ( $\text{H}_2$ ).  $\text{H}_2$  is echter moeilijk waar te nemen, omdat het niet gemakkelijk geëxciteerd wordt bij de lage temperaturen die heersen in het merendeel van de schijf. Van oudsher wordt daarom de aanwezigheid van gas in schijven afgeleid aan de hand van koolstofmonoxide ( $\text{CO}$ ) emissielijnen die wel gemakkelijk geëxciteerd worden. Maar omdat deze emissie in het algemeen optisch dik is is het erg moeilijk, en modelafhankelijk, om met behulp van  $\text{CO}$  de gasmassa nauwkeurig te bepalen. De belangrijkste vragen die in dit proefschrift behandeld worden zijn de volgende:

- Wat kan het best gebruikt worden als maatstaf voor de gasmassa in protoplanetaire schijven? Zijn de minder voorkomende isotopologen<sup>1</sup> van  $\text{CO}$  hiervoor

<sup>1</sup>Isotopologen zijn moleculen die enkel van elkaar verschillen in hun isotoop samenstelling. Simpel

---

geschikt? Kan gedeutereerd waterstofgas (HD) een goed alternatief zijn en wat zijn hiervan de beperkingen?

- Hoe kunnen huidige en toekomstige waarnemingen met ALMA<sup>2</sup> gebruikt worden om de massa's te bepalen van een statistisch significant aantal schijven?
- Wat is de daadwerkelijke verhouding tussen de gas- en stofmassa in schijven, en hoe wordt de bepaling hiervan beïnvloed door het feit dat een deel van de koolstof en zuurstof opgesloten kan zitten in rotsachtig materiaal?

## Dit proefschrift en een toekomstperspectief

Het bepalen van gasmassa's in schijven is vanaf het begin de rode draad geweest door dit proefschrift. CO isotopologen zijn al vele jaren veelbelovende kandidaten voor het meten van de gasmassa, en door de opkomst van ALMA kunnen zij routinematig waargenomen worden in schijven. Openstaande vragen zijn of chemische isotoop-specifieke processen een belangrijke rol spelen in de verhouding waarin de verschillende isotopologen van CO voorkomen en bij het bepalen van de gasmassa. Het minder voorkomende isotopoloog  $C^{18}O$  wordt inderdaad sneller afgebroken door uv-straling dan de hoofdvorm van koolstofmonoxide,  $^{12}C^{16}O$ . Dit proefschrift begint daarom vanuit een modelleerperspectief. Inmiddels heeft de *Lupus Disk Survey*, uitgevoerd met ALMA, het aantal waarnemingen van CO isotopologen in schijven sterk vergroot, en de modellen die gepresenteerd worden in Hoofdstuk 3 zijn hiermee vergeleken. Hiernaast zijn nog een aantal op (toekomstige) waarnemingen gerichte onderzoeken gedaan.

- Hoofdstuk 2 beschrijft voor het eerst de correcte behandeling van isotoop-specifieke fotolyse in een fysisch-chemisch model voor schijven, genaamd DALI. Isotoop-specifieke fotolyse is het proces dat de onderlinge verhoudingen van de CO isotopologen in de laag waar de CO emissie vandaan komt het meest beïnvloedt. In dit model worden de  $^{13}CO$ ,  $C^{18}O$  en  $C^{17}O$  isotopologen behandeld als aparte soorten in een chemisch netwerk. Daarnaast worden de chemie, de temperatuur structuur, en het stralingstransport van zowel lijn- als continuümstraling in beschouwing genomen. Het belangrijkste resultaat is dat in bepaalde gebieden in de schijf isotoop-specifieke processen leiden tot verhoudingen van de isotopologen die afwijken van de isotoopverhoudingen van

---

gezegd heeft een isotopoloog tenminste één atoom met een ander aantal neutronen dan het normale molecuul.

<sup>2</sup>ALMA is een internationaal samenwerkingsverband tussen de European Southern Observatory (ESO), de Amerikaanse National Science Foundation (NSF) en de National Institutes of Natural Sciences (NINS) van Japen, samen met NRC (Canada), NSC en ASIAA (Taiwan), en KASI (Korea), en in samenwerking met Chili.

---

de elementen. Dit betekent dat schijfmassa's onderschat kunnen worden met meer dan een orde van grootte als de verhouding tussen de isotopologen als constant wordt beschouwd.

- In Hoofdstuk 3 wordt de kleine set modellen die in Hoofdstuk 2 gebruikt zijn om de effecten van isotoop-specifieke CO fotolyse te onderzoeken, uitgebreid. Meer dan 800 schijfmodellen zijn gedraaid voor een reeks verschillende parameters voor de ster en schijf. Voor verschillende inclinaties is de totale fluxdichtheid berekend voor lage  $J$  overgangen van verschillende CO isotopologen. Dit hoofdstuk laat zien dat de totale schijfmassa afgeleid kan worden uit een combinatie van de totale intensiteit van  $^{13}\text{CO}$  en  $\text{C}^{18}\text{O}$ , maar met een grotere foutmarge dan uit voorgaande onderzoeken is gebleken. Deze onnauwkeurigheid kan verkleind worden als de grootte van de schijf, de inclinatie en de kromming van het schijfoppervlak bekend zijn uit andere waarnemingen. De totale intensiteit van de lijnemissie van een aantal lage  $J$  overgangen van verschillende CO isotopologen wordt gepresenteerd en beschreven met eenvoudige vergelijkingen. Verder zijn de effecten van een verminderde hoeveelheid koolstof in het gas en van verschillende verhoudingen tussen de hoeveelheid gas en stof onderzocht.
- In Hoofdstuk 4 worden de fysisch-chemische modellen uit Hoofdstuk 3 gebruikt om waarnemingen van stof en CO isotopologen ( $^{13}\text{CO } J = 3 - 2$  en  $\text{C}^{18}\text{O } J = 3 - 2$ ) in schijven in Lupus te analyseren. Uit eerdere studies stond het aantal schijven waarvoor de gasmassa berekend was op tien. Dit aantal is aanzienlijk vergroot door voor 34 objecten de gasmassa te bepalen. Dit hoofdstuk laat zien dat, als aangenomen wordt dat de hoeveelheid vluchtig koolstof niet verlaagd is, de gasmassa's gebaseerd op CO in het algemeen erg laag zijn voor schijven rond sterren met een zonsachtige massa: vaak minder dan  $1 M_{\text{Jup}}$  (massa van Jupiter). Als gevolg hiervan is de globale verhouding tussen de hoeveelheid gas en stof veel lager dan de verwachte waarde van 100 (de waarde in het interstellair medium). Voor de meeste schijven ligt deze waarde tussen 1 en 10. Lage waarden voor de op CO gebaseerde gasmassa en de verhouding tussen gas en stof kan wijzen op een snel verlies van gas. Andere mogelijke oorzaken zijn chemische evolutie, bijvoorbeeld de omzetting van CO in meer complexe moleculen, of de opslag van koolstof in grotere objecten. De eerste hypothese betekent dat de vorming van reuzenplaneten snel moet gaan of zeldzaam is. Voor de andere verklaring is de betekenis voor de tijdschaal waarop planeetvorming plaatsvindt minder duidelijk.
- In Hoofdstuk 5 wordt met de DALI modellen een andere belangrijke schijfeigenschap onderzocht, namelijk de verdeling van de oppervlaktedichtheid van het gas ( $\Sigma_{\text{gas}}$ ). Robuuste metingen van  $\Sigma_{\text{gas}}$  aan de hand van waarnemin-

---

gen is essentieel om de evolutie van schijven, en het onderlinge belang daarbij van verschillende processen, te begrijpen, alsmede hoe planeten gevormd worden. Recentelijk zijn heeft ALMA waarnemingen gemaakt van de intensiteit van  $^{13}\text{CO}$  emissie als functie van de afstand tot de ster. Dit hoofdstuk onderzoekt of zulke metingen gebruikt kunnen worden als maat voor de oppervlaktedichtheid van het gas over de lengte van de schijf. Uit vergelijkingen met de DALI modellen vinden we dat de intensiteitsverdeling van  $^{13}\text{CO}$  alleen vergelijkbaar is met de oppervlaktedichtheidsverdeling van het gas in het middelste gedeelte van de schijf. In het binnenste gedeelte dicht bij de ster is de emissie optisch dik en neemt daardoor (relatief) af. In de buitenste gebieden neemt de emissie af door een combinatie van vastvriezen aan stofdeeltjes en inefficiënte zelfbescherming tegen uv-straling.

- In Hoofdstuk 6 is een simpele deuterium chemie toegevoegd aan het chemische netwerk in DALI om HD lijnemissie te simuleren. Het doel is om te onderzoeken hoe robuust deze emissie is als maat voor de gasmassa in schijven, en dan met name wat het effect is van de gasmassa op de ver-infraroodstraling van HD, en hoe gevoelig deze emissie is voor de verticale structuur van de schijf. De onzekerheid in de op HD gebaseerde massabepaling blijkt schappelijk te zijn, en waarnemingen van HD moeten beschouwd worden als een belangrijk wetenschappelijk doel voor toekomstige ver-infrarood-missies zoals SPICA.

De voornaamste conclusies van dit proefschrift zijn als volgt.

1. Isotoop-specifieke fotolyse van CO moet op de juiste wijze in beschouwing genomen worden bij het modeleren van emissie van zeldzame CO isotopologen. Als dit niet gebeurt kan de lijnemissie van  $\text{C}^{18}\text{O}$  overschat worden, en de hiervan afgeleide gasmassa onderschat met een orde van grootte, of zelfs meer.
2. De gasmassa van een schijf kan bepaald worden aan de hand van een combinatie van de totale  $^{13}\text{CO}$  en  $\text{C}^{18}\text{O}$  intensiteit, alhoewel de foutmarge hierbij niet verwaarloosbaar is: voor de meest zware schijven kan dit wel twee orden van grootte bedragen.
3. Gasmassa's gebaseerd op CO zijn extreem laag voor schijven in Lupus: vaak minder dan  $1 M_{\text{Jup}}$ . De globale verhouding tussen de gas- en stofmassa ligt voornamelijk tussen 1 en 10. Dit zou geïnterpreteerd kunnen worden als een snel verlies van gas. Het alternatief is een snelle chemische evolutie waarbij CO is omgezet in andere moleculen en dus geen goede maat meer is voor de totale gasmassa.



- 
4. Waarnemingen van  $^{13}\text{CO}$  met een hoekoplossend vermogen groter dan de afmetingen van de schijf kunnen de vorm van de schijf's oppervlaktedichtheidsverdeling afbakenen, mits optische diepte, bevriezing en zelfbescherming tegen uv-straling op de juiste manier behandeld worden in de modellen.
  5. Straling van HD in het ver-infrarood kan gebruikt worden om de gasmassa van schijven te bepalen. De foutmarge is hierbij schappelijk en wordt met name veroorzaakt door de verticale structuur in de schijf. Dergelijke waarnemingen moeten beschouwd worden als een belangrijk wetenschappelijk doel voor toekomstige ver-infraroodmissies.

Het blijft een openstaande vraag hoeveel de gasmassa in schijven bedraagt. CO isotopologen zijn nog steeds veelbelovende kandidaten voor het bepalen van de massa, omdat ze routinematig met ALMA kunnen worden waargenomen. Maar deze methode moet wel geïjkt worden. Dit proefschrift laat zien dat isotoop-specifieke fotolyse belangrijk is voor een goede massabepaling aan de hand van CO isotopologen. Fotolyse is echter niet de voornaamste reden voor zwakke lijnmissie van CO isotopologen, in ieder geval niet voor de TW Hya schijf, maar mogelijk ook in andere schijven. Een proces dat verder onderzocht en beter begrepen moet worden is de afname van vluchtig koolstof. Waar belandt dit koolstof? Het waarnemen van iets complexere moleculen zoals de koolwaterstoffen  $\text{C}_2\text{H}$  en  $c\text{-C}_3\text{H}_2$  zou een manier kunnen zijn om de op CO gebaseerde gasmassa's te ijken. Een andere optie is waarnemingen van [CI], omdat hieruit de hoeveelheid vluchtig koolstof in de bovenste lagen van een schijf kan worden afgeleid. Als uiteindelijk HD emissielijnen met voldoende spectrale resolutie waargenomen kunnen worden met SPICA, dan hebben we een onafhankelijke maat voor de gasmassa in schijven.

Het bepalen van de totale massa van protoplanetaire schijven is niet gemakkelijk. Toch is dit cruciaal omdat het de belangrijkste schijfeigenschap is die nodig is om het ontstaan te begrijpen van planeten zoals onze eigen aarde en de grote verscheidenheid aan exoplaneten<sup>3</sup>.

---

<sup>3</sup>Exoplaneten zijn planeten die om een andere ster dan de zon draaien.

# SUMMARY

*The cosmos is within us.  
We are made of star-stuff.  
We are a way for the universe to know itself.*  
Carl Sagan



**Figure 8.1:** The galactic center and dusty Milky Way as seen on March 26, 2017 on a new moon night from Cerro Paranal (photo taken by the author with Reflex camera, exposure 30s).

---

Since the beginning of human history, men have raised their eyes to the night sky and wondered about the meaning of such a majestic show (Fig. 8.1). Ancient civilizations from different parts of the world, from Egypt to China, from Oceania to southern America, have given life to myths and legends about the constellations and nebulosities that they could spot in the sky. Even throughout our European history many poets, painters and artists have taken inspiration from celestial events. The astonishment in front of the sky has always been accompanied by the need to understand the link between mankind and the universe. Now that science and technology have advanced and we are able to explain the physical and chemical structure of astronomical objects, this question has not been abandoned. Science has revealed to us that the connection of the cosmos with our existence is much deeper than any pre-scientific vision had dared to imagine. For example our knowledge on our hosting galaxy tells us that all phenomena happening in the Milky Way, from the presence of a black hole to that of supernova explosions up to the actual location of our Solar System, have cooperated to allow life to evolve up to the current status. Also, the growing zoo of discovered exoplanets allows us to compare their characteristics with those of our planetary system. Despite the large statistics, it seems that the configuration of our own Solar System is very “special”. Based on exoplanet observational surveys, the Sun-Jupiter system is as common as one in a thousand. On the other hand theoretical modeling favors Jupiter as the fundamental player in the Solar System’s evolution.

## Star formation and protoplanetary disks

The question about our origins centers around star and planet formation. How do stars and planets orbiting around them form? What are the initial conditions needed to generate a planetary system similar to our own? Which roles do the physical architecture and chemical composition of these forming systems play?

On large scales, star formation begins with the formation of filamentary structures inside giant molecular clouds. Observations have shown that filaments are elongated structures, within which typically several dozens of smaller fibers are created and eventually fragment into dense cores. These are defined as *prestellar cores*, as they will likely collapse to form one or more stars. As the collapse proceeds, due to conservation of angular momentum a rotating disk-like structure is formed, through which matter accretes onto the forming protostar (Fig. 8.2). This is called *protoplanetary disk* as it is also the place where planets, like our own Earth and the other Solar System planets, are formed.

Disks evolve from an initial phase where they are still embedded in their extended envelope (Class 0 and Class I objects), to a more typical stage in which they are gas-rich and the envelope has been dissipated (Class II objects), to a more evolved

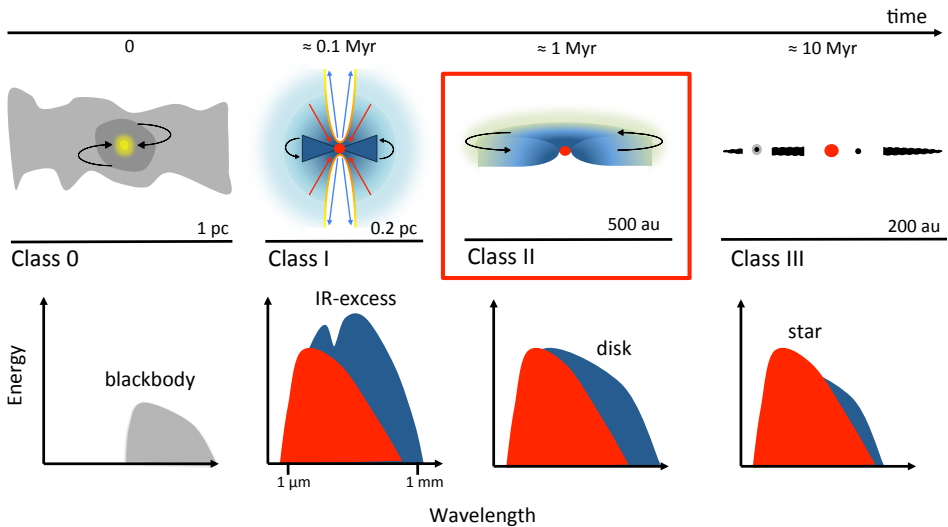


**Figure 8.2:** Sketch of the star and planet formation process in isolation. In the upper panel different evolutionary classes are sketched, while in the lower panel the respective observational features are shown through schematic SEDs. This thesis focuses on the stage of a pre-main sequence star with a disk, called the Class II stage.

phase where they are gas-poor and larger bodies, such as planets and asteroids, must be already formed (Class III objects). As shown by the sketch in Fig. 8.2, the different evolutionary stages have different slopes in their Spectral Energy Distributions (SED). The focus of this thesis is on protoplanetary disks in their gas rich Class II phase through the modeling of their bulk gas component and comparing with brand-new observations of images of gas and dust in disks from the Atacama Large Millimeter/submillimeter Array (ALMA, see Fig. 8.3).

### Open questions in the study of protoplanetary disks

One of the fundamental properties of disks is the total *mass*, as it determines their physics, evolution and the characteristics of the planetary outcomes. Nevertheless disk masses are not yet observationally determined with high confidence. Disks are composed of gas, accounting for 99% of the mass, and dust, which in turn dominates the emission. The bulk of the dust mass is in mm-sized grains, which are not necessarily well mixed with the gas. Accordingly the mass determination of the gaseous and dusty components should in principle be carried out independently. Most of

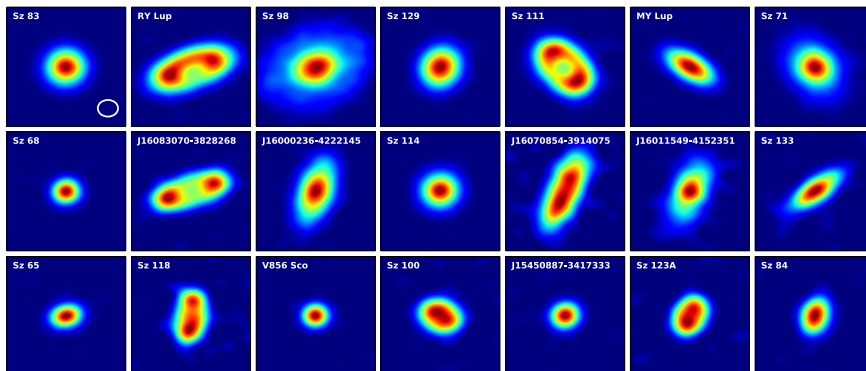


**Figure 8.3:** Image showing the zoo of protoplanetary disks observed with ALMA in the Lupus Star Forming region. These images show the dust thermal emission at  $890 \mu\text{m}$  caused by mm-sized grains present in the disks (Credit: M. Ansdell).

the disk mass is expected to be in the form of molecular gas, essentially molecular hydrogen ( $\text{H}_2$ ). However,  $\text{H}_2$  is not easily excited and observable at the cold temperatures in the bulk of the disk. Hence, traditionally, the presence of gas in disks has been constrained through carbon monoxide (CO) emission lines, easily excited in disks. However the emission is generally very optically thick, so using CO to measure accurately the gas mass is very difficult and model dependent. The main questions that are tackled in this PhD thesis are the following.

- Which is the best gas mass tracer in protoplanetary disks? Could the less abundant isotopologues<sup>1</sup> of CO serve this purpose? Would hydrogen deuteride (HD) be a good alternative and what are its limitations?
- How can current and future ALMA observation be used to determine the masses of a statistically significant sample of disks?
- What is the actual gas-to-dust mass ratio in disks and how is its determination affected by the fact that a fraction of the carbon and oxygen may be locked up in refractory material?

---

<sup>1</sup>Isotopologues are molecules that differ only in their isotopic composition. Simply, the isotopologue of a chemical species has at least one atom with a different number of neutrons than the parent.

---

## This thesis and future outlook

Determining disk gas masses has been the leading question of this PhD thesis since its origin. CO isotopologues have been promising gas mass tracer candidates for many years and with the advent of ALMA their detection in disks has become routine. The still open question is if chemical isotope-selective effects play a major role in setting the mutual abundance ratios of CO isotopologues and in the determination of disk masses. The rarer isotopologue  $C^{18}O$  is indeed destroyed by UV radiation faster than the main form of carbon monoxide,  $^{12}C^{16}O$ . Therefore this thesis starts from the modeling perspective. Subsequently a larger sample of CO isotopologues observations in disks has been provided by the *Lupus Disk Survey* with ALMA. The grid of models presented in Chapter 3 has therefore been compared with observations and some more observation-motivated projects have been carried out.

- In Chapter 2 isotope-selective photodissociation, the main process controlling the relative abundances of CO isotopologues in the CO-emissive layer, was properly treated for the first time in a physical-chemical disk model called DALI. The chemistry, thermal balance, line, and continuum radiative transfer were all considered together with a chemical network that treats  $^{13}CO$ ,  $C^{18}O$  and  $C^{17}O$ , isotopologues as independent species. The main result is that isotope selective processes lead to regions in the disk where the isotopologues abundance ratios are considerably different from the elemental ratios. Accordingly, considering CO isotopologue ratios as constants may lead to underestimating disk masses by up to an order of magnitude or more.
- In Chapter 3 the small grid of models used in Chapter 2 to investigate the effects of CO isotope-selective photodissociation has been expanded. More than 800 disk models have been run for a range of disk and stellar parameters. Total fluxes have been ray-traced for different CO isotopologues and for various low  $J$ -transitions for different inclinations. This chapter shows that a combination of  $^{13}CO$  and  $C^{18}O$  total intensities allows inference of the total disk mass, although with larger uncertainties, compared with the earlier studies. These uncertainties can be reduced if one knows the disk's radial extent, inclination and flaring from other observations. Finally, total line intensities for different CO isotopologue and for various low- $J$  transitions are provided as functions of disk mass and fitted to simple formulae. The effects of a lower gas-phase carbon abundance and different gas-to-dust ratios are investigated as well.
- In Chapter 4 the grid of physical-chemical models presented in Chapter 3 has been employed to analyze continuum and CO isotopologues ( $^{13}CO$   $J = 3 - 2$  and  $C^{18}O$   $J = 3 - 2$ ) observations of Lupus disks. Disk gas masses have been

---

calculated for a total of 34 sources, expanding the sample of 10 disks studied previously. This chapter shows that overall CO-based gas masses are very low for disks orbiting a solar mass-like star, often smaller than  $1M_J$  (mass of Jupiter), if volatile carbon is not depleted. Accordingly, global gas-to-dust ratios are much lower than the expected ISM-value of 100, being predominantly between 1 and 10. Low CO-based gas masses and gas-to-dust ratios may indicate rapid loss of gas, or alternatively chemical evolution, e.g. via sequestering of carbon from CO to more complex molecules, or carbon locked up in larger bodies. The first hypothesis would imply that giant planet formation must be quick or rare, while for the latter the implication on planet formation timescales is less obvious.

- In Chapter 5 another important disk property has been investigated with DALI models, i.e. the gas surface density distribution  $\Sigma_{\text{gas}}$ . Reliable observational measurements of  $\Sigma_{\text{gas}}$  are key to understand disk evolution and the relative importance of different processes, as well as how planet formation occurs. This chapter investigates whether  $^{13}\text{CO}$  line radial profiles, such as those recently acquired by ALMA, can be employed as a probe of the gas surface density profile. By comparing with DALI simulations we find that  $^{13}\text{CO}$  radial profiles follow the density profile in the middle-outer disk. The emission drops in the very inner disk due to optical depth, and in the very outer disk due to a combination of freeze-out and inefficient self-shielding.
- In Chapter 6 simple deuterium chemistry has been added to the chemical network in DALI to simulate HD lines in disks. The aim is to examine the robustness of HD as a tracer of the disk gas mass, specifically the effect of gas mass on the HD far infrared emission and its sensitivity to the disk vertical structure. The uncertainty on HD-mass determination due to disk structure is found to be moderate and HD observations should be considered as an important science goal for future far-infrared missions, such as SPICA.

The main conclusions of this thesis are the following:

1. CO isotope-selective photodissociation needs to be properly considered when modeling rare CO isotopologues emission. Otherwise,  $\text{C}^{18}\text{O}$  lines emission could be overestimated and the derived gas masses could be underestimated by up to an order of magnitude or more.
2. Disk gas masses can be inferred by a combination of  $^{13}\text{CO}$  and  $\text{C}^{18}\text{O}$  total intensities, although with non-negligible uncertainties, up to two orders of magnitude for very massive disks.
3. CO-based disk gas masses derived in Lupus are extremely low, often smaller than  $1 M_J$  and the global gas-to-dust ratios are predominantly between 1 and

- 
10. This may be interpreted as either rapid loss of gas, or fast chemical evolution.
  4. The shape of the disk surface density distribution can be constrained by spatially resolved  $^{13}\text{CO}$  observations, if optical depth, freeze-out and self shielding are properly considered in the modeling.
  5. HD far-infrared emission can be used to determine disk gas masses with moderate uncertainty which depends mainly on the disk vertical structure. Such observations should be considered as an important science goal for future far-infrared missions.

The question on disk gas masses remains open. CO isotopologues are still promising mass tracers candidates, as their detection is routine for ALMA, but they need to be calibrated. This thesis shows that the process of isotope-selective photodissociation is important for a good interpretation of CO isotopologues as gas mass tracers. However photodissociation, at least for the case of TW Hya and possibly for other disks, is not the main process responsible for the observed faint CO isotopologues lines. In turn, volatile carbon depletion is a process that needs to be further investigated and understood. Where does the carbon go? The detection of slightly more complex molecules, such as the hydrocarbons  $\text{C}_2\text{H}$  and  $c\text{-C}_3\text{H}_2$  could be a way to calibrate CO-based gas masses. Another option is to enlarge the sample of [CI] line detections, which allow inference of the volatile carbon abundance in the upper regions of the disk. Finally, if the HD fundamental lines can be covered at high enough spectral resolution with SPICA, their detection will provide an unique independent tracer of the disk mass.

Determining the total mass of protoplanetary disks is challenging but crucial, as this is the main disk property that one needs in order to understand how planets such as our own Earth or the diverse observed exo-planets<sup>2</sup> form.

---

<sup>2</sup>Exo-planets are planets orbiting a star that is not the Sun.





## RIASSUNTO

*Il cosmo é dentro di noi.  
Siamo fatti di materia stellare.  
Noi siamo il modo in cui l'universo può conoscere se stesso.*  
Carl Sagan

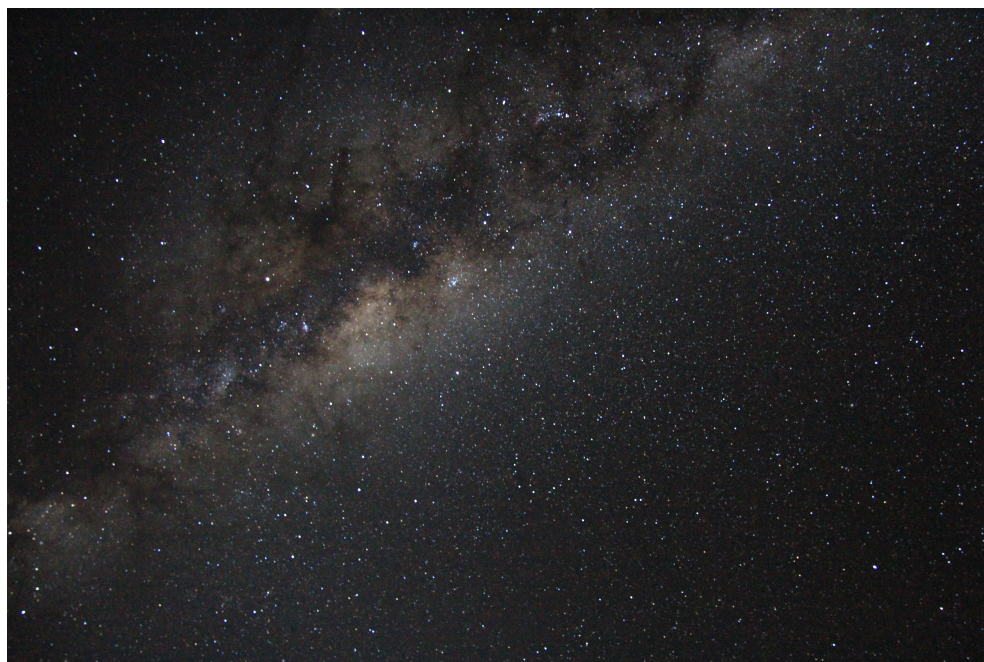


**Figure 9.1:** Fotografia del centro galattico e della Via Lattea ottenuta il 26 Marzo 2017 in una notte di luna nuova a Cerro Paranal in Cile (la fotografia é stata scattata dall'autrice con una macchina fotografica Reflex ed un'esposizione di 30 secondi).

---

**F**In dall'inizio della storia dell'umanità, gli uomini hanno alzato gli occhi al cielo stellato e si sono interrogati sul significato di quello stupendo spettacolo (vedi Figura 9.1). Le più antiche civiltazioni in varie parti del mondo, dall'Egitto alla Cina, dall'Oceania all'America del Sud, hanno dato vita a miti e leggende legati alle costellazioni e alle nebulosità che riuscivano ad identificare nel cielo. Anche in Europa, in varie epoche storiche, poeti, pittori e artisti si sono ispirati agli eventi celesti. Lo stupore davanti al cielo stellato è stato sempre accompagnato dal desiderio di comprendere il legame tra l'umanità e l'universo. Questa domanda non ci ha abbandonato, anche ora che la scienza e la tecnologia si sono svilupppate e siamo in grado di spiegare la struttura chimica e fisica di molti oggetti astronomici. La scienza ci ha rivelato che la connessione tra il cosmo e la nostra esistenza è ancora più profonda di quanto si potesse immaginare in una visione pre-scientifica. Ad esempio, la conoscenza della nostra galassia ci ha permesso di scoprire che tutti i fenomeni che accadono nella Via Lattea, dalla presenza di un buco nero alle esplosioni di supernova fino alla particolare localizzazione del nostro Sistema Solare, hanno cooperato a permettere che la vita si sviluppasse sulla Terra fino allo stato attuale. Inoltre, lo zoo - sempre in crescita - di pianeti scoperti recentemente attorno ad altre stelle ci ha permesso di paragonare le caratteristiche di questi "exo-pianeti" con quelle del nostro sistema planetario. Nonostante la statistica elevata, sembra che la configurazione del Sistema Solare sia "speciale". Basandosi sulle osservazioni di exo-pianeti, la combinazione di una stella come il Sole e di un pianeta come Giove ha la probabilità di accadere una volta su un milione. I modelli teorici ci dicono invece che Giove è stato probabilmente un elemento chiave per lo sviluppo del nostro Sistema Solare.

## Formazione stellare e dischi protoplanetari

La domanda ancora aperta riguardo la nostra origine è strettamente legata alla formazione stellare e planetaria. Come nascono le stelle ed i pianeti che orbitano attorno ad esse? Quali sono le condizioni iniziali necessarie per generare un sistema planetario simile al nostro? Che ruolo giocano la morfologia e la composizione chimica nella formazione ed evoluzione di questi sistemi?

A grandi scale la formazione stellare inizia con la creazione di strutture filamentari all'interno di giganti nubi molecolari. Le osservazioni hanno mostrato che i filamenti sono strutture elongate all'interno delle quali si possono trovare parecchie dozzine di fibre più piccole che infine collasseranno sotto l'effetto della propria gravità e si frammenteranno in nuclei densi. Questi ultimi vengono chiamati *nuclei prestellari*, dato che il loro collasso porterà alla formazione di una o più stelle. Mentre il collasso procede, per la conservazione del momento angolare, una struttura rotante a forma di disco viene generata e permette l'accrescimento di materiale sulla protostella in formazione (Figura 9.2). Questa struttura è chiamata *disco protoplan-*

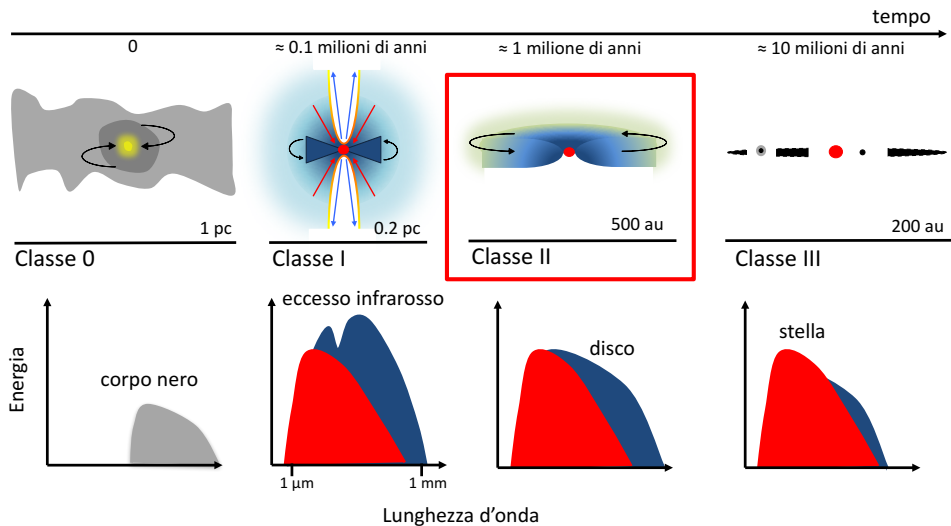


**Figure 9.2:** Rappresentazione schematica della formazione stellare e planetaria in un contesto isolato. Nel pannello superiore vengono presentate le varie classi evolutive, mentre nel pannello sottostante vengono mostrate le caratteristiche osservative legate ad ad ogni fase attraverso una semplificazione della SED (Distribuzione di Energia Spettrale). Questa tesi si concentra sulla fase di una stella di pre-sequenze principale circondata da un disco, chiamata Classe II.

*etario* dato che rappresenta anche il luogo dove i pianeti - come la Terra e gli altri elementi del Sistema Solare - vengono generati.

I dischi evolvono da una fase iniziale nella quale sono ancora immersi nel loro involucro (oggetti di Classe 0 e Classe I), ad uno stadio tipico nel quale essi sono ricchi di gas ed il loro involucro é stato dissipato (oggetti di Classe II), fino ad una fase piú evoluta dove essi sono poveri di gas ed al loro interno oggetti estesi, come pianeti ed asteroidi, devono già essersi formati (oggetti di Classe III). Come mostrato dallo schema in Figura 9.2, da un punto di vista osservativo la forma della Distribuzione Spettrale di Energia (SED) puó darci informazioni sulla fase evolutiva degli oggetti osservati. Questa tesi si focalizza sullo studio dei dischi protoplanetari di Classe II, quindi ricchi di gas, attraverso la modellizzazione della loro componente gassosa ed attraverso il paragone con nuove immagini di gas e polvere in dischi ottenute con l' Atacama Large Millimeter/submillimeter Array (ALMA<sup>1</sup>, vedi Figura 9.3).

<sup>1</sup>ALMA é un partenariato internazionale dello European Southern Observatory (ESO), della Fon-

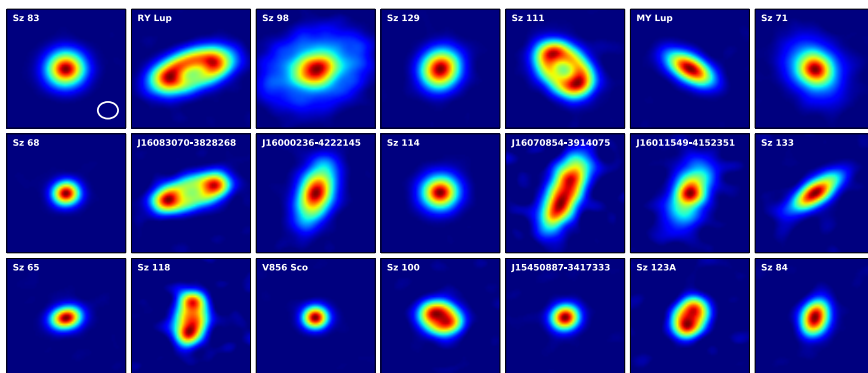


**Figure 9.3:** “Zoo” dei dischi protoplanetari osservati con ALMA nella regione di formazione stellare in Lupo. Queste immagini mostrano l’emissione termica della polvere a  $890 \mu\text{m}$  causata dalla presenza di grani millimetrici nei dischi (Credit: M. Ansdell).

### Domande aperte nello studio dei dischi protoplanetari

Una delle proprietà fondamentali dei dischi è la loro *massa* totale, dato che essa determina la loro evoluzione e le caratteristiche dei pianeti si che andranno a formare. Nonostante ciò, le masse dei dischi non sono ancora state determinate accuratamente tramite osservazioni. I dischi sono composti per il 99 % della loro massa da gas, e da polvere - per il restante 1% della massa - che però domina l’emissione osservabile. La maggior parte della massa di polvere risiede in grani della dimensione del millimetro, che non necessariamente sono ben mescolati con il gas. Proprio per questo la determinazione della massa del gas e della polvere dovrebbe essere fatta indipendentemente. Ci si aspetta che la maggior parte della massa del disco sia nella forma di gas molecolare, in particolare di idrogeno molecolare ( $\text{H}_2$ ). Tuttavia le righe dell’  $\text{H}_2$  non sono facilmente eccitate e quindi osservabili alle basse temperature a cui si trova la maggior parte del materiale nei dischi. Di conseguenza, tradizionalmente la presenza di gas nei dischi è stata rilevata tramite righe di emissione del monossido di carbonio (CO), che invece vengono eccitate facilmente alle condizioni termo-fisiche trovate nei dischi. Tuttavia l’emissione di queste righe è generalmente otticamente spessa, quindi è difficile sfruttarla per determinare le masse dei dischi in maniera accurata e dipende dai modelli utilizzati. Le principali domande affrontate da questa tesi di dottorato sono le seguenti:

---

dazione Nazionale Scientifica negli U.S.A. (NSF) e dell’ Istituto Nazionale di Scienze Naturali (NINS) del Giappone, insieme al NRC (Canada), NSC e ASIAA (Taiwan), e KASI (Repubblica di Korea), in cooperazione con la Repubblica del Cile.

- 
- Qual'è il miglior tracciante della massa dei dischi protoplanetari? Possono gli isotopologi<sup>2</sup> meno abbondanti del CO essere una soluzione? È possibile che il deuterio di idrogeno (HD) sia una buona alternativa e quali sono le sue limitazioni?
  - Come possono osservazioni - presenti e future - ottenute con ALMA essere usate per determinare la massa di un numero statisticamente interessante di dischi?
  - Qual'è la vera frazione di massa in gas e polvere nei dischi e come la sua determinazione è contaminata dal fatto che parte del carbonio e dell'ossigeno possano essere bloccati in materiale refrattario?

## Questa tesi e le sue prospettive future

Determinare la massa di gas nei dischi protoplanetari è stata la domanda che ha guidato questa tesi di dottorato fin dalla sua nascita. Gli isotopologi del CO sono stati considerati come promettenti traccianti della massa per molti anni e con l'avvento di ALMA il loro rilevamento è diventato routine.

La domanda ancora aperta è se effetti chimici, che agiscono selettivamente su diversi isotopologi, giochino un ruolo importante nel regolare le abbondanze relative tra i diversi isotopologi del CO e nella determinazione della massa dei dischi. L'isotopologo più raro, il C<sup>18</sup>O, è infatti distrutto dalla radiazione UV più velocemente del classico monossido di carbonio, il <sup>12</sup>C<sup>16</sup>O. Questa tesi inizia quindi la sua investigazione da un punto di vista teorico. Successivamente un insieme di osservazioni degli isotopologi del CO in dischi sono state rese disponibili dalla *Survey di Dischi in Lupus* con ALMA. La griglia di modelli presentati nel Capitolo 3 sono quindi stati paragonati con le osservazioni e alcuni progetti motivati dai dati osservati sono stati realizzati.

- Nel Capitolo 2 la fotodissociazione selettiva degli isotopologi, ovvero il processo che principalmente controlla le abbondanze relative degli isotopologi del CO nella zona del disco dove esso emette, è stata trattata in modo accurato per la prima volta in un modello fisico-chimico di dischi chiamato DALI. La chimica, il bilancio termico ed il trasporto radiativo del continuo e delle righe sono stati considerati contemporaneamente con un network chimico che tratta <sup>13</sup>CO, C<sup>18</sup>O e C<sup>17</sup>O come specie indipendenti. Il risultato principale è che processi chimici selettivi degli isotopologi portano ad avere regioni del disco dove la

---

<sup>2</sup>Gli isotopologi sono molecole che hanno come unica differenza la loro composizione isotopica. Semplificamente, l'isotopologo di una specie chimica ha almeno un atomo con un numero di neutroni differente dalla molecola madre.

---

frazione delle abbondanze di diversi isotopologi é molto diversa dalla frazione isotopica degli elementi. Di conseguenza, assumere queste frazioni con i valori costanti ottenuti dalle frazioni isotopiche puó portare a sottostimare le masse dei dischi di piú di un ordine di grandezza.

- Nel capitolo 3 la piccola griglia di modelli usata nel Capitolo 2 é stata espansa. Piú di 800 modelli sono stati lanciati per coprire un spettro di parametri stellari e del disco molto piú ampio. I flussi integrati delle righe di emissione sono stati simulati per diversi isotopologi del CO nelle basse transizioni rotazionali e per varie inclinazioni del disco. Questo capitolo mostra che combinando i flussi totali di riga del  $^{13}\text{CO}$  e del  $\text{C}^{18}\text{O}$  é possibile ricavare la massa totale dei dischi, anche se con incertezze non trascurabili in paragone a studi precedenti. Queste incertezze possono essere ridotte se l'estensione radiale e verticale e l'inclinazione del disco sono note da dati osservativi. Infine, le intensitá di linea totali per diversi isotopologi del CO e per varie transizioni rotazionali sono fornite e fittate con semplici relazioni analitiche. Sono stati anche investigati gli effetti provocati sia dalla bassa abbondanza di carbonio nello stato gassoso, che di basse frazioni di massa di gas su massa di polvere.
- Nel capitolo 4 la griglia di modelli presentati nel capitolo 3 é stata utilizzata per analizzare il continuo e le righe degli isotopologi del CO ( $^{13}\text{CO } J = 3 - 2$  e  $\text{C}^{18}\text{O } J = 3 - 2$ ) osservati nei dischi in Lupus. Le masse del gas dei dischi sono state calcolate per 34 sorgenti, espandendo il gruppo di 10 dischi studiati precedentemente. Questo capitolo mostra che in generale le masse di gas basate sul CO sono estremamente basse per dischi che orbitano stelle di tipo solare, spesso piú basse di una massa di Giove se l'abbondanza di carbonio non é ridotta. Di conseguenza, le frazioni di massa di gas-su-polvere sono molto piú basse del valore atteso 100 che é osservato nel mezzo interstellare, oscillando principalmente tra 1 e 10. Masse del gas e frazioni di massa di gas-su-polvere basate sul CO cosí basse possono indicare una perdita di gas molto rapida, o, alternativamente, un'evoluzione chimica che sequestrerebbe il carbonio dal CO per bloccarlo in molecole piú complesse o in oggetti solidi piú grandi. La prima ipotesi implicherebbe che la formazione di pianeti giganti debba essere rapida o rara, mentre per il secondo scenario le implicazioni sui tempi scala della formazione planetaria sarebbe meno ovvia.
- Nel capitolo 5 un'altra fondamentale proprietá dei dischi é stata investigata con i modelli DALI, ovvero la distribuzione di densitá superficiale del gas  $\Sigma_{\text{gas}}$ . Per comprendere l'evoluzione dei dischi, l'importanza relativa dei vari processi coinvolti in essa e la formazione dei pianeti, sarebbe cruciale costringere  $\Sigma_{\text{gas}}$  in maniera solida dalle osservazioni. Questo capitolo si domanda se i profili radiali delle righe del  $^{13}\text{CO}$ , come quelli osservati recentemente con

---

ALMA, possano essere utilizzati per derivare il profilo di densità superficiale del gas. Paragonando i risultati ottenuti con i modelli DALI, troviamo che i profili radiali del  $^{13}\text{CO}$  seguono i profili di densità nella zona intermedia del disco. L'emissione cala a raggi molto piccoli a causa dello spessore ottico e nelle zone esterne del disco, a grandi raggi, a causa del freeze-out e del fatto che il self-shielding è inefficiente.

- Nel capitolo 6 il network chimico in DALI è stato espanso con l'aggiunta della chimica semplificata del deuterio in modo da poter simulare le righe del HD. L'obiettivo è quello di esaminare la robustezza del HD come tracciante della massa dei dischi, in particolare l'effetto della massa del gas e della estensione verticale del disco sulle righe infrarosse dell'HD. Troviamo che la determinazione della massa basata sul HD ha un'incertezza moderata. Osservazioni del HD dovrebbero essere quindi considerate come un importante obiettivo scientifico per future missioni nel lontano infrarosso, come ad esempio SPICA.

Le conclusioni principali di questa tesi sono:

1. La fotodissociazione selettiva degli isotopologi del CO deve essere considerata nei modelli quando si simula l'emissione degli isotopologi rari. Altrimenti le righe di emissione del  $\text{C}^{18}\text{O}$  potrebbero essere sovrastimate e le masse del gas sottostimate fino a un ordine di grandezza o più.
2. La massa di gas nei dischi può essere misurata combinando l'intensità integrata delle righe del  $^{13}\text{CO}$  e del  $\text{C}^{18}\text{O}$ , anche se con incertezze non trascurabili, fino a due ordini di grandezza per dischi molto massivi.
3. Le masse del gas nei dischi in Lupus misurate dall'emissione del CO risultano essere molto basse, spesso minori di una massa di Giove, e le frazioni globali di massa del gas rispetto alla massa della polvere oscillano tra 1 e 10. Questo può essere interpretato come rapida perdita di gas da parte del disco, oppure come rapida evoluzione chimica.
4. La forma della distribuzione superficiale di densità nei dischi può essere caratterizzata da osservazioni spazialmente risolte di  $^{13}\text{CO}$ , se lo spessore ottico, il freeze-out e il self-shielding sono considerati propriamente nei modelli.
5. L'emissione del HD nel lontano infrarosso può essere usata per determinare la massa dei dischi con una moderata incertezza che dipende principalmente dalla struttura verticale del disco. Questo tipo di osservazioni dovrebbe essere considerato come un importante obiettivo scientifico per future missioni nel lontano infrarosso



---

Il quesito sulla massa gassosa dei dischi protoplanetari rimane irrisolto. Gli isotopologi del CO sono ancora dei promettenti candidati come traccianti della massa dato che la loro rilevazione é routine per ALMA, ma hanno bisogno di essere calibrati. Questa tesi mostra che il processo di fotodissociazione selettiva é importante per una buona interpretazione degli isotopologi del CO come traccianti di massa. Tuttavia, la fotodissociazione, almeno per il caso di TW Hya e probabilmente per altri dischi, non é il fenomeno principalmente responsabile delle righe di emissione cosí tenui osservate negli isotopologi del CO. D'altra parte, la riduzione dell'abbondanza di carbonio in forma gassosa, che deve ancora essere investigata in maniera piú precisa, potrebbe esserne la causa principale. Dove va a finire il carbonio? La rilevazione di molecole leggermente piú complesse, come ad esempio gli idrocarburi  $C_2H$  e  $c-C_3H_2$ , potrebbe essere una soluzione per la calibrazione delle masse in gas derivate dal CO. Un'altra opzione é quella di allargare il campione di dischi in cui il [CI] é stato rilevato e ciò permetterebbe di determinare l'abbondanza di carbonio volatile negli strati superficiali del disco. Infine, se la principale transizione rotazionale dell'HD potrà essere osservata a risoluzione spettrale abbastanza alta con SPICA, la sua rilevazione fornirá una misura della massa dei dischi indipendente dal CO.

Determinare la massa totale dei dischi é una sfida, ma é cruciale tentare di risolvere questo enigma dato che essa é una delle proprietá fondamentali che bisogna constringere per poter comprendere come i pianeti si formano, a partire dal nostro pianeta Terra fino all'immensa varietá di esopianeti osservati attorno ad altre stelle.

# LIST OF PUBLICATIONS

## Refereed Publications

1. *New insights into the nature of transition disks from a complete disk survey of the Lupus star forming region*  
van der Marel, N., Williams, J.P., Ansdell, M., Manara, C.F., **Miotello, A.**, Tazzari, M., Testi, L., Hogerheijde, M., Bruderer, S., van Terwisga, S.E., van Dishoeck, E.F., (2018) accepted for publication in the *Astrophysical Journal*.
2. *Physical properties of dusty protoplanetary disks in Lupus: evidence for viscous evolution?*  
Tazzari, M., Testi, L., Natta, A., Ansdell, M., Carpenter, J., Guidi, G., Hogerheijde, M., Manara, C.F., **Miotello, A.**, van der Marel, N., van Dishoeck, E.F., Williams, J.P., (2017) *Astronomy & Astrophysics*, 606, A88.
3. *Far-infrared HD emission as a measure of protoplanetary disk mass (Chapter 6)*  
Trapman, L., **Miotello, A.**, Kama, M., van Dishoeck, E.F., Bruderer, S., (2017) *Astronomy & Astrophysics*, 605, A69.
4. *An ALMA survey of protoplanetary disks in the  $\sigma$  Orionis cluster*  
Ansdell, M., Williams, J.P., Manara, C.F., **Miotello, A.**, Facchini, S., van der Marel, N., Testi, L., van Dishoeck, E.F., (2017) *Astronomical Journal*, 153, 240.
5. *ALMA unveils rings and gaps in the protoplanetary system HD 169142: signatures of two giant protoplanets*  
Fedele, D., Carney, M., Walsh, C., **Miotello, A.**, Klaassen, P., Bruderer, S., Henning, T., van Dishoeck, E.F., (2017) *Astronomy & Astrophysics*, 600, A72.
6. *Lupus disks with faint CO isotopologues: low gas/dust or high carbon depletion? (Chapter 4)*  
**Miotello, A.**, van Dishoeck, E.F., Williams, J.P., Ansdell, M., Guidi, G., Hogerheijde, M., Manara, C.F., Tazzari, M., Testi, L., van der Marel, N., van Terwisga, S., (2017) *Astronomy & Astrophysics*, 599, A113.

- 
7. *Determining protoplanetary disk gas masses from CO isotopologues line observations (Chapter 3)*  
**Miotello, A.**, van Dishoeck, E.F., Kama, M., Bruderer, S., (2017) *Astronomy & Astrophysics*, 594, A85.
  8. *ALMA survey of Lupus protoplanetary disks. I. dust and gas Masses*  
Ansdell, M., Williams, J.P., van der Marel, N., Carpenter, J., Guidi, G., Hogerheijde, M., Mathews, G.S., Manara, C.F., **Miotello, A.**, Natta, A., Oliveira, I., Tazzari, M., Testi, L., van Dishoeck, E.F., van Terwisga, S.E., (2016) *The Astrophysical Journal*, 828, 46.
  9. *Volatile-carbon locking and release in protoplanetary disks. A study of TW Hya and HD 100546*  
Kama, M., Bruderer, S., van Dishoeck, E.F., Hogerheijde, M., Folsom, C.P., **Miotello, A.**, Fedele, D., Belloche, A., Güsten, R., Wyrowski, F., (2016) *Astronomy & Astrophysics*, 592, A83.
  10. *Evidence for a correlation between mass accretion rates onto young stars and the mass of their protoplanetary disks*  
Manara, C.F., Rosotti, G., Testi, L., Natta, A., Alcalá, J.M., Williams, J.P., Ansdell, M., **Miotello, A.**, van der Marel, N., Tazzari, M., Carpenter, J., Guidi, G., Mathews, G.S., Oliveira, I., Prusti, T., van Dishoeck, E.F., (2016) *Astronomy & Astrophysics*, 591, L3.
  11. *Resolved gas cavities in transitional disks inferred from CO isotopologs with ALMA*  
van der Marel, N., van Dishoeck, E.F., Bruderer, S., Andrews, S.M., Pontoppidan, K.M., Herczeg, G.J., van Kempen, T., **Miotello, A.**, (2016) *Astronomy & Astrophysics*, 585, A58.
  12. *Protoplanetary disk masses from CO isotopologue line emission (Chapter 2)*  
**Miotello, A.**, Bruderer, S., van Dishoeck, E.F., (2014) *Astronomy & Astrophysics*, 572, A96.
  13. *Grain growth in the envelopes and disks of Class I protostars*  
**Miotello, A.**, Testi, L., Lodato, G., Ricci, L., Rosotti, G., Brooks, K., Maury, A., Natta, A., (2014) *Astronomy & Astrophysics*, 567, A32.
  14. *Evidence of photoevaporation and spatial variation of grain sizes in the Orion 114-426 protoplanetary disk*  
**Miotello, A.**, Robberto, M., Potenza, M.A.C., Ricci, L., (2012) *The Astrophysical Journal*, 757, 78.

# CURRICULUM VITAE

I was born on July 22<sup>nd</sup> 1988 to Paola Pignoloni and Roberto Miotello in Gallarate, Italy. For the first 20 years of my life my home town has been Arsago Seprio, a small village in northern Italy. There I attended primary and secondary school, while I went to high school at Liceo Scientifico “Leonardo da Vinci” in the nearby town of Gallarate. I have always been particularly passionate about mathematics and science, but also about art, philosophy and sport. My decision to study Physics at the Università degli Studi di Milano was lead by the certainty that this was the subject where I would have learned the most.

Already at the end of my Bachelor my interest was caught by Astrophysics. Under the supervision of Dr. Marco A.C. Potenza and Dr. Massimo Robberto (STScI) I carried out my Bachelor’s degree Thesis on HST (Hubble Space Telescope) observations of a protoplanetary disk in the Orion Star Forming Region to study its dust particles properties. This project was completed during a Summer Studentship program at STScI in 2011 and ended up in my first publication in 2012. I carried out my Master studies in Physics, with a focus on Astrophysics, at the Università degli Studi di Milano. My Master degree Thesis on dust grain growth in Young Stellar Objects was supervised by Prof. Giuseppe Lodato and Dr. Leonardo Testi (ESO) and was mainly carried out at ESO in Garching. There, I met Prof. Ewine F. van Dishoeck for the first time, who, not much later, offered me a PhD position at the Leiden Observatory. I accepted that position and started my PhD in June 2013 as that would have been the best opportunity to learn about the gas content in protoplanetary disks.

In the following four and a half years, during my PhD, I have carried out my research on the molecular gas, in particular carbon monoxide isotopologues, in protoplanetary disks with the aim of determining their total mass. In practice, I have learned about physical-chemical modelling of disks and run many simulations. Toward the end of my PhD I started working with observations, specifically with ALMA data in the Lupus star-forming region and I compared them with my models. The results are presented in this thesis. The different projects have been presented to conferences and workshops all over the world. I worked for the first year of my PhD at the Max Planck Institute for Extraterrestrial Physics in Garching (Germany) and the following three years at Leiden Observatory. There I had the opportunity

---

to train Master's students for their Master Colloquia and to help in their evaluation. Furthermore, I had the pleasure to supervise the M.Sc. project of Leon Trapman, which became one of the Chapters of this thesis. In these four and a half years I also bore three marvellous children.

In October 2017 I have started a three-year postdoctoral position as ESO Research Fellow in Garching (Germany).

# ACKNOWLEDGEMENTS

Quoting G. K. Chesterton, *I would maintain that thanks are the highest form of thought, and that gratitude is happiness doubled by wonder*. I am indeed sincerely grateful for all what happened in the past four and a half years, which was made possible by many people, many more than those I can list here.

I would like to start by thanking those people who have supervised my work day after day. Simon, I had the privilege to start my PhD learning from you how to model a protoplanetary disk and that one should never stop to run checks: you will always be my coding guru. Mihkel, you have accompanied me as an older brother would do and I appreciated how you tolerated me also as office mate; furthermore, you will always be the first Estonian I have met. But more than anybody else I want to express my gratitude to the woman who managed to drag me far from the Alps, introduced me to Astrochemistry, challenged me to always go one step forward, supported me with a lot of little practical things, and made me reach achievements I would have never thought to reach (like swimming with the sharks).

The Sterrewacht has accompanied me, supported me and made me grow as a scientist and as a person. I have always felt challenged to reach for the stars and reassured that I could make it. This went through my fellow PhD students, the postdocs, the faculty members, in particular Elena and Xander, as well as the PBC committee and the dedicated support staff, who has always made my life easier. More specifically, I would like to mention the computer group lead by Erik: you are probably the best IT in the world. Also, a great thanks goes to the Allegro group: Luke, Ciriaco, Michiel, Daniel, Carmen, Liz, your support with ALMA data has been one of the most precious things.

In Leiden I have been part of a fantastic and unique group, which helped me to complete my PhD and, most importantly, made it fun. Its composition evolved during the years and the number of people to acknowledge is very large. Let me start with my office mates. Catherine, you have been a real inspiration for me: I like that you are a tough woman, smart and hard worker, but most of all I enjoyed your Irish accent and your sarcasm. I have learned much from you, from astrochemistry to making fresh coffee with a french press. Xiaohu, sharing office with you showed me the beauty of cultural diversity and I thank you for leaving me your desk and your

---

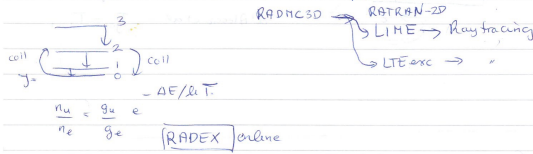
good luck plant. Arthur, you are simply remarkable! Thanks for teaching me many things, from coding to dutch slang, for your loud and contagious laugh and for being in the office with me early in the morning. Sierk, your encyclopaedic knowledge has always impressed me and I have enjoyed learning about dutch culture from you. Lukasz, thanks to you I can claim I know some Polish words and that I shared the office with the second best coffee maker of Poland: I enjoyed your fresh enthusiasm about everything, from the starry sky, to science, to the mountains. Now it is time for the best room mates at conferences. Paola, you have been a true friend to me: I miss our chats and our coffees and I hope that we will work again together in the future. Do not forget to organise that conference in Cartagena! Merel, how would I do without you: you are so accountable! Thanks for all your human and practical support, I will miss that. Then my gratitude goes also to Nienke, for welcoming me in the group, Maria, for her strength, Nadia, for her delicious cakes, Agata, for being a fellow PhD-mother, to Irene per la sua simpatia, Christian for his enthusiasm, and Koju for his optimism. I would not have learned so much without all the postdocs, Vienney, Alvaro, John, Magnus, Alan, Daniel, Joe and Kenji: thanks for being there for me when I needed it. Thanks to Niels and Nico: we started together and I have been so happy to have you there during these years. I owe a lot to Leon, the first Master student I have supervised: you have done such a good job that now I am spoiled! Thanks for contributing to my PhD thesis. Finally, a warm grazie to the Italian members of the group, Davide, Stefano and Paolo. I am grateful to have had you as travel companions: you were there to support me when the motivation was going down, and to rejoice with me for the beautiful things happening. Of course my PhD thesis would not have been so pretty without my favourite designer, Laura.

I have enjoyed very much being part of the Lupus collaboration, both from a scientific and human point of view. Jonathan, thanks for leading our team in such a friendly way, for going often against the grain and for hosting us in your beautiful house in Hawaii. Megan, it was great meeting you and visiting you: thanks for showing me around in Hawaii and for letting me know only one year later that I had indeed swum with the sharks. Marco, we know each other since we were freshmen and working with you as a collaborator has been incredible. Last, but not the least, thanks to Leonardo and Antonella for your curiosity, your love for the data and your mentoring.

I would like to thank my parents and my family for always supporting me and for showing their interest in my research. To conclude, I would like to show my gratitude to the four most important people in my life. Carlo, without your tireless backing and cheering I would have never reached the end of this PhD. Caterina, Ambrogio, and Monica, you have been the most beautiful gifts of these last four years: this PhD without you would have been definitely much less fun!

0) Background reading

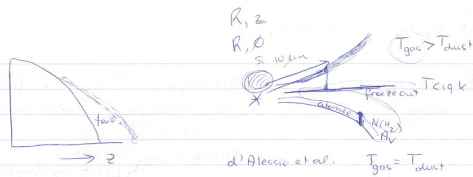
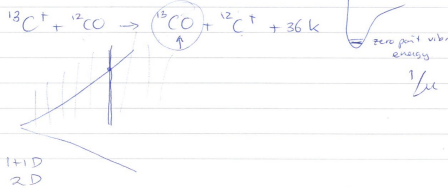
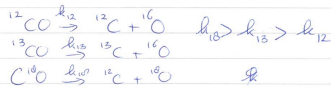
1) Parametrized disk - HD 163296  $^{13}\text{C}$ ,  $\text{C}^{18}\text{O}$  fits to models  $^{12}\text{C}/^{13}\text{C}$  fixed ALMA data.  $r/\text{C}^{18}\text{O}$  at  $6\mu$  fixed at 500



→ Small grid of models

2) Run physical-chemical models Simon.

$$^{12}\text{C}/^{13}\text{C} = 65 \neq ^{12}\text{CO}/^{13}\text{CO}$$



3) Compare with ALMA data

Large sample of disks  $^{13}\text{CO} 3-2$ ,  $\text{C}^{18}\text{O} 3-2$ , cont  
CN 3-2  $\left\{ \begin{array}{l} 34\% \text{ 6 Hz} \\ 110\% \text{ 6 Hz} \end{array} \right.$   
cont disk  $\left\{ \begin{array}{l} 34\% \text{ 6 Hz} \\ 110\% \text{ 6 Hz} \end{array} \right.$

Figure 12.1: Almost everything was there since the beginning - Pen and paper initial overview of this PhD Thesis by Ewine.